Fall 2013

Multiscale Modeling Of The Hierarchical Structure Of Cellulose Nanocrystals

Fernando Luis Dri
Purdue University

Graduate School ETD Form 9
(Revised 12/07)

PURDUE UNIVERSITY
GRADUATE SCHOOL
Thesis/Dissertation Acceptance

This is to certify that the thesis/dissertation prepared

By Fernando Luis Dri

Entitled
MULTISCALE MODELING OF THE HIERARCHICAL STRUCTURE OF CELLULOSE
NANOCRYSTALS

For the degree of   Doctor of Philosophy

Is approved by the final examining committee:

Pablo D. Zavattieri   Louis G. Hector Jr.
                    Chair
Vikas Tomar

W. Jason Weiss

Robert J. Moon

To the best of my knowledge and as understood by the student in the *Research Integrity and Copyright Disclaimer (Graduate School Form 20)*, this thesis/dissertation adheres to the provisions of Purdue University's "Policy on Integrity in Research" and the use of copyrighted material.

Approved by Major Professor(s): Pablo D. Zavattieri
                                _____

Approved by: Michael Kreger   4 Nov. 2013
                    Head of the Graduate Program   Date

MULTISCALE MODELING OF THE HIERARCHICAL STRUCTURE OF

CELLULOSE NANOCRYSTALS

A Dissertation

Submitted to the Faculty

of

Purdue University

by

Fernando Luis Dri

In Partial Fulfillment of the

Requirements for the Degree

of

Doctor of Philosophy

December 2013

Purdue University

West Lafayette, Indiana

TABLE OF CONTENTS

ABSTRACT

Dri, Fernando Luis. Ph.D., Purdue University, December 2013. Multiscale Modeling of the Hierarchical Structure of Cellulose Nanocrystals. Major Professor: Pablo D. Zavattieri.

Cellulose constitutes the most abundant renewable polymeric resource available today. It considered an almost inexhaustible source of raw material, and holds great promise in meeting increasing demands for environmentally friendly and biocompatible products. Key future applications are currently under development for the automotive, aerospace and textile industries. When cellulose fibers are subjected to acid hydrolysis, the fibers yield rod-like, highly crystalline residues called cellulose nanocrystals (CNCs). These particles show remarkable mechanical and chemical properties (e.g. Young Modulus ~200 GPa) within the range of other synthetically-developed reinforcement materials. Critical to the design of these materials are fundamental material properties, many of which are unavailable in the existing literature. A multiscale framework has been developed to predict and describe the thermo-mechanical characteristics of cellulose nanocrystals using state-of-the-art computational tools capable of connecting atomistic based simulations to experiments through continuum based modeling techniques.

First-principle density functional theory and molecular dynamic simulations were utilized at the atomistic level. Longstanding issues regarding the elastic and thermal expansion anisotropies for crystalline cellulose have been studied in terms of the single-crystal elasticity tensor and the thermal expansion tensor components.

First-principles phonon calculations via Van der Waals density functionals as well as reverse non-equilibrium molecular dynamics simulations were used to gain a fundamental understanding of defect-free, crystalline cellulose thermo-mechanical properties. Entropy, enthalpy, constant pressure heat capacity, thermal expansion tensor, thermal conductivity, Young's modulus, and Poisson's ratio, were computed over a wide range of temperatures (0 to 500 K). A comprehensive study of the hydrogen bond structure that characterizes crystalline cellulose has been conducted in an attempt to ascertain the roles that inter- and intra- molecular hydrogen bonds play in determining the mechanical properties of CNCs. Five different force fields/parameter sets were compared with experimental results and first-principles simulations in terms of their ability to predict the following properties: lattice parameters and angles, linear elasticity tensor and linear thermal expansion tensor. Continuum based modeling techniques were used to answer fundamental questions regarding the role of hydrogen bonding in the mechanical response of CNCs. A variety of finite element-based continuum models were specifically developed for cellulose chains and non-bonding interactions (van der Waals, Coulomb and hydrogen bonds). As a result, a complete multiscale framework capable of reproducing the mechanical behavior of cellulose nanocrystals has been developed.

CHAPTER 1. INTRODUCTION

There is an increase awareness of the urgent need to build a sustainable future. Consumers, industries, and governments are increasingly demanding products made from renewable and sustainable resources that are biodegradable, non-petroleum based, carbon neutral, and pose low environmental, animal/human health and safety risks [1]. Cellulose constitutes the most abundant renewable polymer resource available today. As a chemical raw material, it has been used in the form of fibers or derivatives for nearly 150 years for a wide spectrum of products and materials in daily life, such as food, paper production, biomaterials and pharmaceuticals [2, 3]. Representing about 1.5×10^{12} tons of the total annual biomass production [4], it is considered an almost inexhaustible source of raw material for the increasing demand for environmentally friendly and biocompatible products.

When cellulose fibers are subjected to acid hydrolysis, the fibers yield rod-like crystalline residues called cellulose nanocrystals (CNCs). The geometrical characteristic of CNCs showed a high variability depending on the cellulose source and the technique used for the extraction [2]. Cross sectional dimensions of CNCs are in the order of a few nanometers but the length spans from tens of nanometers to several micrometers [1, 2].

These particles show remarkable mechanical and chemical properties within the range of other humanly-developed reinforcement materials. Surface functionalization allows the tailoring of particle surface chemistry to facilitate self-assembly, controlled dispersion within a wide range of matrix polymers, and control of both the particle-particle and particle-matrix bond strength [3]. CNC composites produced to date can be, transparent, have tensile strengths greater than cast iron, and have very low thermal expansion coefficients (CTE) [1].

Some of the potential applications of CNCs are: barrier films, antimicrobial films, transparent films, flexible displays, reinforcing fillers for polymers, biomedical implants, pharmaceuticals, drug delivery, fibers and textiles, templates for electronic components, separation membranes, batteries, supercapacitors, electroactive polymers, and many others [1-3, 5-7].

The advent of cellulose nanomaterials (CN) has spurred new research aimed at understanding the structure and properties of these materials and how to exploit their unique properties in new technologies [1, 7, 8].

1.1   Objectives of the thesis

The research goal of this project is to develop a multiscale framework capable of predicting the mechanical and thermophysical properties of cellulose nanocrystals and that can be extended to any material with similar characteristics such as other polysaccharides (e.g. α-chitin, amylose). In turn, this will help unveiling the *internal mechanical behavior of CNC*, *analyze the CNC/CNC and CNC/substrate interaction* and

study the interaction between CNCs and the surrounding media for future CN-based material design.

The objectives of this thesis are:

1. Investigation of the key mechanisms that define the mechanical response of CNCs.

2. Quantification of the role of each of those mechanisms and the interaction between them.

3. Development of a continuum-based model capable of reproducing the mechanical behavior of a single CNC in vacuum.

Atomistic modeling based on first-principles density functional theory (QM-DFT) and molecular dynamic simulations (MD) are going to be used to study the overall thermo-mechanical properties of CNCs. The role of bonded interactions (covalent bonds) and non-bonded interaction (van der Waals, Hydrogen bonds, Coulomb) is key to understanding the elastic and thermal expansion anisotropies of cellulose. A comprehensive study of the hydrogen bond (H bond) structure is necessary to elucidate the roles of inter- and intra- molecular H bonds in the mechanical response of CNCs.

Traditional continuum modeling techniques at the macroscale level cannot be directly applied to represent the behavior of CNCs. On the other hand, full scale atomistic simulations exceed current technological capabilities. Multiscale modeling allows to tackle the problem bridging several time and length scales. A continuum based multiscale model will be constructed based on the hypothesis that bonded and non-bonded interactions can be decoupled. Bonded interactions determine the cellulose chain mechanical behavior whereas non-bonded interactions define inter-chain mechanical

behavior (i.e., size of the crystal and lattice parameters). The response of the crystal as a whole arises from the mutual work of these two mechanisms. This hypothesis can be extended into two statements:

1. The structural behavior of the cellulose chain is first decoupled from the non-bonded interaction and can be described by structural elements.

2. Non-bonded interaction will be regarded as external forces to these structural elements in a continuous or discrete manner.

To quantify bonded interactions several tasks need to be performed: 1. A comprehensive study on the response of a single cellulose chain under several mechanical and thermal deformations; 2. the effects of intra-chain H bonds (H bonds being formed by atoms that belong to the same cellulose chains) on the overall deformation of the chain; 3. the existence of size effects in the response of the system (mechanical response with respect to the number of glucose rings involved) and; 4. the contribution of end effects (termination of the cellulose chain).

Understanding the non-bonded interaction will require specific simulations of thought-experiments that resemble commonly used fracture mechanics tests (i.e., Double cantilever beam, peel off test, pull out test). Special attention will be given to the response of inter-chain H bonds (H bonds being formed by atoms that belong to different cellulose chains). The existence of size effects in the response of the system also needs to be taken into account.

Numerical simulations will be used to prove the initial hypothesis and will allow to progress in the path towards a complete understanding of the physic involved in the behavior of cellulose nanocrystals.

1.2   Organization of the thesis

Chapter two provides a comprehensive introduction to cellulose nanocrystals known geometrical and thermo-mechanical properties. Reported values for lattice parameters, morphology and dimensions, coefficient of thermal expansion and thermal conductivity are introduced. Longstanding issues regarding the elastic and thermal properties of cellulose are discussed.

The third chapter provides an introduction to multiscale modeling focusing on different simulation techniques from first-principles density functional theory to continuum modeling. The internal hierarchical structure of cellulose is presented and a multiscale approach to CNCs modeling is introduced. The rest of the thesis is divided in three sections, each of them focused in one specific simulation technique: QM-DFT, MD and continuum modeling.

Chapters four and five present a comprehensive study of the elastic and thermal expansion anisotropies for crystalline cellulose in terms of the single-crystal elasticity tensor and the thermal expansion tensor components. First-principles phonon calculations via Van der Waals density functionals as well as reverse non-equilibrium molecular dynamics simulations are used to gain a fundamental understanding of defect-free, crystalline cellulose thermo-mechanical properties. Entropy, enthalpy, constant pressure

heat capacity, thermal expansion tensor, thermal conductivity, Young's modulus, and Poisson's ratio, are computed over a wide range of temperatures (0 to 500 K).

Chapters six, seven and eight focus their attention on bonded and non-bonded interactions. A comprehensive study of the hydrogen bond structure that characterizes crystalline cellulose is conducted in an attempt to ascertain the roles of inter- and intra-molecular H bonds in the mechanical properties of CNCs. Five different force fields/parameters are compared with experimental results and quantum mechanics simulations in terms of their ability to predict three different properties: lattice parameters, elastic constants and thermal expansion.

Chapter nine presents continuum based modeling techniques used to answer fundamental questions regarding the role of hydrogen bonding in the longitudinal mechanical response of CNCs and chapter ten introduces a variety of finite element-based continuum models specifically developed for cellulose chains and non-bonding interactions (van der Waals, Coulomb and hydrogen bonds).

Finally, chapter eleven summarizes the novel findings and relevant conclusions of this thesis.

CHAPTER 2.   BACKGROUND

Cellulose is a linear chain of ringed glucose molecules with a repeat unit comprised of two anhydroglucose rings ($(C_6H_{10}O_5)_n$; n=10,000 to 15,000) linked together through glycosidic oxygen bridges (i.e., β 1-4 glucosidic bond) [7]. It is produced by trees, plants, algae, bacteria, and is found in the dermis of certain marine creatures (tunicates) [1].
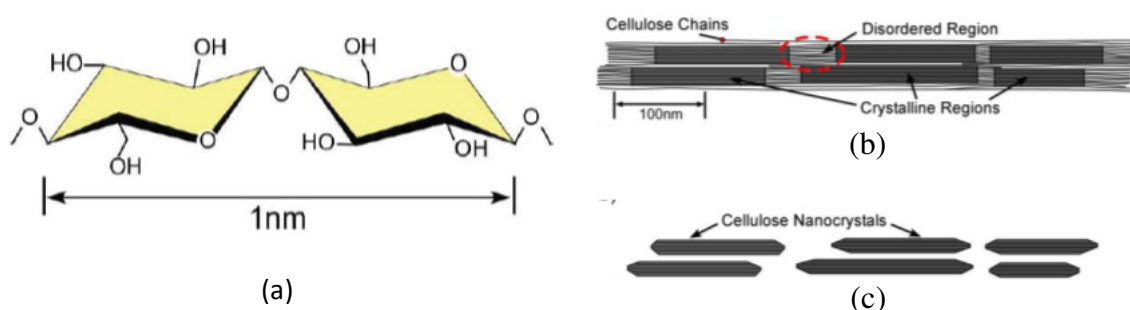
Figure 2-1 Schematics of (a) single cellulose chain repeat unit, (b) idealized cellulose microfibril showing one of the suggested configurations of the crystalline and amorphous regions, and (c) cellulose nanocrystals after acid hydrolysis dissolved the disordered regions. Adapted from [1].

During biosynthesis, multiple cellulose chains form bundles, called cellulose fibrils, which have regions where the cellulose chains arrange with a high degree of order (crystalline-like), and regions that are disordered (amorphous-like). The most basic classification method divides crystalline cellulose types into 4 basic polymorphs that are identified as I, II, III or IV, each one having its own subtype [3].

Cellulose I, also called native cellulose, has a mix of two polymorphs, viz., cellulose I_α, which has a triclinic P_1 (#1) structure, and I_β, which has a monoclinic $P2_1$ (#4) structure, that coexist in various proportions depending on the source of the CNC [9, 10]. The I_α structure is the dominant polymorph in most algae and bacteria, whereas I_β is the dominant polymorph for higher plant cell wall cellulose and in tunicates [1, 11].

| (a) | (b) | (c) | (d) |
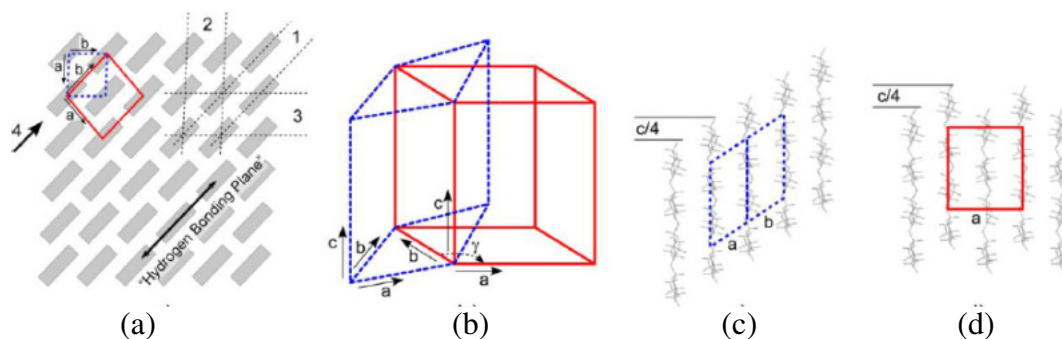
Figure 2-2 Schematic of the unit cells for cellulose I_α (triclinic, dashed line) and I_β (monoclinic, solid line). (a) projection along the chain direction with the I_α and I_β unit cells superimposed on the cellulose I crystal lattice (b) relative configuration of I_α with respect to I_β unit cell and the displacement of the hydrogen bonding sheets for (c) I_α of +c/4, and for (d) I_β alternating +c/4 and –c/4. Adapted from [1].

A further classification of cellulose I can be based on the hydrogen bond network patterns, A and B, proposed by Nishiyama [9]. The relative occupancies of the two networks are different according to the polymorph: network A occupies ~70-80% of all the chain positions in I_β, but only ~55% in I_α [10, 12].

This study focuses on cellulose I_β with network A since it is the most commonly occurring polymorph in higher plant cell wall cellulose and in tunicates [1, 13, 14].

The fundamental thermo-mechanical properties of cellulose I_β (i.e., elasticity tensor, thermal expansion tensor, thermal conductivity, among others) are not completely understood or quantified. This is partially due to difficulties in experimental testing,

propagation of uncertainties in these experimental tests [15], and intrinsic material variability in crystalline cellulose being tested (e.g. different crystal structures, defects, percent crystallinity, etc.) [1]. Recent theoretical efforts to predict cellulose properties, such as the Young's modulus, have shown substantial differences in values which are likely due to differences in model parameters, simulation method, configuration of the modeled structure, and incorporation of hydrogen bonding [14] and Van der Waals interactions [1, 16].

2.1   Morphology and dimensions of cellulose nanocrystals

A wide variety of cellulose nanoparticles can be obtained from different natural sources, ranging from woods and animals to bacteria [1, 2, 17-19]. Different biosynthesis processes generate different particle morphologies and crystalline structures. Moreover, the extraction process (mechanical or chemical) also contributes modifying the final characteristics of the cellulose particles [1, 2].

The segregation of cellulose particles from the cellulose source materials can be divided in two stages [1]. The first step is a purification and pre-treatment of the source material which depends on the cellulose origin. The second step involves separation of the crystalline components from the purified cellulose. The three basic separation approaches are: mechanical treatment, acid hydrolysis, and enzymatic hydrolysis [1, 2, 17].

Acid hydrolysis is the main process used to produce cellulose nanocrystals [3]. Native cellulose consists of a mix of amorphous and crystalline regions. When cellulose fibers are subjected to a harsh acid treatment, the amorphous regions break up, liberating the crystalline regions [17]. The final characteristics of the crystal depend on many

parameters; for example, longer reaction times lead to shorter nanocrystals [20]. Different acids also affect the suspension properties: hydrochloric acid hydrolysis yields cellulose rods with minimal surface charge, whereas the use of sulfuric acid provides highly stable aqueous suspensions [20].

Cellulose nanocrystals size, dimensions and shape are also determined to a certain extent by the nature of the cellulose source [1, 20]. Figure 2-3 provides a graphic representation of the different crystalline sizes and shapes whereas Table 2-1 provides morphology information including approximate number of chains and atoms in the crystal. Wood CNCs are 3-5 nm in width and 100-300 nm in length [1, 3, 20], while those for *Valonia*, a species of algae found in oceans, are reported to be 20 nm in width and 1000-2000 nm in length [1, 3, 20]. Likewise, cotton gives CNCs 5-10 nm in width and 100-350 nm long, and *Tunicate*, a sea animal, gives a 10-20 nm in width and 500-2000 nm long. The aspect ratio, defined as the length-to-width (*L/w*), spans a broad range and can vary from 10 to 30 for cotton and up to 100 for tunicate [3].

Table 2-1 Examples of the length, width and aspect ratio from various CNC sources [1, 3, 18-20]. Number of cellulose chains and atoms in the system (in Millions) computed based on idealized cellulose particle cross-sections [1].

Source	Length (L) [nm]	Width (W) [nm]	Aspect ratio (L/W)	Cellulose chains	Number of atoms
Wood	100	3 - 5	10 - 20	36	0.3 M
	300				0.4 M
Tunicate	500	10 - 20	25 - 200	488	20 M
	2000				80 M
AC Valonia	1000	10 - 20	50 - 200	1170	95 M
	2000				190 M
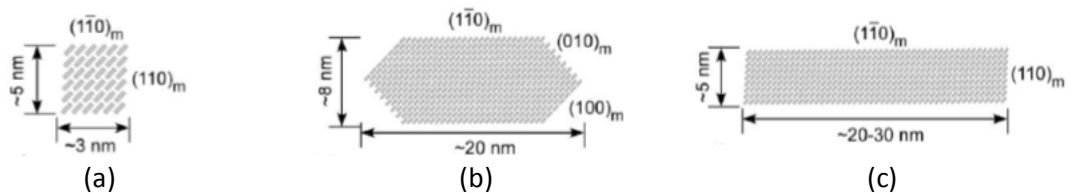
Figure 2-3 Schematics of idealized cellulose particle cross-sections for (a) wood CNC, (b) tunicate CNC and (c) AC Micrasterias. Adapted from [1].

2.2   Cellulose I$_\beta$: lattice parameters

The lattice parameters for cellulose have been measured by several authors [9, 10, 12, 21-27] using different experimental techniques and crystal sources. For the cellulose I$_\beta$ network A structure, Nishiyama et al. [9] reported: $a = 7.784$ Å, $b = 8.201$ Å, $c = 10.380$ Å, $\alpha = 90°$, $\beta = 90°$, $\gamma = 96.55°$, with a 658.3 Å^3 volume at 293 K. Most of the measured lattice parameters exhibit variations around 1% over a wide range of temperatures and crystalline sources, except for the lattice parameter a. As cellulose I$_\beta$ is cooled or heated, the lattice remains remarkably constant in the directions within the hydrogen bonded planes containing the chains (i.e., b and c); the same is not true along the a axis direction where the contractions or expansions are controlled by weak van der Waals interactions and interplanar hydrogen bonding [21, 28]. Nishiyama et al. 2008 [12] reported a change from 7.64 to 7.76 Å in the a lattice parameter when the temperature was raised from 15 K to 295 K. Langan et al. [21] reported a value of 7.83 Å for the same parameter at 298 K. Although hydrogen bond interactions are present along the stacking direction (a-axis), they apparently do not prevent thermal expansion at temperatures up to the transition to a high-temperature phase at ~200 °C [29]. Experimental lattice parameter and cell volume values are summarized in Table 2-2.

Table 2-2 Experimental lattice parameters (*a*, *b*, *c*, and γ) for cellulose I_β from different sources. The temperature at which each experiment was performed is reported in the last column. The symbol "-" means that the temperature was not reported.

Ref	Methodology	Type of cellulose	*a* [Å]	*b* [Å]	*c* [Å]	γ [Deg]	Volume [Å³]	Temp [K]
[24]	X-Ray Diffraction (XRD)	Bleached ramie (cellulose I)	7.9	8.35	10.3	96	675.7 [1]	-
[26]	Electron Diffraction	Green alga	8.01	8.17	10.36	97.3	672.5 [1]	293
[27]	XRD	Valonia (cellulose I_β)	7.85	8.27	10.38	96.3	669.8 [1]	-
			7.82	8.16	10.32	97.5	652.9 [1]	-
[9]	XRD and Neutron Fiber Diffraction (NFD)	Tunicate (cellulose I_β)	7.784	8.201	10.38	96.5	658.3	293
[21]	XRD	Tunicate (cellulose I_β)	7.76	8.19	10.38	96.51	655.4	100
			7.83	8.19	10.38	96.55	661.3	298
[12]	XRD and NFD	Tunicate (cellulose I_β)	7.64	8.18	10.37	96.54	643.9	15
			7.76	8.20	10.37	96.62	655.5	295

1   Not reported, computed based on the lattice parameters

2.3   Cellulose I_β: mechanical properties

Mechanical properties of cellulose nanocrystals are difficult to experimentally characterize owing largely to extreme anisotropy and uncertainties about the structure of these materials. For example, reported experimental values for the Young modulus of cellulose I_β show a wide variation that is hard to explain considering the defect-free crystalline structure typically observed in CNCs [23-25, 30-35]. Unfortunately, there is no standardization of the coordinate system and nomenclature used to measure the elastic moduli making quantitative comparisons of the elastic behavior between experiments and theory rather difficult. Most authors agree on defining both an axial or longitudinal Young modulus, E_A, which is aligned with the longitudinal axis of the cellulose I_β unit cell, and an additional Young modulus, perpendicular to the longitudinal axis, usually reported as the transverse modulus, E_T. Early studies using x-ray diffraction [23-25, 30,

31] measured values of E_A ranging from 90 to 138 GPa. Recently, Diddens et al. [32] reported values of $E_A = 220 \pm 50$ GPa and $E_T = 15 \pm 1$ GPa using inelastic x-ray scattering (IXS). Diddens and coworkers [32] claimed that IXS was not affected by the amorphous zones occurring in natural cellulose, and the elastic behavior was mostly related to the highly crystalline regions. Alternatively, larger uncertainties have been reported from atomic force microscopy (AFM) measurements of cellulose I_β elastic properties. For example, Lahiji et al. [35] and Wagner et al. [33] reported $E_T = 8.1$ GPa with a 95% confidence, which translates into an interval ranging from 2.7 to 20 GPa. Relating experimental measurements to a specific crystallographic orientation is challenging since it is difficult to estimate the alignment of the CNC with respect to the substrate [35]. Moreover, with no additional information on the direction assigned to E_T, it may not be possible to properly interpret the experimental data and, therefore, any attempt to compare experiments with computational predictions is difficult. Uncertainties about the shape of the CNC after sample preparation and the determination of the crystallographic planes during the experiments contribute to this important challenge.

Table 2-3 Summary of Young's modulus and Poisson's ratio values from different crystalline sources and authors. The symbol "-" means that the corresponding value was not reported.

Ref	Methodology	Type of cellulose	E_A [GPa]	E_T [GPa]	ν_t	Temp [K]
[23-25, 30, 31]	X-Ray Diffraction (XRD)	Ramie (cellulose I)	90 to 138	-	-	-
[36]	XRD	Ramie fiber (cellulose I_β)	-	-	$\nu_{[200]/[004]} = 0.377 \pm 0.041$ [1] $\nu_{[110]/[004]} = 0.639 \pm 0.338$ [1]	Room Temp
[32]	Inelastic X-Ray (IXR)	Flax fibers (cellulose I_β)	220 ± 50	14.8 ± 0.8	-	-
[33]	Atomic force microscope (AFM)	Tunicate CNC	-	2.7 to 20	-	-
[34]	AFM+Finite Elements	Wood CNC	-	24.8 ± 7.0	-	-
		Cotton CNC		17.7 ± 5.0		

[1] Upper limit of the standard deviation.

2.4   Cellulose I$_\beta$: coefficient of thermal expansion

The experimentally measured thermal expansion coefficients (TECs) of cellulose I$_\beta$ are also scattered [37-40]. The range of reported TECs along the *a, b,* and *c*-axes of the I$_\beta$ structure are as follows: $9.8\text{-}13.6\times10^{-5}$ K^{-1}, $0.5\text{-}4.6\times10^{-5}$ K^{-1}, and 0.6×10^{-5} K^{-1}, respectively. Additionally, at temperatures approaching 475-500K, the I$_\beta$ structure transitions to a high-temperature phase that shows a different TEC response. Compared with other organic compounds, these previous studies suggest a relatively high elastic and low thermal expansion behavior of cellulose I$_\beta$ and also indicate extreme property anisotropies as a result of the bonding character in cellulose I$_\beta$.

2.5   Cellulose I$_\beta$: thermal conductivity

There is currently a dearth of information on thermal conductivity (k) values for cellulose I$_\beta$ both in the experimental and the theoretical literature. Shimazaki et al. [41] produced Nano Fibrillated Cellulose (NFC) (58 wt%)-epoxy matrix reinforced composite films that had thermal conductivity of 1.1 W m^{-1} K^{-1} in the in-plane direction and 0.23 W m^{-1} K^{-1} in the thickness direction. These values have been experimentally measured at room temperature using calorimetry and thermal wave analysis. Results showed that there is a 7-8 times increase in the in-plane direction of the film and 1-2 in the thickness direction compared to the neat epoxy matrix. The increased thermal conductivity of the composites provides the capability to dissipate more heat for a given input heat flux, which lowers the composite temperature and thus improves the thermal stability preventing chemical and mechanical degradation [1].

CHAPTER 3. MULTISCALE MODELING

3.1   Introduction to multiscale modeling

Given a specific problem, engineers usually focus on a particular scale, disregarding physical phenomena happening beyond the analyzed size and time frame. If our interest is the macroscopic behavior, we model microstructural effects by constitutive equations and well know approximations (e.g., plasticity models). On the other hand, in the study of solid state physics, the interest lies at the atomic or electronic level, often assuming that all processes in larger scales are homogenous [42].

This dichotomy can lead to serious complications when analyzing some of the physical phenomena occurring in nature. Empirically obtained macroscopic models are usually very efficient but are often not accurate enough or fail to reproduce a specific behavior. Micromechanical and atomistic models may offer better accuracy but they are often too expensive to be used in model systems of real interest.

In order to overcome these barriers researchers in different areas began investigating multiscale modeling strategies to connect the different length and time scales.

The philosophy of multiscale modeling is based on the viewpoint that:

1. Any system of interest can be analyzed as a hierarchy of models with different levels of complexity. When a coarse model is not detailed enough to represent a given phenomenon it can be substituted by a finer model. This particular characteristic allows better representations of fundamental physical phenomena without an unnecessary increase in the model complexity.

2. Coarse grained models can be coupled with detailed models that are active only in certain regions. These small regions may contain singularities, cracks, defects, or some other interesting events that could be crucial for the correct evolution of the model. Coupling models of different complexity in different regions allows developing modeling strategies that have efficiency comparable to coarse grained models with accuracy comparable to detailed models.

This particular approach has the advantage that is not only useful for a few isolated problems, but can be applied in many areas of science and engineering [42]. Multiscale modeling techniques are becoming increasingly necessary given the growing interest in nano-composite materials. These materials present macroscale behavior that is direct influenced by effects occurring at the atomic level. Controlling these small-scale properties can be the key to tuning the properties of these materials and opens up a myriad potential applications. Traditional modeling techniques at the macroscale level are not detailed enough to accurate represent the behavior of nano-composite materials. On the other hand, full scale atomistic simulations turn to be impractical for modeling large systems, usually requiring simulation times and computational resources that

exceed current hardware. Multiscale modeling allows to tackle the problem bridging several time and length scales.

Atomistic models used to accurately represent the physical system must be simplified (or coarse-grained) preserving only the relevant degrees of freedom. A series of steps need to be applied to transfer the relevant information from the atomistic models to the coarse grained system. Those steps consist of defining the right parameters (selection or development of the coarse-graining method), systematically determining the values for those parameters from atomistic simulations, and clearly specifying the range of validity of those methods and parameters [43].

Among some of the problems related to this approach it is found that a connection between scales is usually hard to find and, for many applications, the defined parameters are not general and can only be expected to work in certain conditions. That is assuming that the right set of parameters exists and can be transfer to a higher scale, which is not always true. Regardless of the difficulties inherent of the process, the multiscale approach provides a natural mechanism for modeling systems otherwise impossible to analyze [44]. For additional information on successful implementations of multiscale modeling in biological and non-biological materials refer to [45-52].

Today super computers and state-of-the-art parallelized software allows for solving many non-linear problems directly without using any mathematical approximation. This powerful tool provides a bridge between analytic theory and experiment, allowing controlled *computer experiments* that can be used for exploration beyond traditional methods [53]. Computers can be used to analyze any time or length scale, from atoms to

solar systems. Coupled with the multiscale approach, computer simulations can be used to open countless possibilities for researchers.

An efficient modeling strategy requires special simulation techniques appropriate to the respective relevant length and timescales under investigation. The following paragraphs provide a short overview of the hierarchy of length scales common in materials science and present some of the simulation software currently available.

3.1.1   Electronic/Atomistic scale

It is known that electrons moving in atoms and molecules do not obey classical Newton equations of motion. People long ago tried to treat electronic motion classically, only to find out that experimental measurements were not consistent with such a treatment [54].

It was not until scientists developed a new set of laws, those of quantum mechanics, that laboratory observation could be reconcile with analytical models. The mathematical formulations of quantum mechanics are abstract and generally involve solving the Schrödinger equation approximately based on the Born-Oppenheimer approximation. A mathematical function, known as the wavefunction, provides information about the probability amplitude of position, momentum, and other physical properties of a particle inside the system. Modeling on this scale requires taking into account the degrees of freedom of the electrons explicitly [53] which remarkably increase the computational cost of the simulation. With ab-initio methods, the only information that has to be provided is the atom types and their positions within the system. In contrast, semi-empirical or empirical approaches require a model of the interactions between the atoms to be supplied. There are many well-known software packages used in materials science

and quantum chemistry such as QUANTUM ESPRESSO, VASP and GAUSSIAN to name a few. The majority of the simulation packages are based on density-functional theory, plane waves, and pseudopotentials. The results of quantum mechanical calculations are often used in the design of classical molecular force fields, providing a connection to the next scale [53, 55].

3.1.2 Atomistic/Microscopic scale

Atomistic simulations models materials at the level of atoms without explicitly considering electronic interactions [56]. Simulations performed at this level allow more flexibility than those typical of quantum mechanics and a wide range of properties of solids and fluids can be calculated [53]. As a result, a variety of researches in different fields (e.g. physics, chemistry, chemical engineering, molecular biology, biochemistry or even geochemistry) actively use atomistic simulations.

Systems analyzed at the atomistic scale are mainly governed by their energy; hence the motion of electrons can be neglected. As a consequence, individual atoms or even clusters of atoms can be described with methods based on classical interaction potentials [53].

In the case of Molecular Dynamics (MD), the actual motion of the atoms is simulated by evolving the atomic configuration in time according to Newton's equation of motion ($F = m\,a$) [56]. The MD method is simple in concept and easy to implement but is not hassle free. The simulation starts with a set of atomic coordinates and an associated atom type (e.g. Carbon, Oxygen, Hydrogen). Other parameters may also be needed depending on the type of simulation and complexity of the interactions that are being modeled. The

force acting over each atom is computed employing a force field obtained either empirically or based on quantum mechanics simulations. The forces are converted in accelerations, and using numerical time step algorithms, the atomic velocities and/or accelerations are updated to predict the position of each atom after a small time interval (time step). The result of this process is the evolution of the atom positions through time.

The process outlined above is very simple but very powerful. It is possible to compute experimentally measurable phenomena and to run simulations of setups that are impractical (or impossible) to reproduce in normal laboratory conditions. The most common type of analyses includes equilibration of the system at a given temperature, pressure and /or volume or calculating the time evolution of the ensemble when it is reacting to a specific disturbance. Recent developments have led to methods to compute additional properties such as diffusion constants or thermal conductivity [55].

Limitations of the molecular dynamic method are related mostly to the force field representation being used. The results of a simulation will be realistic only if the potential energy functions described in the force field mimics the forces experienced by *real* atoms in a given configuration. At the same time, a force field needs to use simple functional forms to speed up the mathematical evaluation of forces and interactions within the system. Designing a good force field is a challenging task! [57]. Additional problems arise when quantum effects start playing an important role in the evolution of the system. Dynamical events involving quantum effects such as tunneling of protons or electrons cannot be represented using standard force fields. This situations extends to other phenomena that have a partially quantum mechanical nature such as hydrogen bonds [58]. Modern force fields usually describe hydrogen bonds as Coulomb interactions of atomic

point charges. This is a crude approximation that can lead to inaccurate simulation results in systems that are governed by this type of interaction.

State-of-the-art MD simulations can be performed on systems containing millions of atoms and for simulation times close to a microsecond. While these numbers are certainly impressive, it may be possible to run into conditions where time and/or size limitations become important [59]. The time limitation is the most severe problem in MD simulations. Relevant time scales for biologically important processes extend over many orders of magnitude [57]. It is imperative to define the total time duration of the simulation to be long enough to be relevant to the time scales of the natural processes being studied.

For computer simulations using semi-empirical or classical force fields, there are several software packages available such as: CHARMM, GROMACS, AMBER, NAMD and LAMMPS [53]. Different software have different features and their own merits. The vast majority of simulation packages are capable of simulating soft materials (biomolecules, polymers), solid-state materials (metals, semiconductors) and coarse-grained or mesoscopic systems. They can be used to model atoms running on single processors or in parallel supercomputers and are being extended to comply with GPU accelerated computing.

3.1.3   Mesoscopic/Macroscopic scale

Continuum mechanics treats any system of interest as a continuum media rather than a collection of atoms and their interactions [42]. This assumption implies that the matter in the body is continuously distributed and fills the entire region of space it occupies.

Moreover, a continuum is a body that can be continually sub-divided into infinitesimal elements with properties being those of the bulk material.

Continuum theories can be branched in to two related fields: statics and dynamics. Statics models usually take the form of variational principles, for example, the static configuration of a material minimizes the total free energy of the system taking into account the work done by external forces [42]. On the other hand, dynamic models are generally written in the form of conservation laws (mass, momentum and energy).

The advantage of continuum models is that the number of relevant equations is reduced considerably. Constitutive relations are used to reproduce material macroscopic behavior based on an intrinsic microscopic phenomenon (i.e., the atoms that make up the system). This is where most of the empirical modeling in continuum theory comes in. For simple systems, linear constitutive relations have been remarkably successful [42]. For example, the Young modulus and the Poisson's ratio parameters can be used to effectively represent the elastic behavior of an entire family of materials.

Most practical design calculations involve complicated three dimensional geometries and a variety of nonlinear phenomena such as viscoelasticity, plasticity, large shape changes and contact. Most of these problems cannot be tackled using classical methods with closed form solutions, and hence they require the use of computer simulations. The finite element method (FEM) is by far the most widely used and versatile technique for simulating deformable solids [60].

The most distinctive characteristic of the finite element method is that a given domain is divided into a set of simple subdomains called finite elements [61]. By doing so, the original problem is replaced by a simpler one, therefore, only an approximate solution is

reachable. It is possible to improve or *refine* the solution by increasing the amount of elements used to represent the system at the cost of computational effort.

One of the most common applications for the FEM is the prediction of deformation and stress fields within solids subjected to external forces. When a solid is subjected to loading every point moves as the load is applied producing a deformation that can be measured. The displacement field specifies the motion that a particular point in the undeformed solid has experienced. Once the displacement field is known, the strain and stress fields in the solid can be deduced from solid mechanics relations. In most cases, the system of interest is in static equilibrium, this means that both external and internal forces acting on the solid sum to zero. Dynamic behavior of solids can also be studied with the FEM; examples include modeling vibrations in structures, problems involving wave propagation, explosive loading and crash analysis [60]. In addition, special finite element procedures are available to calculate buckling loads and their modes, as well as natural frequencies of vibration and the corresponding mode shapes for a deformable solid.

Many commercial and free codes implementing methods based on continuum theory are available for structural and coupled fluid-structural simulations in engineering applications [53]. A short reference list must include: ABAQUS, LS-DYNA, ANSYS, CalculiX, Code Aster and FEAP.

3.2   Multiscale modeling applied to cellulose nanocrystals

Nature has created efficient strategies to make materials with hierarchical internal structure that often exhibit exceptional mechanical properties. One such example is found in cellulose. These natural materials achieve a high order of functionality and mechanical

properties through a well-designed hierarchical structure with an exceptional control from the atomic level all the way to the macroscopic level. For engineering purposes, cellulose-based materials have been used for thousands of years essentially for their great qualities in many fields. However, nature has used cellulose for very specific and highly specialized purposes (e.g. structural support in plants, trees, etc.) based on its particular mechanical properties.
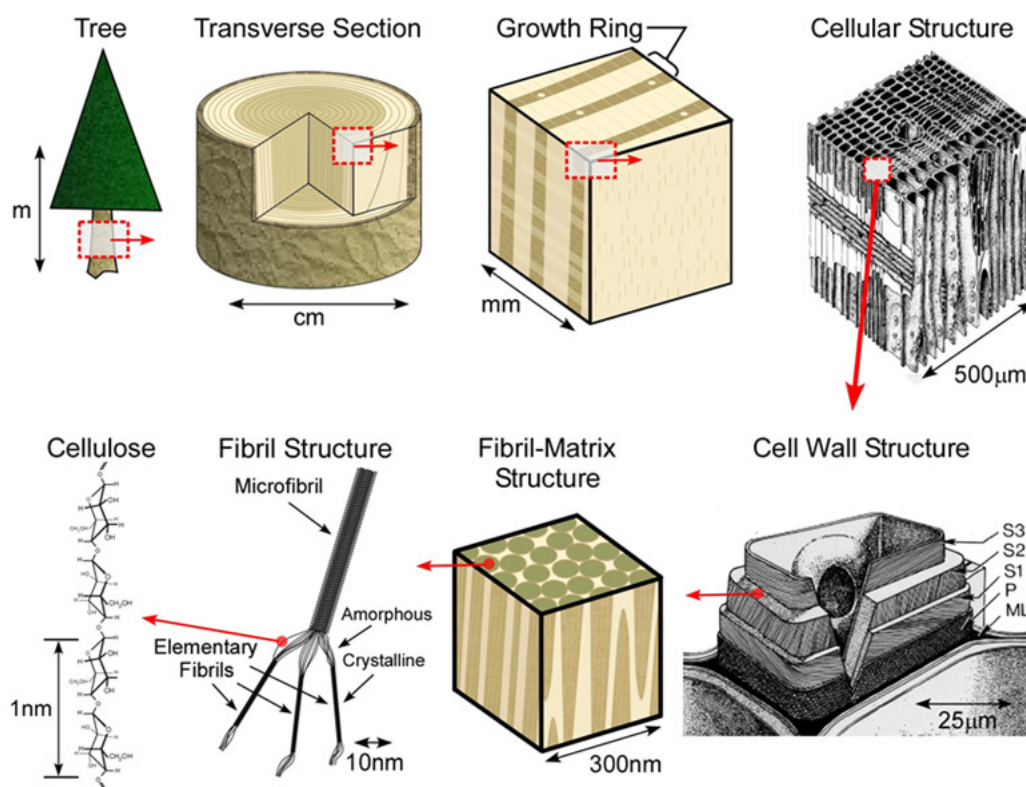
Figure 3-1 Schematic representation of the tree hierarchical structure. Note the different configuration defined at each structural level: Growth ring, earlywood and latewood, cellular structure, layer structure of cell wall, fibril-matrix structure, and the structure/configuration of the main polymer components (cellulose, hemicelluse, and lignin). Adapted from [1].

The native hierarchical structure shown in Figure 3-1 provides the perfect ground for multiscale modeling. It is easy to imagine the use of different modeling strategies based

on the structural level being analyzed, from the single cellulose chain to the fibril-matrix composite or even wood itself. Determining the right simulation strategy requires a deep understanding of the physical process involved in each of the characteristic scales.

Numerical simulations were used to prove the initial assumptions outlined in chapter 2 and were used to progress in the path towards understanding the mechanical behavior of a cellulose nanocrystal. Multiple modeling techniques were used depending on the time and length scale of interest. For the femtoseconds – nanometers scale the use of quantum mechanics techniques provided the model of atomic interactions in the most comprehensive form available today. Invaluable information of crystalline cellulose thermo-mechanical behavior was obtained at the most fundamental level but results were restricted by the system size that was possible to simulate. It is important to keep in mind that given any type of simulation, with any available tool, the restrictions will always be imposed by the size of the system (generally related to accessible memory) and the total time simulation time (generally related to the available computational power). The resources needed to run quantum mechanics simulations of an entire CNC crystal are beyond the capabilities of today most powerful computers.

Molecular dynamics provided the tools needed to reach larger time and length scales without incurring in prohibited simulation times. Whereas quantum mechanics simulations are limited to a hundred of atoms in a picosecond timescale, MD is capable of times up to microsecond with millions of atom involved (state-of-the-art simulations).
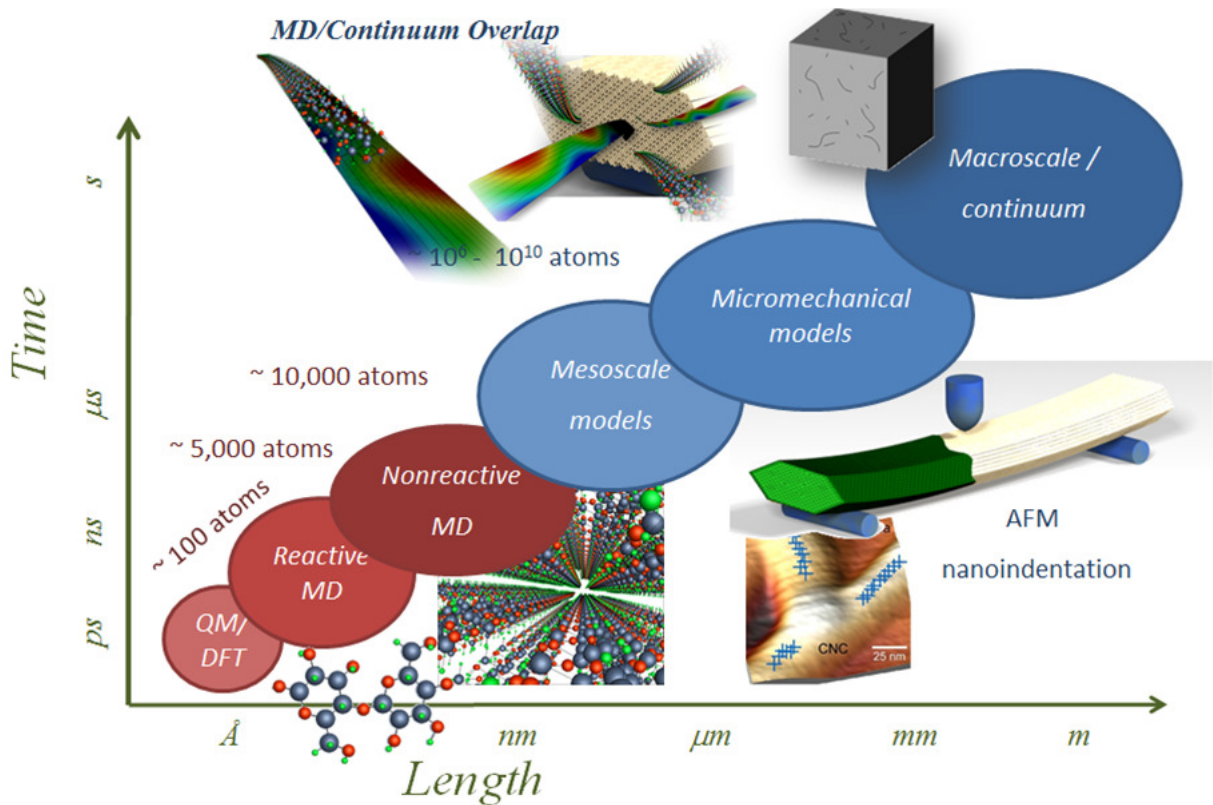
Figure 3-2 Commonly used models of physics at different scales. In red: techniques that take into account atoms explicitly. In blue: "continuum" theories.

Increasing the size and time length of the system does not come without restrictions. The increase is achieved by reducing the details involved in each atomic interaction and the results are highly dependable on the force field parameterization being used to run the simulations. Keeping in mind those limitations, MD has the advantage of simulating large systems that are far beyond the reach of QM. It was possible to simulate an entire CNC crystal for several nano-seconds using molecular dynamics computational tools.

Interaction between large CNCs or the behavior of the crystal as reinforcement material is still out of the reach of current molecular dynamics simulations. Continuum theories are the right tool for systems that range seconds to years in the time scale and millimeters

to kilometers in the length scale. Continuum models do not consider atomic interactions in the same way as QM or MD because the entire system is viewed as a whole and not as a group of individual atoms interacting between each other. A continuum representation of cellulose crystals was developed based on the finite element method. Each individual cellulose chain inside the cellulose crystal was coarse grained into an element specifically designed. Non-bonded interactions such as hydrogen bonds, Coulomb and van der Walls were also taken into account with specially designed finite elements.

It is common to divide multiscale modeling into two different types: hierarchical multiscale and on-the-fly concurrent multiscale methods. Concurrent multiscale methods divide the computational domain into different regions where different simulation methods are applied. This approach is particularly useful for systems where atomistic interactions in a small region can affect the macroscopic properties of a material (e.g. fracture). In the case of hierarchical multiscale, a set of different computational tools are used in sequence following a bottom up approach. First the most accurate method (e.g. quantum mechanics) is used to determine parameters for the next computational approach (e.g. via force field fitting to generate interatomic potentials). Molecular dynamics simulations are then used to determine constitutive equations which are utilized as inputs in finite element approaches. The systematic integration of models that range from quantum mechanics to macroscopic scales allows to make quantitative predictions of complex phenomena with few (or without) empirical parameters. Quantitative predictions are enabled via the validation of key properties, which then enables to extrapolate and predict the behavior of systems not included in the initial set of parameters used to

develop the model. As a result, the need for data fitting to match experimental results is considerably reduced or completely eliminated.

A hierarchical multiscale technique with a bottom-up approach was used in this study. The analysis was started conducting QM-DFT simulations of crystalline cellulose at 0K. A single simulation cell was initially relaxed and then subjected to several deformation states. As a result, groundbreaking information regarding the extreme anisotropies of crystalline cellulose was obtained. Temperature effects over mechanical properties, coefficient of thermal expansion, thermal conductivity and heat capacity were also computed with QM-DFT simulations.

The next natural step was to move to MD simulations allowing a substantial increase in the time and size scale of the system. At this point, the thermo-mechanical properties provided by QM-DFT simulation proved to be invaluable. Several force field parameterizations were systematically tested and compared with QM-DFT simulations. Molecular dynamics simulations of single chains and entire crystals were conducted to characterize the intrinsic mechanical behavior CNCs and define the role of non-bonded interactions.

Finally, a continuum model was developed capable of representing an entire CNC crystal in vacuum. A significant reduction in the number of degrees of freedom needed to represent a cellulose crystal was achieved by introducing continuum approximations. The resulting speedup was of several orders of magnitude, allowing simulations that would have taken months with MD to run in a couple of minutes with FEM.

CHAPTER 4. ANISOTROPY OF THE ELASTIC PROPERTIES OF CRYSTALLINE CELLULOSE FROM FIRST PRINCIPLES

4.1 Introduction

In spite of the significant potential of cellulose nanocrystals (CNCs) as functional nanoparticles for numerous applications, a fundamental understanding of the mechanical properties of defect-free, crystalline cellulose is still lacking. Mechanical properties of CNCs are difficult to experimentally characterize owing largely to extreme anisotropy and uncertainties about the structure of these materials. For example, reported experimental values for the Young modulus of cellulose I_β show a wide variation that is hard to explain considering the defect-free crystalline structure typically observed in CNCs [23-25, 30-35]. Unfortunately, there is no standardization of the coordinate system and nomenclature used to measure the elastic moduli making quantitative comparisons of the elastic behavior between experiments and theory rather difficult. Most authors agree on defining both an axial or longitudinal Young modulus, E_A, which is aligned with the longitudinal axis of the cellulose I_β unit cell, and an additional Young modulus, perpendicular to the longitudinal axis, usually reported as the transverse modulus, E_T. Early studies using x-ray diffraction [23-25, 30, 31] measured values of E_A ranging from 90 to 138 GPa. Recently, Diddens et al. [32] reported values of $E_A = 220 \pm 50$ GPa and $E_T = 15 \pm 1$ GPa using inelastic x-ray scattering (IXS).

Diddens and coworkers [32] claimed that IXS was not affected by the amorphous zones occurring in natural cellulose, and the elastic behavior was mostly related to the highly crystalline regions.

(a)

(b)

Figure 4-1 (a) Atomic force microscope topography image of a tunicate CNC showing its rod-like shape (on a mica substrate) [33]. The blue cross near the bottom of the figure denotes a location for AFM tip indentation. (b) Schematic of a CNC particle during AFM indentation for illustration purposes. Here, the cellulose chains are represented by straight ribbons, and the crystallographic directions indicated as a, b and c. The inset shows details of the layered cellulose structure where red spheres denote oxygen ions, gray spheres represent carbon ions and white spheres represent hydrogen ions. The red dotted lines indicate the repeating unit cell.

Alternatively, larger uncertainties have been reported from atomic force microscopy (AFM) measurements of cellulose I_β elastic properties. For example, Lahiji et al. [35] and Wagner et al. [33] reported E_T = 8.1 GPa with a 95% confidence, which translates into an interval ranging from 2.7 to 20 GPa. A typical AFM indentation test of a CNC particle on a hard substrate is shown in Figure 4-1a. As described by Lahiji et al. [9], this test is used to measure E_T. Figure 4-1b shows schematics of the direction of the load with respect to the expected crystallographic directions (*a*, *b*, and *c*). Relating these experimental measurements to a specific crystallographic orientation is challenging since it is difficult to estimate the alignment of the CNC with respect to the substrate [35]. Moreover, with no additional information on the direction assigned to E_T, it may not be possible to properly interpret the experimental data and, therefore, any attempt to compare experiments with computational predictions is difficult. Uncertainties about the shape of the CNC after sample preparation and the determination of the crystallographic planes during the experiments contribute to this important challenge.

In the present study, the anisotropy of the Young's modulus and Poisson's ratio of monoclinic cellulose I_β was quantified using ab initio first principles density functional theory (DFT) [62] with a semi-empirical correction for van der Waals interactions [63]. The least squares fitting method of Le Page and Saxe [64] is used to compute all unique components of the stiffness and compliance matrices using the VASP code [65-68] as the DFT computational engine. This information enables analysis of the variations of the Young's modulus and Poisson's ratio with crystallographic orientation. These variations are displayed as surfaces which are color contours showing crystallographic dependence of these properties. Polar plots, which show the Young's modulus and Poisson's ratio

variation with angular orientation in a given plane within the cellulose I_β crystal structure, are used to: (i) explain the substantial variability in the literature experimental data on the Young's modulus for cellulose, and (ii) understand the Poisson's effect in selected planes.

4.2 Background

The crystal structure and the hydrogen bond system in cellulose I_β have been characterized by Nishiyama and co-workers [9, 10, 12, 21, 22]. Here, the atomic coordinates for the cellulose I_β network A reported by Nishiyama et al. [9] were adopted. Symmetry and antisymmetry operations provided by the crystallographic space group, commonly accepted to be monoclinic $P2_1$ [26], were used to account for the atomic positions inside the unit cell. Each unit cell contains two molecular chains with a total of 42 ions per chain (84 ions per unit cell). Note that the formula unit (f.u.) for this structure is $C_6O_5H_{10}$; there are two f.u.'s in the primitive cell and four in the crystallographic cell. Figure 4-2 depicts the crystalline structure reported by Nishiyama et al. [9] after the symmetry operations are applied to the atomic coordinates. The represented structure was constructed using the Crystalline cellulose – atomistic toolkit [69]. Intra- and inter-molecular hydrogen bonds are depicted in Figure 4-2b following the hydrogen bond network A pattern reported in [12, 70]. Cellulose chains are organized in hydrogen bonded planes (in the *b-c* plane) that are stacked together and held in position primarily by weak vdW interactions. Out-of-plane intermolecular hydrogen bonds, connecting cellulose chains in different planes, has also been reported [71]. Lattice parameters and crystallographic directions are superimposed in Figure 4-2a and b for reference purposes.

(a)
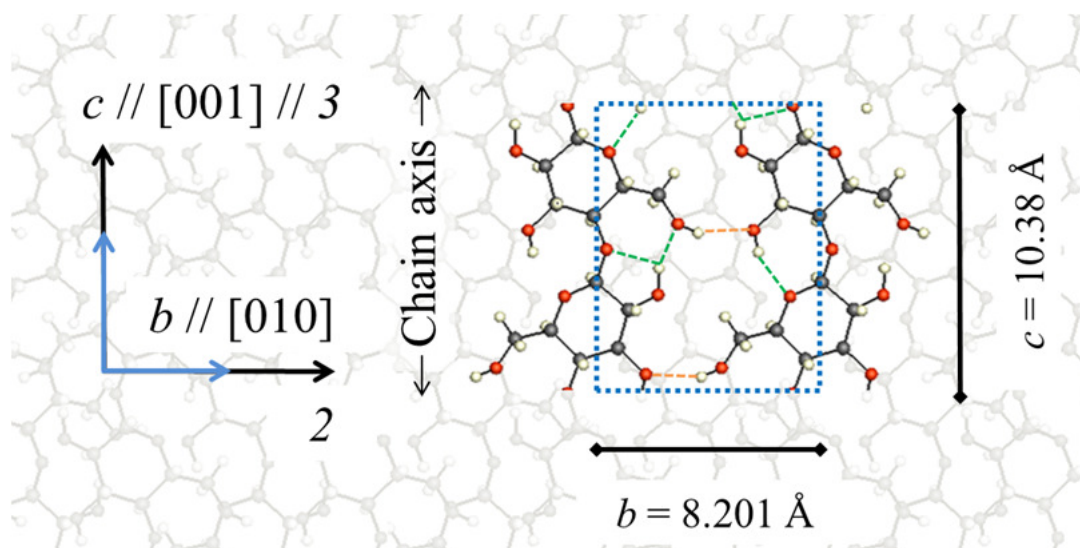
(b)

Figure 4-2 Expanded views of the P2$_1$ unit cell structure of the cellulose I$_\beta$ network A showing the characteristic layered conformation [69]. Experimental (room temperature) lattice parameters *a*, *b*, *c*, from Nishiyama et al. [9] are shown. Red spheres denote oxygen ions, gray spheres represent carbon ions and white spheres repr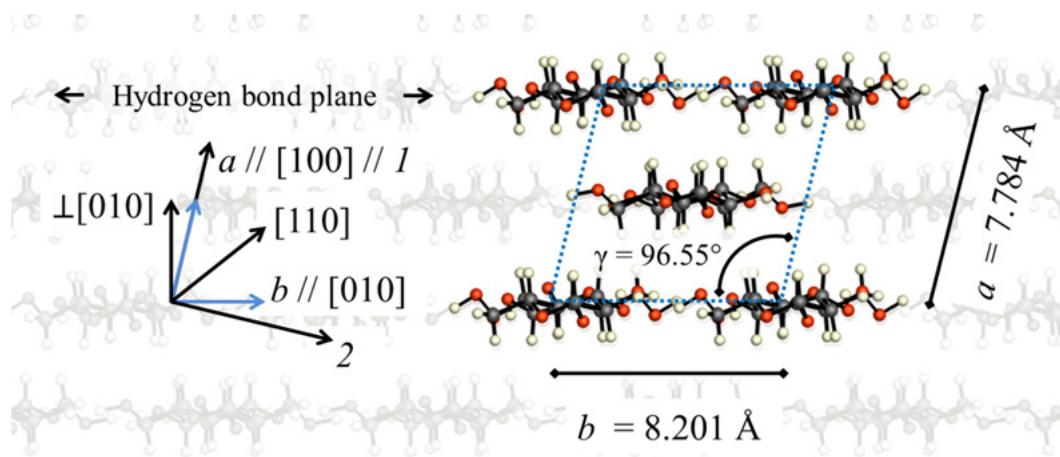esent hydrogen ions. Dotted blue lines denote the unit cell. (a) View along the *c*-axis (in of the page). Layers of I$_\beta$ are stacked along the *a*-axis. (b) View along the a-axis direction. Atomic coordinates were obtained after applying symmetry operations to the original structure reported by Nishiyama et al. [9]. Intra- and inter molecular hydrogen bonds are depicted in green and orange respectively, according to the hydrogen bond network A pattern reported in Refs. [12, 70]. The symbol // in this figure means "parallel to." For example, *a*//[001]//*1* means that the crystallographic direction *a*, with Miller indices [001], is parallel to the Cartesian axis *1*.

To facilitate the predictions of the anisotropy of the Young's modulus and Poisson's ratio of monoclinic cellulose I$_\beta$, a Cartesian system of coordinates *1*, *2* and *3* was defined. Direction *1* is chosen to be parallel to *a* ([001]), and direction *3* is parallel to *c* ([001]). For the monoclinic P2$_1$ structure, *b* is not orthogonal to *a*. Therefore, direction *2* is chosen such that it is orthogonal to directions *1* and *3* as shown in Figure 4-2a and b.

The lattice parameters for cellulose have been measured by several authors [9, 10, 12, 21-27] using different experimental techniques and crystal sources. For the cellulose I$_\beta$ network A structure, Nishiyama et al. [9] reported: $a = 7.784$ Å, $b = 8.201$ Å, $c = 10.380$ Å, $\alpha = 90°$, $\beta = 90°$, $\gamma = 96.55°$, with a 658.3 Å^3 volume at 293 K. Most of the measured lattice parameters exhibit variations around 1% over a wide range of temperatures and crystalline sources, except for the lattice parameter *a*. As cellulose I$_\beta$ is cooled or heated, the lattice remains remarkably constant in the directions within the hydrogen bonded planes containing the chains (i.e., *b* and *c*); the same is not true along the *a* axis direction where the contractions or expansions are controlled by weak vdW interactions and interplanar hydrogen bonding [21, 28]. Nishiyama et al. 2008 [12] reported a change from 7.64 to 7.76 Å in the *a* lattice parameter when the temperature was raised from 15 K to 295 K. Langan et al. [21] reported a value of 7.83 Å for the same parameter at 298 K. Although hydrogen bond interactions are present along the stacking direction (*a*-axis), they apparently do not prevent thermal expansion at temperatures up to the transition to a high-temperature phase at ~200 °C [29]. This thermal sensitivity of the lattice parameter *a* should be kept in mind when comparing 0 K ab initio calculations with experimental values acquired at temperatures above zero K. Experimental lattice

parameter and cell volume values, as well as ab initio simulation results, are summarized

in Table 4-1.

Table 4-1 Ab-initio and experimental lattice parameters (*a, b, c*, and *γ*) of cellulose I$_β$ from different sources are listed. The double lines separate experimental results from simulations. Exchange-correlation functionals used in the ab initio simulations are: LDA (local density approximation), PBE (the generalized gradient approximation of Perdew–Burke–Ernzerhof or GGA-PBE) [72]; PBE-D and PBE-D2 (GGA-PBE with van der Waals corrections) [65-67]. See section 4.4 for additional details. The temperature at which each experiment was performed is reported in the last column. The symbol "-" means that the temperature was not reported.

Ref	Methodology	Type of cellulose	*a* [Å]	*b* [Å]	*c* [Å]	*γ* [Deg]	Volume [Å^3]	Temp [K]
[24]	X-Ray Diffraction (XRD)	Bleached ramie (cellulose I)	7.9	8.35	10.3	96	675.7 [1]	-
[26]	Electron Diffraction	Green alga	8.01	8.17	10.36	97.3	672.5 [1]	293
[27]	XRD	Valonia (cellulose I$_β$)	7.85	8.27	10.38	96.3	669.8 [1]	-
			7.82	8.16	10.32	97.5	652.9 [1]	-
[9]	XRD and Neutron Fiber Diffraction (NFD)	Tunicate (cellulose I$_β$)	7.784	8.201	10.38	96.5	658.3	293
[21]	XRD	Tunicate (cellulose I$_β$)	7.76	8.19	10.38	96.51	655.4	100
			7.83	8.19	10.38	96.55	661.3	298
[12]	XRD and NFD	Tunicate (cellulose I$_β$)	7.64	8.18	10.37	96.54	643.9	15
			7.76	8.20	10.37	96.62	655.5	295
[63]	PBE	Cellulose I$_β$	8.70	8.23	10.46	95.5	744.9	0
	PBE-D2		7.65	8.14	10.39	96.8	642.5	
[73]	PBE	Cellulose I$_β$ network A	8.37	8.23	10.45	96.0	716	0
	PBE-D2		7.57	8.14	10.39	96.5	636	
	PBE-D2	Cellulose I$_β$ network B	7.51	8.55	10.30	98.2	655	
[74]	LDA	Cellulose I$_β$	7.41	7.94	10.24	96.2	599.0 [1]	0
	PBE		Not binding	8.27	10.54	94.7	-	
	PBE-D		7.85	8.18	10.47	96.6	667.9 [1]	
This study	PBE-D2	Cellulose I$_β$ network A	7.56	8.13	10.39	96.7	635	0

[1] Not reported, computed based on the lattice parameters

4.3   Elastic stiffness matrix C_{ij} and compliance matrix S_{ij} for crystalline cellulose I_β

Materials that exhibit directional independence of their mechanical properties are referred to as isotropic. They have the advantage that their elastic response is characterized by only two parameters: the Young modulus (E) and the Poisson's ratio (v). In addition, the stress-strain tensile behavior will be completely independent of the relative orientation of the specimen with respect to the loading direction. Anisotropic materials, however, exhibit variations in their mechanical properties with respect to an intrinsic direction within the material. One of the most common examples of a naturally-occurring anisotropic material is wood, were the grain is oriented along a particular direction. This significantly affects the mechanical response of the material. Hence, it is necessary to define a more general stress-strain relation for anisotropic solids that will account for mechanical property variations with direction within the material. The most general linear stress- strain relation for anisotropic materials is Hooke's Law, which has the form: $\sigma_{ij} = C_{ijkl}\ \varepsilon_{kl}$, where σ_{ij} and ε_{kl} represent the components of the second-order stress and strain tensors, respectively, and C_{ijkl} are the components of the fourth-order elasticity tensor with 81 components [60]. The inverse relation can also be written as $\varepsilon_{ij} = S_{ijkl}\ \sigma_{kl}$, where S_{ijkl} are the components of the elastic compliance tensor. These relationships can be converted to a matrix form based upon symmetries in C_{ijkl} and S_{ijkl}, leading to a stiffness matrix with components C_{ij} and a compliance matrix with components S_{ij}, both with 21 independent components [60].

The monoclinic space group of cellulose I_β dictates that the unit cell has a symmetry plane that is defined by the c-axis. The presence of a symmetry plane has a direct consequence over the C_{ij} and S_{ij} in that it reduces the number of components necessary to

represent the system. This leaves only 13 independent constants in each of C_{ij} and S_{ij}.

Lastly, the matrix representation of the stress-strain relation must follow a coordinate system that allows a direct relationship between the matrix components and the cellulose I_β structure. Figure 4-3a shows a schematic representation of the main directions associated with the cellulose I_β unit cell and S_{ij} associated with the Cartesian system of coordinates denoted by axes *1, 2* and *3*.

(a)

(b)
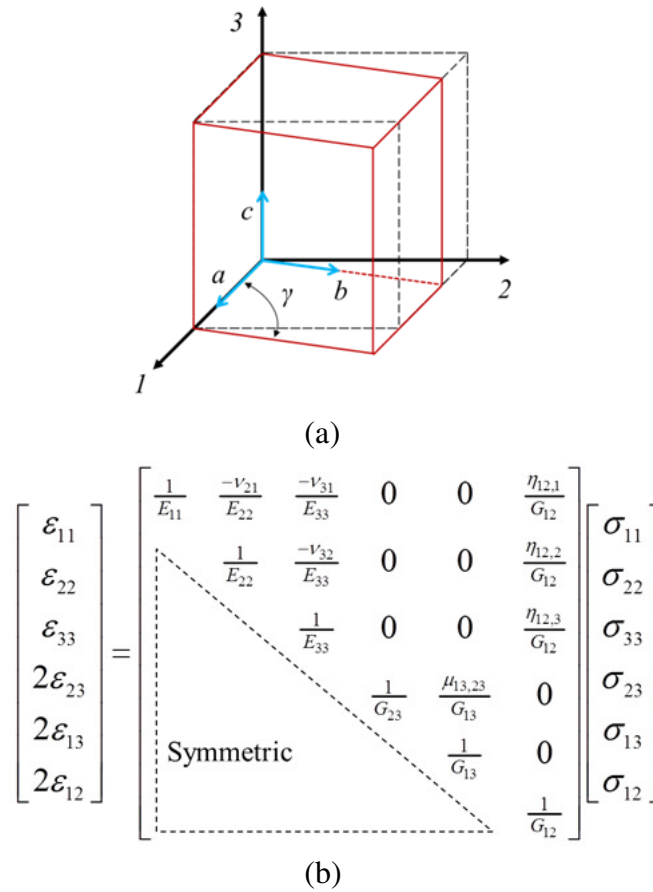
Figure 4-3 (a) Schematic representation of the cellulose I_β monoclinic (P2$_1$) unit cell aligned with the Cartesian coordinate system used in this study (red solid lines). A rectangular prism cell (black dashed lines) is used to help visualize the orthogonally between the *a-c* and *b-c axes*, highlighting the non-orthogonal relationship between *a* and *b*. (b) Relationship between the strain and stress vectors via S_{ij} [75] ($\varepsilon_{ij} = S_{ijkl}\,\sigma_{kl}$) for the P2$_1$ cellulose I_β unit cell. E_{ii} is the Young's modulus in the *i*-direction, G_{ij} is the shear modulus in the *i-j* plane, v_{ij} is the Poisson's ratio which quantifies the contraction in the *j*-direction due to uniaxial loading in the *i*-direction, $\eta_{ij,k}$ are the coefficients of mutual influence of the first kind which characterize normal strain in the *k*-direction due to shear stress in the *i-j* plane, and $\mu_{ij,kl}$ are Chentsov's coefficients which characterize shear strain in the *k-l* plane due to shear stress in the *i-j* plane.

Figure 4-3b shows S_{ij} in terms of the Young's Modulus and Poisson's ratio in each direction for the P2$_1$ cellulose I$_\beta$ unit cell (also appropriate for any monoclinic space group) [75]. With this information, three-dimensional surfaces can be constructed that are color contours of the Young's Modulus and Poisson's ratio. These contours follow variations of these properties with crystallographic direction. Additionally, 2D polar plots of the Young's Modulus and Poisson's ratio can be construct which enable analyzes of the variations of the Young's Modulus and Poisson's ratio with respect to a particular orientation angle within a given plane in the cellulose I$_\beta$ unit cell.

Several relevant directions are depicted in Figure 4-3a. For instance, E_{11}, E_{22} and E_{33} are the Young's moduli with respect to the directions *1*, *2* and *3*, respectively. It is important to note that E_{11} and E_{33} are the Young's moduli defined as the slope of the normal stress - normal strain curve produced in simple tension when the load is applied parallel to axes along *a* and *c*, respectively. Alternatively, E_{22} is defined along a direction determined by the cross product between the *a* and *c*-axes (i.e., *a-c* plane) (see Figure 4-2 and Figure 4-3a). In the *a-b* plane, two additional values of interest are defined, viz., $E_{[110]}$ and $E_{[010]}$, in which the subscripted indices represent the crystallographic direction defined by the Miller indices. Note that $E_{[110]}$ is along the axis that runs through the center chain in the unit cell (see Figure 4-2a), whereas $E_{[010]}$ is aligned with the *b*-axis. The Poisson's ratio is also reported using a similar nomenclature; for example, v_{12} is the Poisson's ratio for the contraction in the *2*-direction due to uniaxial loading in the *1*-direction. It is common to report an average value of the Poisson's ratio using the two perpendicular directions with respect to the loading direction. Hence, only one index is needed. For the direction *1*, this is defined as:

$$\bar{\nu}_1 = \frac{\nu_{12} + \nu_{13}}{2} \qquad (1)$$

4.4   Computational methodology

All calculations in this study were conducted with the Vienna Ab Initio Simulation Package (VASP), a plane wave DFT code [65-68]. The electron–ion interactions were described by the full potential projector augmented wave (PAW) method [76]. Exchange-correlation was treated within the generalized gradient approximation of Perdew, Burke and Ernzerhof (GGA-PBE) [72]. Standard density functionals within the GGA or LDA cannot correctly describe vdW interactions resulting from dynamical correlations between fluctuating charge distributions [63]. This makes them intrinsically unsuitable for computing structural parameters of cellulose I_β. Using PBE functionals, Bučko et al. [63, 73] reported a value of *a* that is overestimated by ~15% compared to experimental results at 15 K [12]. Li et al. [74] found that cellulose fails to retain its crystalline structure when using PBE functionals (see Table 4-1 for more information). In order to circumvent this problem, a semi-empirical correction for the vdW interactions (now incorporated as PBE-D and PBE-D2 in VASP [65-67]) was proposed by Grimme et al. [77, 78]. Using this dispersion-corrected DFT method (PBE-D2), Bučko et al. [63, 73], Li et al. [74] and Parthasarathi et al. [11] showed that vdW and hydrogen bonding interactions play an equally important role in defining the final shape of the cellulose I_β monoclinic (P2$_1$) structure and hence they cannot be neglected. Therefore, all calculations in this study are conducted using the dispersion corrected PBE-D2 in VASP [63, 73].

Structural parameters and mechanical property calculations were computed by simultaneously minimizing all atomic forces and stress tensor components via a conjugate gradient method. Three successive full-cell optimizations were conducted (adapting basis vectors and computational grids to the cell parameters) to ensure convergence of cell energies and structural parameters. Total energies were calculated for the relaxed cellulose I_β structure by integrating over a Monkhorst-Pack mesh of k-points in the Brillouin zone with the linear tetrahedron method with Blöchl corrections. The plane wave cutoff energy for all calculations was 500 eV. The total energy was converged to 10^{-7} eV/cell and the force components were relaxed to at least 10^{-4} eV/Å. For all calculations (i.e., structural and elastic properties), a 7×7×7 k-point mesh, corresponding to a k-point spacing of $0.110 \times 0.086 \times 0.110$ per Angstrom, was used.

Components of the stiffness matrix, C_{ij}, were computed from the first derivatives of the stresses computed in VASP, rather than from the second derivatives of the total energy with respect to strain, using the least squares method of Le Page and Saxe et al. [64]. This method avoids the numerical difficulties often encountered with evaluations of the latter and reduces the number of required VASP calculations. All C_{ij} values were computed simultaneously rather than as independent sums. The C_{ij} are sensitive to the k-point mesh, and this required a series of ancillary calculations to test k-point convergence of each of the 13 unique C_{ij} for monoclinic cellulose I_β structure. In addition, it was determined that the application of four successive strains, viz., 0.05%, 1.0% 1.5%, and 2.0% was adequate to obtain $\leq 1.0\%$ statistical error in each C_{ij}. The quality of the least squares fit, as gauged by the computed least squares residual, was $\leq 1.0\%$ for all calculations. The small residuals are consistent with negligible anharmonic effects in the computed C_{ij} due

to the applied strains. Note that the Le Page and Saxe method for computing elastic properties with DFT has been successfully used to compute elastic properties for a wide variety of materials, including hydrides [79-81], batteries [82, 83], ceramics [84, 85], metals [86, 87] and defects [88] Once the stiffness matrix was computed, it was then inverted to obtain the compliance matrix, S_{ij}. As explained in the previous section, the C_{ij} and the S_{ij} depend on the definition of the coordinate system used in the simulations. Rotation techniques, such as those detailed in Ref. [60], a to convert the computed compliance matrix to any desired orientation. The basis change follows from:

$$S^{(1'2'3')} = K^{-T} \, S^{(123)} \, K^{-1} \tag{2}$$

For the particular case of rotation through an angle θ in a counterclockwise sense about the 1, 2 and 3 axes, respectively, the rotation matrix K reduces to

$$
\begin{bmatrix}
1 & 0 & 0 & 0 & 0 & 0 \\
0 & c^2 & s^2 & 2cs & 0 & 0 \\
0 & s^2 & c^2 & -2cs & 0 & 0 \\
0 & -cs & cs & c^2-s^2 & 0 & 0 \\
0 & 0 & 0 & 0 & c & -s \\
0 & 0 & 0 & 0 & s & c
\end{bmatrix}
\begin{bmatrix}
c^2 & 0 & s^2 & 0 & 2cs & 0 \\
0 & 1 & 0 & 0 & 0 & 0 \\
s^2 & 0 & c^2 & 0 & -2cs & 0 \\
0 & 0 & 0 & c & 0 & -s \\
-cs & 0 & cs & 0 & c^2-s^2 & 0 \\
0 & 0 & 0 & s & 0 & c
\end{bmatrix}
\begin{bmatrix}
c^2 & s^2 & 0 & 0 & 0 & 2cs \\
s^2 & c^2 & 0 & 0 & 0 & -2cs \\
0 & 0 & 1 & 0 & 0 & 0 \\
0 & 0 & 0 & c & s & 0 \\
0 & 0 & 0 & -s & c & 0 \\
-cs & cs & 0 & 0 & 0 & c^2-s^2
\end{bmatrix}
\tag{3}
$$

where $c = \cos(\theta)$ and $s = \sin(\theta)$. Clearly, applying the three rotations successively can produce an arbitrary orientation change. This provides the basis to construct the 3D surface contour plots and polar plots.

4.5   Results and discussion

Results from VASP calculations with the semi-empirical correction for the vdW interactions were used to generate the surface contour plot of the Young's modulus variation with crystallographic direction shown in Figure 4-4a. This is based upon

Equations (2) and (3) and the S_{ij} computed from application of 1.0% strain in the Le Page and Saxe method [64].). A post processing software package, the Anisotropy Calculator - 3D Visualization Toolkit, was specifically developed to generate the surface contour plot of the Young's modulus based on S_{ij} and is now publically available [89]. Each point on the surface represents the magnitude of Young's modulus in the direction of a vector from the origin of the surface (i.e., at the intersection of the *1*, *2*, and *3* axes in the interior of the surface) to a given point on the surface. The shape of this surface is indicative of the anisotropy of cellulose I$_\beta$. For instance, the computed Young modulus surface for a linearly elastic isotropic material would be a perfect sphere with the same value in any direction. However, the cellulose I$_\beta$ surface in Figure 4-4a exhibits extreme variations in the Young's modulus, as denoted by the accentuated contour lobe along the *3*-axis (i.e., along the cellulose chains) relative to the smaller lobes along the *1* and *2* directions. The largest values (red contours) are along the *3*-axis, with the smallest values along the *1*-axis. The greatest value of the Young's modulus is 206 GPa, which is comparable to that of steel (~207 GPa) [90]. Figure 4-4b, c and d show side views of the same surface in Figure 4-4a to put differences in Young's moduli for directions lying on the *1-2*, *1-3* and *2-3* planes in better perspective.

Polar plots of the angular variation of the Young modulus within a given crystallographic plane of the monoclinic cellulose I$_\beta$ crystal structure are shown in Figure 4-5 and 10. These plots can be used to help provide insight into the variability in the reported experimental values (ranging from 90 to 220 GPa) of the Young's modulus. Figure 4-5 shows the angular variation of the Young's modulus along the *1-3* plane (as shown by the gray plane in the inset on the upper left of the figure).
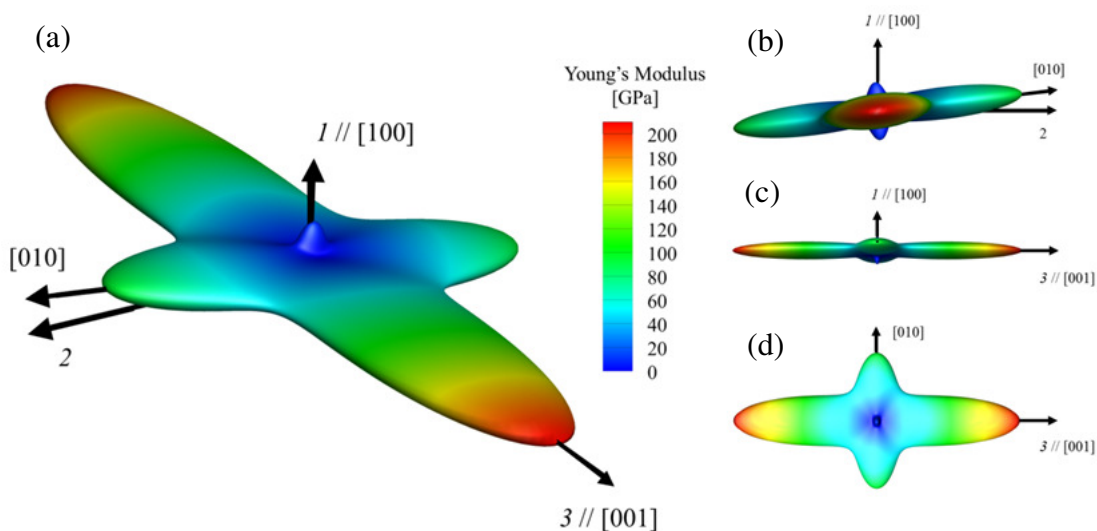
Figure 4-4 (a) Surfaces showing contours of computed Young's modulus values for cellulose I$_\beta$ based on an S$_{ij}$ from application of a 1% strain in the Le Page and Saxe method [64]. Each point on the surface represents the magnitude of Young's modulus in the direction of a vector from the origin of the surface to that point. The color contours help to identify the Young modulus variation of cellulose I$_\beta$ and emphasizes its extreme anisotropy (note the significant elongation of the surface along axis *3*). Side views of the same surface are shown for the (b) *1-2* plane, (c) *1-3* plane, (d) *2-3* plane. Note that axis *2* is not seen in these additional view.

Three axes are considered: direction *1* (which is the vertical axis), direction *3* (the horizontal axis) and the semi-circular line showing the angle with respect to the origin. The scale of the vertical axis denotes the magnitude of E_{11}, whereas the scale of the horizontal axis denotes the magnitude of E_{33}. The inset in the bottom semi-circular part shows the orientation of the directions *1* and *3* with respect to the cellulose I$_\beta$ unit cell. Here, θ is the angle between the *3'*-direction, along which the load is applied, and the *3*-direction (in the *1-3* plane). The plot is generated by computing S_{ij} for different angles using Equations (2) and (3), and extracting the Young modulus value in the *3'*-direction from the rotated compliance matrix. Components of the S_{ij}, computed in the Cartesian coordinate system shown in Figure 4-3a were obtained following the Le Page and Saxe

method [64] for three values of applied strains, viz. 1.0% 1.5%, and 2.0%. A change of only 10° in the longitudinal alignment (c-axis) reduces the DFT-predicted Young modulus from 206 GPa to ~70 GPa. This considerable reduction is related to the deformation mechanism in which the cellulose I_β structure is under simple tension in each of the *1*, *2*, *3* directions. For instance, imposing a deformation perfectly aligned with the c-direction presumably implies a stretching of the covalent bonds between carbon and oxygen ions that form the cellulose chain (shown as the ball and stick features Figure 4-2). This results in the highest value of the Young modulus (206 GPa) along the c-direction (the *3*-direction). In the a-direction (which corresponds to the *1*-direction), hydrogen bonded planes are stacked together and held in position primarily by weak vdW interactions. Any deviation of the stretching direction in the *1-3* plane will produce a rapid decrease in the Young's modulus due to sliding between adjacent planes. In the b-direction, the intermolecular hydrogen bonds (See Figure 4-2b) provide additional reinforcement to keep the cellulose chains from sliding. As a consequence, the effects of misalignments in the *2-3* plane are less severe compared with those in the *1-3* plane. Note that deviations between the curves from the applied strains, viz. 1.0% 1.5%, and 2.0% are very minimal.
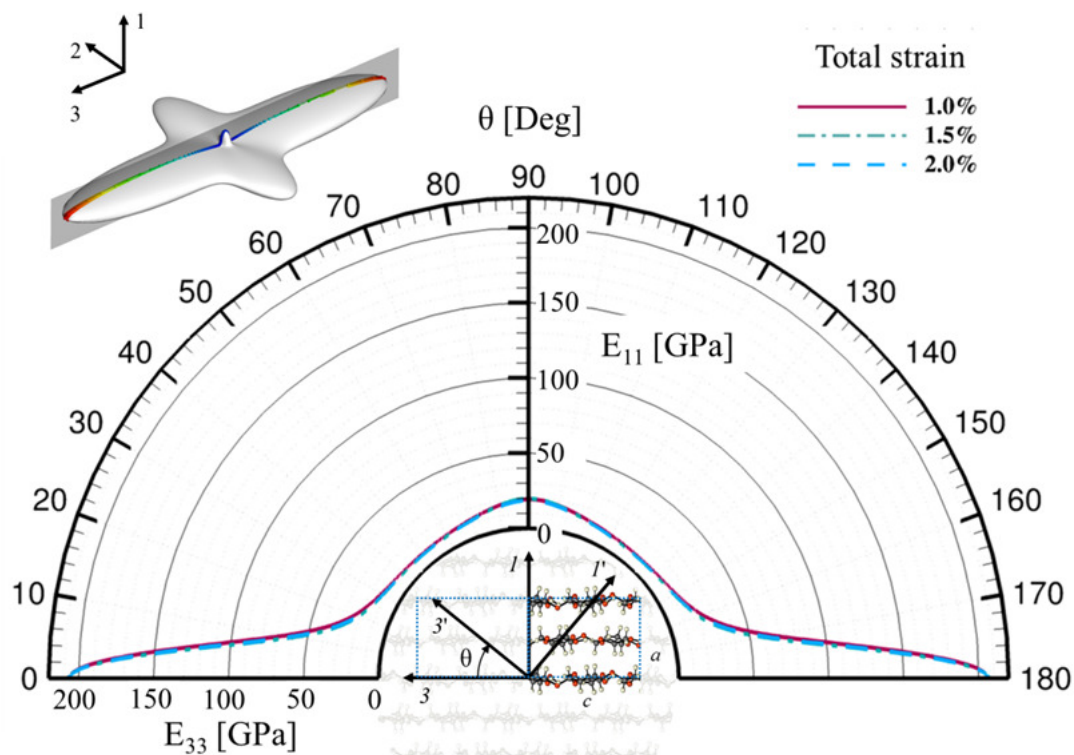
Figure 4-5 Angular variation of longitudinal Young's modulus (E$_A$) within the *1-3* plane for applied strains of 1.0%, 1.5%, and 2.0%. The *2*-axis (pointing in the page) is considered to be the rotation axis; the value of the longitudinal moduli for a given direction can be read directly from the figure by defining a straight line from the origin to the desired angle. It is important to notice how small misalignments between the cellulose I$_\beta$ *c*-axis and the *3*-direction will produce an important reduction in the interpretation of EA during experimental characterization. The inset in the bottom semi-circular part shows the orientation of *1* and *3* directions with respect to the cellulose I$_\beta$ unit cell.

Upon comparing DFT-computed results with experimental data (Table 4-2), E_{33} can be regarded as the axial Young's modulus (E_A). However, the experimental value of E_T can be interpreted as any of the Young's moduli in any of the directions lying in the *1-2* plane. Figure 4-6 is polar plot that shows the variation of the Young's modulus with angular orientation within the *1-2* plane. Here, θ is the angle between the *1′*-direction, at which the load is applied, and the *1*-direction (in the *1-2* plane). The plot is generated by computing S_{ij} for different angles using Equations (2) and (3) and extracting the Young

modulus value in the *1'*-direction from the rotated S_{ij}. Stretching in the *b*-direction implies separating chains in the hydrogen bonded planes which explains why $E_{[010]}$ has the highest value for E_T (98 GPa).
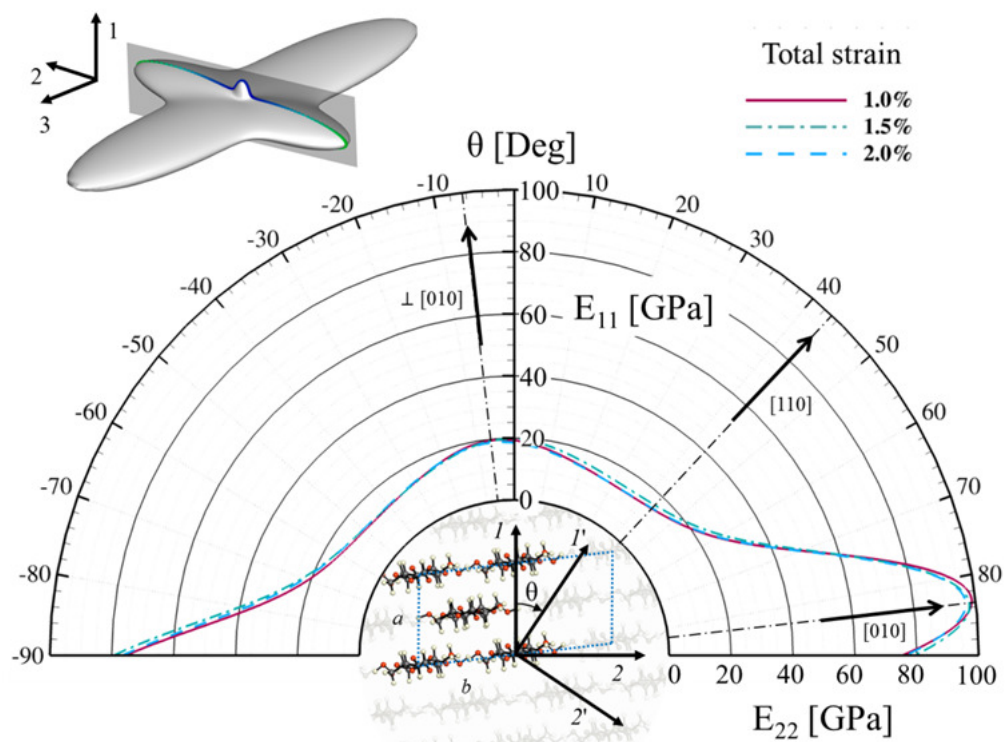
Figure 4-6 Angular variation of the E_T at applied strains of 1.0%, 1.5%, and 2.0%. The *3*-axis (pointing in of the page) is considered to be the rotation axis; the value of E_T for a given direction can be read directly from the figure by defining a straight line from the origin to the desire angle. The intersection between the straight line and the curves for different strains provides the value of E_T. Three critical directions (// to *b*, through the center chain and ⊥ to *b*) are marked for reference using Miller indices; the direction parallel to the *a*-axis coincides with the vertical axis of the figure. The superposition of the three strain curves allows to concluded that the crystal behaves linearly for strains up to 2%. The inset in the bottom semi-circular part shows the orientation of the *1* and *2* directions with respect to the cellulose I_β unit cell.

Perpendicular to the *b*-direction (marked as ⊥[010] in Figure 4-6), the weak vdW forces have to be overcome to increase the distance between adjacent planes, producing a relative maximum (19 GPa) in the Young's modulus. Another observation is that E_T

reaches its minimum (13 GPa) between the *b*-direction and the direction perpendicular to the *b*-direction (~30° in the plot). This could be caused by the relative sliding between hydrogen bonded planes. Based on Figure 4-6, it can be estimated that there is a 65% probability of measuring E_T under 20 GPa during experimental measurements; misalignments in the *c*-direction could increase this probability. Simulations at 0 K (this work) yielded values from 13 to 98 GPa, in good agreement with reported experimental results [32-35] and numerical simulations [25, 91, 92]. A summary is shown in Table 4-2. The calculated Young's moduli in selected directions are reported for different total strains (applied in the Le Page and Saxe method [64]) in Table 4-3.

Table 4-2 Summary of Young's modulus and Poisson's ratio values from different crystalline sources and authors. The double line in the table separates experimental from theoretical results. The symbol "-" means that the corresponding value was not reported.

Ref	Methodology	Type of cellulose	E_A [GPa]	E_T [GPa]	v_t	Temp [K]
[23-25, 30, 31]	X-Ray Diffraction (XRD)	Ramie (cellulose I)	90 to 138	-	-	-
[36]	XRD	Ramie fiber (cellulose I_β)	-	-	$v_{[200]/[004]} = 0.377 \pm 0.041$ [2] $v_{[110]/[004]} = 0.639 \pm 0.338$ [2]	Room Temp
[32]	Inelastic X-Ray (IXR)	Flax fibers (cellulose I_β)	220 ± 50	14.8 ± 0.8	-	-
[33]	Atomic force microscope (AFM)	Tunicate CNC	-	2.7 to 20	-	-
[34]	AFM+Finite Elements	Wood CNC	-	24.8 ± 7.0	-	-
		Cotton CNC		17.7 ± 5.0		
[25]	Theoretical derivation	Cellulose I	167.5	$E_{t1} = 50.2$ [1] $E_{t2} = 10.6$ [1]	$v = 0.42$ [1]	-
[91]	Molecular mechanics (MM) [COMPASS]	Cellulose Iβ - Nishiyama	149	$E_{t1} = 46.8$ [1] $E_{t2} = 18.9$ [1]	$v = 0.439$ [1]	Min [3]
		Cellulose Iβ - Finkenstadt	116	$E_{t1} = 50.9$ [1] $E_{t2} = 11.9$ [1]	$v = 0.86$ [1]	
[92]	Molecular dynamics (MD) [ReaxFF]	Cellulose Iβ	139.5 ± 3.5	$E_{t1} = 28.8 \pm 2.9$ $E_{t2} = 7.0 \pm 1.7$	-	300 K

[1] Not reported, computed based on reported S_{ij} or C_{ij}

[2] Upper limit of the standard deviation.

[3] The authors perform energy minimization without specifying any temperature.

Table 4-3 Young's moduli as a function of orientation for applied strains of 1.0%, 1.5%, and 2.0%. This table summarized the results shown in Figure 4-6. Young modulus measured in GPa, computed at 0K using DFT with van der Waals interactions (this work).

Young's modulus	Total strain			Average
	1.0%	**1.5%**	**2.0%**	
E_{33}	206.7	206.7	206.2	206.5
E_{11}	19.3	19.7	18.5	19.1
$E_{\perp[010]}$	19.6	19.4	18.9	19.3
$E_{[110]}$	14.8	16.3	15.0	15.3
$E_{[010]}$	98.7	97.9	96.7	97.8
E_{22}	75.4	79.2	76.4	77.0

The variation of $\bar{\nu}_{1'}$ with respect to the crystallographic orientation was computed from the S_{ij} by applying Equation (1) to the rotated compliance matrix obtained using Equations (2) and (3) . Here the *1'*-direction indicates the orientation of the load (which is the orientation that is being evaluated). Figure 4-7a shows one view of the computed $\bar{\nu}_{1'}$ surfaces. Figure 4-7b, 7c, and 7d show views of the same surface in the *1-2*, *1-3*, and *2-3* planes, respectively. Figure 4-8 shows a polar plot of $\nu_{1'2'}$, $\nu_{1'3}$ and $\bar{\nu}_1$ using the *c*-axis as the rotation axis, in which variations of these quantities are examined over the *1-2* plane (where θ is the angle between the *1'*-direction, at which the load is applied, and the *1*-direction in the *1-2* plane). In order to quantify lateral expansion, a local Cartesian system *1'-2'* that rotates with respect to the *1* and *2* directions and remains in the *1-2* plane was defined. First, $\nu_{1'2'}$ provides the lateral deformation in the *2'*-direction as uniaxial stress is applied along the *1'*-direction. It is important to remember that the *2'*-direction rotates perpendicular to the *1'*-direction in the *1-2* plane in Figure 4-8.
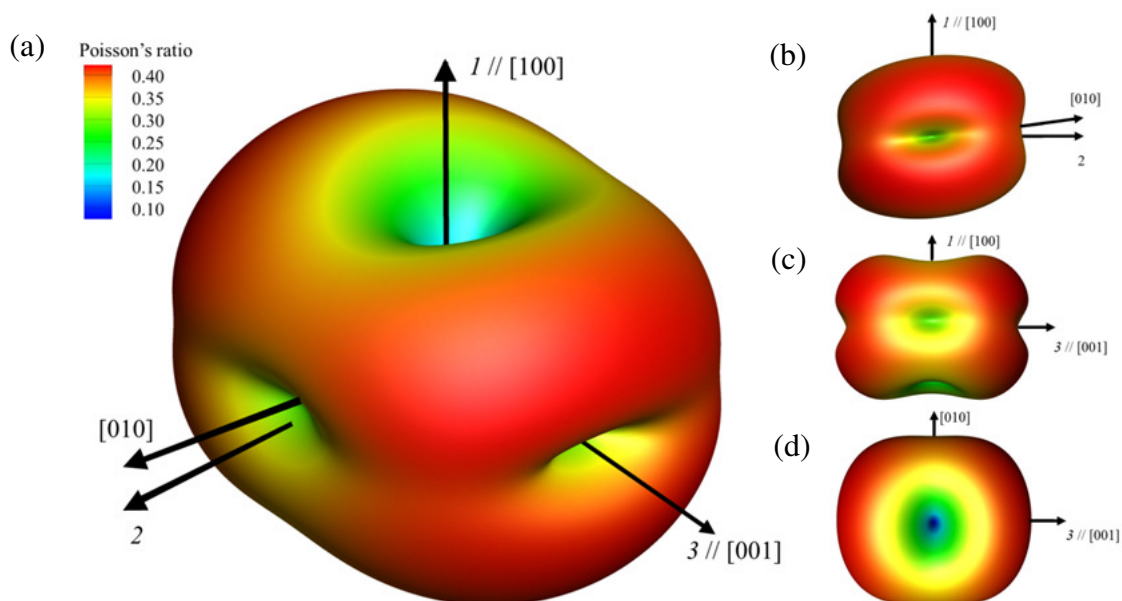
Figure 4-7 Average Poisson's ratio $\overline{v}_{1'}$ surfaces for cellulose I$_\beta$ computed using Eq. 1 based on S$_{ij}$ for 1% of total deformation in the Le Page and Saxe method [64]. Each point on the surface represents the magnitude of Poisson's ratio in the direction of a vector from the origin to that point. The color contours help to identify the Poisson's ratio variation and emphasizes the extreme anisotropy of the system. Side views of the same surface are shown for the (b) *1-2* plane, (c) *1-3* plane, (d) *2-3* plane. Note that axis *2* is not seen from this view.

The smallest value of $v_{1'2'} \approx 0.1$ is found when the *1'*-direction is aligned with the direction marked as ⊥[010] in the plot. This happens to be the direction perpendicular to the hydrogen bonded planes which contain the cellulose chains. This small value is expected since increasing the separation between hydrogen bonded planes, held together by weak vdW interactions, has little effect over the arrangement of the cellulose chains inside the plane. The next local minimum is found to be in the [010]-direction where the opposite effect is observed. Trying to separate cellulose chains from each other has little effect over the arrangement of hydrogen bonded planes. The axial deformation of the system shows a different behavior. Here, $v_{1'3}$ measures the contraction in the *3*-direction

as uniaxial stress is applied in the *1'*-direction (since the *1'* and the *2'* directions remain in the *1-2* plane, the *3'*-direction coincides with the *3* direction).
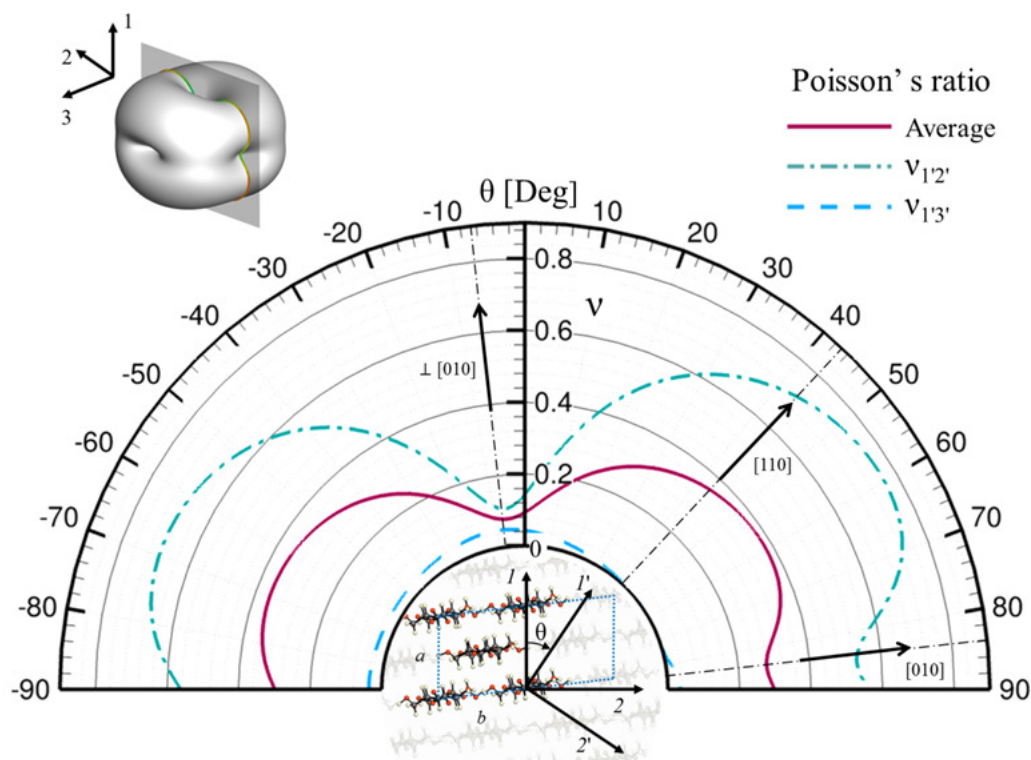

Figure 4-8 Poisson's ratio as a function of the rotation angle for 1% of total strain. The inset in the upper-left corner depicts the surface of the average Poisson ratio as shown in Figure 4-7 and the selected plane in which the polar plot lies. The *3*-axis (pointing inside the page) is considered to be the rotation axis; the value of the Poisson's ratio for a given direction can be read directly from the figure by defining a straight line from the origin to the desire angle. The intersection between the straight line and the curves will provide the values of $v_{1'2'}$, $v_{1'3}$ and the average of them ($\overline{v}_{1'}$) for that direction. Three critical directions (// to *b*, through the center chain and ⊥ to *b*) are marked for reference using Miller indices; the direction parallel to the *a*-axis coincides with the vertical axis of the figure.

In Figure 4-8, the *3*-direction coincides with the rotation axis (perpendicular to the plane of the plot), meaning that this direction is always coincident with the cellulose chain regardless of the orientation angle. The small values of $v_{1'3}$ for all directions (ranging from 0 to 0.05) can be easily justified by the covalent bonds between carbon and oxygen

ions that govern the mechanical response in the *c*-direction: these are largely unaffected by deformation in other directions. When the cellulose I$_\beta$ is deformed along a direction that passes near the center chain (around 45° in the plot), practically no Poisson effect (no lateral expansion in the *3*-direction) is observed in the axial direction.

The extreme anisotropies observed in cellulose I$_\beta$ can be once again evidenced in the high variations of the Poisson's ratio. Depending on the selected direction, the material will range from almost 0 to a relatively high (0.71) value of Poisson's ratio. Comparison with previous publications [25, 36, 91] shows results that are in good agreement with the values reported in this study. Finally, computed C_{ij} and S_{ij}, based on the Cartesian system shown in Figure 4-2, are reported for each applied strain.

$$S_{1.0\%} = \begin{bmatrix} 51.9 & -7.4 & -2.2 & 0.0 & 0.0 & 11.2 \\ & 13.3 & -0.5 & 0.0 & 0.0 & -25.6 \\ & & 4.8 & 0.0 & 0.0 & 2.2 \\ & & & 60.0 & -43.3 & 0.0 \\ \text{Symmetric} & & & & 372.7 & 0.0 \\ & & & & & 239.7 \end{bmatrix}$$

$$C_{1.0\%} = \begin{bmatrix} 21.5 & 13.0 & 11.0 & 0.0 & 0.0 & 0.3 \\ & 102.8 & 11.3 & 0.0 & 0.0 & 10.2 \\ & & 213.3 & 0.0 & 0.0 & -1.3 \\ & & & 18.2 & 2.1 & 0.0 \\ \text{Symmetric} & & & & 2.9 & 0.0 \\ & & & & & 5.3 \end{bmatrix}$$

$$S_{1.5\%} = \begin{bmatrix} 50.9 & -6.6 & -2.1 & 0.0 & 0.0 & 3.6 \\ & 12.6 & -0.5 & 0.0 & 0.0 & -21.4 \\ & & 4.8 & 0.0 & 0.0 & 2.3 \\ & & & 60.9 & -26.5 & 0.0 \\ \text{Symmetric} & & & & 427.8 & 0.0 \\ & & & & & 222.7 \end{bmatrix}$$

$$C_{1.5\%} = \begin{bmatrix} 21.7 & 13.1 & 10.5 & 0.0 & 0.0 & 0.8 \\ & 102.8 & 11.8 & 0.0 & 0.0 & 9.5 \\ & & 213.1 & 0.0 & 0.0 & -1.3 \\ & & & 16.9 & 1.0 & 0.0 \\ \text{Symmetric} & & & & 2.4 & 0.0 \\ & & & & & 5.4 \end{bmatrix}$$

$$S_{2.0\%} = \begin{bmatrix} 54.1 & -8.0 & -2.1 & 0.0 & 0.0 & 11.5 \\ & 13.1 & -0.5 & 0.0 & 0.0 & -23.2 \\ & & 4.8 & 0.0 & 0.0 & 2.1 \\ & & & 62.2 & -31.6 & 0.0 \\ \text{Symmetric} & & & & 411.9 & 0.0 \\ & & & & & 229.8 \end{bmatrix}$$

$$C_{2.0\%} = \begin{bmatrix} 20.8 & 13.5 & 10.4 & 0.0 & 0.0 & 0.2 \\ & 102.1 & 12.0 & 0.0 & 0.0 & 9.5 \\ & & 212.5 & 0.0 & 0.0 & -1.3 \\ & & & 16.7 & 1.3 & 0.0 \\ \text{Symmetric} & & & & 2.5 & 0.0 \\ & & & & & 5.3 \end{bmatrix}$$

Figure 4-9 Elastic compliance (*S*) and stiffness (*C*) matrices for cellulose I$_\beta$ based upon the Nishiyama et al. initial structure [9] with respect to the Cartesian system of coordinates shown in Figure 4-3a. All components were computed using the Le Page and Saxe method with with the dispersion-corrected DFT method (PBE-D2) in VASP for three different total strains (1.0, 1.5 and 2.0%). Values of *S* are given in [1/GPa]x1000, and those for *C* are in [GPa].

Table 4-4 Computed Poisson's ratio components or values, as a function of the orientation with respect to the Cartesian system of coordinates *1-2-3*, for different total strains. This table summarizes the results shown in Figure 4-8.

Poisson's ratio	Total strain Applied in the Le Page and Saxe Method [34]			Average over strains
	1.0%	**1.5%**	**2.0%**	
ν_{12}	0.143	0.130	0.148	0.140 ± 0.010
ν_{13}	0.042	0.042	0.039	0.041 ± 0.002
$\overline{\nu}_1$	0.092	0.086	0.094	0.091 ± 0.005
$\nu_{\perp[010]/[010]}$	0.107	0.111	0.114	0.111 ± 0.003
$\nu_{\perp[010]/[001]}$	0.048	0.046	0.044	0.046 ± 0.002
$\overline{\nu}_{\perp[010]}$	0.077	0.078	0.079	0.078 ± 0.001
$\nu_{[110]/\perp[\bar{1}\bar{1}0]}$	0.715	0.714	0.683	0.704 ± 0.021
$\nu_{[110]/[001]}$	0.004	0.003	0.004	0.004 ± 0.001
$\overline{\nu}_{[110]}$	0.360	0.359	0.344	0.354 ± 0.010
$\nu_{[010]/\perp[0\bar{1}0]}$	0.537	0.558	0.586	0.560 ± 0.026
$\nu_{[010]/[001]}$	0.024	0.025	0.026	0.025 ± 0.001
$\overline{\nu}_{[010]}$	0.280	0.291	0.306	0.292 ± 0.014

4.6   Conclusion

The full elasticity tensor was computed for cellulose I_β network A using DFT with van der Waals correction using a least squares fitting method with VASP as the computational engine. Results show a good agreement with previous experimental work, in particular, a remarkable agreement is found with the IXS experiments conducted by Diddens et al. [32]. Three dimensional surfaces, which are color contours showing the crytstallographic dependence of the Young modulus and Poisson's ratio, were computed to examine the extreme anisotropy of these important elastic properties. A clear correlation between the stiffness of the crystal and the different deformation mechanisms

was noted. The largest Young's modulus (206 GPa) was found to be aligned with the *c*-axis were covalent bonds determine the mechanical response of the crystal. Perpendicular to the cellulose chain axis, the *b*-direction shows the next greatest value for the Young modulus (98 GPa); this can be explained by the presence of the hydrogen bond network linking the cellulose chains. Finally a value for the Young modulus of only 19 GPa was computed along the direction perpendicular to the previous two, where only weak vdW forces play a role in the mechanical response of the material. Based on 0 K simulations with dispersion-corrected DFT in VASP, the transverse Young Modulus for crystalline cellulose can be defined in the range between 13 to 98 GPa, in good agreement with reported experimental results [32-35] and other numerical simulations [25, 91, 92].

CHAPTER 5. TEMPERATURE DEPENDENCE OF MECHANICAL AND
THERMODYNAMIC PROPERTIES OF CRYSTALLINE CELLULOSE FROM
FIRST PRINCIPLES

5.1   Introduction

Understanding the structure and properties of crystalline cellulose (I_β) and how these relates to the properties of cellulose nanoparticles (CNs) at a fundamental level can facilitate development of CN composites as well as broaden the general knowledge of CN behavior as a nanomaterial.

The fundamental thermo-mechanical properties of cellulose I_β are not completely understood or quantified. This is partially due to difficulties in experimental testing, propagation of uncertainties in these experimental tests [15], and intrinsic material variability in the crystalline cellulose being tested (e.g. different crystal structures, defects, percent crystallinity, etc.) [1]. Recent theoretical efforts to predict cellulose properties, such as the Young's modulus, have shown substantial differences in values which are likely due to differences in model parameters, simulation method, configuration of the modeled structure, and incorporation of hydrogen bonding [14] and Van der Waals interactions [1, 16]. On the other hand, experimental values of Young's modulus obtained from X-Ray Diffraction were reported to range from 90 to 138 GPa [23-25, 30, 31]. Recently, Diddens et al. [32] reported an axial elastic modulus of 220 ± 50 GPa and transverse elastic modulus of 15 ± 1 GPa using Inelastic X-ray Scattering (IXR).

Lahiji et al. [35] and Wagner et al. [33] have measured a transverse elastic modulus of 8.1 GPa through nanoindentation using an atomic force microscopy (AFM). Unfortunately, this technique can only offer a 95% confidence interval of 2.7-20 GPa. Similarly, the experimentally measured thermal expansion coefficients (TEC's) of cellulose I_β are also scattered [37-40]. The range of reported TEC along *a, b,* and *c*-axis of the crystalline cellulose (I_β) are as follows: $9.8\text{-}13.6\times10^{-5}$ K^{-1}, $0.5\text{-}4.6\times10^{-5}$ K^{-1}, and 0.6×10^{-5} K^{-1}, respectively. Additionally, at temperatures approaching 475-500 K, the I_β structure transitions to a high-temperature phase that shows a different TEC response. To the author knowledge there has only been one study of TEC of crystalline cellulose [93] reporting TEC of 7.3×10^{-5} K^{-1}, and 1.5×10^{-5} K^{-1}, in the *a* and *b*-axis, respectively. The studies listed above suggest high elastic and low thermal expansion behavior of I_β and also indicate extreme property anisotropies as a result of the unique bonding nature within I_β.

There is currently a dearth of information on thermal conductivity (*k*) values for cellulose I_β both in the experimental and the theoretical literature. Shimazaki et al. [41] produced Nano Fibrillated Cellulose (58 wt%)-epoxy matrix reinforced composite that had thermal conductivity of 1.1 W m^{-1} K^{-1} in the in-plane direction and 0.23 W m^{-1} K^{-1} in the thickness direction. Results showed that there is a 7-8 times increase in the thermal conductivity in the in-plane direction and 1-2 times in the thickness direction compared to the neat epoxy matrix.

The present work aims to probe the extreme anisotropies of elasticity, thermal conductivity and thermal expansion at finite temperatures as well as their origins for cellulose I_β with the help of first-principles phonon calculations and molecular dynamic

simulations. To these ends, first-principles Van der Waals density functionals [77] were employed to compute phonon properties, finite temperature thermodynamic properties (entropy, enthalpy, and constant pressure heat capacity via the quasiharmoic approach) [94-97], thermal expansion tensor components, ξ_i, and elasticity tensor components, C_{ij}, of the monoclinic cellulose I_β structure. Reverse non-equilibrium molecular dynamics (RNEMD) simulations are used for the first time to compute the thermal conductivity of the monoclinic cellulose I_β. The temperature dependences of ξ_i and C_{ij} are studied via a quasistatic approach proposed recently with the main input being the predicted strain/elasticity-volume-temperature relationships [98, 99]. Variations of the Young Modulus and Poisson's ratio with respect to the crystallographic orientation are computed based on the elasticity tensor at different temperatures.

5.2   Structural information

The structure of cellulose I_β has a monoclinic lattice with space group $P2_1$ [100] including two functional unites of $C_6H_{10}O_5$ in the primitive cell and four in the crystallographic cell. The initial lattice parameters are defined as: $a = 7.784$ Å, $b = 8.201$ Å, $c = 10.380$ Å, $\alpha = 90°$, $\beta = 90°$, and $\gamma = 96.55°$ [100]. Figure 5-1 illustrates the projected structures of cellulose I_β along a-axis and b-axis directions. Within the a-b plane (Figure 5-1b) the energetically favorable hydrogen-bond pattern A [13] determined by Nishiyama et al. [100] using X-ray and neutron fiber diffraction is adopted herein. The layer structure of I_β perpendicular to a-axis, is where the Van der Waals forces dominant the stacking interactions [13]. Within the b-c plane, the bonding along

c-axis direction is stronger than those along *b*-axis direction according to the bond lengths.
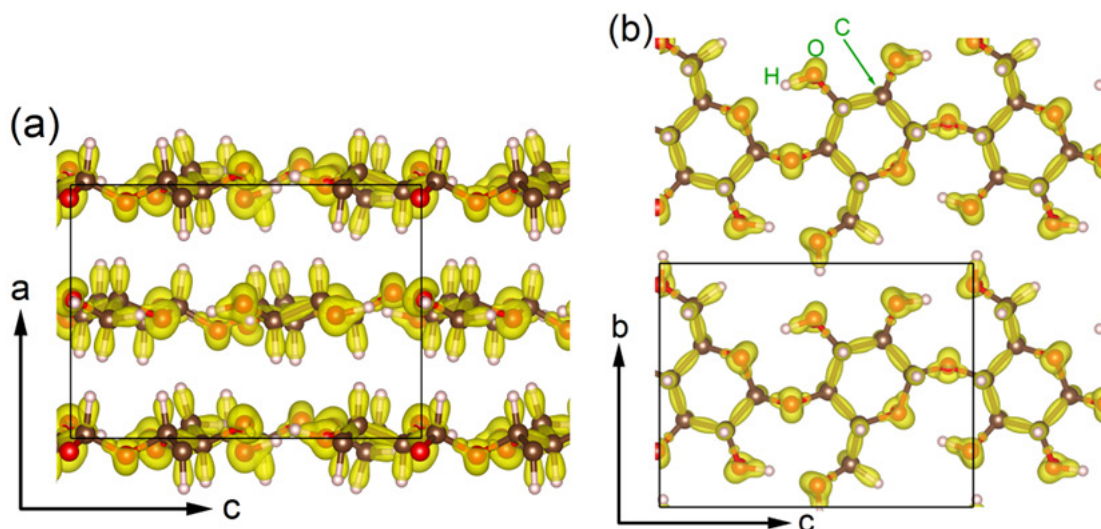

Figure 5-1 Projected structures of cellulose I_β (space group $P2_1$) along *b*-axis direction (a) and along *a*-axis direction (b), showing obvious layered structure of I_β along the *a*-axis direction, and weaker bonding along the *b*-axis direction with respect to that of *c*-axis direction. The change gains calculated with PBE-D2 are also shown, illustrated in the change density difference ($\Delta\rho/Å^3$, the yellow colors) isosurfaces, where the reference density is the initial charge density calculated in one electronic step. The rectangles in (a) and (b) indicate the lattices of I_β.

5.3   First-principles calculations: total energy, elasticity and phonon

All density functional theory (DFT) based first-principles calculations in the present work are performed with the VASP 5.2 code [66, 67]. The Kohn-Sham equations have been solved in a plane-wave basis set using the projector augmented wave (PAW) method [101] and the exchange-correlation energy is described by the generalized gradient approximation of Perdew-Burke-Ernzerhof (GGA-PBE) [72]. For C, four electrons ($2s^2 2p^2$) are treated as valence, one for H ($1s^1$), and six for O ($2s^2 2p^4$). To account for London dispersion interactions, the PBE-D2 correction scheme proposed by Grimme [77]

has been used together with the standard set of parameters as implemented in VASP [102]. Compared to the standard DFT functionals, which fail to describe the Van der Waals forces, the D2 scheme as employed in the present work can describe correctly the three-dimensional lattice structure of cellulose as demonstrated by Bucko et al. [13].

Regarding first-principles phonon calculations to estimate temperature-dependent properties, the supercell approach using the PHONON code was adopted as implemented in the MedeA environment [103, 104] with VASP as the computational engine. The longitudinal and transverse optical (LO-TO) zone center splittings were ignored for the infrared active modes in cellulose I_β, since the LO-TO splitting has a negligible effect on thermodynamic properties as has been clearly demonstrated in the literature [95, 96]. Force constants, i.e., the Hessian matrix, are calculated in real space using the crystallographic cells of cellulose I_β including 84 atoms. The atomic displacements of ±0.02 Å are employed in the present work for the ions positioned at symmetry-unique sites in the lattice. More details about phonon calculations using PHONON code as implemented in MedeA can be found in e.g. references [96, 105, 106].

First-principles calculations of elasticity tensor components, C_{ij}, are also calculated within the MedeA environment using the strain-stress method as developed by Le Page and Saxe [64, 107]. Strains of ±0.5% and the crystallographic cells of cellulose I_β are used. More details about the elastic calculations using the Le Page and Saxe method as implemented in MedeA can be found in e.g. references [96, 105, 106, 108-110].

During VASP calculations performed on the crystallographic cells of cellulose I_β, the tetrahedron method with Blöchl corrections [111], a Γ-centered 2×2×2 k-point mesh, and

a 800 eV plane wave energy cutoff are employed for structural relaxations and final static calculations of energy, stress and electronic structure. Electronic degrees of freedom are converged to 10^{-7} eV/cell, while the Hellman-Feynman force components are relaxed to at least 2×10^{-3} eV/Å. Concerning the calculations of elasticity tensor components, a $7\times7\times7$ k-point mesh and a 520 eV plane wave cutoff energy are employed.

5.4   First-principles thermodynamics

First-principles thermodynamics at finite temperatures can be calculated using the quasiharmonic approach with the Helmholtz energy, $F(V,T)$, at volume V and temperature T given by [94-97]:

$$F(V,T) = E(V) + F_{el}(V,T) + F_{vib}(V,T) \tag{4}$$

Here, $F_{el}(V,T)$ represents the thermal electronic contribution evaluated from the electronic density of states (DOS). This term, which is important for metals with non-zero electronic density at the Fermi level, is ignored since cellulose I_β is an insulator. The vibrational contribution to $F(V,T)$, which is obtained from the total phonon DOS at six volumes in the present study, is $F_{vib}(V, T)$. Note that F_{vib} at 0 K contains a zero-point vibrational energy (ZPE) contribution due to quantum fluctuations at the ground state, which can be estimated from the phonon DOS [112]. The static energy at 0 K without the ZPE in Equation (4) is $E(V)$: this term can be determined by fitting the first-principles energy vs. volume (E-V) data points according to a four-parameter Birch-Murnaghan equation of state (EOS) [94]:

$$E(V) = k_1 + k_2 \times V^{-2/3} + k_3 \times V^{-4/3} + k_4 \times V^{-2} \tag{5}$$

where k_1, k_2, k_3 and k_4 are fitting parameters. The equilibrium properties estimated from this EOS include the volume (V_0), energy (E_0), bulk modulus (B_0) and its pressure derivative (B_0'). Seven *E-V* data points are used for EOS fitting. In the present work the quasiharmonic method as shown in Equation (4) is used to compute the entropy, enthalpy, isobaric heat capacity, C_P, equilibrium volume as a function of temperature, and the (average) linear thermal expansion coefficient (TEC), see detailed methodologies in references [94, 97].

5.5   Elasticity tensor and thermal expansion components at finite temperatures

Most, but not all, polycrystalline materials have identical values of their mechanical properties in all directions; therefore, a stress-strain tensile behavior will be completely independent of the relative orientation of the specimen with respect to the loading direction. Such materials are call isotropic and have the advantage that, if they present a linear elastic response, they can be easily characterized by only two parameters, the Young modulus (*E*) and the Poisson's ratio (*v*).

As opposed to isotropic materials, single crystals or textured materials present anisotropic properties with respect to an intrinsic direction in the material. The most general linear stress-strain relation to characterize the mechanical behavior of a material has the form: $\sigma_{ij} = C_{ijkl}\, \varepsilon_{kl}$ (Einstein notation) whereas σ_{ij} and ε_{kl} represent the second order stress and strain tensor, respectively, and C_{ijkl} is a fourth order stiffness tensor with 81 components [60]. The existence of symmetries in the stiffness tensor allows a matrix representation with only 36 components using Voigt's notation. Furthermore, if the stress-strain relation is derived from a strain energy density functional, the arbitrariness of the order of

differentiation implies that the matrix representation must be symmetric resulting in only 21 independent constants [60].

The monoclinic structure of cellulose I$_\beta$ implies that the unit cell has a symmetry plane that is defined by the *c*-axis. The presence of a symmetry plane has a direct consequence over the stiffness matrix in that it reduces the number of coefficients necessary to represent the system to only 13 independent constants. The strains and stresses and hence C_{ij} are defined in a Cartesian coordinate system related to the original crystalline structure. Using the computed stiffness matrix at different temperatures and knowing the crystallographic orientation of the unit cell with respect to a global coordinate system it was possible to compute the resulting Young's Modulus and Poisson's ratio in any direction. 3D representations of their values can be constructed to enable understanding of their variations with the crystalline coordination. Additionally, 2D projections over the most important planes are used to analyze in detail variations with respect of a particular orientation angle and temperature. All orientations are univocally defined by Miller indices in conjunction with a reference Cartesian system of coordinates. For detailed methodologies see Chapter 4 and Dri et al. [113].

With increasing temperature, six independent linear thermal expansion coefficients (TEC's), ξ_i, can be derived at a given pressure, P,

$$\xi_i = \left(\frac{\partial \varepsilon_i(T)}{\partial T} \right)_P \tag{6}$$

After first-principles calculations at a series of volumes and 0 K, strains as a function of volume, $\varepsilon_i(V)$, with respect to a given volume (e.g., the equilibrium volume), can be estimated using the relaxed lattice vectors at different volumes. Meanwhile, the volume-

temperature relation, $V(T)$, or inversely the $T(V)$ relation, can be predicted according to the quasiharmonic approach of Equation (4). By employing a quasistatic approach without considering the kinetic energy and the fluctuation of microscopic stress tensors at high temperatures, i.e., by combining $\varepsilon_i(V)$ and $T(V)$ merely, the temperature-dependent strains, viz., the TEC's ξ_i, are functional of V, $\xi_i(T) = \varepsilon_i(T(V))$.

Similarly to the TEC's estimated by $\xi_i(T) = \varepsilon_i(T(V))$, the isothermal elasticity tensor components $C_{ij}(T)$ can be estimated using the obtained C_{ij} as a function of volume, $C_{ij}(V)$, and the $T(V)$ relation as mentioned above, viz., $C_{ij}(T) = C_{ij}(T(V))$, see more details in references [98, 99]. Note that the measured elasticity tensor components at high temperatures (e.g. using the resonance method) are usually isentropic since the system is adiabatic due to the faster speed of elastic waves relative to heat diffusion [98]. The thermodynamic relations between the isothermal and isentropic elasticity tensors were given by Davies [114], see also reference [98].

5.6   Molecular dynamics calculations: thermal conductivity

The thermal conductivity, λ, is the proportionality constant that relates the heat flux, j, to the driving force of a temperature difference, dT/dz:

$$j_z = -\lambda \frac{dT}{dz} \tag{7}$$

where the z direction is arbitrarily taken for convenience. The obvious way to implement this in a molecular dynamics code is to produce the temperature profile across a slab of the material by coupling one side to a cold temperature bath and the other to a hot one, measuring the heat flux. This, however, creates issues with the conservation of energy in

the system since it is coupled to two heat baths which are adding and removing energy, so the details of the coupling to the heat baths affects the calculations.

Müller-Plathe [115] realized that there was an elegant solution to this issue: rather than drive the temperature of the system as one would do in a physical system, in the computational experiment one can produce a heat flux by exchanging the momenta of particles in the cold region with those in the hot region, and then measure the resulting temperature profile. This is the reverse non-equilibrium molecular dynamics (RNEMD) approach to transport, which neatly circumvents the issues of conservation of energy. In practice, the simulation is performed on a sample of material elongated in, e.g., the z-direction, which is conceptual divided into a number of layers – typically about 30 – in that direction. Every so often, the momentum of the hottest particle in the cold layer is swapped with that of the coldest particle in the hot layer. This has the effect of producing a heat flux, which is measured, from the cold layer to the hot layer. In response, the system develops a temperature gradient between the hot and cold layers, which can be measured through the average temperature in each of the layers between the hot and cold layers. The rate of momentum transfer is adjusted to provide a reasonable ramp in the temperature. If the system is driven too hard, the temperature profile will not be linear, but if driven too gently the natural fluctuations of the temperature in a small sample will reduce the accuracy of the measured temperature ramp.

5.7   Results and discussion

5.7.1   Bonding strength

Phonon calculations enable quantitative analysis of the bond strengths between atomic pairs using force constants [106]. Force constants quantify the extent of interaction or bonding between the atoms. A large positive force constant suggests bonding, while a negative force constant suggests that the two atoms in question would prefer to move apart. A zero or near-zero force constant indicates that the interactions between two atoms are negligible [96, 106, 112]. Figure 5-2 shows the key stretching force constants of cellulose I_β at its theoretical equilibrium volume at 0 K (see Table 5-1).

As expected, the strongest bond strength (~ 36 eV/ Å^2) belongs to the O-H atomic pairs with the minimal bond lengths (~ 1 Å), followed by the second strongest C-H atomic pairs (~ 27 eV/ Å^2 with bond lengths ~ 1.1 Å). The strongest hydrogen bond (H bond) indicates its critical role to stabilize cellulose. Besides H bond, the C-O and C-C atomic pairs also possess quite large bond strength as shown in Figure 5-2. Additionally, the strong bondings between O-H, C-H, C-O, and C-C atomic pairs are also clearly shown in the isosurfaces of the charge density difference contours ($\Delta\rho/\text{Å}^3$) of Figure 5-1, where the reference (or non-interacting) charge density is calculated from one electronic step. It is seen that the charge gains are mainly between these atomic pairs, indicating the strong bondings between them. The charge gains in Figure 5-1 also show the apparent bond directivities between atomic pairs of O-H, C-H, C-O, and C-C, implying the covalent nature between them. In addition, the charge gains between atoms as well as the bond lengths between them point out the strong bonding is along *c*-axis direction, and the weak

one along *a*-axis direction. Predicted properties of elasticity and thermal expansion as shown below confirm further these observations.
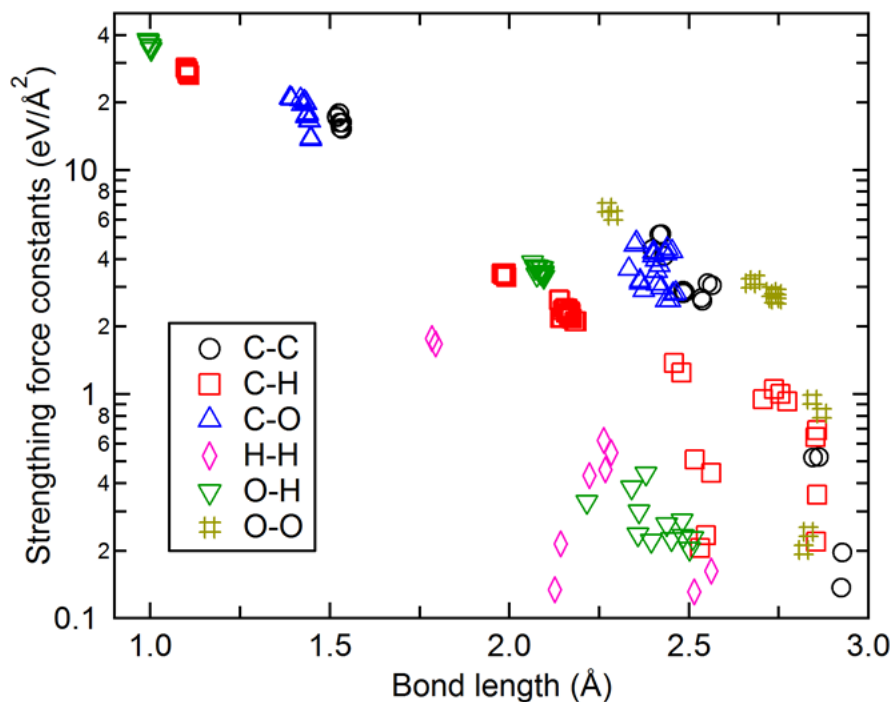

Figure 5-2 Key stretching force constants of cellulose I_β according to phonon calculations.

5.7.2   Structural properties

Table 5-1 summarizes the predicted structural properties for cellulose I_β based on the PBE-D2 method, including the lattice parameters and angle γ for the crystallographic cell, and the equilibrium properties V_0, B_0, and B_0' estimated using the EOS of Equation (5). It is found that the structural properties of I_β are in good agreement with experimental data [116, 117] and other PBE-D2 predictions [13, 102, 118]. For example, the present predictions of lattice parameter a = 7.618 or 7.752 Å at 0 K (without and with the ZPE effects, respectively) agree with the measured 7.64 Å at 15 K [116]; the present b = 8.139

or 8.153 Å at 0 K (without and with the ZPE effects, respectively) versus the measured

8.18 Å at 15 K [116]; and the present c = 10.399 or 10.409 Å at 0 K (without and with

the ZPE effects, respectively) versus the measured 10.37 Å at 15 K [116], see Table 5-1

for more detailed comparisons.

Table 5-1 First-principles calculated (using the PBE-D2 method) and experimental properties of cellulose I_β, including the lattice parameters a, b, c, angle γ, equilibrium volume (V_0), bulk modulus B_0 and its pressure directive (B_0').

Method	a (Å)	b (Å)	c (Å)	γ (°)	V_0 (Å^3)	B_0 (GPa)	B_0'
PBE-D2, this work, 0 K[a]	7.618	8.139	10.399	96.59	640.57	16.1	6.69
PBE-D2, this work, 0 K[b]						17.4	7.46
PBE-D2, this work, 0 K[c]	7.752	8.153	10.409	96.40	653.80	13.9	
PBE-D2, this work, 295 K[c]	7.896	8.167	10.418	96.12	667.92	10.0	
PBE-D2, other work, 0 K	7.57[d]	8.14[d]	10.39[d]	96.5[d]	636[d]	16[e]	
PBE-D2, other work, 0 K[f]	7.85	8.18	10.47	96.5	668		
Expt., 15 K[g]	7.64	8.18	10.37	96.54	643.9		
Expt., room temperature	7.76[g]	8.20[g]	10.37[g]	96.62[g]	655.5[g]	19.8±2.9[h]	27.6±6.2[h]
Expt., room temperature[i]	7.82	8.26	10.40	96.3			

[a] Calculated results without ZPE based on the energy-volume EOS, i.e., Equation (5)

[b] Calculated results without ZPE based on the pressure-volume EOS based on Equation (5)

[c] Calculated with ZPE based on the quasiharmonic approach, see Equation (4)

[d] Calculated without ZPE [13].

[e] Fitted using first-principles data points and Murnaghan's EOS [102].

[f] Calculated by ESPRESSO using norm-conserving pseudopotentials [118].

[g] Measured by neutron diffraction [116].

[h] Fitted using the Birch-Murnaghan EOS based on the measured pressure-volume data points, but these data points are scattered [117].

[i] Measured by X-ray [117].

Besides the equilibrium volume V_0, another key parameters of bulk modulus B_0 and its

pressure derivative B_0' can be used to (i) judge the quality of first-principles calculations

in comparison with experimental data; (ii) re-build EOS (Equation (5)) used in the

quasiharmonic approach of Equation (4); and (iii) indicate qualitatively the extent of

thermal expansion [94]. As for bulk modulus, the present prediction of 16.1 GPa (using

the E-V EOS of Equation (5)) or 17.4 GPa (using the P-V EOS derived from Equation (5))

is in good agreement with a previous PBE-D2 prediction (16 GPa) [102] and the

measured data (19.8±2.9 GPa) [117]. Concerning the pressure derivative of bulk modulus, B_0', the present study gives a reasonable value of 6.69 (based on the *E-V* EOS of Equation (5)) or 7.46 (based on the *P-V* EOS derived from Equation (5)), however, the measured one is too large (27.6±6.2 according to the scattered *P-V* data points [117]) compared with the common values around 3~6 for most materials [119]. The good agreement between predictions and experiments as shown in Table 5-1 indicates that the Van der Waals forces existed in cellulose I_β can be described satisfactorily by the PBE-D2 method.

5.7.3   Thermodynamic properties

Figure 5-3 illustrates the predicted thermodynamic properties of cellulose I_β up to 500 K under external pressure $P = 0$ GPa using the quasiharmonic approach of Equation (4), including enthalpy, entropy, and heat capacity at constant pressure. Here, (i) the reference state of enthalpy is set to zero at 0 K, and (ii) the temperature of 500 K is close to the phase transition temperature of I_β to a high temperature phase [39, 40]. Figure 5-3 shows that the present predictions of enthalpy, entropy, and heat capacity at constant pressure agree well with experimental data measured using cotton microcrystalline cellulose with the degree of crystallinity of 90% as well as the extrapolated data at high temperatures (>300 K) [120]. Figure 5-3 also indicates that the present predictions are slightly lower than the measurements, especially at high temperatures (>300 K). Based on the quasiharmonic approach of Equation (4) as well as the quasistatic approach as mentioned

above, the predicted lattice parameters a, b, c, angle γ of cellulose I_β are shown in Figure 5-3 as a function of temperature.
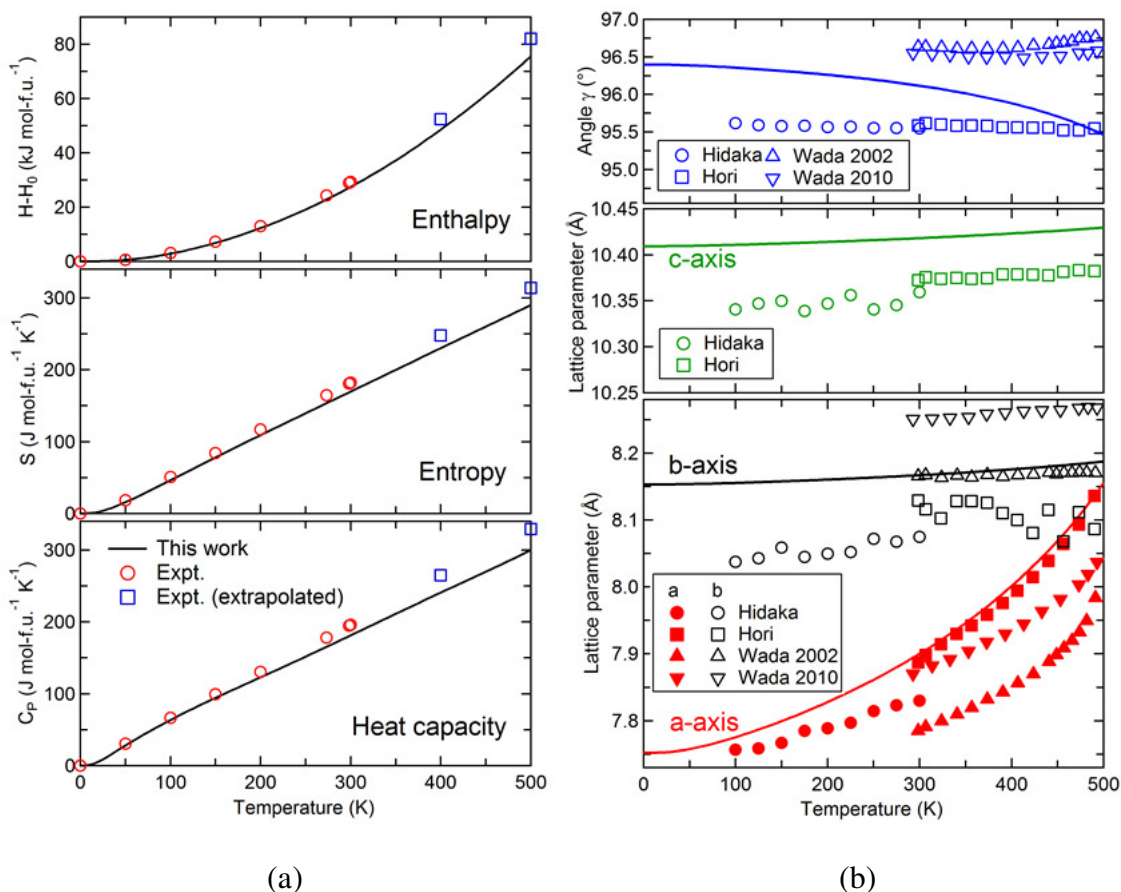

(a)　　　　　　　　　　　　　　　　　　(b)

Figure 5-3 (a) Thermodynamic properties of cellulose I_β including enthalpy H, entropy S, and heat capacity at constant pressure C_P. Note that (i) enthalpy at 0 K, H_0, is the reference state of H, and (ii) the experimental data are measured using cotton microcrystalline with the degree of crystallinity of 90% [120], (b) Predicted lattice parameters a, b, c, angle γ of cellulose I_β compared with experimental data measured by Hidaka et al. using wood cellulose [37], by Hori using wood cellulose [38], by Wada (2002) using tunicate (halocynthia) [39], and by Wada et al (2010) using green algae [40].

The present predictions agree reasonably well with the scattered data measured by Hidaka and coworkers using wood cellulose [37], by Hori using wood cellulose [38], by Wada using tunicate (halocynthia) [39], and by Wada et al. using green algae [40]. Lattice parameter a increases quickly with increasing temperature compared to lattice

parameters b and c due to the weak bonding along a-axis direction (see Figure 5-1 and the discussion above). As for the angle γ, the present work predicts a decrease trend, while the measured values show a constant or an increasing trend with increasing temperature. Variations of lattice parameters and angles with respect to temperature can be re-plotted as the linear thermal expansion tensor components, ξ_i.
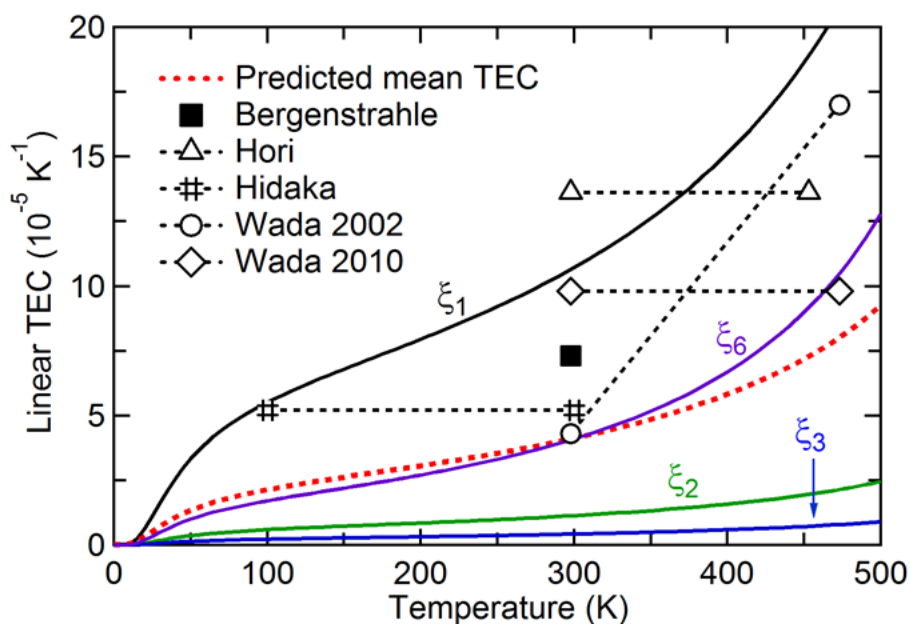

Figure 5-4 Predicted thermal expansion tensors (TEC's, 10^{-5} K^{-1}) and the mean TEC of cellulose I$_\beta$. Experimental TEC's along a-axis (ξ_1) are shown in open symbols with dashed lines (measured by Hidaka et al. using wood cellulose [37], by Hori using wood cellulose [38], by Wada 2002 using tunicate [39], and by Wada et al. 2010 using green alga [40]), and the TEC along a-axis (ξ_1) predicted by molecular dynamics simulation [93] is shown in filled square.

Figure 5-4 shows that ξ_1 (along a-axis direction) agree reasonably with the rough estimations from measurements [37-40] and molecular dynamics simulations [93]. In addition, ξ_1 is quite larger compared with the smaller ξ_2 (roughly along b-axis direction) and ξ_3 (along c-axis direction), agreeing with measurements [37-40]. It is worth

mentioning that the present TEC's (e.g., ξ_1) are larger than the measured data (Figure 5-4), but the other thermodynamic properties predicted in the present work are smaller than the measurements (see Figure 5-3), implying (i) the uncertainties of measurements and (ii) the reasonable predictions in the present work.
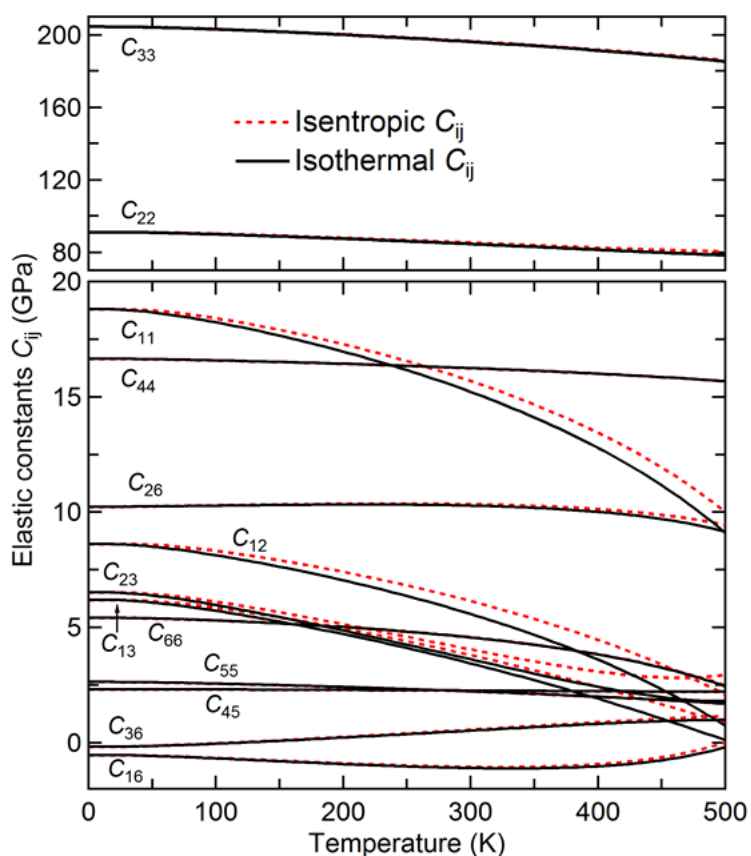
5.7.4   Elastic properties

Figure 5-5 Predicted isothermal and isentropic elastic constants C_{ij} of cellulose Iβ based on the quasistatic approach.

At finite temperatures, Figure 5-5 shows the predicted isothermal and isentropic elastic constants C_{ij} using the quasistatic approach. The isothermal C_{ij} are greater than (or equal

to) the isentropic ones due to the positive thermal expansion tensor components (see Figure 5-5) [98, 114]. With increasing temperature, these C_{ij} decrease expect for C_{16} and C_{36}, which are close to zero. In addition, the largest decrease with increasing temperature is C_{11}, followed by C_{12}, C_{13}, and C_{23}, etc, caused by the extremely large TEC ξ_1 along a-axis direction (see Figure 5-5).

Table 5-2 Elastic properties (in GPa) of cellulose I_β at T = 0 K without the effects of ZPE, including elasticity tensor components (C_{ij}) and material properties of bulk modulus (B), Young's modulus (E) and Poisson's ratio (ν). Note that Young's modulus as a function of direction is shown in Figure 5-6 and the C_{ij} at high temperatures predicted by quasistatic approach are shown in Figure 5-5.

C_{ij} [GPa]						B [GPa]	E [GPa]	ν
22.1	11.5	9.2	0	0	0.7	19.8±2.9[a]	145, 150[b]	0.377[i]
	98.9	10.3	0	0	9.7		120-135[c]	0.639[i]
		213.3	0	0	−1.1		134,[d] 143[e]	0.442[i]
			17.1	2.4	0		15, 220[f]	
				3.1	0		100-160[g]	
					5.9		12-27[h]	

[a] Fitted using the Birch-Murnaghan EOS based on the measured pressure-volume data points, but these data points are scattered.[117]
[b] Measured by atomic force microscopy using tunicate microfibrils.[121]
[c] Measured by X-ray using microfibers.[122]
[d] Measured by X-ray using microfibers.[123]
[e] Measured by Raman spectroscopy using tunicate whiskers.[124]
[f] Measured by inelastic X-ray scattering with 15 GPa perpendicular to the fiber direction and 220 GPa parallel to it.[125]
[g] Typical values by measurements for highly crystalline cellulose types.[126]
[h] Typical values measured under tensile stress conditions.[117]
[i] Measured by X-ray on ramie for tension along [004] direction and negative strain along [200] direction, i.e., 0.377 for [200]/[004], 0.639 for [110]/[004], and 0.442 for [1̄10]/[004].[127]

Table 5-2 summarizes the predicted elastic properties of cellulose I_β (space group $P2_1$ with the unique c-axis setting) under the theoretical equilibrium volume, $T = 0$ K, and without the effects of ZPE. The predicted elasticity tensor components indicate that the largest $C_{33} = 213$ GPa, which is comparable to the values of 3d transition metals of Fe, Ni,

and Cu, etc. [128, 129] However, the other C_{ij} are quite small, e.g., the second largest one C_{22} = 99 GPa and the third largest one C_{11} = 22 GPa. The trend of $C_{33} \gg C_{22} > C_{11}$ is consistent with the TEC trend of $\xi_1 \gg \xi_2 > \xi_3$ (see Figure 5-4) as well as the (relative) charge density distribution as shown in Figure 5-1, indicating the strong bonding along c-axis direction but the weak one along a-axis direction as discussed above. The large difference between different C_{ij} is also a signal of extremely elastic anisotropy, see details below. The extreme anisotropies encountered in the analysis of the elastic constants (C_{ij}) can be better understood by considering the variation of Young's modulus with the crystallographic orientation. Figure 5-6 gives a 3D representation of the Young modulus for crystalline cellulose computed at 300 K. Each point on the given surface represents the magnitude of Young's modulus in the direction of a vector from the origin to the point; the color map helps identifying the Young modulus variation and emphasizes the extreme anisotropy of the system.

Two-dimensional (2D) polar plots of the variation of the Young modulus with respect to the crystallographic orientation and temperature were also generated. Figure 5-7 shows the variation of the Young modulus with the orientation angle considering the *2*-axis as the rotation axis. Three different temperatures (0, 300 and 500 K) are superimposed in the same figure to analyze the influence over the Young modulus. The direction defined by the *3*-axis (c-axis) exhibits the highest value of Young modulus changing from 202 GPa at 0 K to 196 GPa at 300 K and down to 190 GPa at 500 K. The small variations of the Young modulus (12 GPa at 500 K) could be explained by the strong covalent bonds that govern the deformation in the chain direction (c-axis). It is important to note that a change of only 10° in the longitudinal alignment (c-axis) will reduce the theoretical

Young modulus from ~200 GPa to a mere ~70 GPa. This important reduction in the stiffness could be explained by the deformation mechanism involved in the cellulose crystal (see Chapter 4 and Dri et al. [113] for a comprehensive explanation).

A similar analysis can be performed on Figure 5-8, where the variation of Young modulus is analyzed over the *1-2* plane. The [010] directions (*b*-axis) shows the highest value of Young modulus in the plane with values of 91 GPa at 0 K, 87 GPa at 300 K and 83 GPa at 500 K. The moderate high value of the Young modulus in the [010] direction could be explained by the H bond network present in-between cellulose chains. Stretching in the [010] direction implies increasing the in-plane separation of the chains which has direct impact over the inter-chain hydrogen bonds. A second relative maximum is found in the direction marked as ⊥[010] in Figure 5-8; weak van der Waals forces govern the response of the system in this direction. The lowest values of Young modulus are found to be 12 GPa at 0 K, 9 GPa at 300 K and 7 GPa at 500 K. Results are consistent with reported experimental values [23-25, 30-35] and other numerical simulations [25, 91, 92, 113].
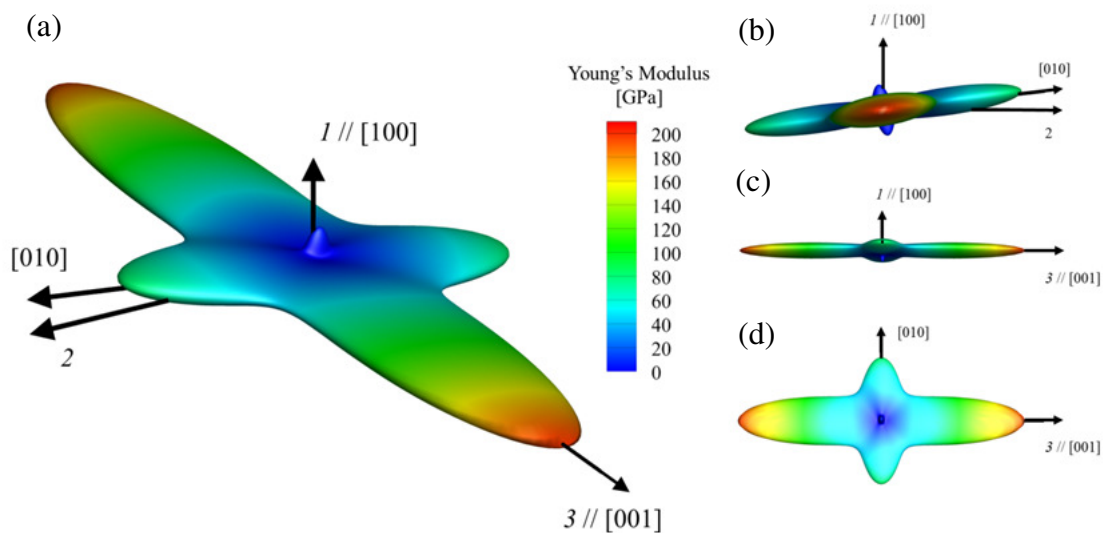
Figure 5-6 Young's modulus surfaces for cellulose I$_\beta$ computed at 300 K. Each point on the given surface represents the magnitude of Young's modulus in the direction of a vector from the origin to the point; the color map helps identifying the Young modulus variation and emphasizes the extreme anisotropy of the system.
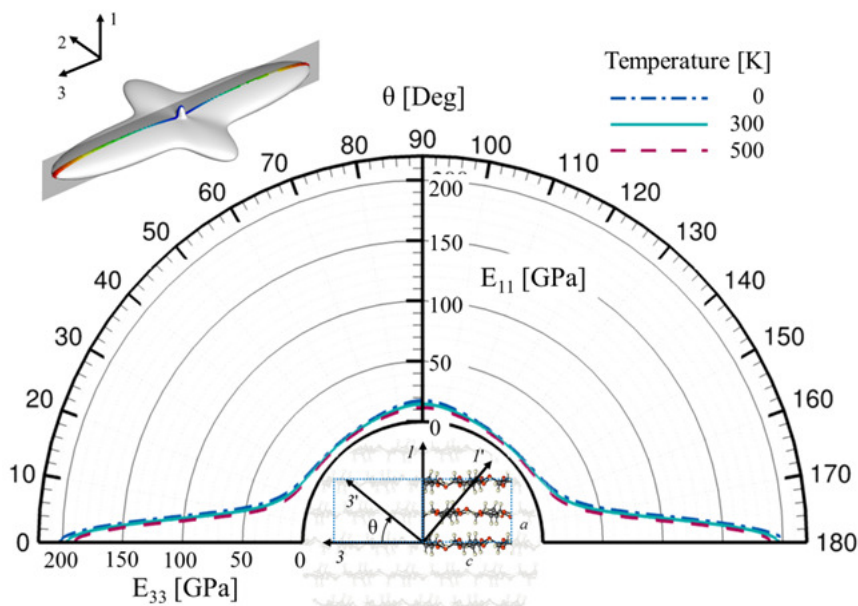

Figure 5-7 Young's modulus as a function of the rotation angle for different temperatures. The *2*-axis (pointing inside the page) is considered to be the rotation axis; the value of the Young modulus for a given direction can be read directly from the figure by defining a straight line from the origin to the desire angle.
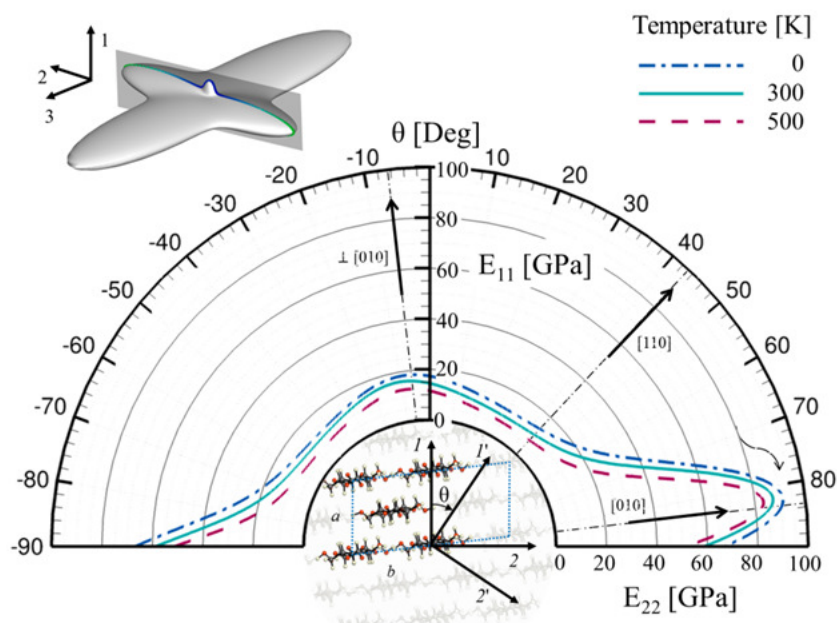
Figure 5-8 Young's modulus as a function of the rotation angle for different temperatures. The *3*-axis (pointing inside the page) is considered to be the rotation axis; the value of the Young modulus for a given direction can be read directly from the figure by defining a straight line from the origin to the desire angle.

Variations of the Poisson's ratio with respect to the crystalline orientation were computed applying the same procedure as that for the Young modulus. Since the Poisson's ratio is the negative ratio of transverse to axial strain, its interpretation is not as straight forward as the Young modulus. Figure 5-9 shows the average Poisson's ratio [113] as a function of the crystallographic orientation computed at 300 K. The extreme anisotropies observed in crystalline cellulose can be once again evidenced in the high variations of the average Poisson's ratio. It can be observed in Figure 5-9 that the three main crystallographic directions exhibit the lowest values for the average Poisson's ratio (~0.1) whereas other directions present values up to 0.4. Figure 5-10 analyzes the variation of the average Poisson's ratio over the *1-2* plane for different temperatures. The

first relative minimum can be found in the [010] direction (*b*-axis). As the temperature

increases, the Poisson effect is less evident (decreasing value of the Poisson's ratio)

suggesting a reduction in the effects of separating cellulose chains over the final shape of

the crystal. A similar behavior is found in the direction marked as ⊥[010], where weak

van der Waals interaction govern the response of the system. For direction [110],

temperature appears to have no effect over the Poisson's ratio. Comparison with previous

publications [25, 36, 91, 113] showed results that are in good agreement with the values
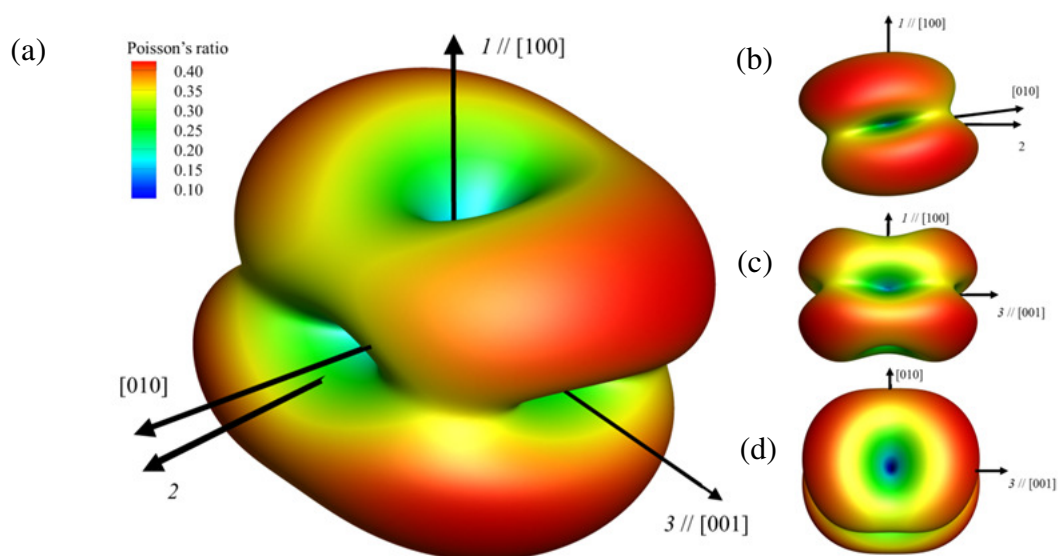
reported in this work.

Figure 5-9 Average Poisson's ratio surfaces for cellulose I_β computed at 300 K. Each point on the given surface represents the magnitude of Poisson's ratio in the direction of a vector from the origin to the point; the color map helps identifying the Poisson's ratio variation and emphasizes the extreme anisotropy of the system.
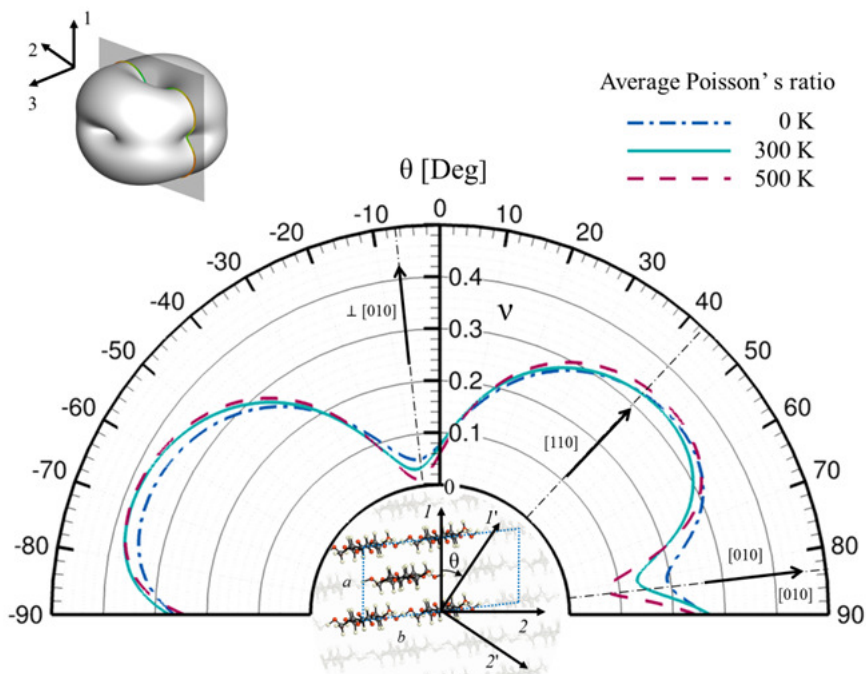
Figure 5-10 Average Poisson's ratio as a function of the rotation angle for different temperatures. The *3*-axis (pointing inside the page) is considered to be the rotation axis; the value of the Poisson's ratio for a given direction can be read directly from the figure by defining a straight line from the origin to the desire angle.

5.7.5 Thermal conductivity

Table 5-3 summarizes the predicted thermal conductivity of cellulose I_β. These results were obtained in terms of the RNEMD simulations with the pcff+[130] force field, using the molecular dynamics simulation code LAMMPS [131] within the MedeA framework [132].

Table 5-3 Calculated thermal conductivity of cellulose I_β obtained using reverse non-equilibrium molecular dynamics (RNEMD) with the pcff+ forcefield.

Method	*x* [W/m.K]	*y* [W/m.K]	*z* [W/m.K]
pcff+, RNEMD, this work	0.22 ± 0.02	0.52 ± 0.05	0.90 ± 0.06

Due to a limitation in the LAMMPS code, it was convenient to perform these calculations based on an orthorhombic cell. This was achieved using a simulation cell with 8 times the volume of the conventional unit cell. Inspection of the lattice shows that the following transformation yields an almost exactly orthorhombic cell:

$$a' = a$$
$$b' = -a + 8b \tag{8}$$
$$c' = c$$

where a, b and c are the original lattice vectors and a', b' and c' are the lattice vectors of the orthorhombic cell. Adjusting the resulting cell to be perfectly orthorhombic effectively fixes the cell angle γ at 96.67°, which is within a fraction of a degree of that found in this work and from experiment, as shown in Table 5-1. The lattice used for these calculations, which came from initial DFT calculations, was $a = 7.563$ Å, $b = 8.133$ Å, $c = 10.395$ Å, $\alpha = \beta = 90°$ and $\gamma = 96.67°$, resulting in an orthorhombic cell with $a' = 7.563$ Å, $b' = 64.621$ Å and $c' = 10.395$ Å.

As mentioned previously, the simulation cell for RNEMD needs to be reasonably large in the direction of the measurement because it must be subdivided into layers for the measurement of the temperature profile. For each of the three Cartesian directions, a supercell of the orthorhombic cell with a dimension in the direction of interest between 60 and 70 Å was constructed and used for the RNEMD calculations. For the x-direction, a 9×1×1 supercell with an extent in x of 68.068 Å, containing 6,048 atoms was used. In the y-direction, the original orthorhombic cell, with an extent of 64.621 Å and 672 atoms was used. In the z-direction, a 1×1×6 supercell with an extent of 62.371 Å and 4,032 atoms was used. For each simulation, the system was thermally equilibrated using NVT

(N: number of particles, V: volume, and T: temperature) dynamics for 50 ps, and then constant energy (NVE) dynamics was applied, during which the RNEMD was carried out by swapping momenta of one pair of particles every 600 steps for the x-direction, 250 steps for the y-direction and 200 steps for the z-direction. For the x- and z-directions, a total time of 2 ns was simulated during this phase, using a 1 fs time step. The simulation in the y-direction was more sensitive, perhaps because of the small system size, so was simulated for 1 ns using a 0.5 fs time step. The cell was divided into 30 layers in the direction of the heat flow for the measurement of the temperature. The temperature of the hot and cold layers and the two adjacent layers were not used to fit the temperature profile, since non-linear effects are often observed close to where the system is being driven. This left 24 layers for which the temperature was measured, from which the slope was obtained using a linear least-squares fit. The error bars were obtained from a statistical analysis of the points, and reflect a 95% level of certainty.

The results in Table 5-3 are consistent with the results for the thermal expansion coefficients and also the bonding patterns in the structure. The thermal conductivity is largest in the z direction, which is along the chains. This is the direction of the strongest bonding and the lowest thermal expansion. In the y-direction, which is roughly the direction of the hydrogen bonded network the thermal conductivity is intermediate, as is the thermal expansion, while in the x-direction, which corresponds to the weak van der Waals interactions between the sheets of cellulose, the thermal conductivity is quite low and the thermal expansion is large.

5.8   Conclusion

In terms of the Van der Waals density functional, i.e., the PBE-D2 method, the extreme anisotropies of the thermal expansion and elastic properties have been probed for the native cellulose I_β. It was found that the PBE-D2 method describes satisfactorily the three-dimensional structural properties as well as the phonon, thermodynamic, and elastic properties of cellulose I_β. The predicted single-crystal elastic constants indicate that C_{33} is the extremely largest one, followed by a moderate C_{22}, and then a small C_{11}. Other C_{ij} of the monoclinic cellulose I_β are all quite small ($< C_{11}$). The large difference between C_{ij} indicates the extremely elastic anisotropy, represented also by the direction-dependent Young's modulus and Poisson's ratio plots. At finite temperatures, thermodynamic properties predicted via the first-principles quasiharmonic approach are in good agreement with available measurements, such as entropy, enthalpy, and constant pressure heat capacity. Regarding the thermal expansion tensor components, ξ_i, it was found that ξ_1 is an extremely large one, whereas ξ_2 and especially ξ_3 are quite small. The predicted results, such as the large ξ_1 and C_{33}, and the quick decrease of C_{11} with respect to temperature, are traceable from the weak Van der Waals force between layers perpendicular to a-axis direction and the strong hydrogen bond along c-axis direction. These features of cellulose I_β can be viewed quantitatively by the stretching force constants between atomic pairs and qualitatively by the relative change density, i.e., the charge gain or loss.

The calculated thermal conductivity coefficients are consistent with the thermal expansion coefficients and the bonding patterns in the structure. The thermal conductivity

has its maximum along the z direction (0.90 ± 0.06 W/mK), where the strongest bonds are present and its lowest values in the x and y directions.

CHAPTER 6. PREDICTION OF THE MECHANICAL AND THERMAL PROPERTIES OF CELLULOSE NANOCRYSTAL

6.1   Introduction

First principles density functional theory (QM-DFT) as well as molecular dynamics (MD) simulations can be used to probe the structure and dynamics of cellulose nanocrystals (CNCs). While recent advances enable larger simulation sizes with ab-initio methods, the use of classical potential energy functions (force fields) are more appropriate to reach the relevant temporal and spatial scales for many questions of interest [71].

It is well known that molecular dynamics simulations depend heavily on the force field and its parameterization that are used to describe energetic interactions. Researchers have been performing molecular dynamics simulations of cellulose for years but still there is no force field specially developed for cellulose. A force field (FF) can contain a large number of parameters, even if it is intended for calculations on a small set of molecules. Parameterization of a FF is not a trivial task. A significant amount of effort is required to create a new FF, and even the addition of new parameters to an existing FF in order to model a new class of molecules, or to reproduce certain properties, can be complicated and time-consuming procedure [133]. Very simple FFs may easily be extended to diverse systems but are not expected to yield quantitatively accurate results. On the other hand, more complex FFs, while limited in scope, may be better able to provide quantitative accounts of molecular geometry and conformation [134].

Five different force fields/parameter sets were compared with experimental results and quantum mechanics simulations in terms of their ability to predict three different properties: lattice parameters, elastic constants and thermal expansion coefficients. The aim of this work is to help deciding which force field will produce the best results depending on the objective of the research.

Three types of FFs were analyzed to assess their ability to accurately represent cellulose I_β under different simulation conditions. COMPASS [135] is a type II force field, used previously to compute elastic parameters [91, 136]. GLYCAM [137] is a type I force field, used in the literature to compute cellulose crystalline structure and thermal expansion [138-140]. Both of these FFs are non-reactive. The third type is a reactive force field, ReaxFF [141], which has the ability to simulate bond forming and breaking. Unfortunately, none of the available ReaxFF parameterizations were originally generated to model crystalline cellulose, limiting their accuracy.

6.2   Background

The crystal and molecular structure together with the hydrogen bonding system in cellulose I_β has been accurately characterized by Nishiyama and co-workers [9, 10, 12, 21, 22]. The atomic coordinates for cellulose I_β network A reported by Nishiyama et al. [9] were adopted. Symmetry and antisymmetry operations provided by the crystallographic space group were used to account for the atomic positions inside the unit cell. For cellulose I_β the space group is commonly accepted to be $P2_1$ [26]. Figure 6-1 depicts the crystalline structure reported by Nishiyama et al. [9] after the symmetry operations are applied to the original atom coordinates.
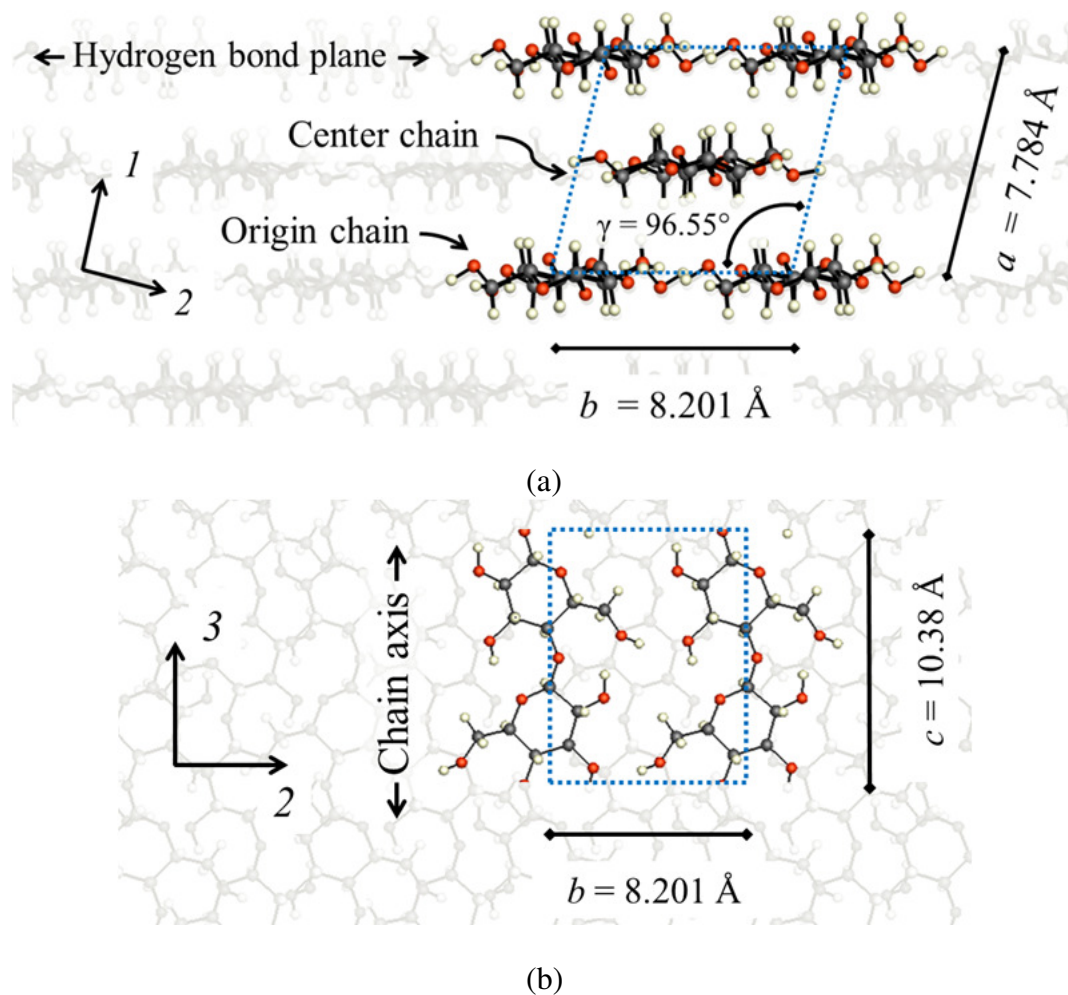
Figure 6-1 Expanded views of the P2₁ unit cell structure of cellulose I$_\beta$ network A showing the characteristic layered conformation [69]. Experimental (room temperature) lattice parameters *a*, *b*, *c*, from Nishiyama et al. [9] are shown. Red spheres denote oxygen ions, gray spheres represent carbon ions and white spheres represent hydrogen ions. Dotted blue lines denote the unit cell. (a) View along the *c*-axis (in of the page). Layers of I$_\beta$ are stacked along the *a*-axis. (b) View along the *a*-axis direction. Atomic coordinates were obtained after applying symmetry operations to the original structure reported by Nishiyama et al. [9]. Cartesian system coordinates (*1, 2, 3*) are superimposed on the figure for reference.

An additional structure was generated using Materials Studio commercial software. Two glucose rings were bridged by the 1→4 glycosidic bond in a parallel "up" configuration, so that the -coordinates of the O_5 atom in the chain direction is greater than that of the C_5 atom. The hydroxymethyl conformation was chosen to be *tg* (i.e., the C_6-O_6 bond points

in the direction of the O_2 in the adjoining glucose ring). Cellulose I_β unit cell was generated by arranging two parallel cellulose chains (as opposed to antiparallel), one positioned at the corner (origin chain) and the other at the center of the unit cell (center chain). The center chain is shifted by *c*/4 relative to the corner chain in the axial direction. Using two different structures, where N refers to the structure reported by Nishiyama et al. [13] and MS refers to the structure optimized in Materials Studio, will allow determination of the sensitivity of the system to the initial atomic coordinates.

Previous studies have shown the important role of hydrogen bonding on crystalline stability and properties [10, 22, 71, 74, 91, 142]. A hydrogen bond is a short-range, angularly dependent interaction between a small electronegative donor atom (such as oxygen, nitrogen, or fluorine) that has covalently a bonded hydrogen atom and an electronegative acceptor atom. This interaction is mostly polar, but there is a partial covalent character that is strongest when the donor-hydrogen—acceptor angle is nearly linear (D-H—A = 180°) [143]. Long range interactions are treated differently by each FF; COMPASS and GLYCAM use an implicit representation of hydrogen bonds therefore its effect is contained in the electrostatic and van der Waals interaction terms. ReaxFF has an explicit description of hydrogen bonds with input parameters that define this type of interaction. As a result, ReaxFF can provide more information about the intra- and inter-chain hydrogen bonding network in the cellulose crystal but the results are susceptible to the FF parameterization being used. Figure 6-2 provides a schematic representation of the H bond network A reported in [12, 70] for both origin and center chains.
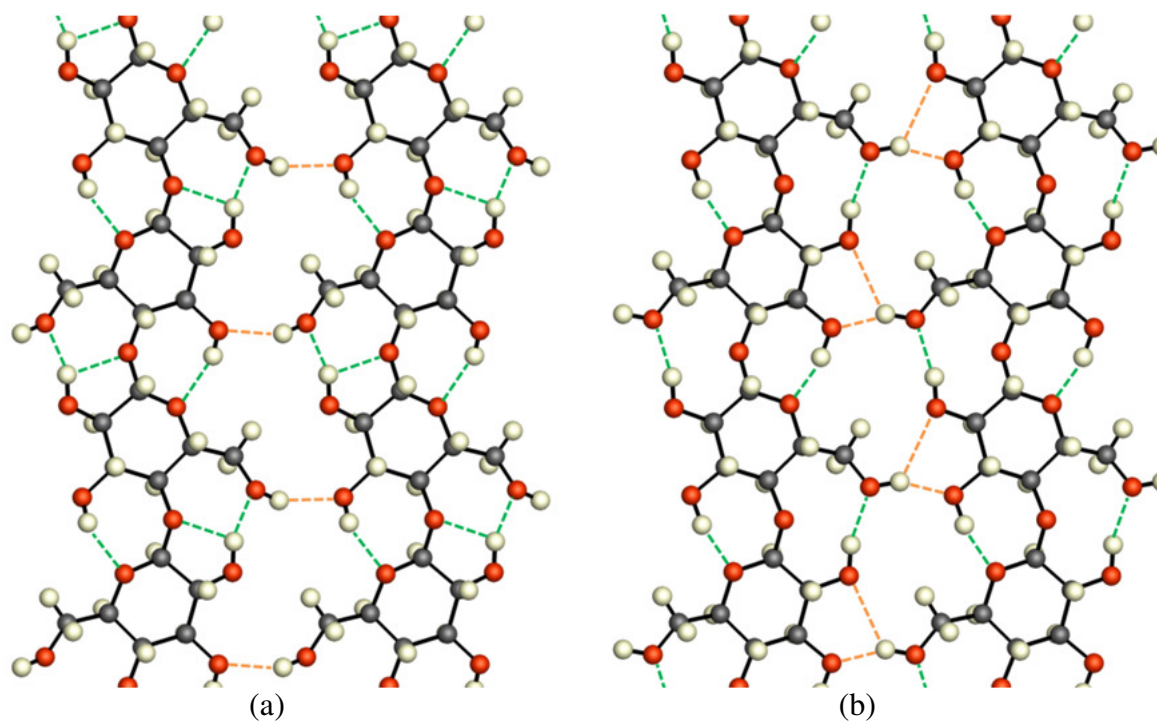
Figure 6-2 Hydrogen-bonding patterns in cellulose I_β network A. Intra- and inter-molecular hydrogen bonds are depicted in green and orange respectively. (a) Chains at the origin of the unit cell and (b) chains at the center of the unit cell as reported in [12, 70].

Cellulose structure simulations can be very sensitive to force field parameters and treatment of long-range interactions (vdW, coulomb, hydrogen bonds). Differences between force field conformational preferences, at the scale of a single cellobiose molecule, lead to radically different macroscopic properties [71]. The ability of a FF to correctly describe long-range interactions is critical to accurately modeling the I_β structure and properties, and is the focus of the current study.

6.3   Computational methodology

LAMMPS simulation software [144] and Accerlys Materials Studio commercial package were used to compare COMPASS, GLYCAM and ReaxFF force fields and their ability to

accurately represent cellulose I_β nanocrystals under different simulation conditions. All the force fields include bonded and non-bonded interactions, such as covalent bonds, covalent angles, torsions, van der Waals and Coulomb. Multiple parameterizations exist for ReaxFF, regrettably, none of them where originally intended to be used to simulate cellulose. Three sets of ReaxFF parameterization (ReaxFF_Mattsson [145], ReaxFF_CHO [141] and ReaxFF_Glycine [146]) were used, that combined with the two non-reactive force fields, give a total of five different possible options to simulate cellulose I_β. This work was done in collaboration with Xiawa Wu and Ashlie Martini [147].

Non-bonded interactions are handled differently accordingly to each FF. For the non-reactive FF (COMPASS and GLYCAM) the non-bonded interaction cutoff distance was set to be 10 Å. This limit affects equally vdW, Coulomb and hydrogen bonds. For ReaxFF, only the H bonds cutoff distance is required to be defined. Hydrogen bonds are usually defined as having the electronegative donor and acceptor atoms less than 3.5 Å apart and with a D-H—A angle of greater than 120°. Matthews et al. [143] report D-H—A angles greater than 100° and distances up to 4 Å for molecular dynamics simulations of cellulose I_β. These results appear to be contradicted by experimental data reported by Nishiyama et al. [22] where a hydrogen bond survey on cellulose I_β reveals angles between 108° and 170° and distances between 1.6 and 2.8 Å.
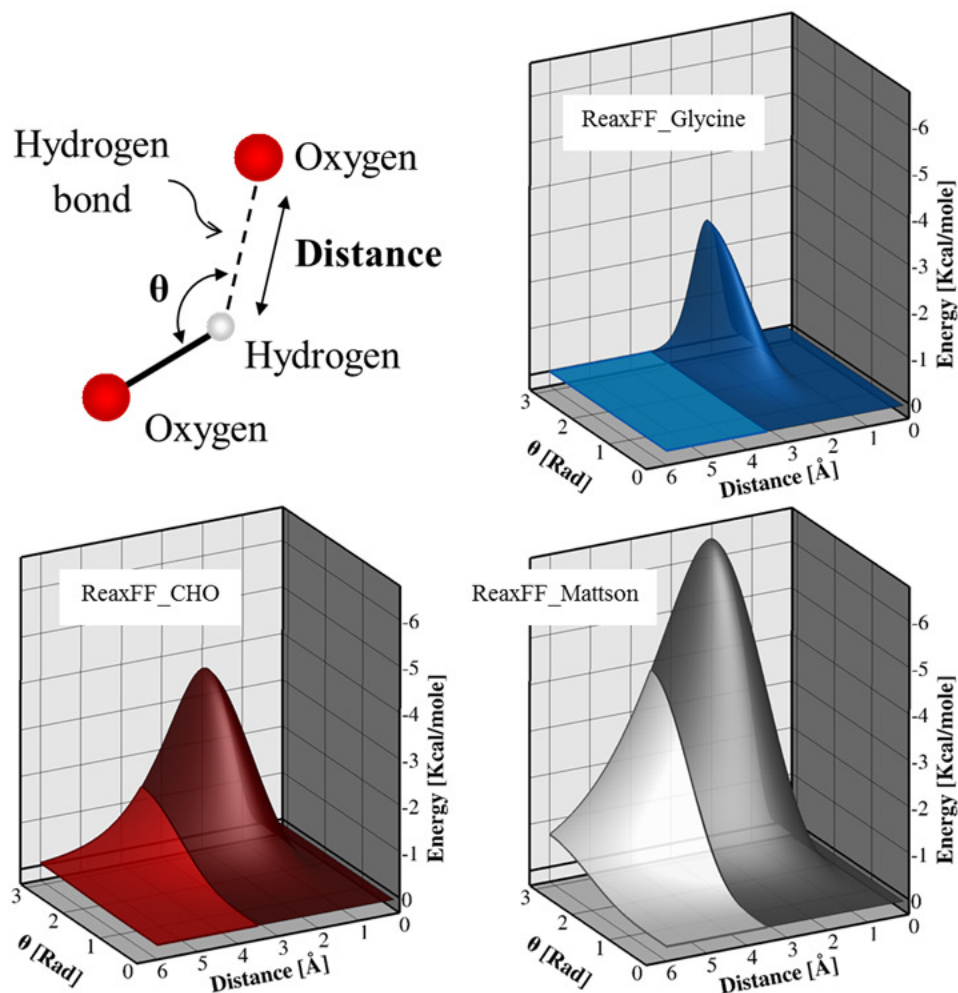
Figure 6-3 Hydrogen bond energy surface as a function of the distance and angle for each of the ReaxFF parameterizations: ReaxFF_Mattsson [145], ReaxFF_CHO [141] and ReaxFF_Glycine [146]. In dark color the surface up to 3.5 Å of cutoff distance. In light color the continuation up to 6 Å cutoff distance. The inset in the upper left shows the definition of distance and angle for a O-H—O hydrogen bond. All the figures are plotted in the same scale; notice the discrepancies in the hydrogen bond energy assigned to the interaction by each of the parameterizations.

Figure 6-3 shows the hydrogen bond energy surface for each of the ReaxFF

parameterizations as a function of the distance and the angle between the hydrogen atom

and the acceptor atom. Three hydrogen bond cutoff distance values were selected after

careful examination of the hydrogen bond energy surfaces. A cutoff value of 0.0 Å was

used to completely deactivate H bonds interactions in the crystal. A cutoff value of 3.5 Å will coincide with standard definition of hydrogen bond interactions [148] and will force the numeric simulation to comply with the experimental results reported in [22]. Finally, a cutoff value of 6.0 Å was used to obtain a zero or near-zero energy value at the cutoff distance, according to the energy surfaces defined in the ReaxFF force field (See Figure 6-3). The default cutoff distance value for H Bond interactions in LAMMPS simulation software is 6.0 Å. It is important to notice that ReaxFF_Glycine [146] parameterization produces zero-energy H bond interactions after 3.5 Å, as a result, no differences exist between energies predicted with the 3.5 and 6.0 Å cutoff distances.

The study was focused on three material properties: crystal structure, elastic constants and thermal expansion. The following section describes the simulation procedures for each case.
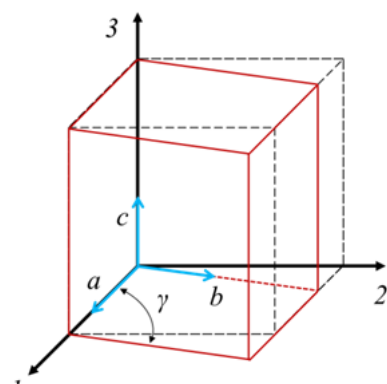
6.3.1   Equilibration

An initial equilibration step precedes all simulations; the procedure is performed to obtain the crystal structure of cellulose I$_\beta$. First a unit cell was built based on the experimental measurements by Nishiyama et al. [9]. An initial Gaussian velocity distribution was imposed over the system to produce an equivalent 300 K temperature. The unit cell was expanded 4x4x8 times in the *a*, *b* and *c* directions to create a simulation cell whose dimensions are large enough to satisfy the criteria: the cutoff distance is smaller than half the length of the simulation cell. The simulation cell was, then, equilibrated in a canonical ensemble for 50 ps with a time step 0.25 fs, and coupled with a thermal bath at 300 K controlled by the Nose-Hoover thermostat. This equilibration process allows

relaxing inter-atomic stress without changing the size of the simulation box. The second equilibration was conducted in an isothermal–isobaric ensemble at temperature 300 K and pressure 1 atm, also controlled by Nose-Hoover thermostat and barostat methods, for 300 ps with a time step of 0.25 fs. This equilibration process relaxes the simulation box as well as the atomic configurations under 1 atm pressure. The dimensions of the simulation cell are averaged over the last 10 ps in the second equilibration process in order to calculate the lattice parameters of cellulose I_β.

6.3.2 Elasticity

Molecular mechanics are used to calculate the elastic matrices of the simulation cell with different force fields. After equilibrating the simulation cell in the isothermal–isobaric ensemble, it is stretched in one direction through successive small length steps (e.g., elongate in the z-direction by 0.2%) while keeping the other two directions fixed. The simulation cell then undergoes an energy minimization process using the conjugate gradient (CG) method to allow it to reach its minimum energy state. The elongation and minimization processes are repeated until the total strain in the extending direction reaches 4%. The strain and stress values at each step are recorded and a linear fit of the stain-stress relationship provides the stress vectors corresponding to the strain. The same procedure is performed in the orthogonal directions, *1*, *2* and *3*, as well as the shear directions, *12*, *13* and *23* (see Figure 6-4). After all six simulations are conducted, it is possible to obtain the stiffness matrix that relates the strain and stress as following: $\sigma_i = C_{ij}\, \varepsilon_j$ where σ is stress and ε is strain. The inverse of the matrix C_{ij} is the compliance matrix S_{ij}. The elastic moduli in the *1*, *2* and *3* directions can be calculated by

$1/S_{11}$, $1/S_{22}$ and $1/S_{33}$, and are reported in the results section. The elastic matrix is calculated for all reactive and non-reactive force fields. In addition, the elastic modulus for the reactive force fields with the hydrogen bonds manually turned off (implemented by setting the hydrogen bond cutoff distance as 0.0 Å) are also reported to further analyze the prediction ability of different force fields.

$$[\sigma]=[C][\varepsilon]$$

$$
\begin{bmatrix} \sigma_1 \\ \sigma_2 \\ \sigma_3 \\ \sigma_4 \\ \sigma_5 \\ \sigma_6 \end{bmatrix}
=
\begin{bmatrix}
C_{11} & C_{12} & C_{13} & 0 & 0 & C_{16} \\
C_{12} & C_{22} & C_{23} & 0 & 0 & C_{26} \\
C_{13} & C_{23} & C_{33} & 0 & 0 & C_{36} \\
0 & 0 & 0 & C_{44} & C_{45} & 0 \\
0 & 0 & 0 & C_{45} & C_{55} & 0 \\
C_{16} & C_{26} & C_{36} & 0 & 0 & C_{66}
\end{bmatrix}
\begin{bmatrix} \varepsilon_1 \\ \varepsilon_2 \\ \varepsilon_3 \\ 2\varepsilon_4 \\ 2\varepsilon_5 \\ 2\varepsilon_6 \end{bmatrix}
$$

(a)   (b)

Figure 6-4 (a) Schematic representation of the cellulose I$_\beta$ monoclinic unit cell aligned with the Cartesian coordinate system used in this work (red solid lines). A cubic cell (black dashed lines) is used to help visualizing the orthogonally between axis *a-c* and *b-c*, highlighting the non-orthogonal relation between *a* and *b*. (b) Stiffness matrix relating stresses and strains in the monoclinic unit cell [75].

6.3.3 Thermal expansion

The thermal expansion of a single cellulose I$_\beta$ crystal is calculated with the simulation cell equilibrated at different temperatures. The simulation cell lattice parameters are analyzed from 200 K to 500 K with a temperature interval of 20 K and a constant pressure of 1 atmosphere. The atoms in the simulation cell are assigned with initial velocities at the desired temperature, and then equilibrated following the same two step procedure as described in the crystal structure section: the simulation cell is first equilibrated in the canonical ensemble and then in the isothermal–isobaric ensemble for

50 ps and 300 ps, respectively, with controlled temperature and pressure. The lattice constants are calculated at each temperature to provide of the structures predicted with different force fields over a wide temperature range.

6.4   Results and discussion

6.4.1   Lattice parameters

The lattice parameters for cellulose have been measured by several authors [9, 10, 12, 21-27] using different experimental techniques and crystal sources. For cellulose I_β network A Nishiyama et al. [9] reports: $a = 7.784$ Å, $b = 8.201$ Å, $c = 10.380$ Å, $\gamma = 96.55°$, Volume $= 658.3$ Å^3 at 293 K. Most of the lattice parameters exhibit variations around 1% over a wide range of temperatures and crystalline sources, except for the lattice parameter a. As cellulose I_β is cooled or heated, the lattice remains remarkably constant in the directions within the hydrogen bonded plane; the same is not true along the a axis direction where the contractions or expansions are controlled primarily by weak vdW interactions [21, 28]. Nishiyama et al. 2008 [12] reported a change from 7.64 to 7.76 Å in the a lattice parameter when the temperature is raised from 15K to 295K. Langan et al. [21] reported a value of 7.83 Å for the same parameter at room temperature. Although H bonds interactions are present in the stacking direction (a-axis) they apparently do not prevent expansion at temperatures up to a transition point at about 200 °C [29].

Figure 6-5 and Figure 6-6 summarize the comparison of simulation predictions with the experimental values reported by Nishishama et al. [9] for cellulose I_β structure A. Each bar represents the difference between the reported experimental value and the simulation

result; smaller bars represent better agreement. QM-DFT calculations performed at 300 K [149] were also included for reference.
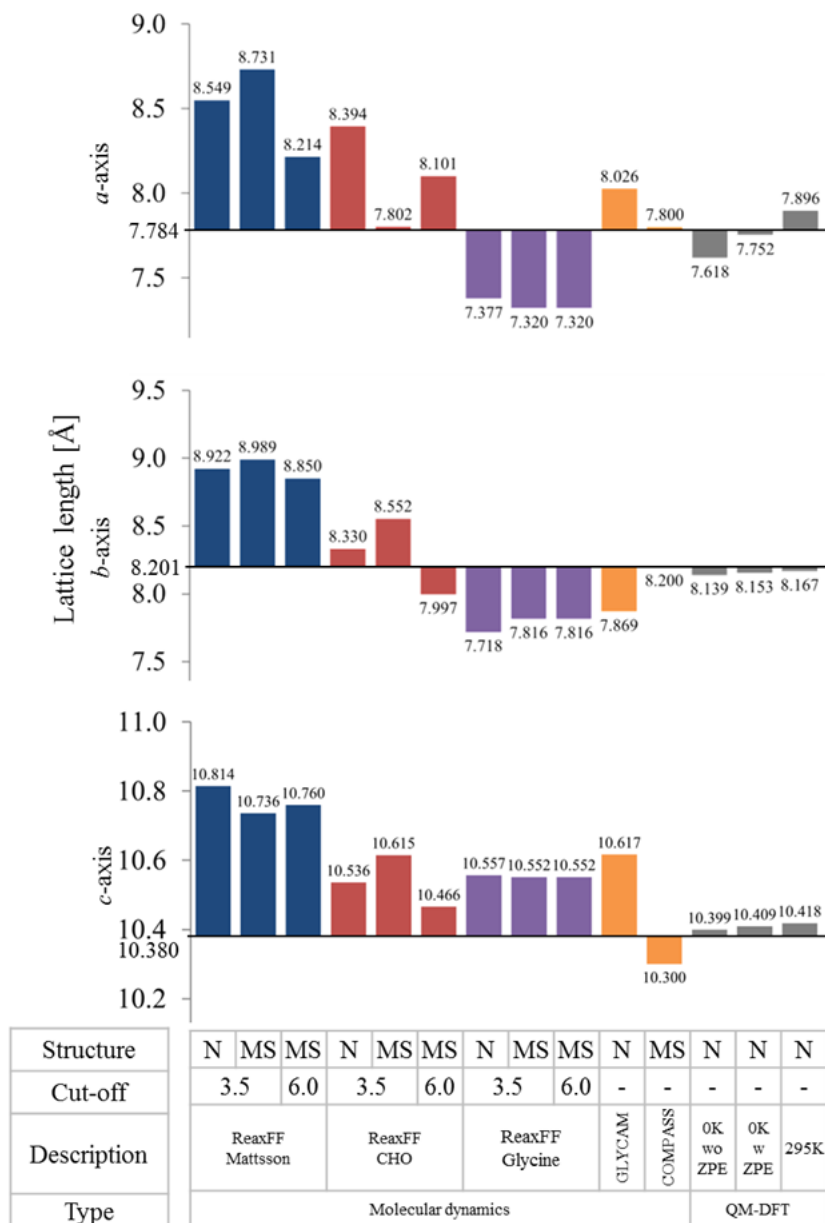

Figure 6-5 Lattice parameters (*a*, *b* and *c*) for Cellulose I$_\beta$ accounting for different atomistic structures, H bond cutoff distance and simulation parameters. Structures: Nishiyama (N) and Material Studio (MS). Cut-off: 3.5 and 6.0 Å. Description: for MD, the force field used (this work); for QM-DFT, vibrational energy and temperature [149]. Comparison lines defined for Nishishama et al. [9] structure A at 293 K.
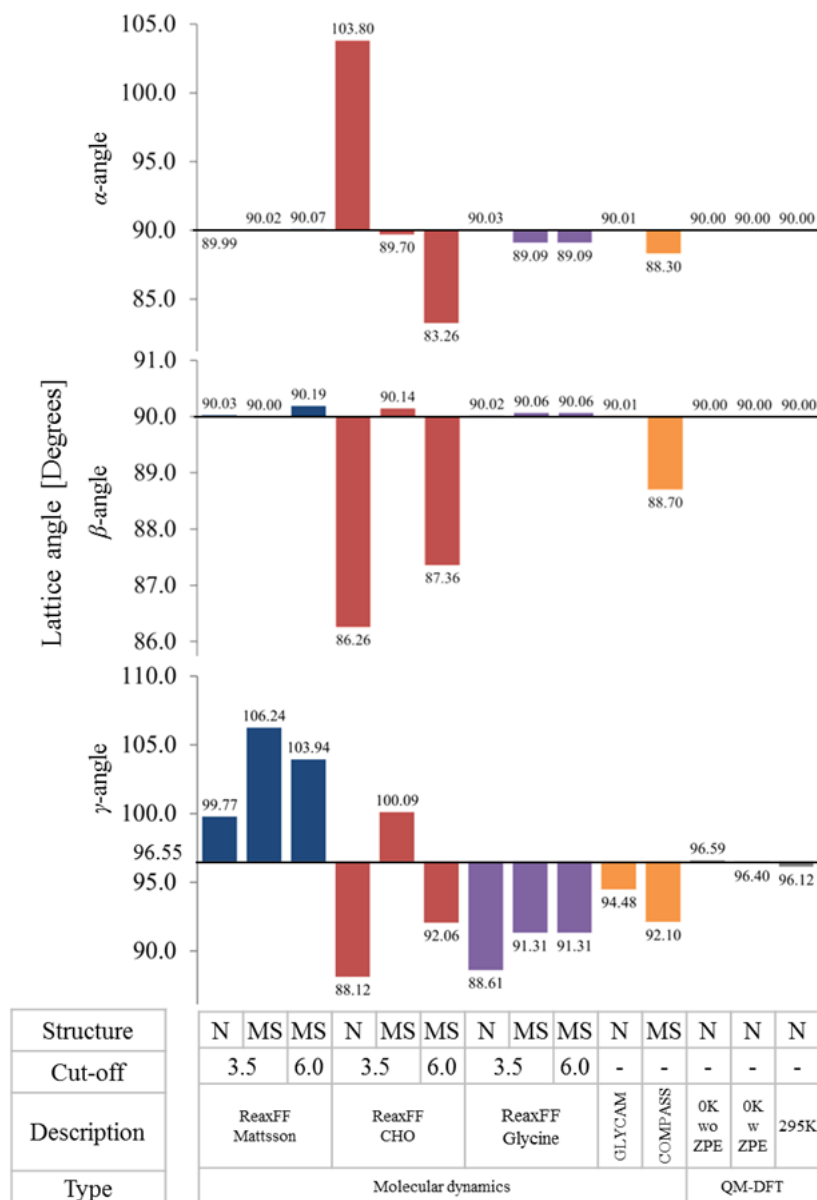
Figure 6-6 Lattice parameters (α, β and γ) for Cellulose I$_\beta$ accounting for different atomistic structures, H bond cutoff distance and simulation parameters. Structures: Nishiyama (N) and Material Studio (MS). Cut-off: 3.5 and 6.0 Å. Description: for MD, the force field used (this work); for QM-DFT, vibrational energy and temperature [149]. Comparison lines defined for Nishishama et al. [9] structure A at 293 K.

For the non-reactive FF, COMPASS exhibits the best approximation for the lattice parameters with a total difference smaller than 0.08 Å (<0.8%) in each value. GLYCAM overestimates the *a* axis by 0.42 Å (5.4%) and the *c* axis by 0.237 Å (2.3%) while underestimating the *b* axis by 0.32 Å (4.0%). The lattice angles show the opposite behavior, COMPASS underestimate the α angle by 1.7° (1.9%), the β angle by 1.3° (1.4%) and the γ angle by 4.45° (4.6%) whereas GLYCAM has a negligible deviation in the α and β angle but underestimates the γ angle by 2.07° (2.1%). It is important to notice that the comparison is conducted for different initial structures; GLYCAM results are extracted from the Nishiyama et al. [9] initial structure whereas COMPASS results are obtained using the Materials Studio initial structure.

Each ReaxFF parameterization exhibits a unique behavior which emphasizes the importance of this comparison. ReaxFF_Mattsson gives the less accurate approximation for the lattice axis, with maximum deviations that exceeds 12.2% in the *a*-axis, 9.6% in the *b*-axis and 4.2% in the *c*-axis. The lattice angles show one of the best approximations for reactive FFs with α and β angles that exhibit almost no deviation from the Nishiyama structure. The γ angle is being overestimated by 3.22° (3.3%) for the same structure. ReaxFF_CHO produces results with the highest angular deviation and prove to be very sensitive to the initial structure being used. The best approximation is achieved by Material Studio's initial structure with a H bond cutoff distance of 3.5 Å. In this particular case, α and β angles exhibit negligible deviations (<0.5%) whereas the γ angle is being overestimated by 3.54° (3.9%). The same structure exhibits good agreement in the *a*-axis direction with values comparable to QM-DFT results [149]. Finally, ReaxFF_Glycine underestimates both *a* and *b*-axis by less than 6% but overestimates the

c-axis by roughly 1.7%. The α and β angles exhibit almost no deviation from experimental values (less than 1°) whereas the γ angle is being underestimated by 7.98° (8.2%) in the Nishiyama structure and 5.24° (5.4%) in the Material Studio structure. It is important to remark that for ReaxFF_Glycine, the 6.0 Å cutoff distance yield virtually the same results as the 3.5 Å cutoff due to the shape of the H bond energy surface (see Figure 6-3).

None of the FF used in this study is capable of representing the experimental lattice parameters accurately. Similar limitations were found in previous analyses of three other force fields (CHARMM35, GLYCAM06, and Gromos45a4) [71]. However, it is possible to achieve a good representation of lattice axes or angles (but not both) by choosing the appropriate combination of FF, initial structure and H bonds cutoff distance.

6.4.2   Mechanical properties

For some applications, the lattice parameters and the final shape of the crystalline structure, are not as important as the elastic behavior of the materials. Figure 6-7 compares the Young's modulus in the three principal directions according to the Cartesian coordinate system defined in Figure 6-4. For the *3*-direction (coincident with the *c*-axis) all the FF produce results in good agreement with experimental values reported in [23-25, 30-32]. Most of the results are below ~130GPa, with relatively small influence of the H bonds on the Young's modulus value. This could be appropriately explained by the weak force produced by H bonds interactions compared to the covalent bonds that govern the mechanical response in the *c*-axis direction. ReaxFF_Glycine is the only parameterization that produces results in the order of 200 GPa. Diddens et al. [32]

reported values of 220 ± 50 GPa for the *3*-direction using Inelastic X-ray Scattering (IXR). Diddens and coworkers [32] claimed that IXS was not affected by the amorphous zones occurring in natural cellulose, and the elastic behavior was mostly related to the highly crystalline region. Recently, Dri et al. [113, 149] reported QM-DFT simulations for crystalline cellulose in the range of 200 GPa.

The transverse directions, both *1* and *2* (Figure 6-7), exhibit a similar trend. ReaxFF_Mattsson generates the smallest values of Young's modulus barely exceeding the lower limit reported by Wagner et al. [33]. ReaxFF_CHO produces values in good agreement with QM-DFT simulations for the *1*-direction but yields lower values in the *2*-direction. ReaxFF_Glycine produces a value of Young's modulus in the 1-direction which almost double the value of Young's modulus reported with QM-DFT. On the other hand, for the *2*-direction, this parameterization presents the only value that exceeds the 50 GPa when H bonds are turned off (0.0 cutoff distance) and the highest reported value in this work, 38.1 GPa, when the H bonds are on (3.5 cutoff distance). Diddens and coworkers [32] reported a value of Young modulus in the *1-2* plane (uncertain direction) of 15 ± 1 GPa. Lahiji et al. [35] and Wagner et al. [33] reported a mean value of 8.1 GPa and a 95% confidence interval of 2.7-20 GPa. For a more comprehensive discussion please see Dri et al. [113].
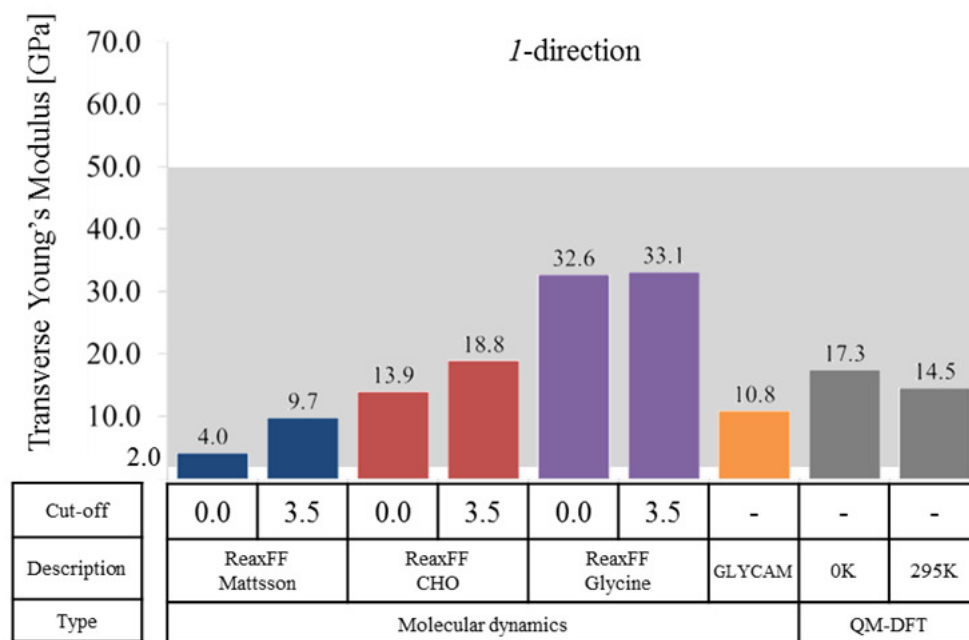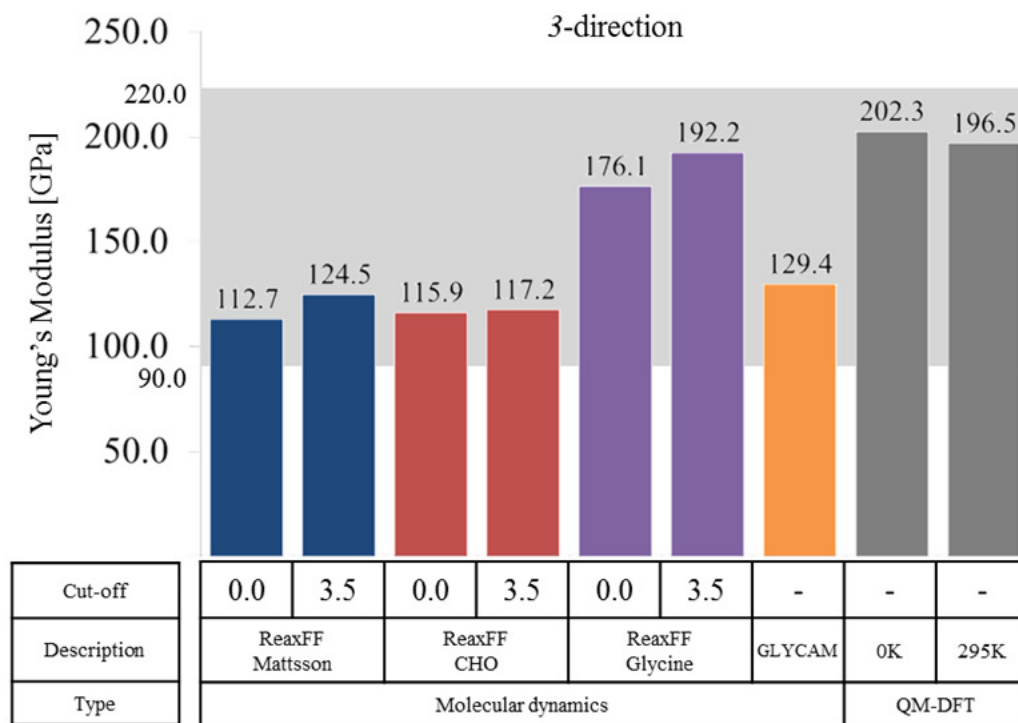
(a)
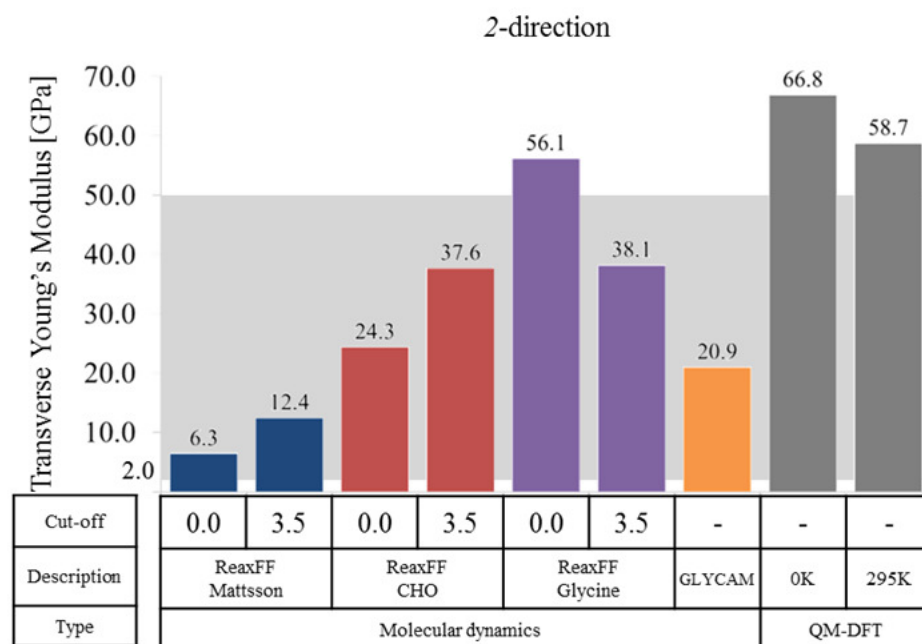
(b)

Figure 6-7 Young's modulus computed in three principal directions for molecular dynamics (this work) and QM-DFT [149]. Upper and lower limits for experimental results were extracted from [31-33, 35] and are represented as a shaded region in the background. Cellulose I$_\beta$ structure A is used as the initial structure accounting for different H bond cutoff distance (3.5 and 6.0 Å) and simulation parameters (force field and temperature). (Continued)

(c)

Figure 6-7 Young's modulus computed in three principal directions for molecular dynamics (this work) and QM-DFT [149]. Upper and lower limits for experimental results were extracted from [31-33, 35] and are represented as a shaded region in the background. Cellulose I_β structure A is used as the initial structure accounting for different H bond cutoff distance (3.5 and 6.0 Å) and simulation parameters (force field and temperature).

Additional mechanical information can be extracted from the computed compliance matrix by generating surface contour plot of the Young's modulus variation with crystallographic direction. A post processing software, Anisotropy Calculator - 3D Visualization Toolkit [89], was used for this purpose. Each point on the surface represents the magnitude of Young's modulus in the direction of a vector from the origin (i.e., at the intersection of the *1*, *2*, and *3* axes in the interior of the surface) to a given point on the surface. The shape of this surface is indicative of the anisotropy of cellulose I_β. For instance, the computed Young's modulus surface would be a perfect sphere with

the same value in any direction for a linearly elastic isotropic material. However, the cellulose I$_\beta$ surfaces in Figure 6-8 through 18 exhibit extreme variations in the Young's modulus, as denoted by the accentuated contour lobe along the *3*-axis (i.e., along the cellulose chains) relative to the smaller lobes along the *1* and *2* directions.

Figure 6-8 reports the variation of the Young's modulus with respect to the crystallographic direction computed based on QM-DFT results at 300 K [149]. This figure is presented as a reference for comparison to MD simulation results. All the remaining Young's modulus surfaces (Figure 6-9 through 18) were plotted maintaining the same view angle and color contour levels to facilitate comparisons between results. The largest values (red contours) are along the *3*-axis, with the smallest values in the *1-2* plane. It is important to remark that the deformation along the *3*-direction is governed by covalent bonds that form the cellulose chains whereas the mechanical behavior in the *1-2* plane is governed by non-bonded interactions. The shape of the surfaces predicted by the various FFs is analyzed. The role of the non-bonded interactions will be examined by focusing on the mechanical response in the *1-2* plane.

Figure 6-9 shows the Young's modulus variation with crystallographic direction based on MD results with ReaxFF_Mattsson parameterization. The surface shown in Figure 6-9a is obtained without considering H bonds, whereas Figure 6-9b was computed using a 3.5 Å cutoff distance for H bonds interactions. The presence of H bonds in the system has a small impact over the *3*-direction but widens the Young's modulus surface in the *1-2* plane. Figure 6-10 shows the opposite behavior for the results computed using ReaxFF_Glycine parameterization. The presence of H bonds (Figure 6-10b) appears to reduce the anisotropy of the system compared to results without H bonds (Figure 6-10a).

This result contradicts the standard belief that hydrogen bonds help to stabilize the system; a plausible explanation for this behavior is given in the next chapter (Chapter 7). In the *3*-direction, ReaxFF_Glycine parameterization is the only one that produces results close to the reported by QM-DFT [149]. Figure 6-11a was computed for the non-reactive FF, GLYCAM. The general shape of the Young's modulus surface resembles the one presented in Figure 6-8 but exhibit softer transitions between directions. Figure 6-11b was computed based on ReaxFF_CHO parameterization with 3.5 Å cutoff distance. Results without H bonds interaction (0.0 cutoff distance) produce an unstructured surface and is not reported. Finally, Figure 6-12 reports the variation of the Young's modulus with respect to the crystallographic direction computed based on COMPASS results from Ref. [91]. The presence of H bonds (Figure 6-10b) appears to completely modify the anisotropy of the system, yielding results that are remarkable different when compared to the same FF without H bonds (Figure 6-10a) or other simulations (Figure 6-8 through 17).
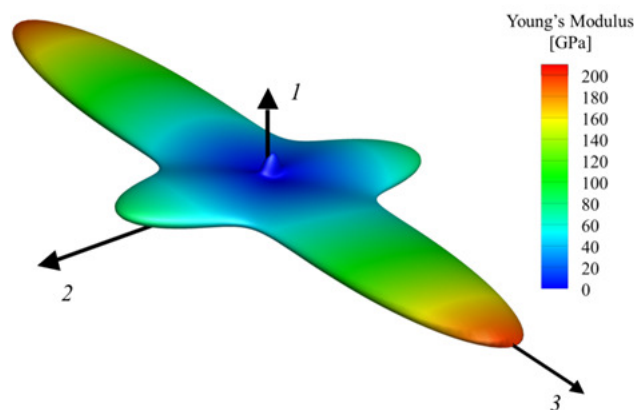

Figure 6-8 Surfaces showing contours of Young's modulus for cellulose I_β from Ref. [149] (computed with QM-DFT at 300K). Each point on the surface represents the magnitude of Young's modulus in the direction of a vector from the origin to that point. The color contours help to identify the Young modulus variation of cellulose I_β and emphasize its extreme anisotropy.
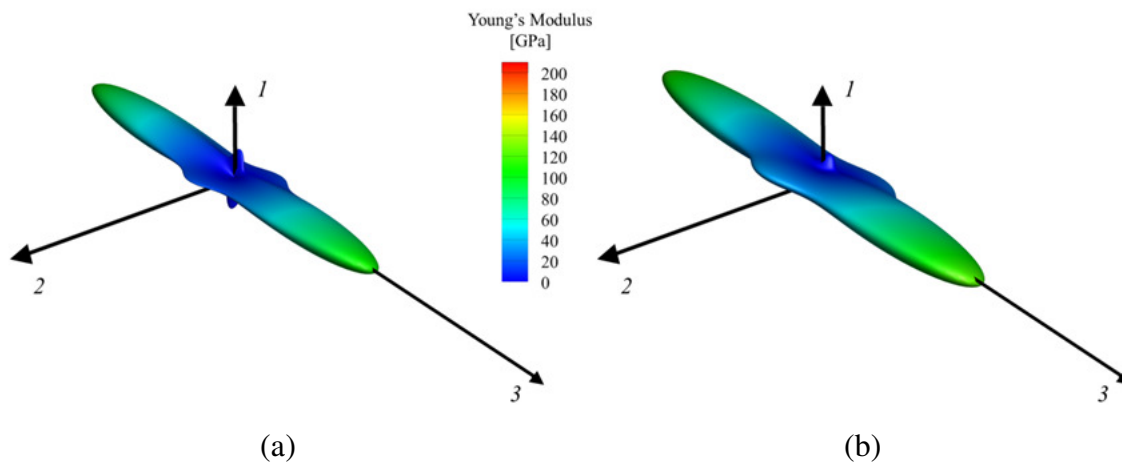
Figure 6-9 Surfaces showing contours of Young's modulus for cellulose I$_\beta$ computed using ReaxFF_Mattsson parameterization. (a) H bonds turned off (b) H bonds turned on with 3.5 Å cutoff distance.
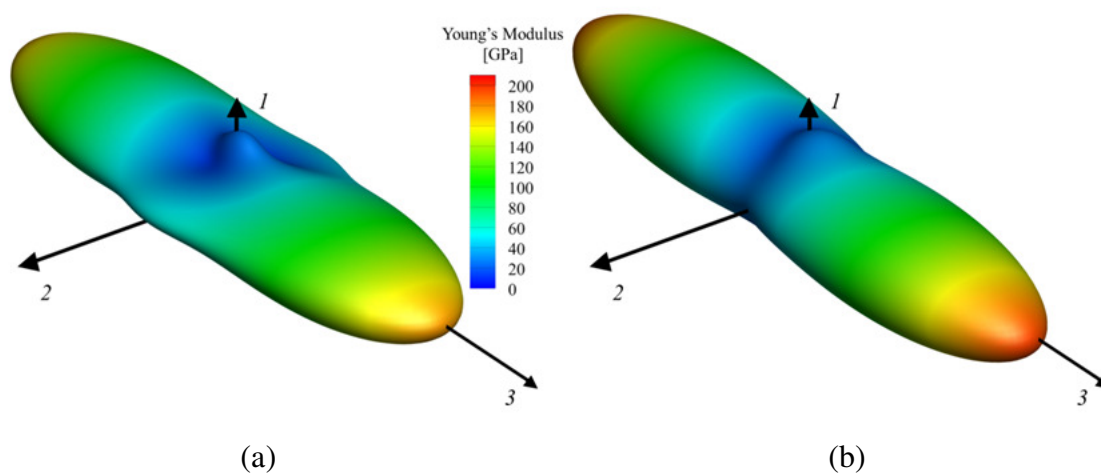

Figure 6-10 Surfaces showing contours of Young's modulus for cellulose I$_\beta$ computed using ReaxFF_Glycine parameterization. (a) H bonds turned off (b) H bonds turned on with 3.5 Å cutoff distance.
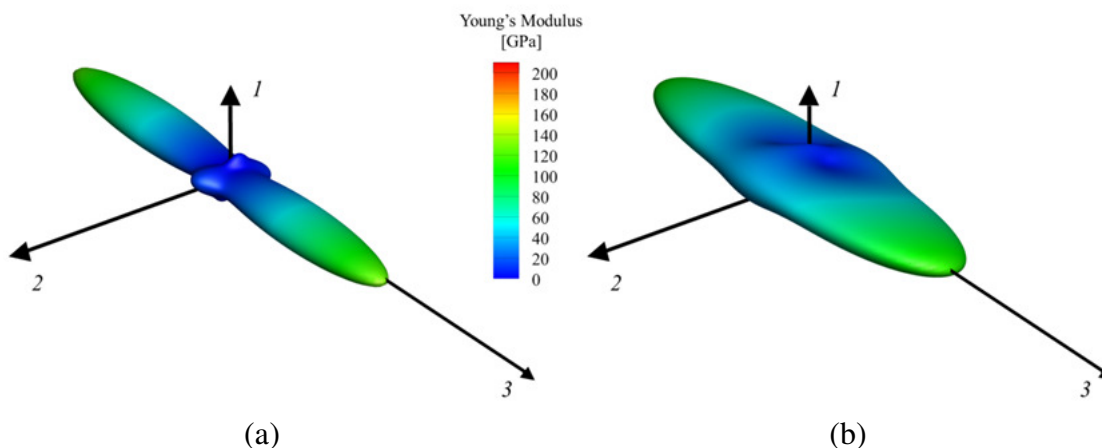
(a)   (b)

Figure 6-11 Surfaces showing contours of Young's modulus for cellulose I_β. (a) Computed using GLYCAM (b) computed using ReaxFF_CHO parameterization with 3.5 Å cutoff distance for H bonds.
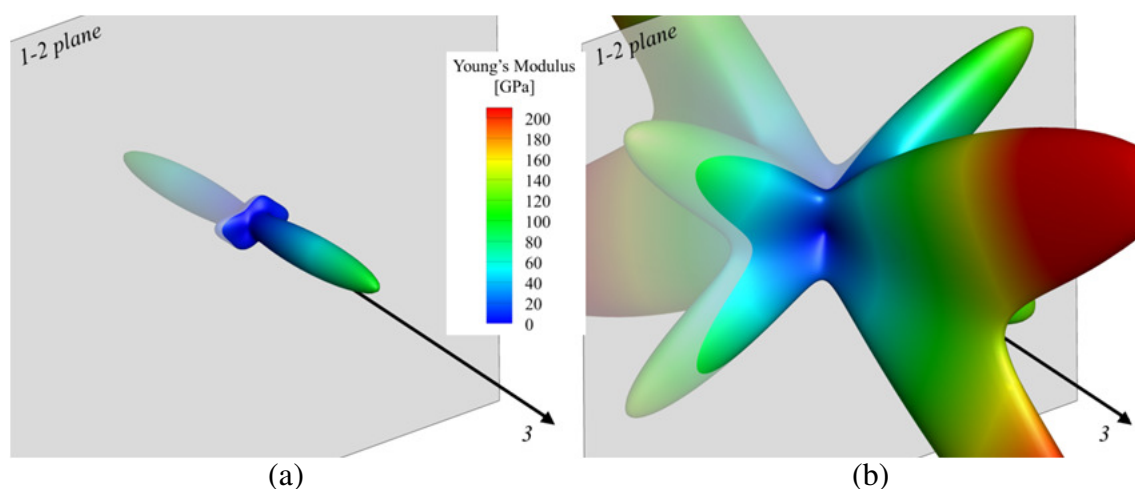

(a)   (b)

Figure 6-12 Surfaces showing contours of Young's modulus for cellulose I_β from Ref. [91] (computed with COMPASS). (a) H bonds turned off (b) H bonds turned on. The Cartesian coordinate system used to define the stiffness matrix was not explicitly reported in the reference. The *3*-direction and *1-2* plane positions were estimated.

Variations of the Young's Modulus within a given crystallographic direction in the *1-2* plane are shown in Figure 6-13 and Figure 6-14. Only non-bonded interaction are present in the *1-2* plane (see Figure 6-1a), making it an ideal plane to analyze how vdW, Coulomb and hydrogen bonds interactions affect the mechanical behavior representation

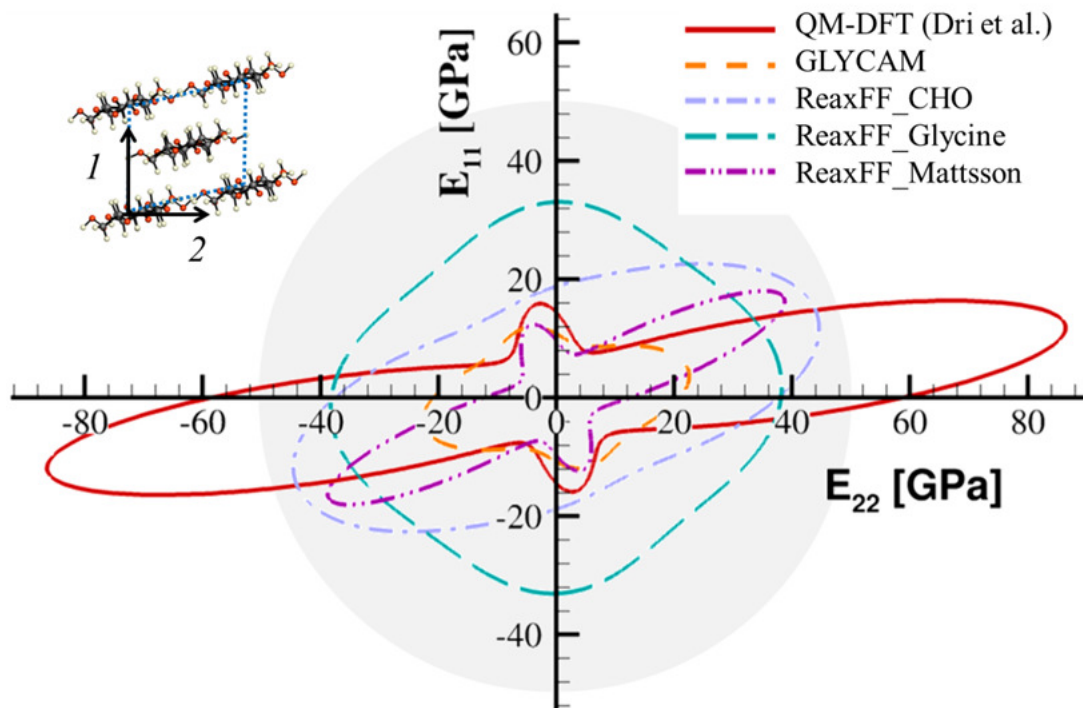for each FF. Experimental [15] as well as QM-DFT [149] results are superimposed on both figures for reference.

Figure 6-13 Variation of the *transverse* Young's modulus (*1-2* plane) for different FF parameterizations with H bonds on (3.5 Å cutoff distance for ReaxFF and 10 Å cutoff distance for GLYCAM). QM-DFT results at 300K [149] and experimental results (in grey) [15] added for reference. The inset in the upper left corner shows the orientation between the original input structure and the Cartesian system of coordinates. The final structure (after analysis) may not be aligned as shown in the inset figure.

Figure 6-13 shows the variation of the *transverse* Young's modulus (*1-2* plane) when non-bonded interactions are being considered in the simulation. The non-bonded interaction cutoff distance was set to 10 Å for the GLYCAM force field and the H bond cutoff distance was defined as 3.5 Å for each of the three ReaxFF parameterizations. The four MD simulations produced values within the limits of experimental characterizations [15]. Most of the curves present an oblong shape with smooth variations with orientation.

ReaxFF_Matsson is the only parameterization that produces a curve resembling QM-DFT results [149] but with a different size (smaller) and orientation.
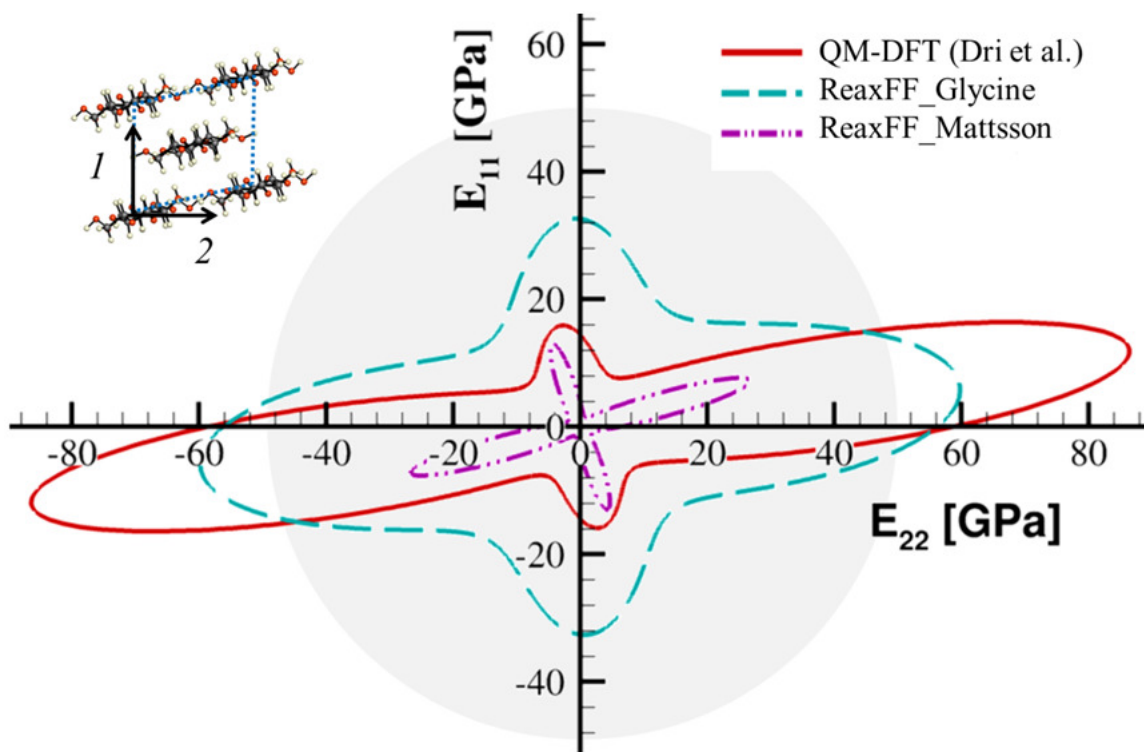

Figure 6-14 Variation of the *transverse* Young's modulus (*1-2* plane) for different FF parameterizations with H bonds off (0.0 Å cutoff distance). QM-DFT results at 300K [149] and experimental results (in grey) [15] added for reference. The inset in the upper left corner shows the orientation between the original input structure and the Cartesian system of coordinates. The final structure (after analysis) may not be aligned as shown in the figure.

Figure 6-14 shows the variation of the *transverse* Young's modulus (*1-2* plane) when H bond interactions are not being considered in the simulation. When H bonds are turned off, ReaxFF_Mattson shows shrinkage in the Young's modulus curve and a slight change in orientation (closer to QM-DFT results). Both relative maximum peaks became sharper, but are still within the values defined by the curve where H bonds were considered. ReaxFF_Glycine parameterization exhibits the opposite behavior: when H bonds are turned off the Young's modulus curve expands and the anisotropy of the system increases

as compared to the curve shown in Figure 6-13 for the same FF and with QM-DFT results [149]. It is important to note that when H bonds were turned off, the ReaxFF_CHO parameterization produced unphysical results and no clear trend could be identified.

6.4.3   Thermal expansion

The ability of a given FF to predict the lattice variations with temperate is of remarkabe importance when computing thermal expansion coefficients (TEC). Figure 6-15 shows predicted lattice parameters *a*, *b*, *c* and angle γ of the cellulose I_β network A as functions of temperature for the reactive and non-reactive FFs studied in this work. QM-DFT [149] and experimental values [37-40] were also added for comparison. It is important to understand that the actual values of the lattice parameters are not as important as the trend (slope) of the results needed to compute the thermal expansion coefficients. The lattice structures of the simulation cell were study for temperatures from 200 K to 500 K with an interval of 20 K. The analysis was limited to the interval 250 K to 350 K due to the high variability of the simulation data. Even within this reduced range, GLYCAM and ReaxFF_CHO results are too scattered to produce consistent values. In all cases the coefficient of thermal expansion was computed using the equilibrated structure at 300K as a reference. A linear regression line, fitted by least squares method with 6 simulation points, was used to extract the TEC value.
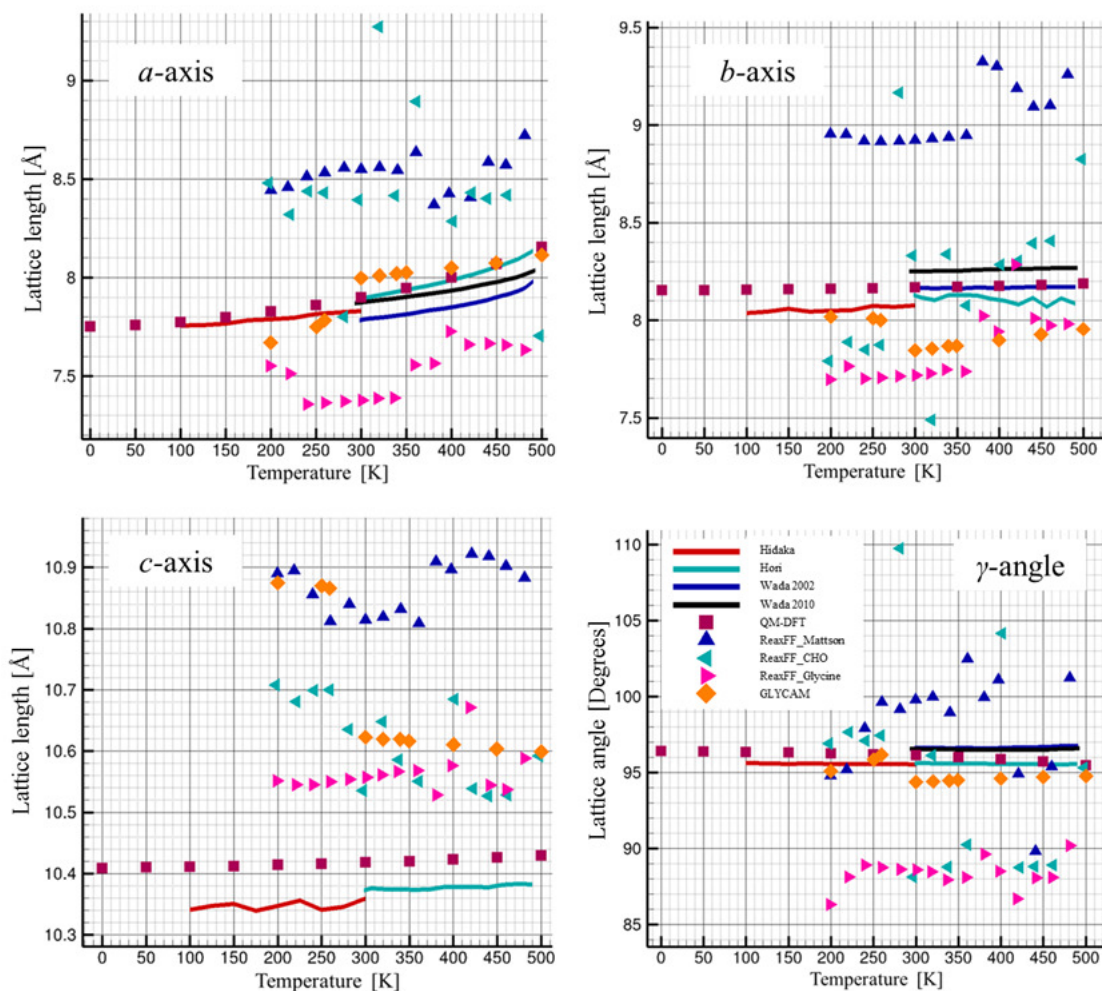
Figure 6-15 Predicted lattice parameters *a*, *b*, *c*, angle γ of cellulose I$_\beta$ network A compared with QM-DFT [149] and experimental data measured by Hidaka et al. using wood cellulose [37], by Hori using wood cellulose [38], by Wada (2002) using tunicate (halocynthia) [39], and by Wada et al. (2010) using green algae [40].

For the *a*-axis, a TEC value of 5.05×10^{-5} K^{-1} was computed with ReaxFF_Mattson whereas ReaxFF_Glycine yields a higher 13.9×10^{-5} K^{-1} showing remarkably good agreement with experimental results. Hori [38] reported a value of 13.6×10^{-5} K^{-1} using wood cellulose while Wada et al. [40] reported a value of 19.3×10^{-5} K^{-1} using green alga. For the *b*-axis, the computed values were 9.25×10^{-5} K^{-1} for ReaxFF_Mattson and

19.2×10^{-5} K^{-1} for ReaxFF_Glycine. For this particular axis, the computed TEC values were an order of magnitude larger than the 0.5×10^{-5} K^{-1} reported in [29] and the 0.3×10^{-5} K^{-1} value reported in [40]. In the *c*-axis direction a TEC value of 2.08×10^{-5} K^{-1} was computed using ReaxFF_Mattson whereas ReaxFF_Glycine yields a higher 5.88×10^{-5} K^{-1}. Hori [38] reported a value of 0.6×10^{-5} K^{-1} while Wada et al. [40] reported -1.9×10^{-5} K^{-1}. The variability in the experimental results makes comparison rather difficult.

6.5 Conclusion

Three reactive and two non-reactive force fields were tested to analyze how accurately they can reproduce cellulose I$_\beta$ crystalline structure and the response of that structure to thermal and mechanical stress. Not surprisingly, none of the tested force fields yield results in perfect agreement with experimental data for all predicted properties. It is possible to select a particular force field that will give moderately good results for a given case but the same force field may fail miserably when used for some other case. This situation makes analyzing combined cases (i.e., mechanical response and thermal expansion) rather difficult.

However, a specific property can be predicted quite accurately if an appropriate force field is chosen. This chapter provides the information researchers need to choose the best FF and parameterization based on the focus of their study. Most significantly, in highlighting the limitation of current force fields, this work encourages development of a force field parameterized and optimized for cellulose that can support extensive future research on CNCs using molecular dynamics simulation.

CHAPTER 7. EXPLICIT QUANTIFICATION OF HYDROGEN BOND STRENGTH USING REACTIVE FORCE FIELDS

7.1   Introduction

Hydrogen bonding is one of the most important forms of intermolecular interaction; it is a critical component of biomolecular structure, molecular recognition, and protic solvent effects to name a few [150]. Previous studies have shown the important role of hydrogen bonding on crystalline stability and properties of cellulose I_β [10, 22, 71, 74, 91, 142]. However, a complete understanding of the intrinsic behavior of hydrogen bonds is still an active topic of research.

The special considerations required to model hydrogen bonds impose addition challenges in the development of empirical force-fields. Since hydrogen bonds have a relatively long range coulombic component, electrostatic terms needs to be added to account for some of the observed effects. Within the electrostatic model, the added complications of exchange repulsion, penetration effects and covalent bonding interactions are lumped together into coulombic and Van der Waals terms [151]. Highly parameterized empirical potential functions are required to adequately represent hydrogen bonding. Cellulose structure simulations can be very sensitive to force field parameters and treatment of long-range interactions (vdW, coulomb, hydrogen bonds). Differences between force field conformational preferences, at the scale of a single cellobiose molecule, lead to radically different macroscopic properties [71].

A comprehensive analysis over hydrogen bond behavior in cellulose I_β was conducted using ReaxFF reactive force field. ReaxFF has an explicit description of hydrogen bond interactions; providing detailed information of each hydrogen bond accounted in the model.
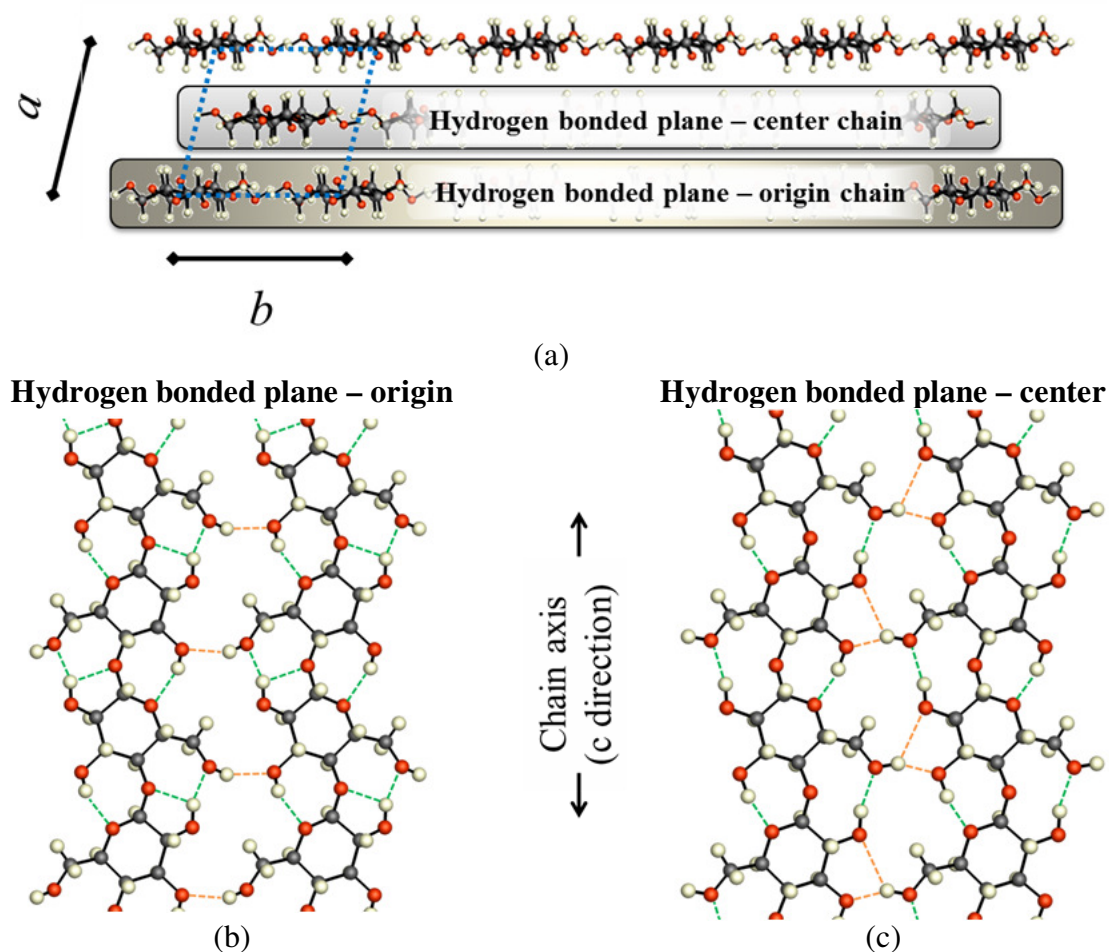

Figure 7-1 Expanded views of the $P2_1$ unit cell structure of the cellulose I_β network A showing the characteristic layered conformation [9]. (a) Projected structure along the *c*-axis direction showing obvious layered structure of I_β along *a*-axis direction, and weaker bonding along *b*-axis direction with respect to that of *c*-axis direction. (b) and (c) Hydrogen-bonding patterns, intra- and inter- molecular hydrogen bonds are depicted in green and orange respectively. (a) Chains at the origin of the unit cell and (b) chains at the center of the unit cell as reported in [12, 70].

The crystalline structure of cellulose I$_\beta$ as well as its hydrogen bond pattern has been extensible study [9, 12, 70]. Nishiyama et al. [9] reported a monoclinic lattice with space group P2$_1$ including two functional unites of C$_6$H$_{10}$O$_5$ in the primitive cell and four in the crystallographic cell. Figure 7-1 illustrates the projected structures of cellulose I$_\beta$ along the *a*-axis and *c*-axis directions. Within the *a-b* plane (Figure 7-1b and c), the energetically favorable hydrogen-bond pattern A [13] determined by Nishiyama et al. [9] using X-ray and neutron fiber diffraction is adopted herein. The layer structure of I$_\beta$ perpendicular to *a*-axis, is where Van der Waals forces dominate the stacking behavior [9, 13, 29, 152, 153].

7.2   Computational methodology

A modified version of LAMMPS simulation software [144] (details in appendix C) was used to compare three different ReaxFF parameterization (ReaxFF_Mattsson [145], ReaxFF_CHO [141] and ReaxFF_Glycine [146]) and their ability to represent cellulose I$_\beta$ hydrogen bonds patterns.

Long range interactions are treated differently by each FF; ReaxFF has an explicit description of hydrogen bonds with input parameters that define its behavior. As a result, ReaxFF can provide more information about the intra- and inter- chain hydrogen bonding network in the cellulose crystal but the results are susceptible to the FF parameterization being used. Equation (9) provides the potential energy contribution for each hydrogen bond as it is computed by ReaxFF [154].

$$U_{H-Bond} = P_{hb1} \times \left(1 - e^{-P_{hb2} \times BO}\right) \times e^{-P_{hb3} \times \left(\frac{R_0}{R} + \frac{R}{R_0} - 2\right)} \times \sin^4\left(\frac{\theta}{2}\right) \tag{9}$$

Parameters P_{hb1}, P_{hb2}, P_{hb3} and R_0 are inputs that depend exclusively on the parameterization being used whereas BO (Bond Order), R (distance between donor and acceptor – marked as distance in Figure 7-2) and θ (hydrogen bond angle) depend upon the geometry configuration.

The derivative of the potential energy with respect to the interatomic distance between donor and acceptor (R) can be consider as the local *force* that the hydrogen bond is applying over the affected atoms. Equation (10) provides the analytical description of this force:

$$force = \frac{\partial U_{H-Bond}}{\partial R}$$

$$force = -P_{hb1} \times \left(1 - e^{-P_{hb2} \times BO}\right) \times P_{hb3} \times \left(\frac{-R_0}{R^2} + \frac{1}{R_0}\right) \times e^{-P_{hb3} \times \left(\frac{R_0}{R} + \frac{R}{R_0} - 2\right)} \times \sin^4\left(\frac{\theta}{2}\right)$$

(10)

The second derivative of the potential energy with respect to the interatomic distance between donor and acceptor (R) will resemble the *stiffness* of the hydrogen bond and will provide an idea of the force need to change the current geometrical configuration.

$$stiffness = \frac{\partial^2 U_{H-Bond}}{\partial R^2}$$

(11)

The definition stated in Equation (11) does not include any possible angular variation. Since all the calculations are performed locally, it is assumed that this limitation will have minor impact over the computed values of *force* and *stiffness*.

Values of energy, first and second derivatives are computed at each time step for each hydrogen bond in the system. The modified version of LAMMPS keeps track of all the information during the totality of the simulation, providing a remarkably powerful tool to analyze hydrogen bonds interactions.

Figure 7-2 shows the hydrogen bond *force* surface for each of the ReaxFF parameterizations as a function of the distance and the angle between the hydrogen atom and the acceptor atom. The surface representation has been limited to interatomic distances up to 3.5 Å, coincident with standard definition of hydrogen bond interactions [148]. ReaxFF_Glycine *force* surface assign a value of zero force at the cutoff distance, vanishing all forces regardless of the angular configuration. ReaxFF_Mattsson and ReaxFF_CHO exhibit a different behavior, the value of the forces at the cutoff distance are different from zero and depend on the angular orientation. This could be considered as a very dangerous practice from the numerical stability point of view due to the artificial nature of cutoff distances. When the hydrogen bond cutoff distance is exceeded, the interaction will suddenly disappear. Since the force being applied by the interaction is not zero, the affected atoms will suffer from a sudden change in momentum. The same problem will occur in the opposite direction, two atoms that are getting close enough (close to the cutoff distance) will suddenly experience an abrupt change in the applied force. It is important to remark that this situation could be completely avoided by appropriately setting the cutoff distance value, at the cost of computational efficiency.

Figure 7-2 Hydrogen bond force surface as a function of the distance and angle for each of the ReaxFF parameterizations: ReaxFF_Mattsson [145], ReaxFF_CHO [141] and ReaxFF_Glycine [146]. The inset in the upper left shows the definition of distance and angle for a O-H—O hydrogen bond. All the figures are plotted in the same scale; notice the discrepancies in the hydrogen bond force assigned to the interaction by each of the parameterizations.

The shape of the hydrogen bond *force* surface (Figure 7-2) is directly influenced by the parameterization being used. ReaxFF_Mattsson and ReaxFF_CHO have a similar overall shape with different values for the peak forces. On the other hand, ReaxFF_Glycine exhibit sharper peaks with an abrupt change from repulsion (negative values) to attraction (positive values). It is expected to observe higher *stiffness* values for hydrogen bond being represented by ReaxFF_Glycine parameterization. Figure 7-3 shows hydrogen bond force as a function of the distance for a fixed angle (180 degrees) allowing direct visualization of the differences in stiffness for each parameterization.

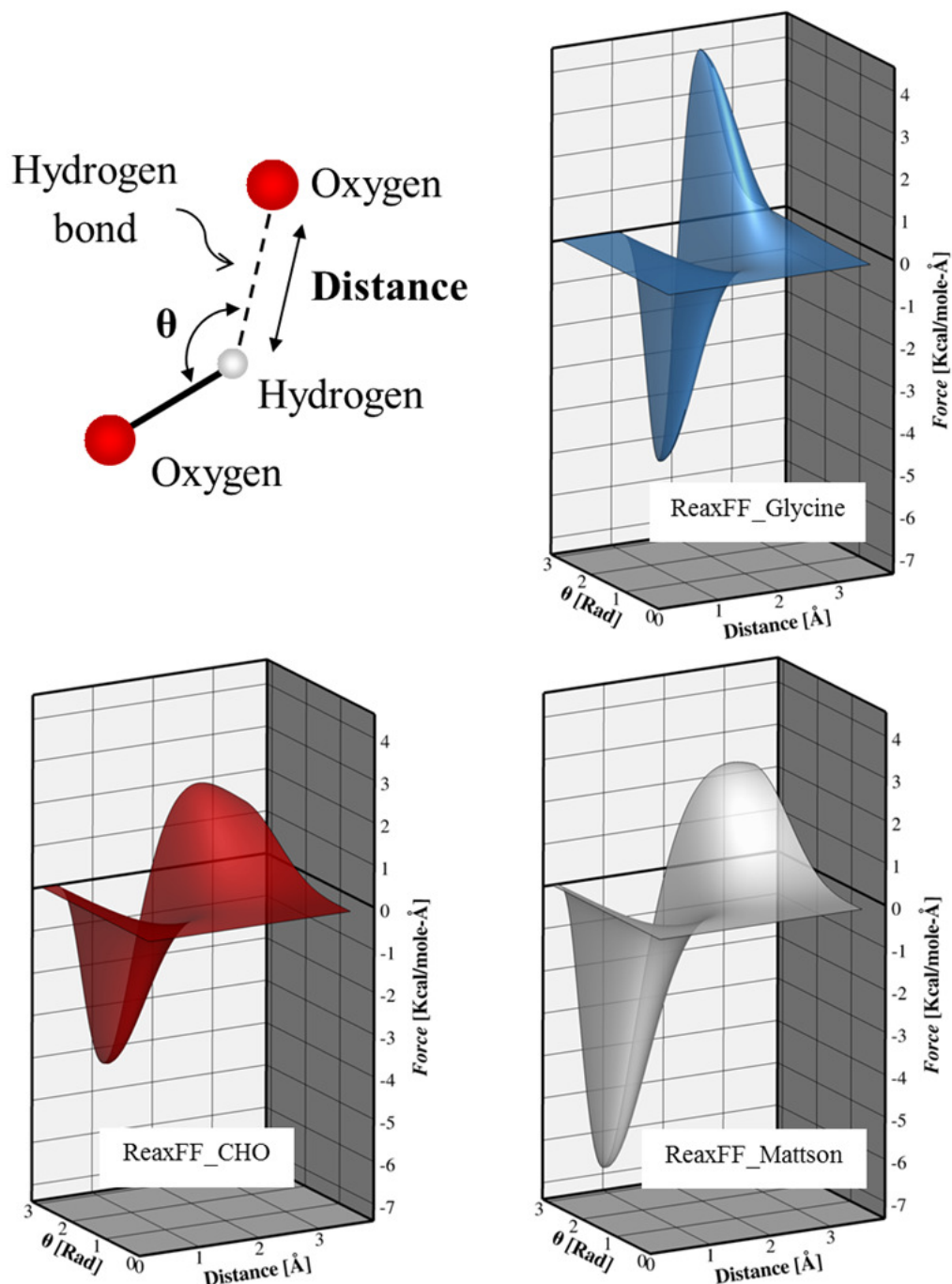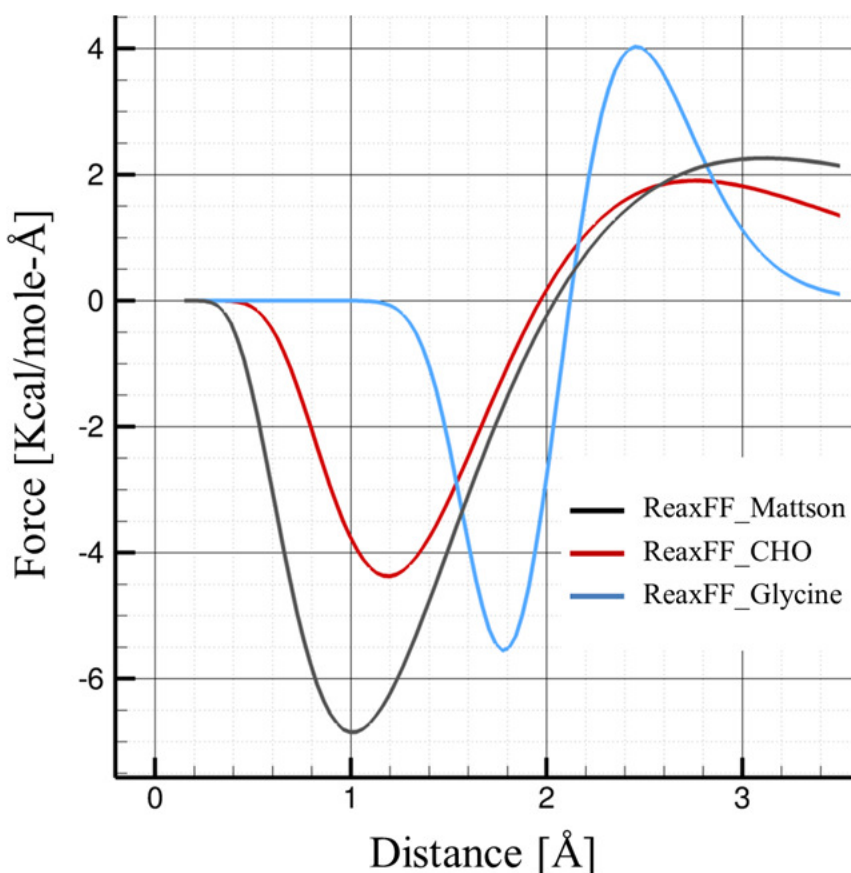Figure 7-3 Hydrogen bond force surface as a function of the distance for each of the ReaxFF parameterizations: ReaxFF_Mattsson [145], ReaxFF_CHO [141] and ReaxFF_Glycine [146]. Angle fixed to 180° according to the hydrogen bond angle (θ) definition presented in the inset of Figure 7-2.

Special post-processing tools have been developed to super-impose each hydrogen bond in the simulated system over the surfaces represented in Figure 7-2. Tracking hydrogen bonds over the *force* surfaces will allow determining the overall behavior of the interaction. Moreover, it will allow recognizing any hydrogen bond interaction that is dangerously close to the cutoff distance.

7.2.1   Simulation cell

Two simulation cells were constructed to analyze the effects of each ReaxFF parameterization over the hydrogen bond structure in cellulose. The first cellulose I_β crystal was constructed by arranging four origin chains and one center chain (see Figure 7-4) according to the geometrical definition provided by Nishiyama et al. [9]. A total of 64 glucose rings were used to construct each cellulose chain using the crystal-building facilities provided by Crystalline cellulose – atomistic toolkit [69], This particular configuration provides the smallest possible crystalline cross-section that can be simulated without the use of periodic boundary conditions. As a result, all the atomic interactions occur between atoms that are explicitly modeled inside the simulation cell, facilitating the quantification of hydrogen bonds. The use of a small cross-section also reduces the number of interactions present in the system, simplifying the analysis.
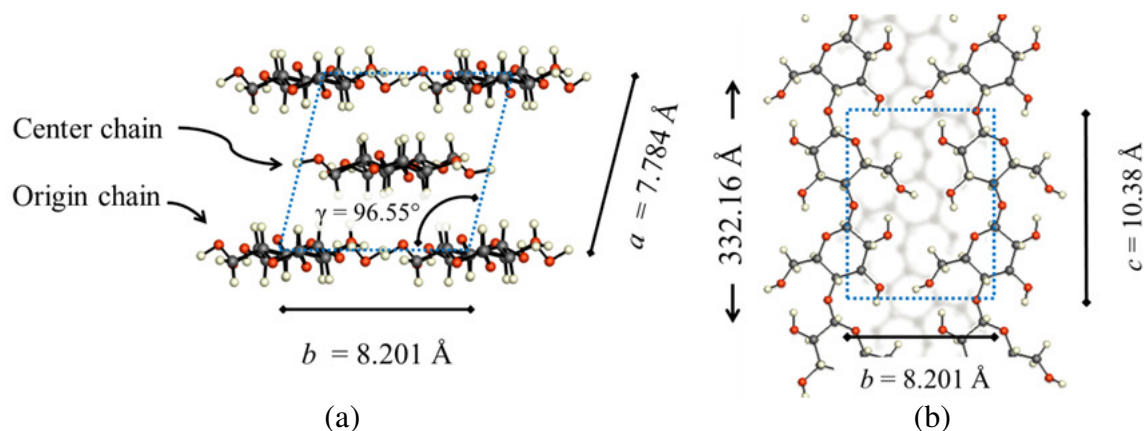
Figure 7-4 Atomistic cellulose I$_\beta$ model consisting in four origin chains and one center chain (SMALL model). (a) View along the *c*-axis (perpendicular to the page). (b) View along the *a*-axis direction. Note that only a fraction of the total length is being showed. Atomic coordinates were obtained after applying symmetry operations to the original structure reported by Nishiyama et al. [9].

A second cellulose I$_\beta$ crystal was constructed by expanding the crystallographic cell reported by Nishiyama et al. [9] by five times in the *a* and *b* directions and 32 times in the *c* direction (64 glucose ring per chain). A snapshot of the simulation cell illustrating these dimensions is given in Figure 7-5. The 61 cellulose chains contained in the second simulation cell will allow analyzing the effect of the initial chain type (origin or center) in the hydrogen bond pattern, providing several hydrogen bond planes (see Figure 7-1) and reducing size effects.

These two crystals will hereafter be referred to as the SMALL and BIG crystals.
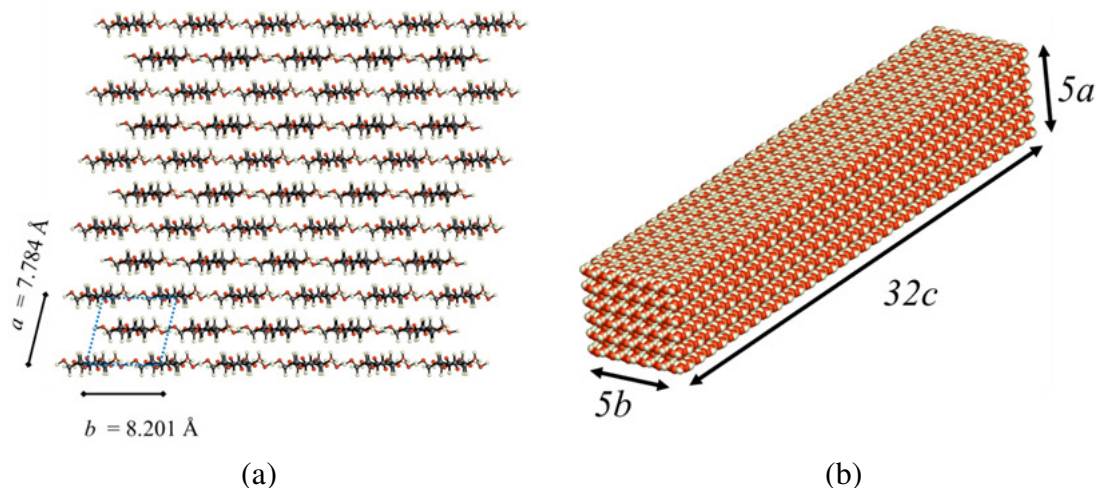
(a)   (b)

Figure 7-5 Atomistic cellulose I_β model obtained by expanding the crystallographic cell reported by Nishiyama et al. [9] by five times in the *a* and *b* directions and 32 times in the *c* direction (BIG model). (a) View along the *c*-axis (perpendicular to the page). (b) Three dimensional view of the simulation model.

7.2.2   Equilibration

It is impossible to perform standard equilibration procedures to the SMALL simulation cell due to the reduced size of the system and the lack of periodic boundary conditions. To overcome this limitation, molecular dynamics simulations at extremely low temperatures (0.01 K) were performed for a short period of time (5 ps). This initial simulation will add randomness to the crystalline structure and will help overcoming any initial energy barrier that may exist. A series of deformation steps consisting in energy minimization techniques followed by stretching steps were used to move the system into a potential energy minimum. Each deformation step stretched the crystal along the longitudinal direction (*c* direction) a factor of 0.01% of the total length (~0.03 Å). This infinitesimal deformation is uniformly applied over all the atoms in the system. Energy minimization (HFTN algorithm) was performed after each deformation increment. After several repetitions of aforementioned procedure, the system is in a local energy minimum

achieved without introducing excessive distortions in the cellulose crystal. The same procedure was applied to the BIG crystalline structure for comparison purposes.

It is important to understand than in this particular study, the final relaxed configuration of the cellulose crystal is not a priority. The focus lays on understanding the hydrogen bond interactions product of each force field parameterization. Moreover, the initial un-relaxed structure is also used for comparison.

7.3   Results and discussion

Two simulation steps are of particular interest in the analysis of hydrogen bond interactions. The first step consists in the initial step, where no minimization or deformation has been applied. For the initial step, all the simulations have the same atomic positions, allowing direct comparison between parameterizations. In other words, the first step is key to understand how different each ReaxFF parameterization represents hydrogen bonds. The second simulation step of interest is the one at which the energy of the system is minimum. This step is different for each parameterization, implying different atomic positions, different potential energy and different time step number. This step is referred as the step of minimum energy to avoid confusion.

7.3.1   Hydrogen bond pattern

The first attempt to understand the hydrogen bond pattern produced by each parameterization consisted in explicitly representing all the hydrogen bond interactions being computed by the force field. ReaxFF only requires a cutoff distance as the user input; each parameterization control all other aspects of the hydrogen bond formations.

As a consequence, each parameterization produces a different hydrogen bond pattern for the same initial structure.

Figure 7-6 through Figure 7-8 display all the hydrogen bonds being computed for the SMALL crystalline structure at the beginning of the simulation. The atomic coordinates at this point are the same for the three cases, as it was reported by Nishiyama et al. [9]. Ideally, the hydrogen bond pattern show in these figures should coincide with the one represented in Figure 7-1. ReaxFF_Glycine and ReaxFF_CHO generated an enormous amount of hydrogen bonds between chains that lay on different planes, contradicting the experimental results reported in [9, 13, 29, 152, 153]. Moreover, a very intricate and unphysical intra-chain hydrogen bond pattern is observed for both parameterizations. ReaxFF_Mattsson show promising results, exposing a hydrogen bond pattern that resembles experimental results reported in [9, 13, 29, 152, 153].

ReaxFF_Glycine

(a)   (b)

Figure 7-6 Hydrogen bond pattern (represented as continuous cyan lines) for the SMALL crystalline struture with ReaxFF_Glycine [146]. Initial simulation step; atomic coordinates coincident with Nishiyama et al. [9]. (a) View along the *c*-axis (perpendicular to the page). (b) Reduced view along the *a*-axis direction for the origin chains in the lower hydrogen bond plane of the crystal. Only four glucose ring per chain are being shown.

ReaxFF_CHO

(a)   (b)
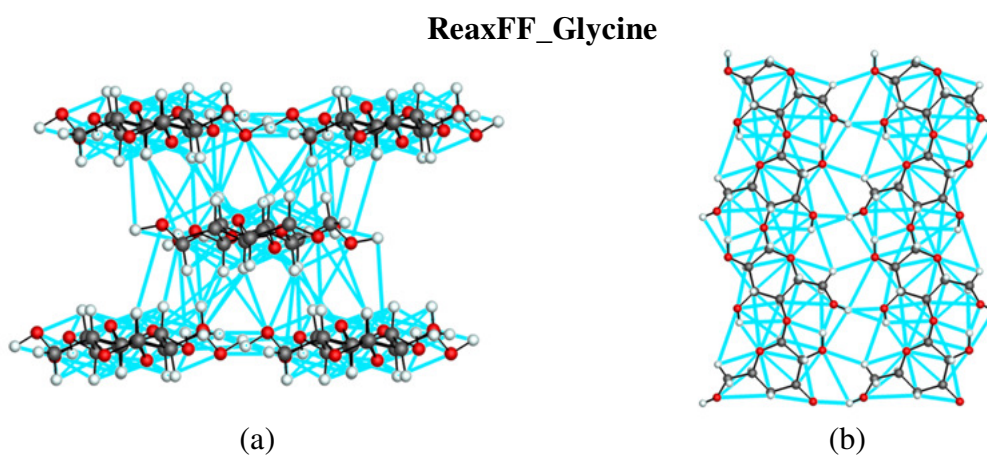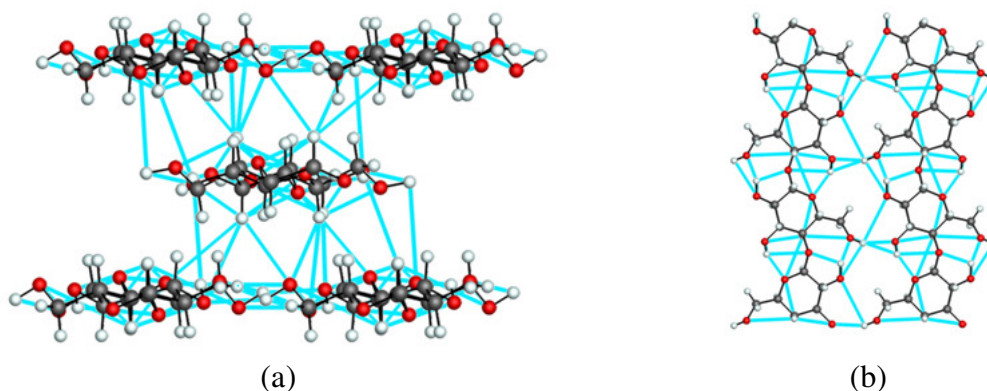
Figure 7-7 Hydrogen bond pattern (represented as continuous cyan lines) for the SMALL crystalline struture with ReaxFF_CHO [141]. Initial simulation step. (a) View along the *c*-axis (perpendicular to the page). (b) Reduced view along the *a*-axis direction.

ReaxFF_Mattsson

(a)   (b)

Figure 7-8 Hydrogen bond pattern (represented as continuous cyan lines) for the SMALL crystalline struture with ReaxFF_Mattsson [145]. Initial simulation step. (a) View along the *c*-axis (perpendicular to the page). (b) Reduced view along the *a*-axis direction.

Before jumping in conclusion regarding the accuracy of each parameterization, it is important to understand that ReaxFF is a bond ordered force field. As a result, each interaction inside the system has a weight parameter (the bond order) that controls its contribution. In other words, the fact that a given hydrogen bond is being computed doesn't necessary mean that it is influencing the system behavior.

7.3.2   Hydrogen bond energy

Figure 7-9 through Figure 7-11 show the energy contribution of each hydrogen bond inside the SMALL crystalline structure at the beginning of the simulation. The atomic coordinates at this point are the same for the three cases, as it was reported by Nishiyama et al. [9].

ReaxFF_Glycine

(a)   (b)

Figure 7-9 Hydrogen bond energy contribution (represented as colored brown lines) for the SMALL crystalline struture with ReaxFF_Glycine [146]. Energy values in Kcal/mole. Initial simulation step; atomic coordinates coincident with Nishiyama et al. [9]. (a) View along the *c*-axis (perpendicular to the page). (b) Reduced view along the *a*-axis direction for the origin chains in the lower hydrogen bond plane of the crystal. Only four glucose ring per chain are being shown.

ReaxFF_CHO

(a)   (b)

Figure 7-10 Hydrogen bond energy contribution (represented as colored brown lines) for the SMALL crystalline struture with ReaxFF_CHO [141]. Energy values in Kcal/mole. Initial simulation step (a) View along the *c*-axis (perpendicular to the page). (b) Reduced view along the *a*-axis direction.
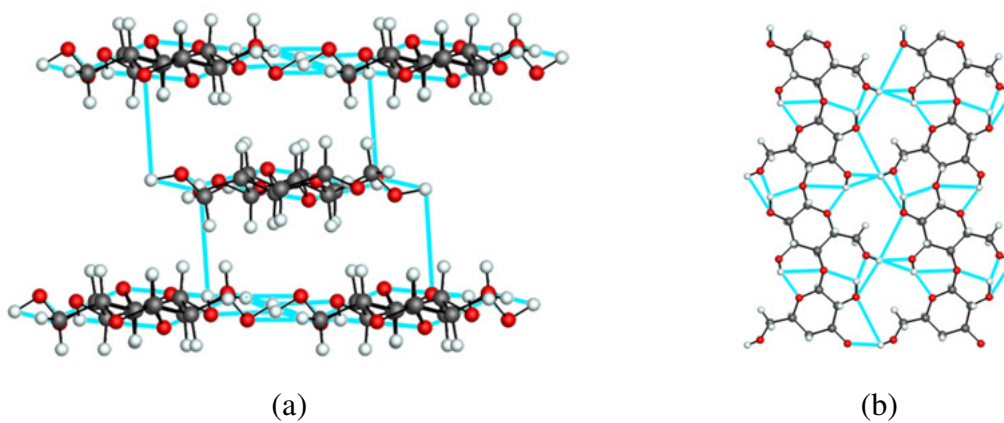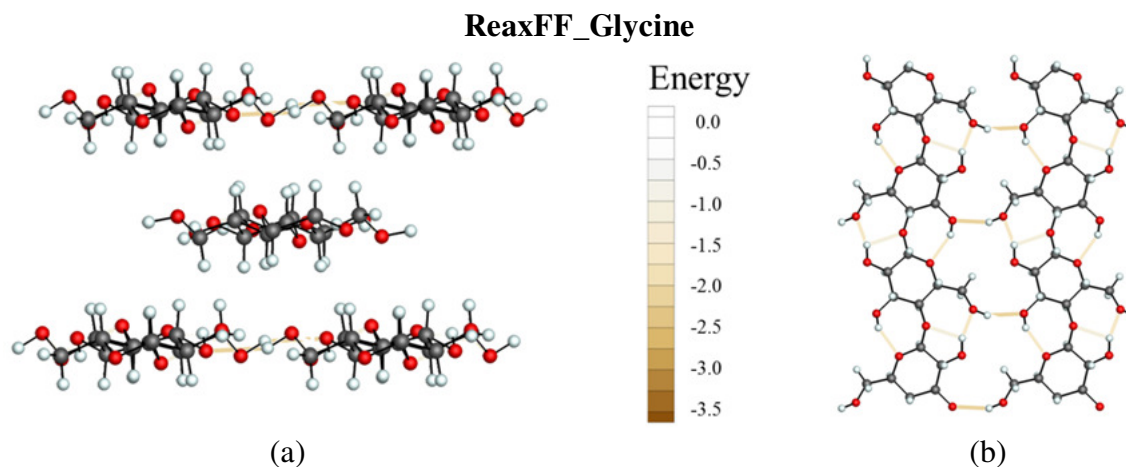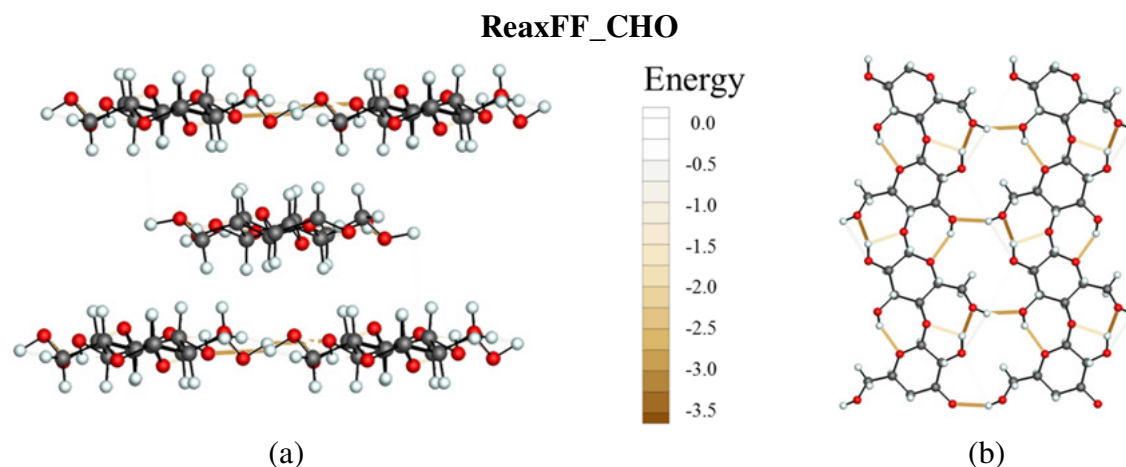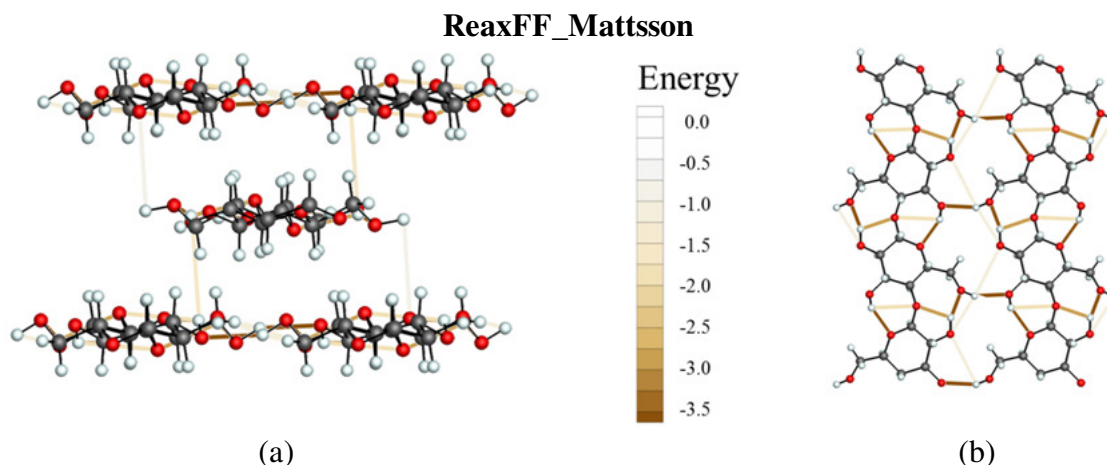
ReaxFF_Mattsson

(a)   (b)

Figure 7-11 Hydrogen bond energy contribution (represented as colored brown lines) for the SMALL crystalline struture with ReaxFF_Mattsson [145]. Energy values in Kcal/mole. Initial simulation step (a) View along the *c*-axis (perpendicular to the page). (b) Reduced view along the *a*-axis direction.

ReaxFF_Glycine, Figure 7-9 indicates a remarkable agreement with experimental values reported in [9, 13, 29, 152, 153]. Moreover, Figure 7-9b shows a hydrogen bond pattern that perfectly matches the experimental values reported in [12, 70] for the origin chain (refer to Figure 7-1). ReaxFF_CHO shows a very similar behavior as it can be observed in Figure 7-10. The hydrogen bond pattern experimentally reported (see Figure 7-1 and [12, 70]) is also being matched; a higher value of energy is assigned to each hydrogen bond when compared with ReaxFF_Glycine. On the other hand, Figure 7-11 shows that ReaxFF_Glycine reports hydrogen bonds linking cellulose chains in separate planes and a hydrogen bond pattern that is not entirely consistent with experimental reports [12, 70]

Additional insides can be obtained analyzing the hydrogen bond pattern once the crystalline structure has been relaxed (atomic coordinates for the minimum potential energy). For example, Figure 7-12 shows that the relaxed structure obtained with ReaxFF_Glycine parameterization practically vanish all hydrogen bond interaction. Only a few inter-chain hydrogen bond interaction are visible in Figure 7-12a. Moreover, only

isolated intra-chain hydrogen bonds are evident in Figure 7-12b. These results appear to contradict the common understanding that hydrogen bonds help stabilizing the cellulose crystal [10, 22, 71, 74, 91, 142] and generate doubts about the validity of this parameterization to model crystalline cellulose.

Figure 7-13 shows simulation results for ReaxFF_CHO parameterization. A complex hydrogen bond network is form between chains belonging to different planes as it can be seen in Figure 7-13a. Even more interesting is the fact that the hydrogen bond network pattern depicted in Figure 7-13b perfectly matches the one reported for center chains (see Figure 7-1). This suggests that at one point during the stabilization procedure, the hydrogen bond pattern has changed from the origin chain pattern to center chain pattern. Crystal reorganization has been reported in several studies [91, 143, 155, 156] indicating that the hydrogen bond structure is not static and can be interchanged. This assumption is consistent with the total arbitrariness in the definition of the center and origin chains. The capability of interchanging hydrogen bond patterns without user intervention is a clear advantage towards the use of ReaxFF_CHO parameterization.

ReaxFF_Mattsson produces hydrogen bond interactions with the highest energy values of the three parameterization analyzed. Figure 7-14a shows an anti-symmetrical hydrogen bond arrangement, with high energy valued hydrogen bonds connecting chains in different planes. Figure 7-14b presents a hydrogen bond pattern somewhat similar to the one reported in [12, 70] for center chains (Figure 7-1) but with some additional inter-chain hydrogen bonds.

ReaxFF_Glycine

(a)   (b)

Figure 7-12 Hydrogen bond energy contribution (represented as colored brown lines) for the SMALL crystalline struture with ReaxFF_Glycine [146]. Energy values in Kcal/mole. Minimum energy step. (a) View along the c-axis (perpendicular to the page). (b) Reduced view along the a-axis direction for the origin chains in the lower hydrogen bond plane of the crystal. Only four glucose ring per chain are being shown.

ReaxFF_CHO

(a)   (b)

Figure 7-13 Hydrogen bond energy contribution (represented as colored brown lines) for the SMALL crystalline struture with ReaxFF_CHO [141]. Energy values in Kcal/mole. Minimum energy step. (a) View along the c-axis (perpendicular to the page). (b) Reduced view along the a-axis direction.

ReaxFF_Mattsson

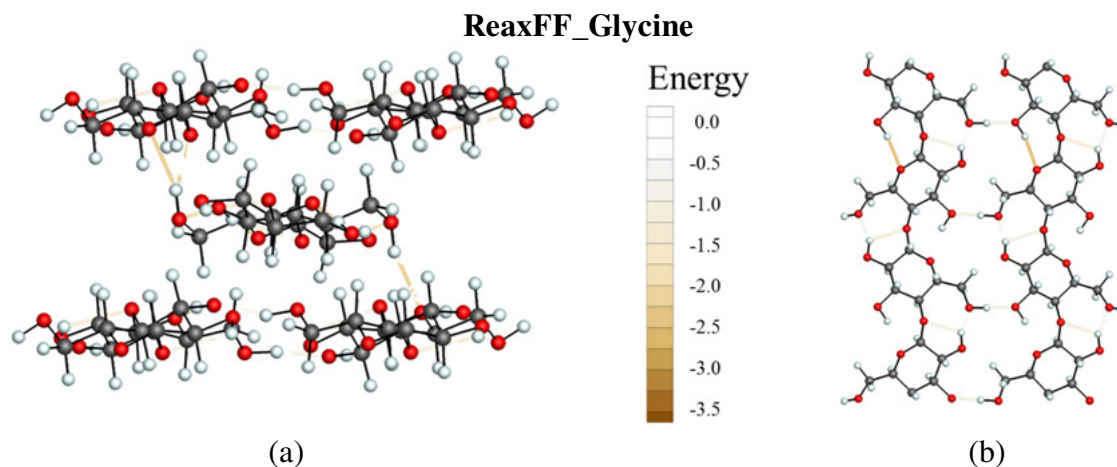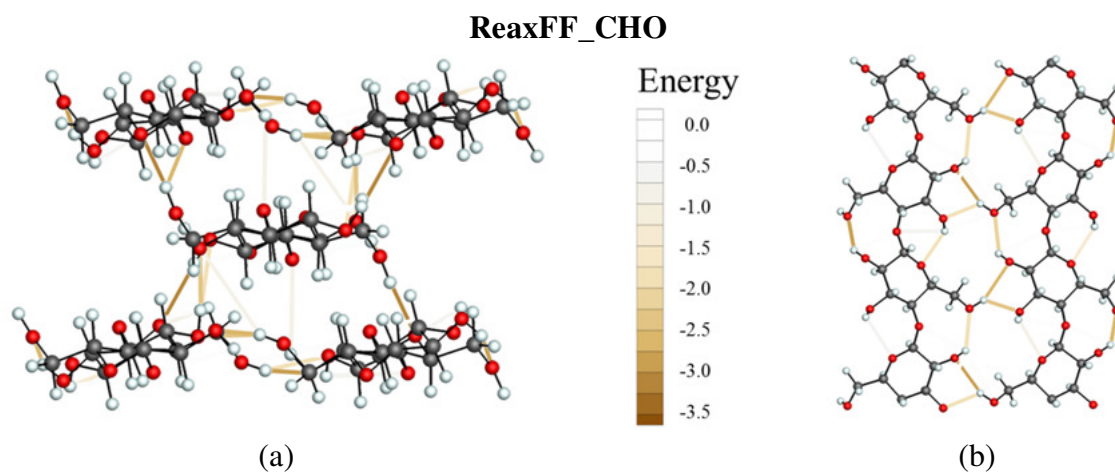(a)   (b)
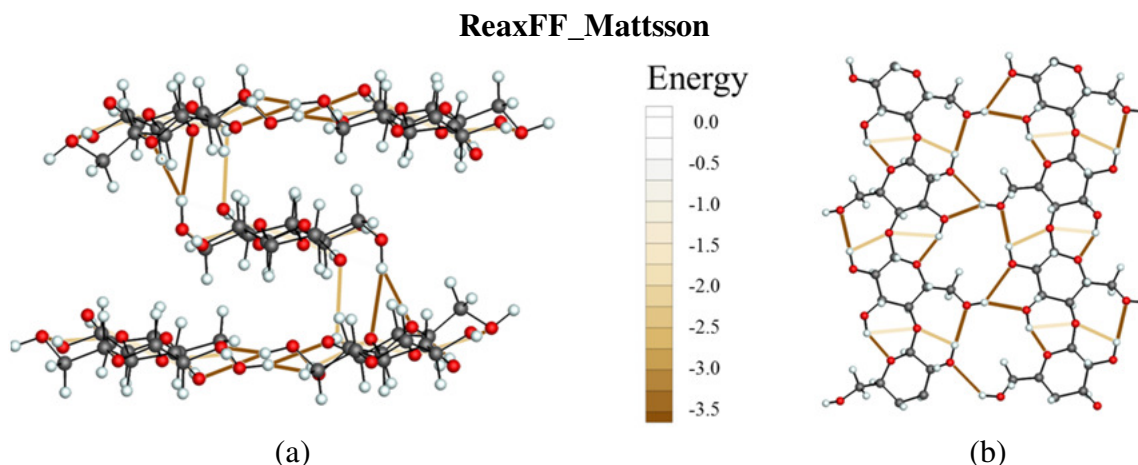
Figure 7-14 Hydrogen bond energy contribution (represented as colored brown lines) for the SMALL crystalline struture with ReaxFF_Mattsson [145]. Energy values in Kcal/mole. Minimum energy step (a) View along the *c*-axis (perpendicular to the page). (b) Reduced view along the *a*-axis direction.

7.3.3 Hydrogen bond *force* and *stiffness*

The internal energy value for each hydrogen bond is a good parameter to analyze the level of activity of each interaction but does not provide any insights regarding the mechanical response of the system. The *force* that each hydrogen bond is exerting over the structure and the *stiffness* of the interaction is analyzed in an attempt to understand the effects of hydrogen bond in the mechanical response of crystalline cellulose.

Figure 7-15 through Figure 7-20 show the *force* and *stiffness* values for each hydrogen bond inside the SMALL crystalline structure at the beginning of the simulation. The atomic coordinates at this point are the same for the three cases, as it was reported by Nishiyama et al. [9].

ReaxFF_Glycine, Figure 7-15 and Figure 7-16, present no *force* and no *stiffness* for hydrogen bonds connecting chains that lay on different planes, indicating a state of local neutral equilibrium. Figure 7-15b shows a negative *force* value (repulsion) whereas

Figure 7-16b indicates a positive *stiffness* value (stabilization) for hydrogen bond interactions between chains belonging to the same hydrogen bond plane.

ReaxFF_CHO, Figure 7-17 and Figure 7-18, also present no *force* and no *stiffness* for hydrogen bonds connecting chains that lay on different planes, indicating a state of local neutral equilibrium. Figure 7-15b shows almost no *force* applied by hydrogen bond interactions between chains belonging to the same hydrogen bond plane. At the same time, Figure 7-18b indicates a positive *stiffness* value, synonym of stable behavior.

ReaxFF_Mattsson, Figure 7-19 and Figure 7-20, show positive values of *force* along many of the hydrogen bonds, indicating interactions that are not in local equilibrium. Positive *stiffness* values shown in Figure 7-20 indicate tendencies towards equilibration.

ReaxFF_Glycine

| (a) | (b) |

Figure 7-15 Hydrogen bond force contribution (represented as colored lines) for the SMALL crystalline struture with ReaxFF_Glycine [146]. *Force* values in Kcal/mole-Å, positive values indicate attration and negative values repulsion. Initial simulation step; atomic coordinates coincident with Nishiyama et al. [9]. (a) View along the *c*-axis (perpendicular to the page). (b) Reduced view along the *a*-axis direction for the origin chains in the lower hydrogen bond plane of the crystal. Only four glucose ring per chain are being shown.

ReaxFF_Glycine

(a)   (b)

Figure 7-16 Hydrogen bond stiffness (represented as colored lines) for the SMALL crystalline struture with ReaxFF_Glycine [146]. *Stiffness* values in Kcal/mole-Å^2. Initial simulation step; atomic coordinates coincident with Nishiyama et al. [9]. (a) View along the c-axis (perpendicular to the page). (b) Reduced view along the a-axis direction for the origin chains in the lower hydrogen bond plane of the crystal. Only four glucose ring per chain are being shown.

ReaxFF_CHO

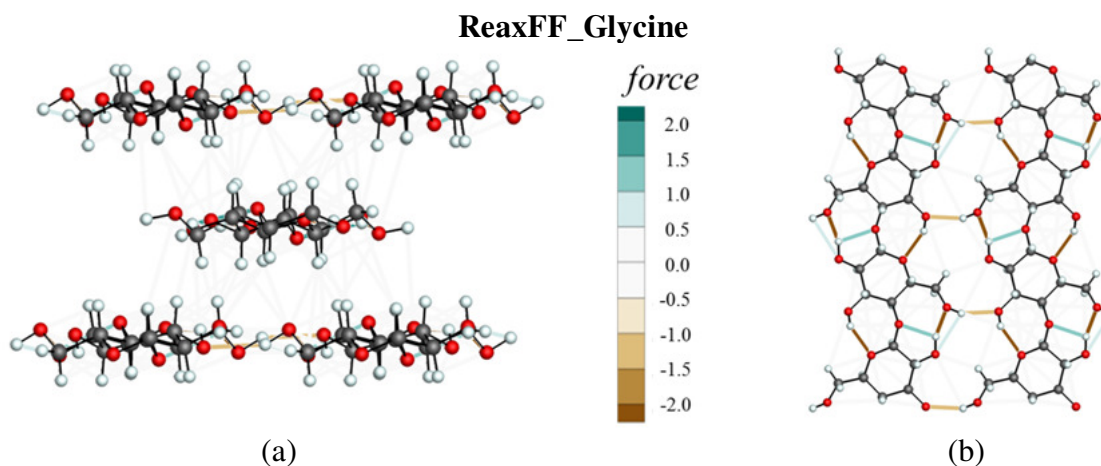(a)   (b)

Figure 7-17 Hydrogen bond force contribution (represented as colored lines) for the SMALL crystalline struture with ReaxFF_CHO [141]. *Force* values in Kcal/mole-Å. (a) Initial simulation step. View along the c-axis (perpendicular to the page). (b) Reduced view along the a-axis.

ReaxFF_CHO

(a)   (b)
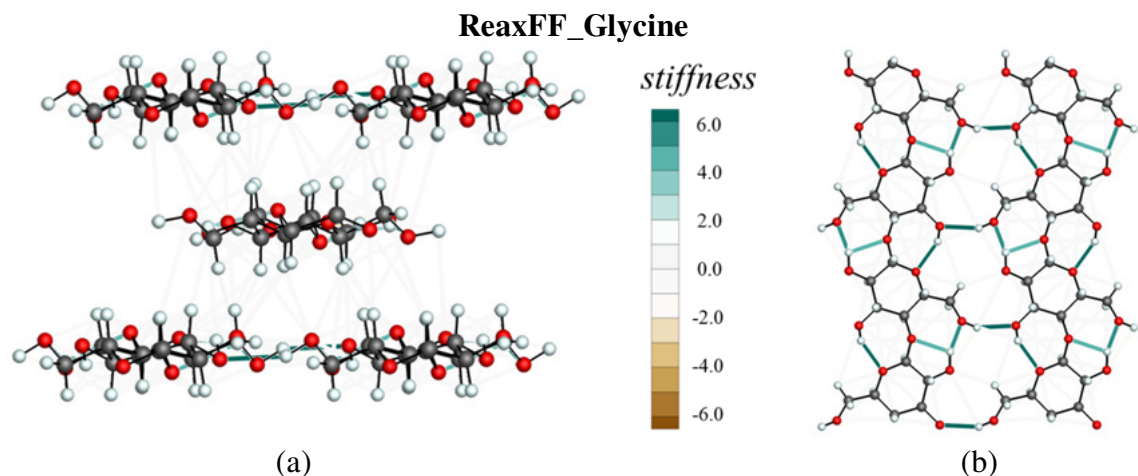
Figure 7-18 Hydrogen bond stiffness (represented as colored lines) for the SMALL crystalline struture with ReaxFF_CHO [141]. *Stiffness* values in Kcal/mole-Å^2. (a) Initial simulation step. View along the *c*-axis (perpendicular to the page). (b) Reduced view along the *a*-axis.

ReaxFF_Mattsson

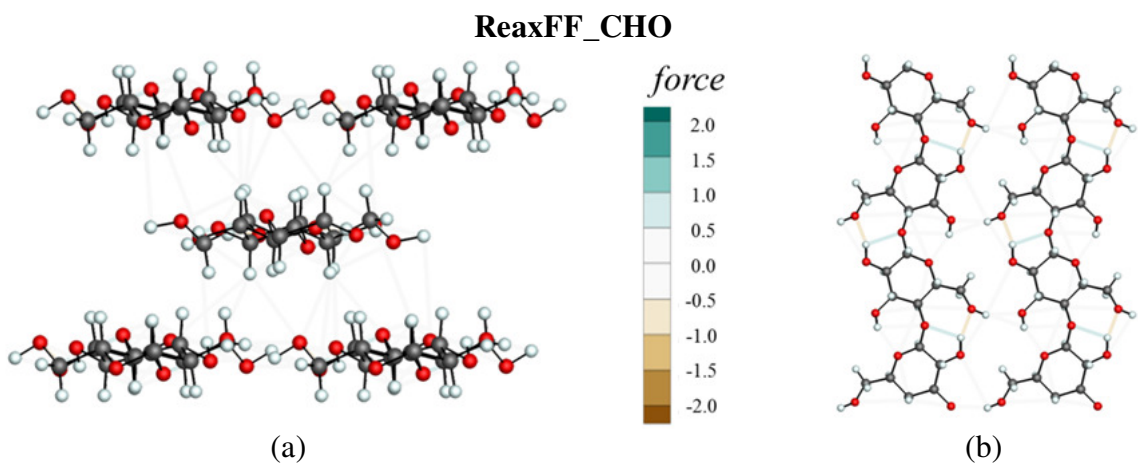(a)   (b)

Figure 7-19 Hydrogen bond force contribution (represented as colored lines) for the SMALL crystalline struture with ReaxFF_Mattsson [145]. *Force* values in Kcal/mole-Å. Initial simulation step. (a) View along the *c*-axis (perpendicular to the page). (b) Reduced view along the *a*-axis.
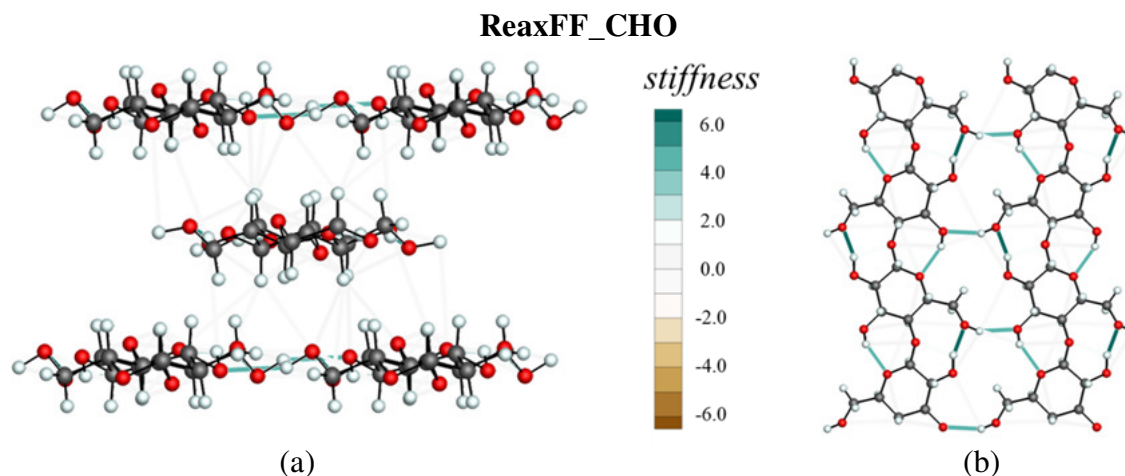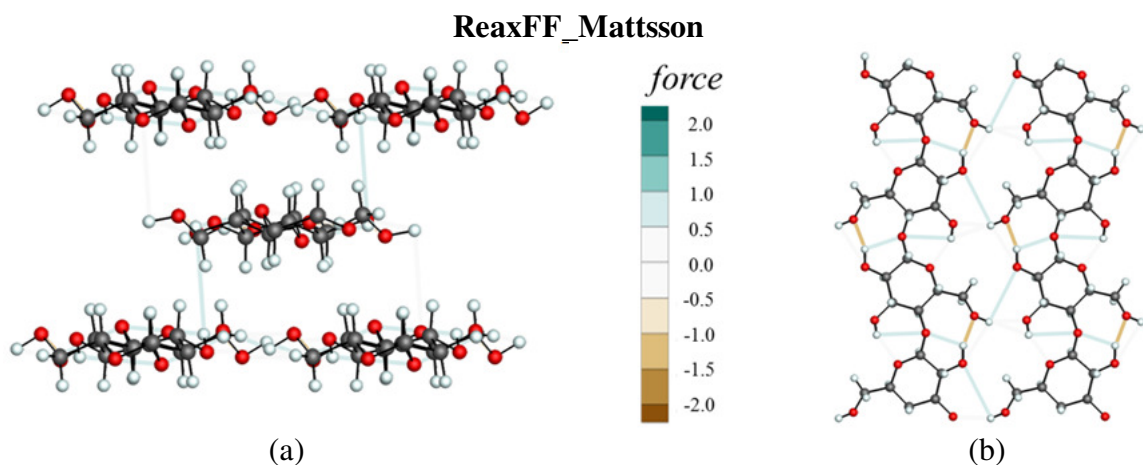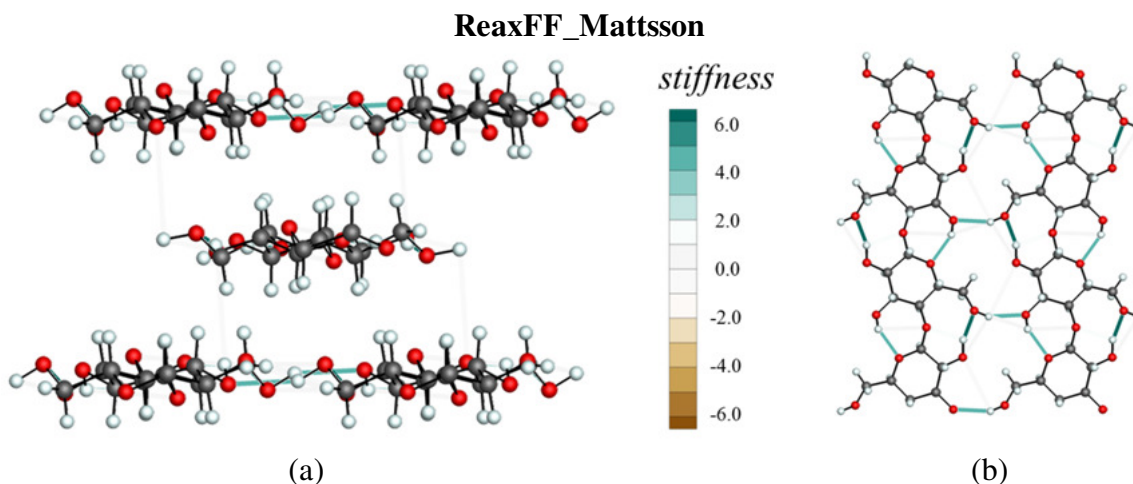
ReaxFF_Mattsson

| | (a) | (b) |

Figure 7-20 Hydrogen bond stiffness (represented as colored lines) for the SMALL crystalline struture with ReaxFF_Mattsson [145]. *Stiffness* values in Kcal/mole-$Å^2$. Initial simulation step. (a) View along the *c*-axis (perpendicular to the page). (b) Reduced view along the *a*-axis.

Additional information was obtained by analyzing the hydrogen bond pattern once the crystalline structure has been relaxed. ReaxFF_Glycine presents a very particular behavior for hydrogen bonds interactions connecting chains that belong to the same plane. Figure 7-21 shows hydrogen bonds exerting repulsion *forces* (negative values in the plot) whereas Figure 7-22 reports a negative *stiffness* value for the same interaction. This particular combination could lead to an unstable behavior of the entire cellulose crystal. Moreover, it was found that molecular dynamic simulations performed with ReaxFF_Glycine and hydrogen bond interactions manually disabled produce values of lateral Young's modulus that are higher than the ones obtained when the interactions are being considered (see Chapter 6). It is important to remark that this behavior contradicts previously reported molecular dynamic and quantum mechanics results [23-25, 30, 31, 113, 149]. On the other hand, the study conducted in Chapter 6 showed ReaxFF_Glycine as the only parameterization capable of producing longitudinal Young modulus in the

order of QM-DFT predictions (192.2 GPa for ReaxFF_Glycine and 196.5 GPa for QM-DFT).

ReaxFF_Glycine

Figure 7-21 Hydrogen bond force contribution (represented as colored lines) for the SMALL crystalline struture with ReaxFF_Glycine [146]. *Force* values in Kcal/mole-Å, positive values indicate attration and negative values repulsion. Minimum energy step. (a) View along the *c*-axis (perpendicular to the page). (b) Reduced view along the *a*-axis direction for the origin chains in the lower hydrogen bond plane of the crystal. Only four glucose ring per chain are being shown.

ReaxFF_Glycine

Figure 7-22 Hydrogen bond stiffness (represented as colored lines) for the SMALL crystalline struture with ReaxFF_Glycine [146]. *Stiffness* values in Kcal/mole-Å^2. Minimum energy step. (a) View along the *c*-axis (perpendicular to the page). (b) Reduced view along the *a*-axis direction for the origin chains in the lower hydrogen bond plane of the crystal. Only four glucose ring per chain are being shown.

ReaxFF_CHO

(a)   (b)

Figure 7-23 Hydrogen bond force contribution (represented as colored lines) for the SMALL crystalline struture with ReaxFF_CHO [141]. *Force* values in Kcal/mole-Å. (a) Minimum energy step. View along the *c*-axis (perpendicular to the page). (b) Reduced view along the *a*-axis.

ReaxFF_CHO

(a)   (b)
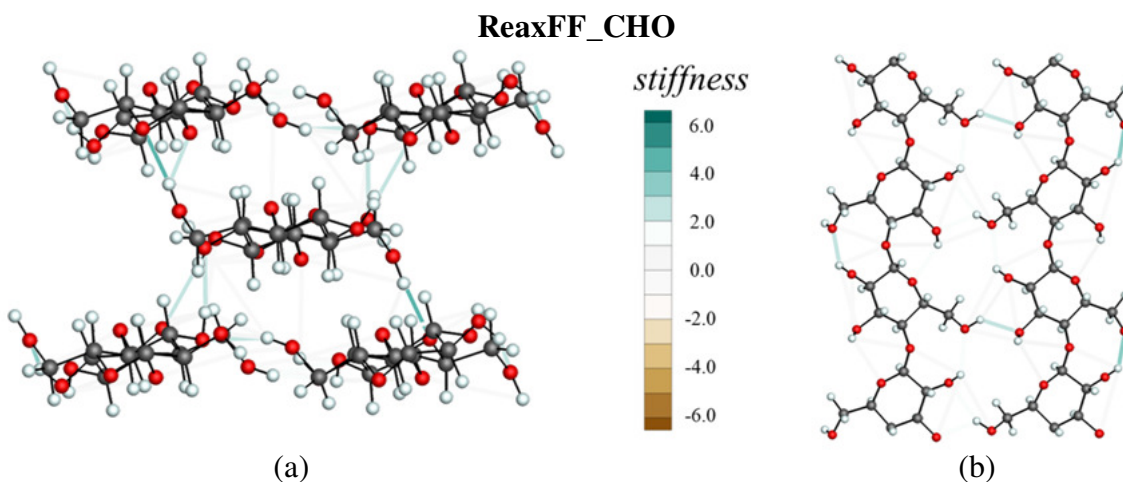
Figure 7-24 Hydrogen bond stiffness (represented as colored lines) for the SMALL crystalline struture with ReaxFF_CHO [141]. *Stiffness* values in Kcal/mole-Å^2. (a) Minimum energy step. View along the *c*-axis (perpendicular to the page). (b) Reduced view along the *a*-axis.

ReaxFF_Mattsson

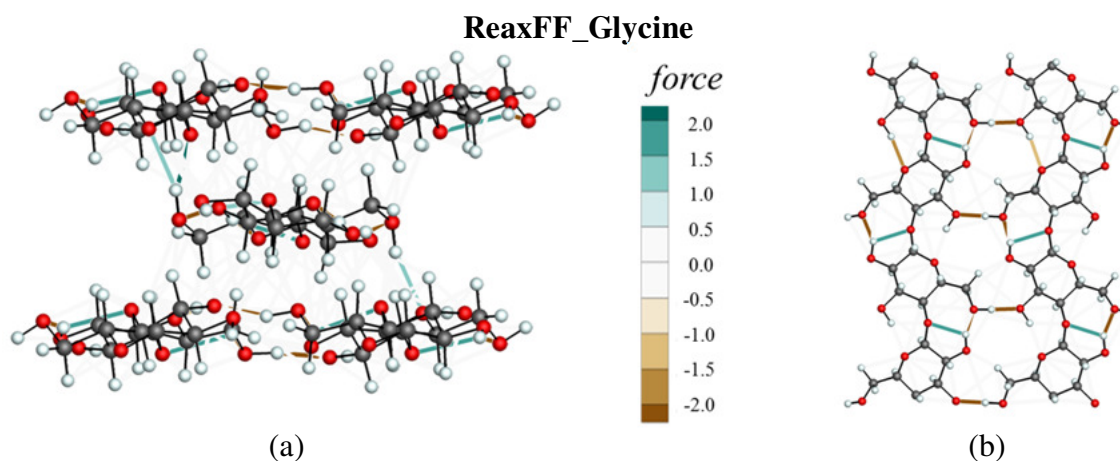(a)   (b)
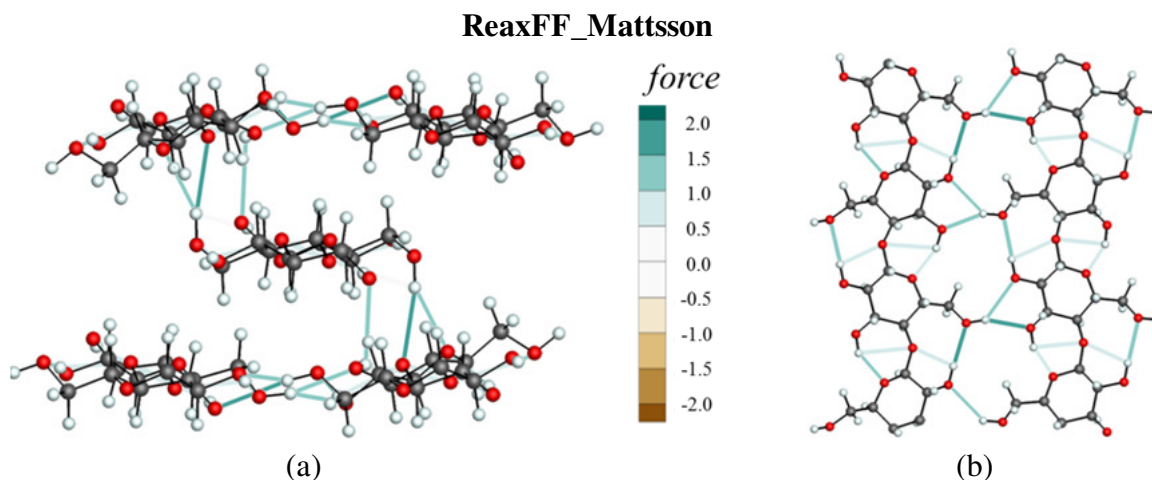
Figure 7-25 Hydrogen bond force contribution (represented as colored lines) for the SMALL crystalline struture with ReaxFF_Mattsson [145]. *Force* values in Kcal/mole-Å. Minimum energy step. (a) View along the *c*-axis (perpendicular to the page). (b) Reduced view along the *a*-axis.

ReaxFF_Mattsson

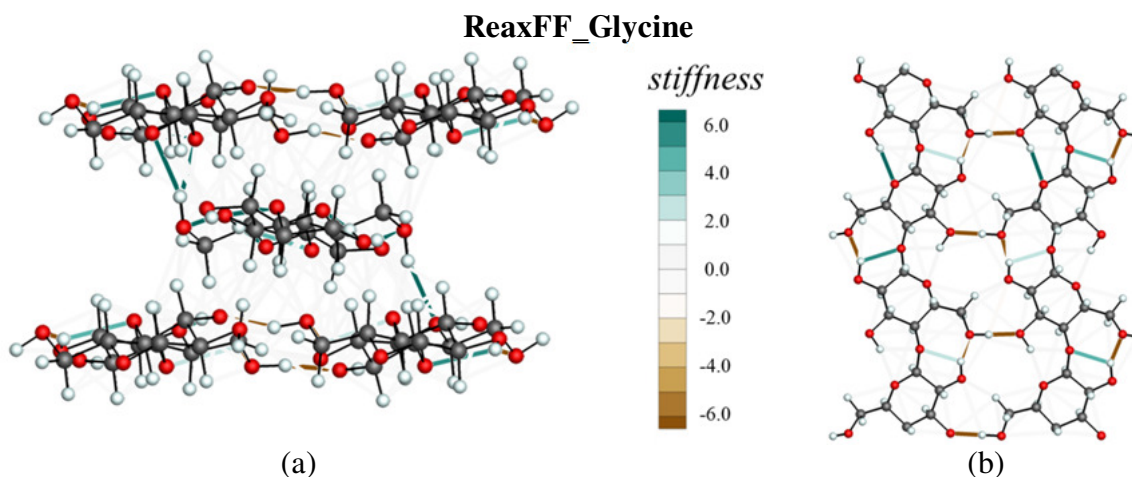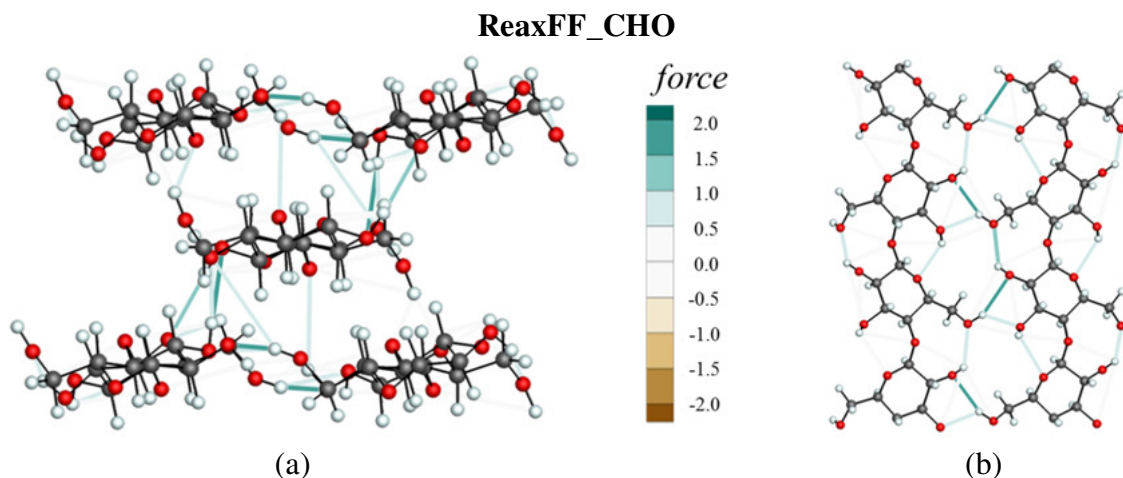(a)   (b)
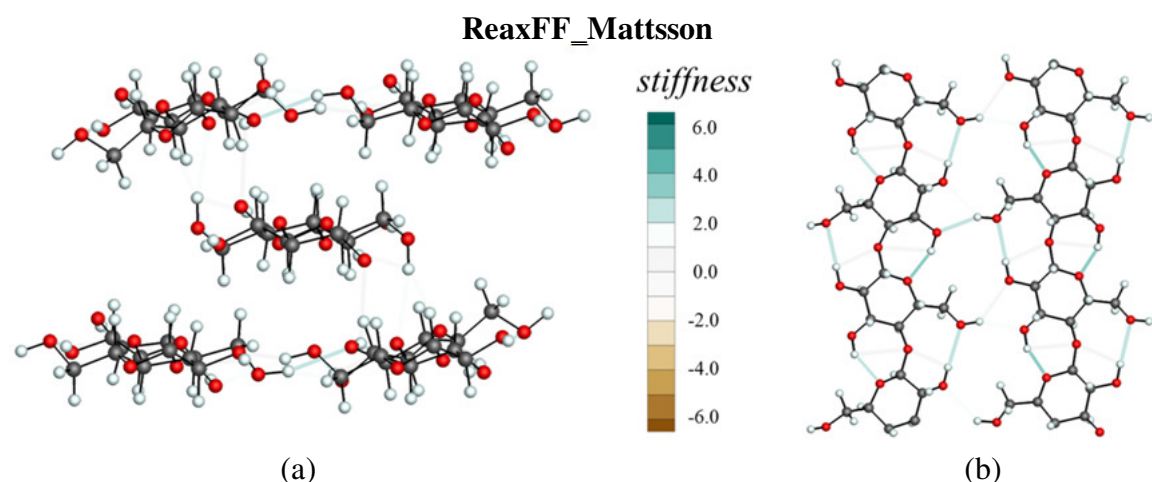
Figure 7-26 Hydrogen bond stiffness (represented as colored lines) for the SMALL crystalline struture with ReaxFF_Mattsson [145]. *Stiffness* values in Kcal/mole-Å^2. Minimum energy step. (a) View along the *c*-axis (perpendicular to the page). (b) Reduced view along the *a*-axis.

Both, ReaxFF_CHO and ReaxFF_Mattsson, Figure 7-23 and Figure 7-25, show positive values of *force* along many of the hydrogen bonds indicating interactions that are not in local equilibrium. Positive *stiffness* values shown in Figure 7-24 and Figure 7-26 indicate tendencies towards equilibration.

7.3.4   Size effects

This section summarizes results for the BIG cellulose model in the initial and minimized configurations. ReaxFF_CHO provides the most promising results based on previous analyses, producing the best outcomes for energy, *force* and *stiffness* of the three analyzed force fields. As a consequence, only simulations results for this particular parameterization are going to be presented in this section.

Figure 7-27 and Figure 7-28 analyze the hydrogen bond pattern for the initial undeformed structure (atomic coordinates coincident with Nishiyama et al. [9]) and the relaxed structure. The total amount of hydrogen bond interactions in the system increases as a direct consequence of increasing the cross-sectional area of the simulation cell. Additional hydrogen bond planes (center-chain planes) lead to interactions that were not possible in the reduced simulation cell.

A complex hydrogen bond network is form between chains belonging to different planes as it can be seen in Figure 7-28a. Evidence of crystal reorganization is now clear; the hydrogen bond network associated to origin chains at the beginning of the simulation (Figure 7-27b) is found in the center chains at the minimization step (Figure 7-28c). The opposite effect occurs to the pattern associated to center chains at the beginning of the simulation (Figure 7-27b to Figure 7-28b). It is worth notice that this particular configuration increases the number of hydrogen bonds contributing to the axial stiffness of the crystal by changing their alignment. It is possible to theorize that the hydrogen bond pattern interchange occurs to maximize the capabilities of the crystal to withstand axial deformation as the stretching process occurs.

Figure 7-29 and Figure 7-30 show positive values of *forces* and *stiffness* for all the inter-chain hydrogen bonds. Based on this result, it is possible to assume that hydrogen bonds play a role in keeping the different hydrogen planes in position. Previously conducted studies using different force fields and simulation software have encountered similar results [91, 143, 156].

(a)

Origin chains   **Center chains**
(b)   (c)

Figure 7-27 Hydrogen bond energy contribution (represented as colored brown lines) for the BIG crystalline struture with ReaxFF_CHO [141]. Energy values in Kcal/mole. Initial simulation step, atomic coordinates coincident with Nishiyama et al. [9]. (a) View along the *c*-axis (perpendicular to the page). (b) Reduced view along the *a*-axis direction for cellulose chains originally labeled as origin chains according to their geometrical position [12, 70]. (c) Reduced view along the *a*-axis direction for cellulose chains originally labeled as center chains according to their geometrical position [12, 70].

(a)

Origin chains

(b)

Center chains

(c)
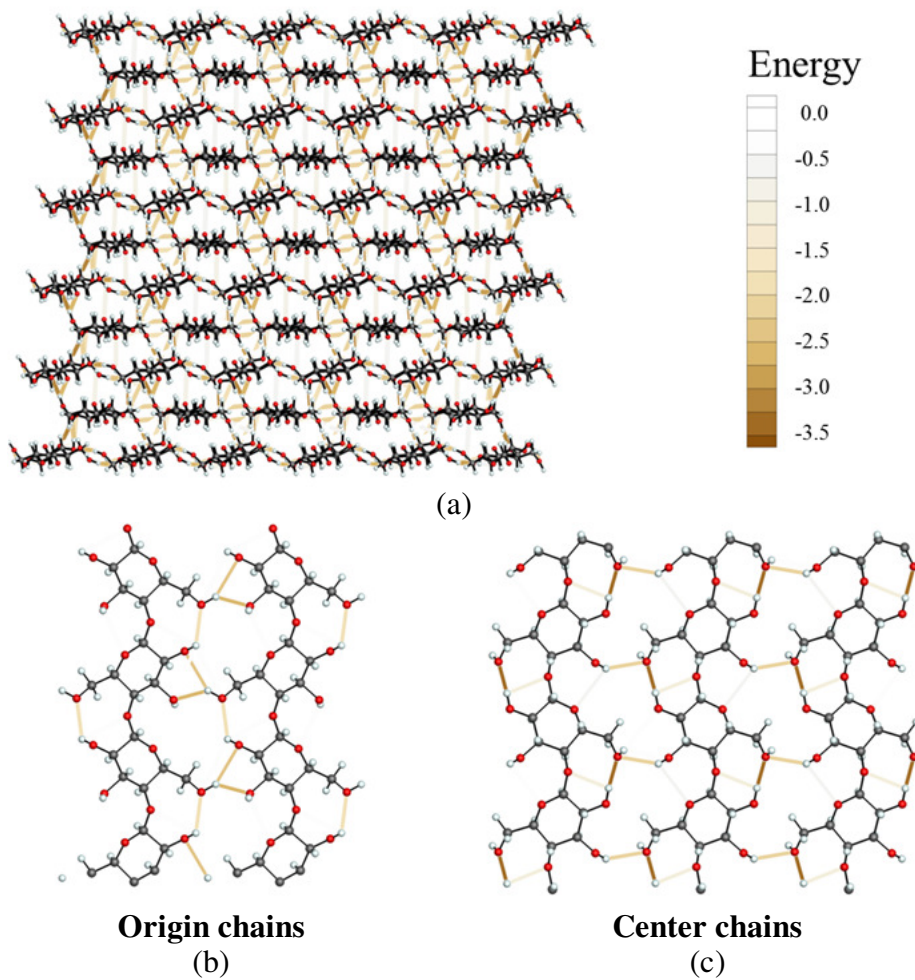
Figure 7-28 Hydrogen bond energy contribution (represented as colored brown lines) for the BIG crystalline struture with ReaxFF_CHO [141]. Energy values in Kcal/mole. Minimum energy step. (a) View along the *c*-axis (perpendicular to the page). (b) Reduced view along the *a*-axis direction for cellulose chains originally labeled as origin chains according to their geometrical position [12, 70]. (c) Reduced view along the *a*-axis direction for cellulose chains originally labeled as center chains according to their geometrical position [12, 70].
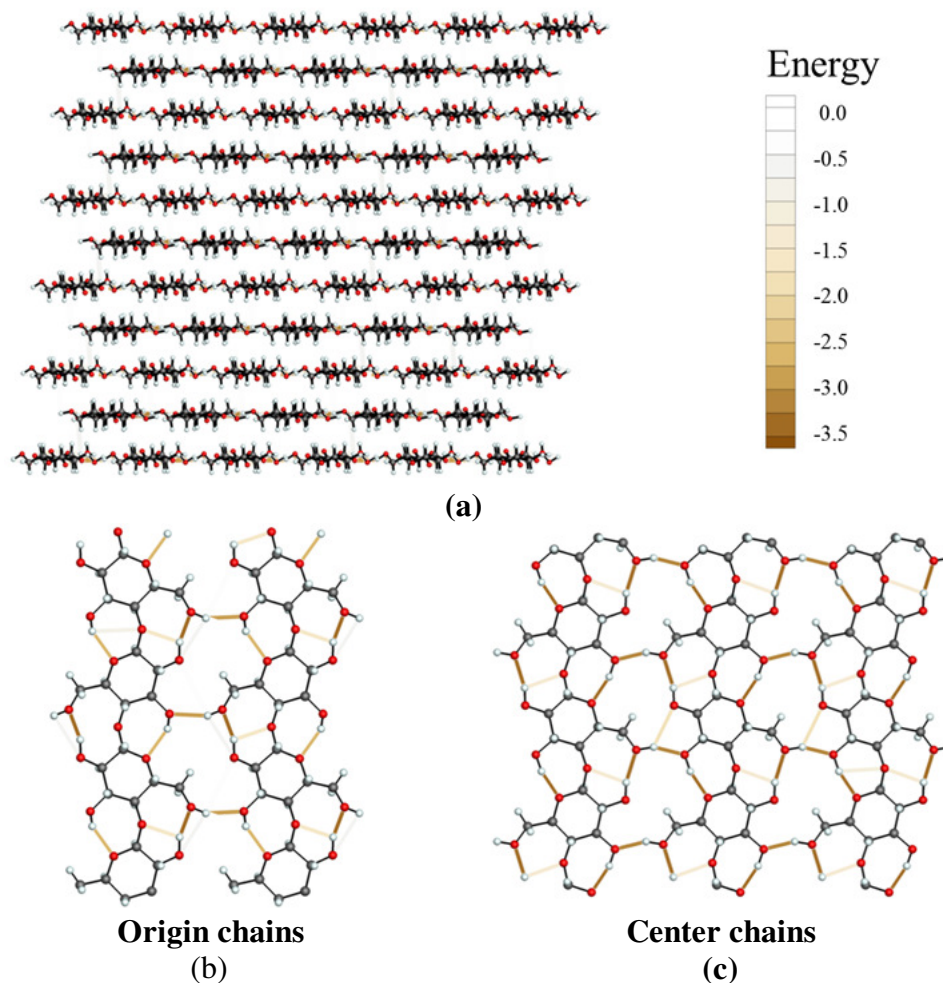
(a)

Origin chains

(b)

Center chains

(c)
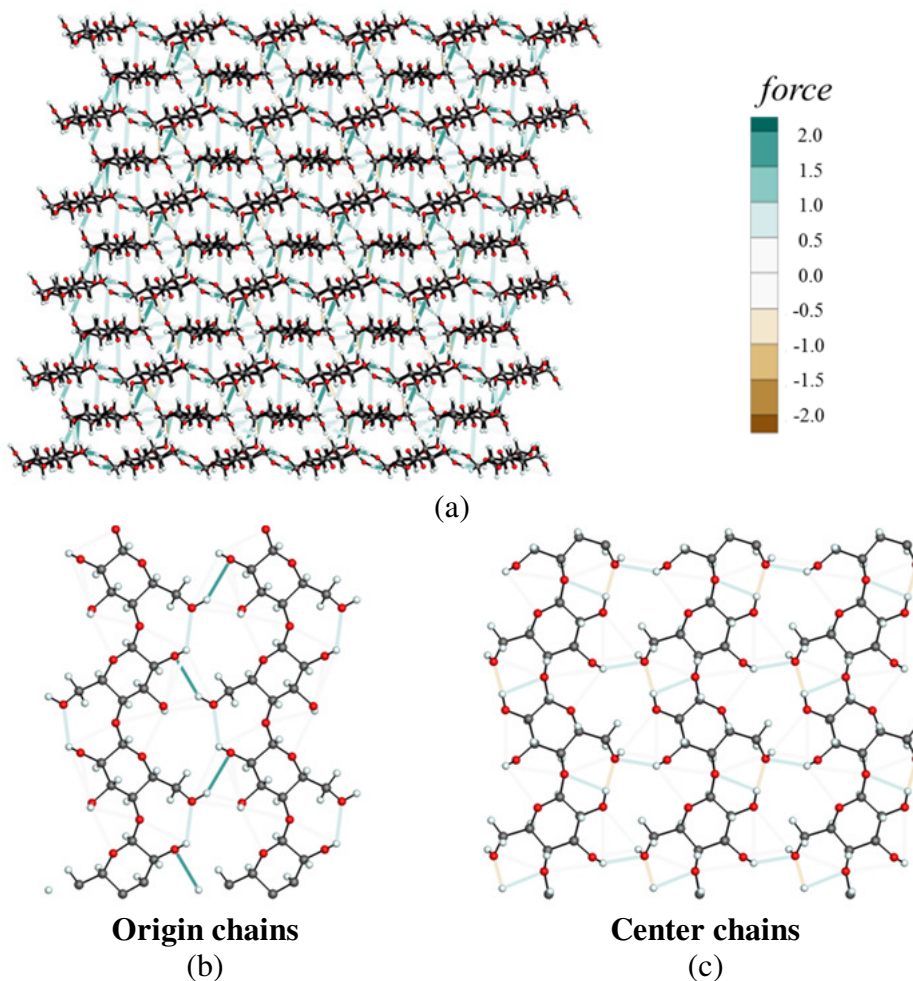
Figure 7-29 Hydrogen bond force contribution (represented as colored lines) for the BIG crystalline struture with ReaxFF_CHO [141]. *Force* values in Kcal/mole-Å. Minimum energy step. (a) View along the *c*-axis (perpendicular to the page). (b) Reduced view along the *a*-axis direction for cellulose chains originally labeled as origin chains according to their geometrical position [12, 70]. (c) Reduced view along the *a*-axis direction for cellulose chains originally labeled as center chains according to their geometrical position [12, 70].

(a)

Origin chains
(b)

Center chains
(c)
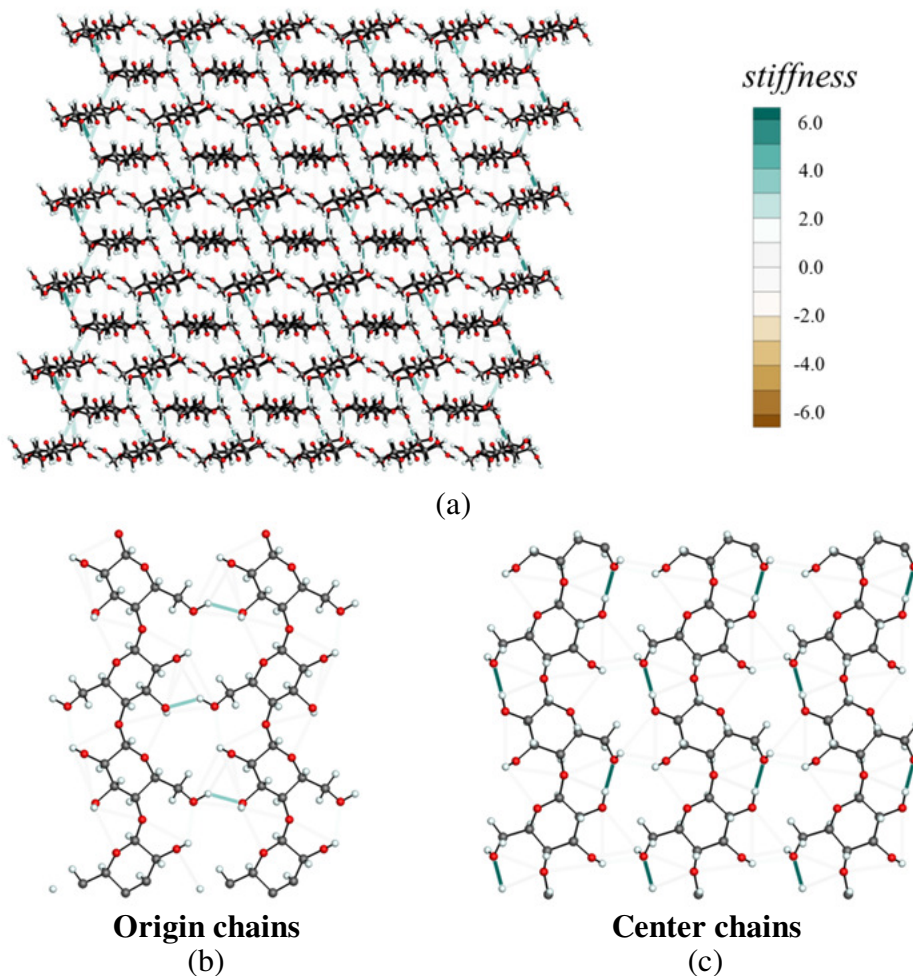
Figure 7-30 Hydrogen bond stiffness (represented as colored lines) for the BIG crystalline struture with ReaxFF_CHO [141]. *Stiffness* values in Kcal/mole-$Å^2$. Minimum energy step. (a) View along the *c*-axis (perpendicular to the page). (b) Reduced view along the *a*-axis direction for cellulose chains originally labeled as origin chains according to their geometrical position [12, 70]. (c) Reduced view along the *a*-axis direction for cellulose chains originally labeled as center chains according to their geometrical position [12, 70].

7.4   Conclusion

A comprehensive analysis over hydrogen bond behavior in cellulose I$_\beta$ was conducted.

Three force field parameterizations were study to assess their ability to represent energy,

force and *stiffness* of individual hydrogen bonds. As expected, none of the tested

parameterization yield results in perfect agreement with experimental data.

ReaxFF_CHO [141] provides the most promising results based on previous analyses, showing the capability of interchanging hydrogen bond patterns on-the-fly and producing consistent results through the entire analysis. It is important to remember that hydrogen bond interactions are not the only interactions defined by the force field parameterization. The apparently good results show in this section also needs to be compared with relatively poor performance of ReaxFF_CHO in predicting mechanical properties.

ReaxFF_Glycine [146] shows the exact opposite behavior, performing remarkably well in predicting longitudinal mechanical properties (compared with QM-DFT) but failing in maintaining a stable hydrogen bond configuration. It is worth notice that this behavior was already evidenced in the previous chapter (Chapter 6) when computing transverse Young modulus values. ReaxFF_Glycine predicted a reduction in lateral stiffness when hydrogen bonds where activated in the simulations. The detailed analysis conducted in this chapter allowed a complete understanding on the reasons for this behavior.

It is important to emphasize that this analysis does not solve the "parameterization problem" but provides invaluable information on the intrinsic behavior of hydrogen bonds and explains many of the results obtained in previous chapters.

CHAPTER 8. ANALYSIS OF THE MECHANICAL RESPONSE OF A SINGLE CELLULOSE CHAIN USING REACTIVE FORCE FIELDS

8.1 Introduction

The remarkable mechanical properties of cellulose nanocrystals are a result of its specific structural configuration. As a first approximation, cellulose I_β can be described by a monoclinic unit cell which contains two cellulose chains in a parallel orientation [9]. Further investigation will reveal two conformationally distinct chains, which are referred to as the origin and center chains [12].

(a)   (b)
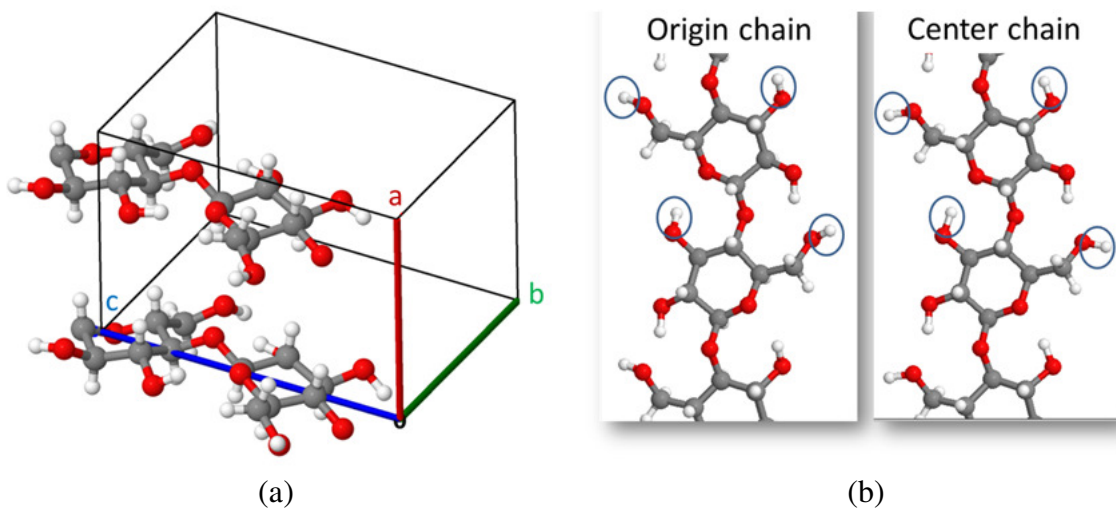
Figure 8-1 (a) Three dimensional representation of the cellulose I_β unit cell based on Nishiyama et al. [9]. Notice the origin chain positioned at the corner of the unit cell. The center chain has been shifted about $c/4$ with respect to the origin chain in the c-axis direction. (b) Origin and center chains viewed along the a-axis according to Nishiyama et al. [9]. Blue ellipses added to highlight the conformational differences.

Figure 8-1 show a schematic representation of the cellulose I_β unit cell. The origin chain is positioned at the corner of the unit cell parallel to the c axis direction. The center chain, passes through the center of the a-b plane and is translated in the c-axis direction by about $c/4$ with respect to the origin chain [9].

Calculations of probable conformations of an isolated cellulose chain [157] showed that the cellulose molecule is not likely to exist by itself, requiring extended hydrogen-bonded arrangements [158]. However, the study of isolated cellulose chains could help understanding the intrinsic behavior of cellulose nanocrystals by providing mechanical properties of the basic "building block". Molecular dynamic simulations with ReaxFF reactive force field were used to analyze the axial stiffness of a single cellulose chain. By combining this results with the ones obtained in previous chapters, it is expected to fully address the effects of non-bonded interactions on the axial mechanical response of crystalline cellulose.

8.2   Computational methodology

A modified version of LAMMPS simulation software [144] (details in appendix C) was used to compare three different ReaxFF parameterization (ReaxFF_Mattsson [145], ReaxFF_CHO [141] and ReaxFF_Glycine [146]) and their ability to accurately represent cellulose mechanical properties and hydrogen bond patterns.

Long range interactions are treated differently by each FF; ReaxFF has an explicit description of hydrogen bonds as oppose to an implicit representation (COMPASS, GLYCAM). As a result, ReaxFF can provide additional information about the intra-chain hydrogen bonding present in cellulose chains but the results are susceptible to the FF

parameterization being used. Values of energy, *force* and *stiffness* were computed at each time step for each hydrogen bond in the system and recorded for further analysis. Two hydrogen bond cutoff distance values were selected. A cutoff value of 0.0 Å was used to completely deactivate H bonds interactions inside the chain. A cutoff value of 3.5 Å will coincide with standard definition of hydrogen bond interactions [148]. Comparing results with and without intra-chain hydrogen bonds will allow evaluating the influence of this interaction in the axial stiffness.

8.2.1   Simulation cell

Two simulation cells were constructed, each containing one cellulose chain of origin or center type, according with Nishiyama et al. [9] atomic coordinates. A total of 64 glucose rings were used to construct each cellulose chain using the crystal-building facilities provided by Crystalline cellulose – atomistic toolkit [69]. Non periodic boundary conditions were used, all the atomic interactions occurred between atoms that were explicitly modeled inside the simulation cell. This approach facilitated the quantification of hydrogen bonds and allowed direct comparison with results previously presented [159, 160].
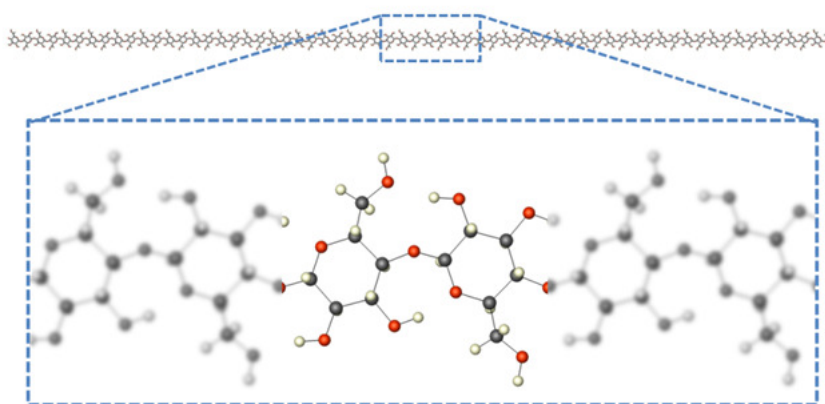
Figure 8-2 Single chain simulation cell showing the 64 glucose ring structure according to Nishiyama et al. [9] atomic coordinates. The insert in the figure emphasizes the repeating units. No periodic boundary condition are being used in the simulation.

8.2.2 Equilibration and stretching procedure

It is impossible to perform standard equilibration procedures to a single chain model without introducing enormous amount of deformation as it can be seen in Figure 8-3.

(a)   (b)
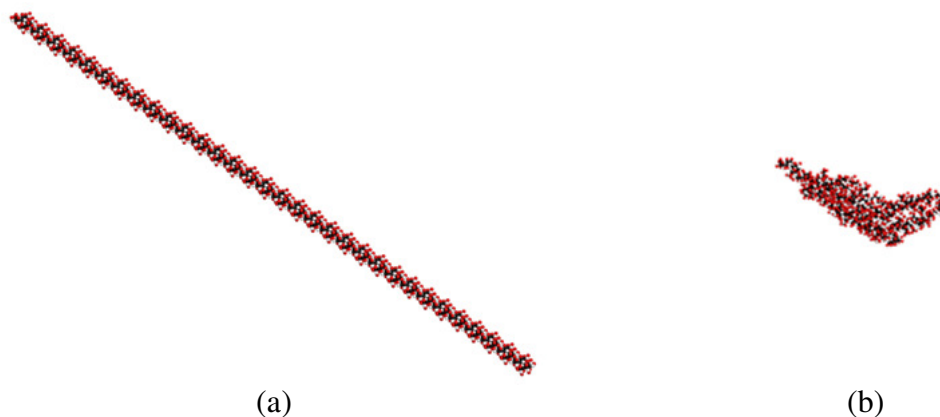
Figure 8-3 Equilibration procedure at 300K for a single chain (a) initial configuration and (b) final configuration. Same visualization scale used for both views. The extreme deformation suffered by the chain motivated the use of the alternative method described in the text.

This behavior is a consequence of the reduced size of the system and the lack of periodic boundary conditions. To overcome this limitation, molecular dynamics simulations at extremely low temperatures (0.01 K) were performed for short periods of time (5 ps, 6 ps and 10 ps). This initial procedure added randomness to the chain structure and helped overcoming any initial energy barrier that may exist. A series of deformation steps consisting in energy minimization techniques followed by stretching steps were used to move the system into a potential energy minimum. Each deformation step stretched the chain along the longitudinal direction (*c*-direction) a factor of 0.01% of the total length (~0.03 Å). This infinitesimal deformation was uniformly applied over all the atoms in the system. Energy minimization (HFTN algorithm) was performed after each deformation increment. After several repetitions of aforementioned procedure, the system is in a local energy minimum achieved without introducing excessive distortions in the cellulose chain. Once system is in the energy minimum, the stretching and minimization steps continue. The equilibrium length l and the corresponding potential energy U is recorded at each step for further analysis.

8.2.3 Stiffness calculation

Traditional methods to compute the Young modulus of materials involved experimentally obtained stress–strain curves. An alternative method, proposed by Tanaka et al. [136] is based on the linear relation between the changes in energy density and the half of the square of the compressive or tensile strains. This calculation does not require the stress applied to the system but changes in energy during deformation as described in equation (12).

$$\frac{U - U_0}{A \times l} = \frac{E}{2} \times \left(\frac{l - l_0}{l_0}\right)^2 \tag{12}$$

Where U is the potential energy of the system; U_0, the potential energy of the system in the relaxed configuration; A, the cross-sectional area; l, the length of the system; l_0, the equilibrated length and E, the elastic modulus.

This particular approach has the advantage that does not require a definition of stress. Stress is inherently a continuum concept and has been proven difficult to define in a physically reasonable manner at the atomic scale [161].

The equation, as it was derived is ideal to analyze crystalline structures with an identifiable cross sectional area. Defining the cross section of single cellulose chain will inevitably lead to an arbitrary decision. As a result, the uniqueness of the Young's modulus value is compromised as it is directly connected to the cross-sectional area. This situation is known to materials scientists working with carbon nanotubes as the "Yakobson's Paradox" [162].

Previous studies have defined a cross-sectional area for a single cellulose chain as half of the cross sectional area of a unit cell [159, 160, 163]. A different approach was proposed based on the idea that the actual Young modulus of the chain is not of interest in this study. By moving the area term, A, to the right hand side of equation (12) it is possible to compute the *stiffness* of the chain as $E \times A$. This approach has a direct advantage, the values of A and E cannot be univocally defined but the multiplication of them is unique. Equation (13) shows the final form used to compute the *stiffness* of the cellulose chain:

$$stiffness = E \times A = \frac{2 \times (U - U_0)}{l} \times \left(\frac{l_0}{l - l_0}\right)^2 \tag{13}$$

It is important to clarify that this definition of *stiffness* is different than the one described for hydrogen bonds interactions in the previous chapter.

8.3   Results and discussion

8.3.1   Potential energy and chain stiffness

The first analysis compares potential energy curves with and without hydrogen bond interactions. Quadratic regression was used to fit molecular dynamics simulation results; equation (13) was applied to obtain the chain stiffness parameter.
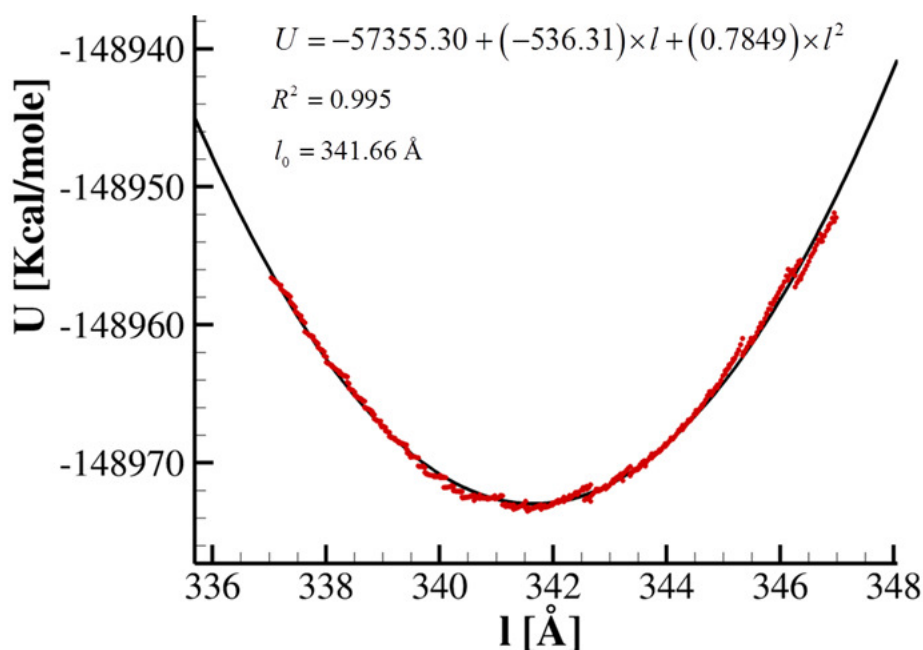
Figure 8-4 Cellulose chain potential energy (U) as a function of the chain length (l). Red dots represent computational data points. Fitting equation, coefficient of determination (R^2) and equilibrated length (l_0) added for reference. Results obtained using a center chain model, ReaxFF_CHO [141] parameterization and 10 ps of stabilization time.

Figure 8-4 shows computational data points and the quadratic fitting being applied. In all the analyzed cases the coefficient of determination (R^2) remained above 0.93. Successive

analyses only focused in the quadratic fitting curves to simply comparison between parameterizations.

The first step was to analyze the shape of the potential energy curves as a function of the change in length (l-l_0) for each case. This qualitative analysis can provide very intuitive information on the mechanical behavior of a single chain under different parameterizations. The axial stiffness of a chain is directly related to the derivative of the potential energy curve, in other words, the steeper the parabola the higher the axial stiffness. Figure 8-5 summarizes all potential energy curves for each of the analyzed parameterizations. Averaged curves were included to facilitate comparison between cases with and without hydrogen bond interactions.

A quick analysis on Figure 8-5 revealed different behaviors for each parameterization. ReaxFF_CHO and ReaxFF_Glycine generated small differences between averaged curves when hydrogen bond interactions were deactivated. On the other hand, ReaxFF_Mattsson showed a clear differentiation between cases with and without hydrogen bond interactions. At the same time, ReaxFF_Glycine showed a wider dispersion between results, with curves without hydrogen bond interactions that were steeper than the ones that consider hydrogen bonds.
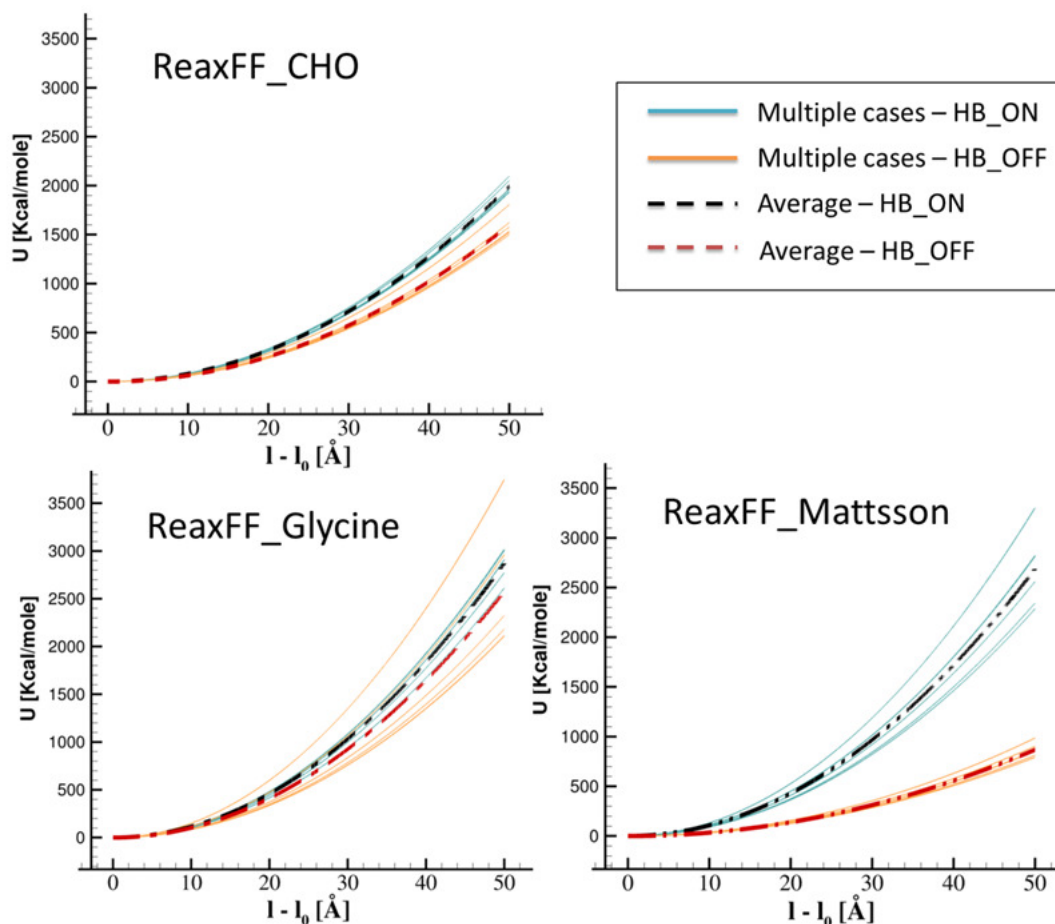
Figure 8-5 Potential energy (U) as a function of the change in length (l-l_0). Each solid line represents quadratic regression functions obtained from fitting numerical simulations. Dashed lines computed as the average of the quadratic fitting. Results with hydrogen bond interaction activated (HB_ON) and deactivated (HB_OFF).

Averaged curves of potential energy as a function of the change in length (l-l_0) were plotted in Figure 8-6 for comparison. ReaxFF_Glycine and ReaxFF_Mattsson showed very similar curve shapes when hydrogen bond interactions were considered. However, each parameterization assigned different influences to hydrogen bonds. ReaxFF_Mattsson showed an important influence of hydrogen bonds in defining the axial stiffness whereas the small influence of hydrogen bonds interactions predicted by ReaxFF_Glycine was clearly evidenced by slight differences between curves of the same

parameterization. These results suggest different strengthening mechanisms proposed by each parameterization.
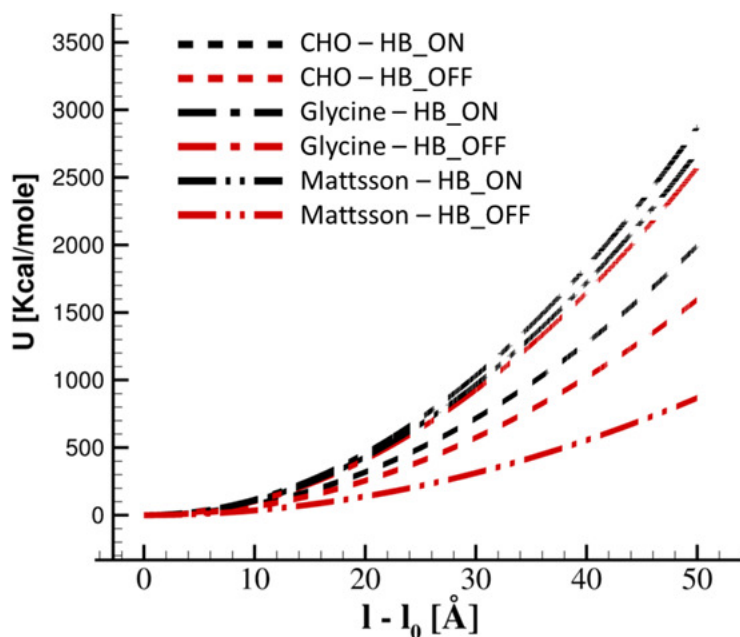
Figure 8-6 Comparison of potential energy (U) as a function of the change in length (l-l$_0$). Each dashed line represent the average of the quadratic fitting for an specific parameterization. Results with hydrogen bond interaction activated (HB_ON) and deactivated (HB_OFF).

Table 8-1 summarizes results shown in Figure 8-5 and Figure 8-6 by presenting the minimum, maximum and average *stiffness* values for a single cellulose chain under different force field parameterizations. Based on average result, it was possible to compute a decrease of 20% in stiffness when hydrogen bonds are turned off in ReaxFF_CHO parameterization. At the same time, ReaxFF_Glycine show a decrease of only 11% whereas ReaxFF_Mattsson produced the biggest decrease with almost 70% difference. These results are in agreement with previously reported data [159, 163] for other atomistic simulations.

Table 8-1 Predicted chain stiffness (EA) for different force field parameterizations and simulation conditions. Hydrogen bond "No" implies that hydrogen bond interactions have been deactivated in the simulations. Minimum (Min), Maximum (Max) and Average values obtained over six different simulations for each parameterization. Young modulus values computed from stiffness averages assuming a cross-sectional area of 31.71 $Å^2$.

Parameterization	Hydrogen Bonds	Stiffness [Pa · m^2]			Young Modulus [GPa]
		Min	Max	Average	
ReaxFF_CHO [141]	Yes	3.67E-08	3.98E-08	3.79E-08	119.4
	No	2.85E-08	3.44E-08	3.03E-08	95.6
ReaxFF_Glycine [146]	Yes	4.90E-08	5.71E-08	5.41E-08	170.7
	No	3.99E-08	6.97E-08	4.82E-08	151.9
ReaxFF_Mattsson [145]	Yes	4.42E-08	6.38E-08	5.20E-08	163.9
	No	1.45E-08	1.82E-08	1.60E-08	50.4

8.3.2   Hydrogen bond *force*

The role of hydrogen bonding was explicitly evaluated by analyzing the force that each hydrogen bond interaction was exerting over the cellulose chains. The relaxed state (minimum potential energy) was used to facilitate comparison between different parameterizations.

A detailed analysis of Figure 8-7 revealed that ReaxFF_Mattsson and ReaxFF_CHO, parameterization produced a hydrogen bond pattern that contributes to increase the axial *stiffness* of the cellulose chain. In both cases, hydrogen bonds aligned with the chain longitudinal direction produced attraction forces between atoms inside the chain. Figure 8-7a showed less amount and weaker hydrogen bond for ReaxFF_CHO compared to ReaxFF_Mattsson (Figure 8-7c). This difference could be used to explain the important decrease (~70%) of *stiffness* experienced by the ReaxFF_Mattsson when hydrogen bonds are deactivated. On the other hand, ReaxFF_CHO only undergoes a 20% reduction in *stiffness*.
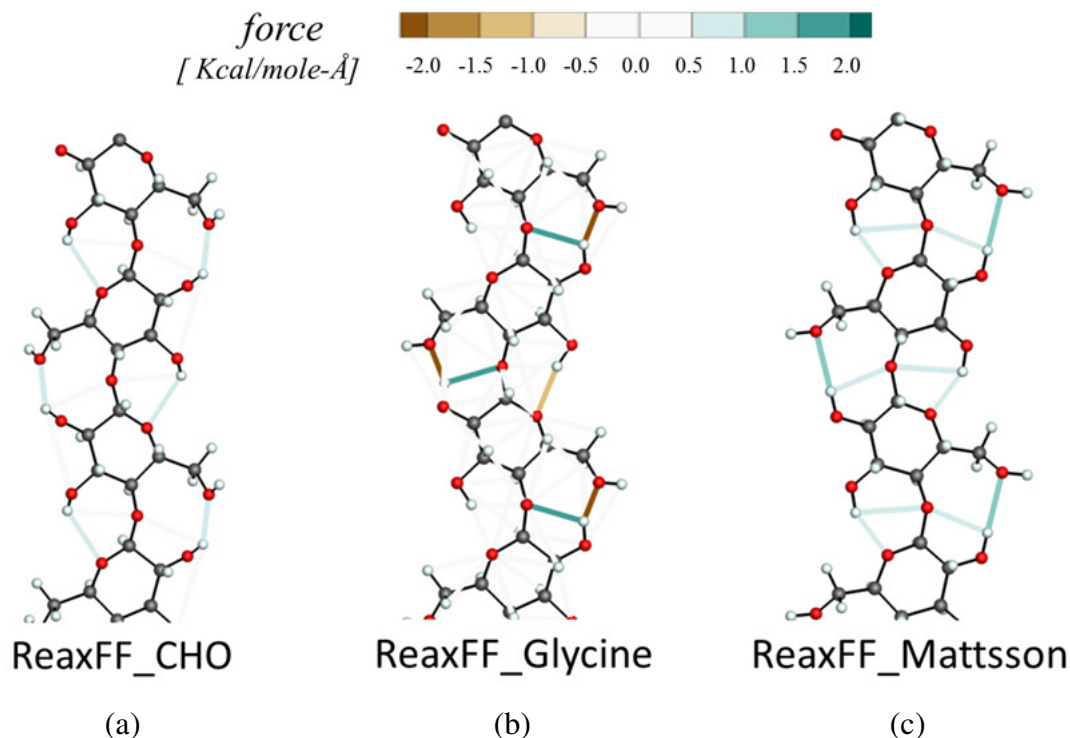
Figure 8-7 Hydrogen bond force distribution (represented as colored lines) for a single cellulose chain under diferent paramterizations. Force values in Kcal/mole-Å, positive values indicate attration and negative values repulsion. Results for (a) ReaxFF_CHO [141], (b) ReaxFF_Glycine [146] and (c) ReaxFF_Mattsson [145]. Atomistic coordinates that yield the minimum potential energy. Only four glucose ring per chain are being shown.

ReaxFF_Glycine produced unexpected results; Figure 8-7b showed that this parameterization lead to hydrogen bond interactions exerting both repulsive and attractive forces inside the chain. These results could be used to explain the dispersion in the potential energy curves presented in Figure 8-5. Small conformational alterations will lead to hydrogen bond interactions applying repulsion forces in different directions, and consequently, reducing the total *stiffness* of the chain. This behavior is directly evidence by the small difference (11%) between simulations with and without hydrogen bonds interactions. Moreover, Figure 8-5 show potential energy curves for simulations without

hydrogen bond interactions that exceed the *stiffness* measured with hydrogen bond interactions.

8.3.3   Qualitative comparison – single chain vs crystalline structure

The mechanical response of a single chain is here compared with previous results obtained for entire crystals. *Stiffness* values for single chains were converted to Young modulus by assuming a cross-sectional area of 31.71 Å^2. It is important to point out that the Young modulus values were not used in the multiscale model framework presented here and were only added for comparison purposes.
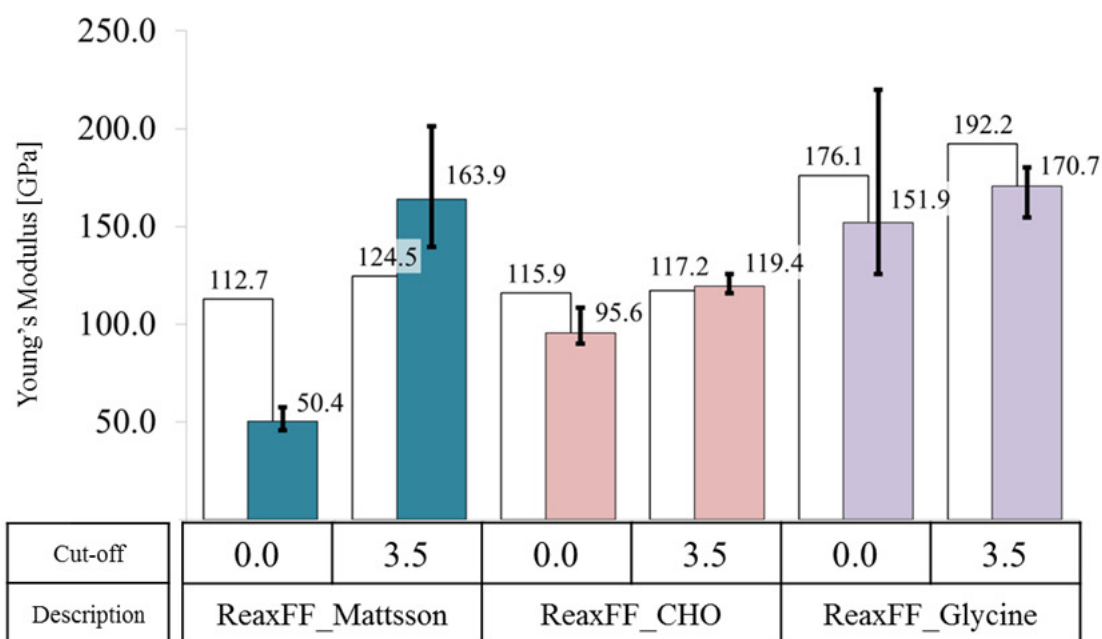
Figure 8-8 Axial Young modulus comparison between crystalline cellulose (white bars in the background) and single chains (colored bars). Young modulus values computed from chain *stiffness* based on an estimated cross sectional area of 31.71Å^2. Error bars obtained from minimum and maximum *stiffness* values reported in Table 8-1.

Figure 8-8 showed that each parameterization produced a distinct and unique behavior. ReaxFF_CHO displayed a ~20GPa difference between chain values and crystalline

values when comparing simulations without hydrogen bonds. It is possible to theorize that this difference was produced by other non-bonded interactions (van der Waals, Coulomb) but the discrepancy vanishes when comparing the same simulations with hydrogen bonds activated. Even more interesting is the fact that ReaxFF_Glycine evidenced roughly the same difference (~20GPa) between single chain and crystal results. In this particular case, the gap remains almost unchanged when hydrogen bonds are added or removed. These results reinforce the theory that other non-bonded interactions were influencing the axial stiffness for the crystal. However, the wide ranges in the error bars for ReaxFF_Glycine make this comparison rather difficult.

Finally, ReaxFF_Mattsson produced curious results; there is a 12 GPa difference when analyzing crystalline simulations with and without hydrogen bonds but almost 115 GPa difference when analyzing the influence of hydrogen bonds in single chains. Moreover, single chain results for simulations that consider hydrogen bonds yield higher values of Young modulus than crystalline simulations under the same condition. These results suggest a change in the intra-chain hydrogen bond pattern when single chains become part of a crystal. Nevertheless, a close inspection of the hydrogen bond pattern obtained in Chapter 7 revealed no differences between intra-chain hydrogen bonds for single chains and hydrogen bonded chains. Figure 8-9 provides this comparison. No plausible explanation can be given for the differences encountered in Figure 8-8 based only in hydrogen bond interactions patterns. It is important to remark that changing the area assumed for a cellulose chain will produce a shift in the Young modulus value reported in Figure 8-8. For this reason, the previous comparison should be considered with caution and regarded only as qualitative.

(a)   (b)
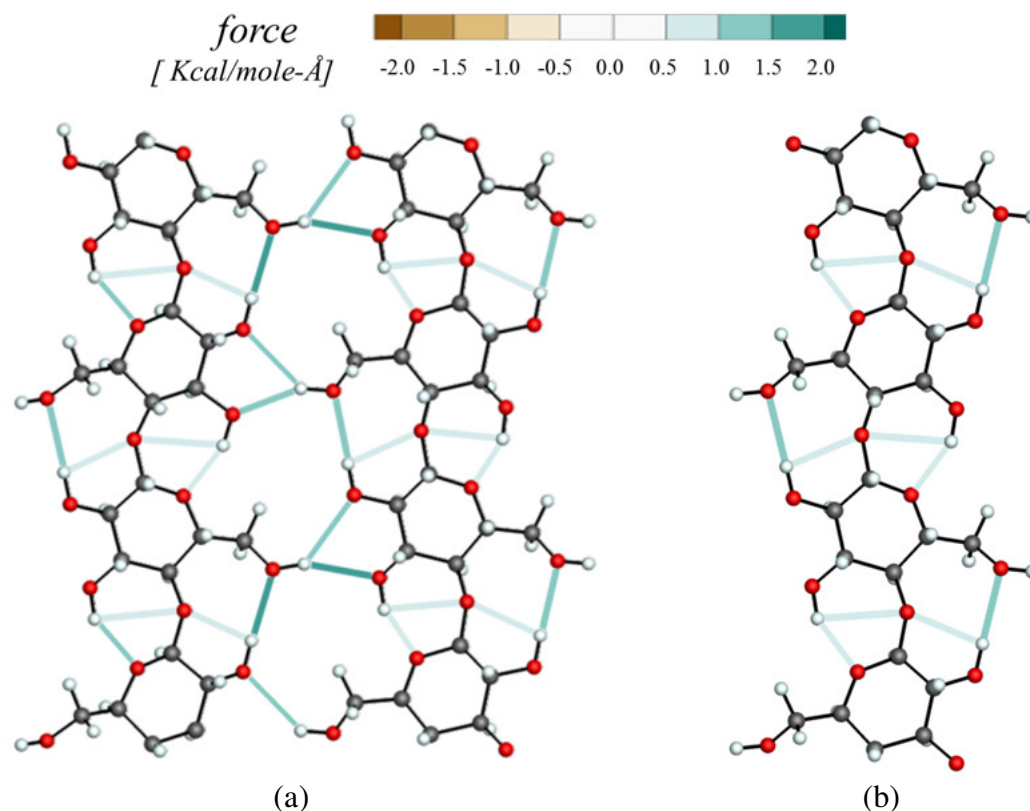
Figure 8-9 Comparison of hydrogen bond force distribution (represented as colored lines) with ReaxFF_Mattsson [145] for (a) SMALL crystalline struture computed in Chapter 7 and (b) a single cellulose chain. Atomistic coordinates that yield the minimum potential energy. Only four glucose ring per chain are being shown. Notice the almost identical inter-chain hydrogen bond patter for both figures.

8.4   Conclusion

Potential energy curves, atom trajectories and hydrogen bond patterns were analyzed for the three different ReaxFF parameterizations under study. The lack of a specific force field parameterization designed for cellulose was evidenced by continue disagreements found between analysis of similar cases.

It was possible to directly correlate hydrogen bonds interactions with the mechanical response of a single cellulose chain. The three parameterizations reported a decrease in the axial stiffness when hydrogen bonds were deactivated showing the reinforcement

capabilities of this particular interaction. Nevertheless, the effect measured was different in each case; ReaxFF_CHO and ReaxFF_Glycine reported small differences in the Young modulus with and without hydrogen bonds (~20 GPa) whereas ReaxFF_Mattsson produced an average difference of more than 110 GPa. It was impossible to justify this result based merely on the understanding of hydrogen bond interactions.

8.5   Notes on bending and torsional stiffness

(a)

(b)
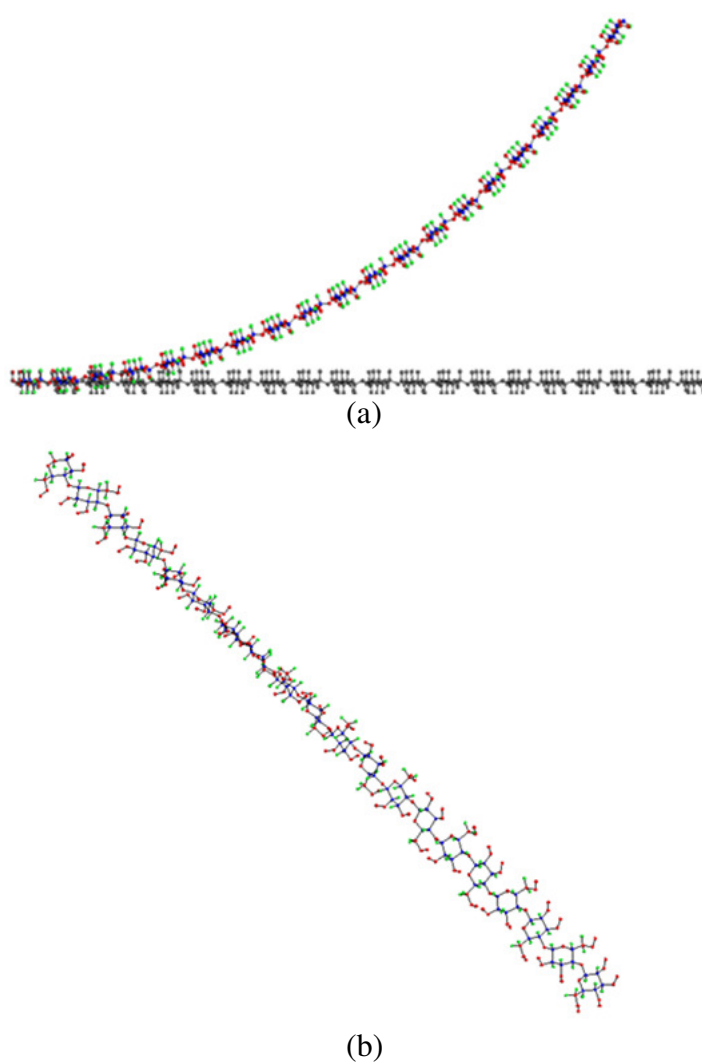
Figure 8-10 Deformation map effects over a single chain for (a) constant curvature bending and (b) twisting. Note that in both cases the length of the chain is kept constant by the deformation map.

The bending and torsional stiffness of cellulose chains are also important mechanical properties that need to be analyzed. A modified version of LAMMPS (details in appendix C) provides the necessary capabilities to compute these two mechanical properties by producing bending and torsional deformations as it can be seen in Figure 8-10.

The extreme deformations observed for a single chain during minimization procedures (Figure 8-3) suggest that the bending and torsional stiffness of the chain are extremely low compared to the axial stiffness. A limited amount of simulations conducted for bending deformation appear to support this assumption. From now one, the bending and torsional stiffness of a single chain will be considered as zero.

CHAPTER 9.   A SIMPLIFIED CONTINUUM MODEL TO UNDERESTAND THE MECHANIZAL RESPONSE OF CELLULOSE NANOCRYSTALS

9.1   Introduction

Understanding the relationship between structure and mechanical properties of cellulose nanocrystals is of paramount importance in the development of theoretical models capable of predicting mechanical responses. The highly complicated crystalline structure of cellulose I_β have made it practically impossible to theoretically calculate the three-dimensional elastic constants [136, 164]. The role of hydrogen bonding has also been controversial. Several studies agreed that intra-molecular hydrogen bond interactions affect the axial Young modulus with reported variations up to 60% [91, 92, 164, 165]. Molecular dynamic simulations presented in previous chapters confirm these results.

In contrast, the effect of inter-molecular hydrogen bond is less clear. Tanaka et al. [136, 166] highlights the importance of inter-chain hydrogen bonds in the axial stiffness. On the other hand, Santiago Cintrón et al. [165] claims that inter-molecular hydrogen bonding does not significantly affect the elongation stiffness of cellulose. Molecular dynamic simulations showed evidence that supports both authors depending on the force field and parameterization being used. For example, ReaxFF_CHO showed no statistical difference between the axial Young modulus of a single chain and the Young modulus of the entire crystal, suggesting no effects produced by inter-chain hydrogen bonds.

Alternatively, ReaxFF_Glycine estimates an average increase in the axial Young modulus of 20 GPa due to inter-chain hydrogen bond interactions.

Reliable calculations that use theoretical strategies could provide insights into the role of inter-chain hydrogen bonds. A simplified continuum model based on linear springs was constructed for such purposes. The objective of this model is to determine if it is theoretically possible for inter-chain hydrogen bonds to increase the stiffness of crystalline cellulose and to quantify the upper limit of that increment. Moreover, the proposed model is independent of any force field parameterization since no atomistic simulations are needed.

9.2   Spring model

A three-step procedure was used to construct the simplified continuum model used in this study. First, the hydrogen bond pattern for inter-chain hydrogen bonds was analyzed and simplified using continuum techniques. Linear springs were used to replace inter-chain hydrogen bond interactions. In the second step, the atomistic representation of cellulose chain was replaced by truss bars with linear axial stiffness. The relative distances between interactions (springs) was kept unchanged. Finally, the system was reduced to one dimension by restricting all lateral displacement. This approximation facilitates focusing the study on the longitudinal direction and is expected not to affect the results. It is worth notice that molecular dynamic simulation under periodic boundary conditions are subjected to the same approximation [136].

The atomistic structure and hydrogen bond pattern used in the analysis have a direct influence over the results as consequence of the applied simplifications. Fortunately, the

crystalline structure of cellulose I$_\beta$ as well as its hydrogen bond pattern has been extensible study [9, 12, 70]. The energetically favorable hydrogen-bond pattern A [13] determined by Nishiyama et al. [9] using X-ray and neutron fiber diffraction is adopted herein. Figure 9-1 shows the characteristic layered structure of crystalline cellulose. Two hydrogen bonded planes with different hydrogen bond patterns coexist inside the crystal [9]. Each plane, regarded as center plane and origin plane, was reduced to a simplified continuum independently. The axial stiffness of the entire crystal resulted from the axial stiffness of each plane multiplied by the number of planes in the system. This approach assumes no hydrogen bond interactions between planes [9, 13, 29, 152, 153].
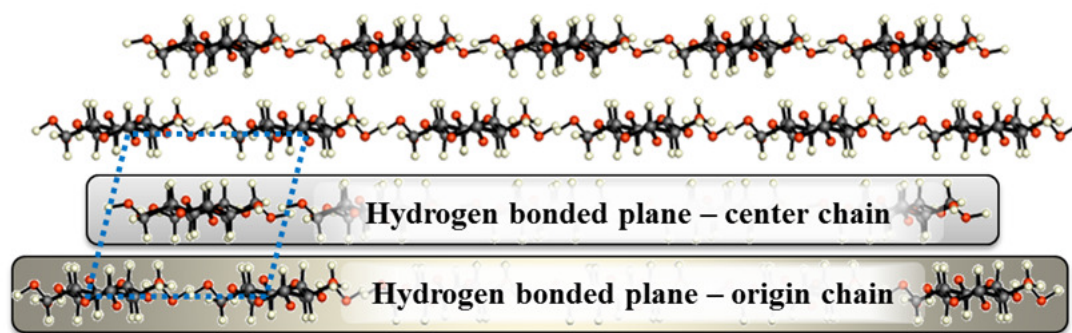
Figure 9-1 Expanded view of the P2$_1$ unit cell structure of the cellulose I$_\beta$ network A showing the characteristic layered conformation. The conformationally different hydrogen bonded planes have been highlighted for the first two layers. The insert in blue dashed lines represent the original unit cell reported by Nishiyama et al. [9].

Schematic representations of the conversion from an atomistic model to a 1D continuum are presented in Figure 9-2 for the center plane and Figure 9-3 for the origin plane. Figure 9-2a shows four inter-chain hydrogen bond interactions connecting each cellulose molecule. The final configuration shown in Figure 9-2c results in four vertical springs with the same stiffness constant: K$_{\text{H-Bond}}$. Each cellulose chain was replaced with a truss element with an axial stiffness: K$_{\text{Chain}}$. The hydrogen bond pattern existing in the origin plane produces interactions that are perpendicular to the longitudinal direction as it can

be seen in Figure 9-3a and Figure 9-3b. As a result, only the stiffness of the cellulose

chain contributes to the stiffness of the plane (Figure 9-3c).

(a)

(b)

(c)
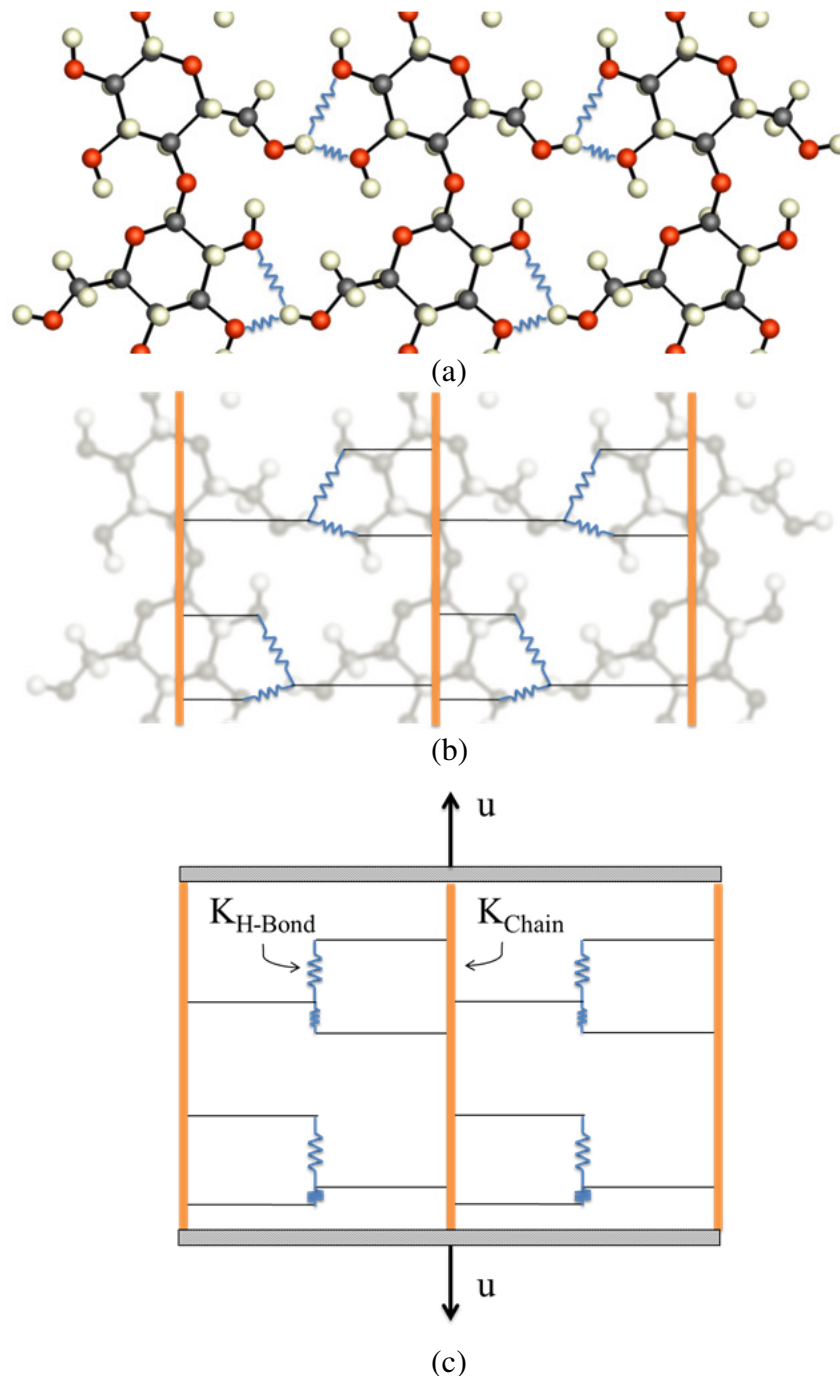
Figure 9-2 Schematic representation of the conversion from an atomistic model to a 1D continuum for a center plane with three cellulose chains (a) Inter-chain hydrogen bonds replaced by linear springs. (b) Cellulose chains replaced by truss members. (c) Reduction of the model to 1D. $K_{H\text{-Bond}}$ has the same value for every spring in the model.
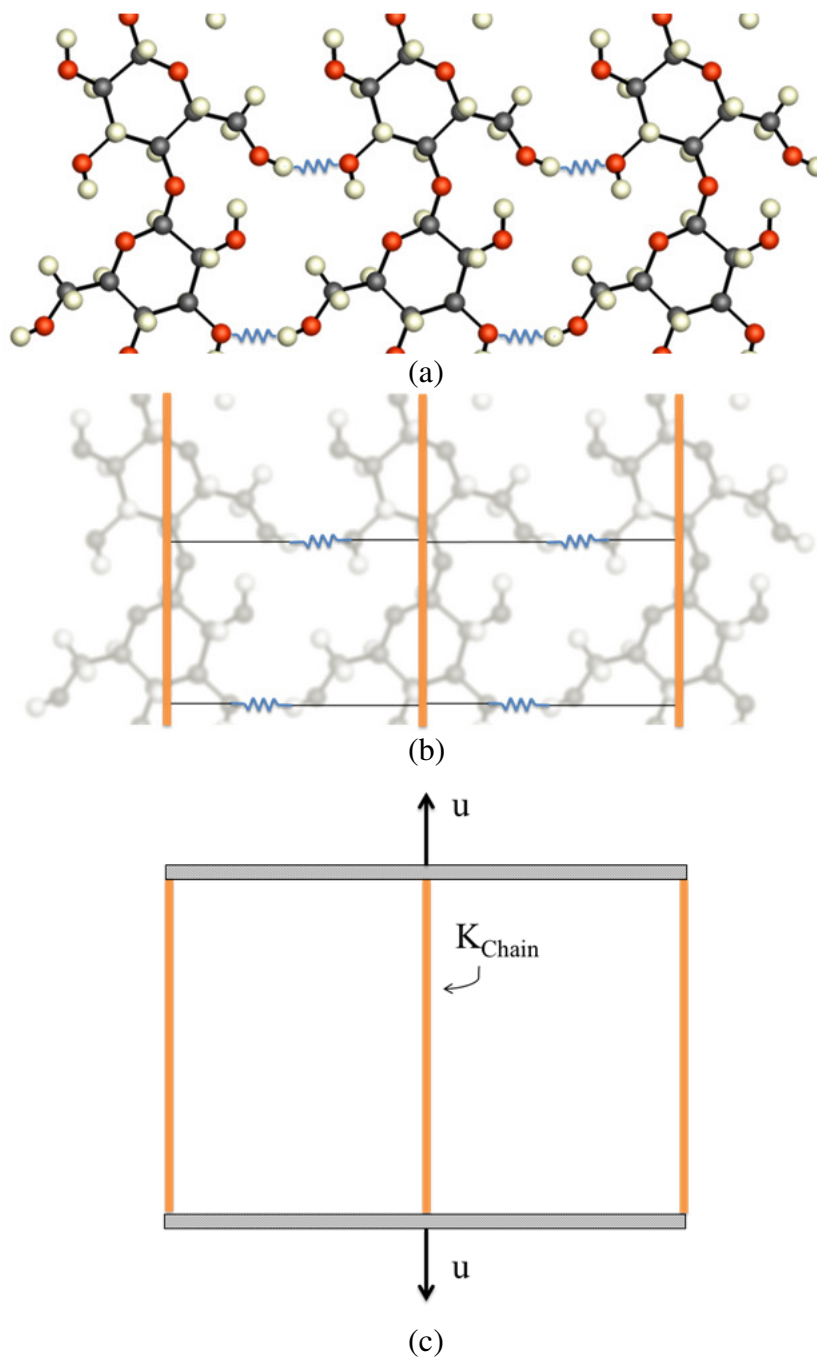
Figure 9-3 Schematic representation of the conversion from an atomistic model to a 1D continuum for a origin plane with three cellulose chains (a) Inter-chain hydrogen bonds replaced by linear springs. (b) Cellulose chains replaced by truss members. (c) Reduction of the model to 1D.

9.3   Computational methodology

The resulting system of springs is too complex to be solved analytically. Maple [167] computer algebra system was used to numerically solve the mathematical model. A change of variables was introduced to simplify the analysis:

$$
\begin{aligned}
K_{Chain} &= k \\
K_{H-Bonds} &= \alpha \times k
\end{aligned}
\tag{14}
$$

Modifications introduced by equation (14) produced two new parameters. The parameter k is equal to the stiffness of a single cellulose chain whereas α represent the ratio of stiffness between hydrogen bonds and a single chain.

The stiffness of an entire crystal is computed as follow: the number of origin and center planes is obtained from the size of the crystal. The number of individual chains in each plane is also considered. The stiffness of each center plane is computed based on the schematic model shown in Figure 9-2c. The stiffness of each origin plane is computed as the stiffness of a chain (k) times the number of chains in the plain. The total stiffness of the crystal results from summation over all planes in the system. The result is a function of the chain stiffness and the ratio α. The total stiffness of the crystal is not of particular interest per se, but it can be used to define the normalized stiffness increment (ΔS) produced by hydrogen bonds as shown in Equation (15).

$$
\Delta S = \left(\frac{K_{Crystal}}{N_{Chains} \times k} - 1 \right) \times 100\%
\tag{15}
$$

Where $K_{Crystal}$ a function of α and k representing the total stiffness of the crystal, N_{Chains} is the total number of cellulose chains in the crystal and k is stiffness of a single chain. The

great advantage of Equation (15) is that by dividing $K_{Crystal}$ by k the normalized stiffness increment (ΔS) becomes only a function of α.

9.4   Results and discussion

The normalized stiffness increment (ΔS) was computed for the array of crystals shown in Figure 9-4. Curves of stiffness increment as a function of the crystalline size for different values of α were condensed in Figure 9-5.

1x1 – 5 chains

2x2 – 13 chains

3x3 – 25 chains

4x4 – 41 chains

5x5 – 61 chains

10x10 – 221 chains
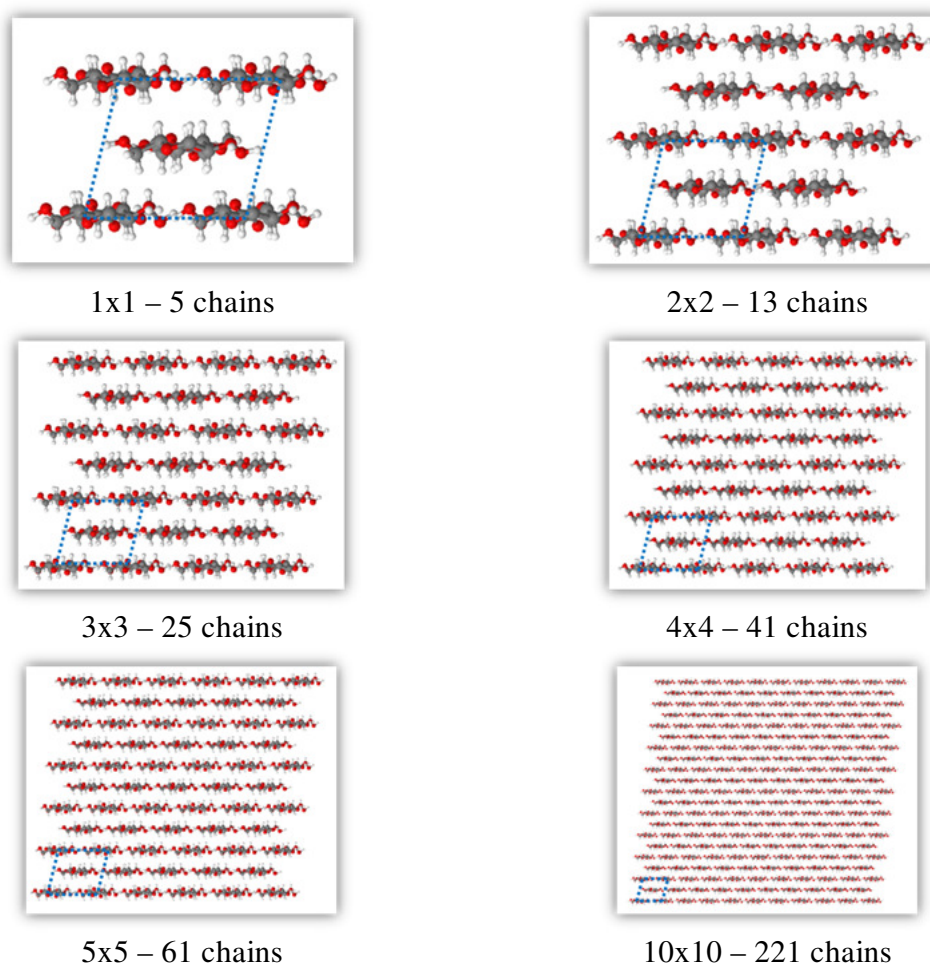
Figure 9-4 Cross-sectional representation of the analyzed crystals. Each model is identified by the number of times a unit cell was repeated in the *a* and *b* crystallographic directions respectively, according to the crystal orientation defined by Nishiyama et al. [9]. The number of chain in each crystal and a schematic representation of a unit cell (blue dashed lines) were added for reference.
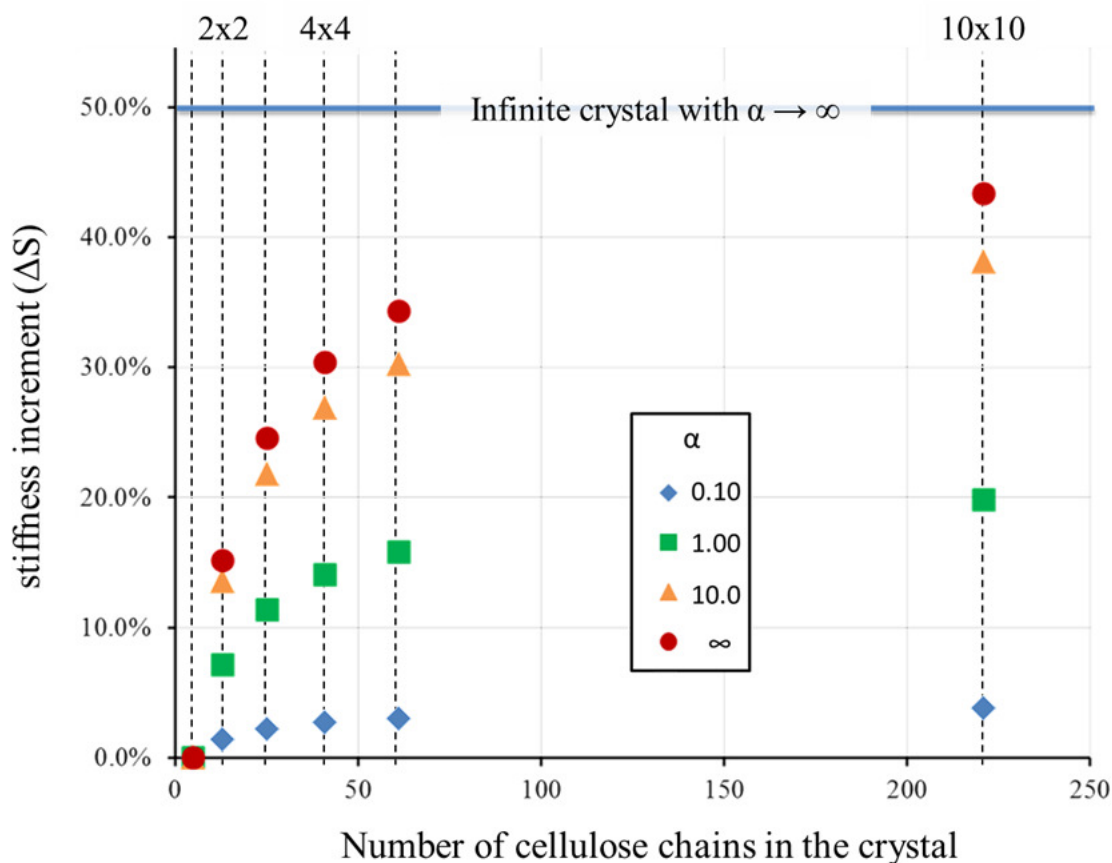
Figure 9-5 Stiffness increment (ΔS) as a function of the crystalline size for different values of α. An upper limit of 50% increment is reached for an infinite crystal (size ∞×∞) with infinitely rigid hydrogen bonds (α = ∞).

The 1x1 crystal has two origin planes and none center planes as it can be observed in Figure 9-4. As a result, the theoretical stiffness of the 1x1 crystal coincides with the stiffness of 5 chains. The normalized stiffness increment due to hydrogen bonding (ΔS) is equal to zero regardless of the value of α as it can be seen in Figure 9-5.

The normalized stiffness increment (ΔS) increases with the size of the crystal till a plateau is reached. This guarantees the existence of an upper limit for the stiffness increment. In the extreme case of infinity cross-section (size ∞×∞) and infinitely rigid

hydrogen bond interactions ($\alpha = \infty$) this study predicts a stiffness increment of 50%. In other words, inter-chain hydrogen bonds can increase the axial stiffness of a crystal with respect to a single chain by 50% at most.

The value of α (ratio of stiffness between hydrogen bonds and a single chain) was computed from molecular dynamic simulation previously presented in Chapter 7 and 8. It is important to remark that the upper limit presented in Figure 9-5 is independent of any atomistic simulation and was obtained based on pure theoretical models.

The stiffness of a single chain (k) was computed in Chapter 8 for different force field parameterizations. A stiffness value of 2.02 Kcal/mole-Å^2 (1.41 N/m) is obtained from the average stiffness over each parameterization for the chain axial stiffness. Previously reported values of hydrogen bond stiffness are an order of magnitude bigger than the computed chain axial stiffness, its value being 40 N/m [158, 168]. These results suggest a ratio of stiffness α equal to ~29. The highest stiffness reported for hydrogen bonds in Chapter 7 was 6 Kcal/mole-Å^2 (4.17 N/m). These results suggest a ratio of stiffness α equal to 3. The average value of stiffness multiplied by the average angle between the longitudinal direction and the hydrogen bond interaction produced an average longitudinal hydrogen bond stiffness of 1.5 Kcal/mole-Å^2. Considering $\alpha = $ ~1 produce an increase up to 20% in the expected axial stiffness for a 5x5 crystal product of inter-chain hydrogen bonding with respect to a single chains. In other words, if the chain's Young modulus is 150 GPa, a 5x5 crystal can reach values up to 180 GPa. A value of $\alpha = $ ~30 is really close to the infinite limit, approaching a 30% increment for a 5x5 crystal. In this case, if the chain's Young modulus is 150 GPa, a 5x5 crystal can reach values up to 195 GPa.

It is important to clarify that the increase in stiffness is based on geometrical considerations, the actual increase in stiffness could be much lower than the values presented here. Nevertheless, the objective of defining an upper limit product of the inter-chain hydrogen bond interactions was accomplished.

9.4.1   Qualitative comparison – Theory vs molecular dynamics

Molecular dynamics simulations are performed to demonstrate part of the previous results. Only inter-chain hydrogen bond interactions and single chain stiffness are being considered in the simplified model. Additional corrections need to take place to compare this results with molecular dynamic simulations. Several non-bonded interactions (Coulomb, van der Waals and intra-chain hydrogen bonds) are being considered when simulating an entire crystal. Moreover, previous analysis for different force field parameterizations showed the presence of inter-chain hydrogen bonds connecting chains that belong to different hydrogen bonded planes. To account for this effect it is necesarry to modify Equation (15) into Equation (16):

$$\Delta S^{MD} = \left[\frac{K^{MD}_{Crystal}}{N_{Chains} \times \left(K^{MD}_{1x1}/5 \right)} - 1 \right] \times 100\% \tag{16}$$

Where $K^{MD}_{Crystal}$ is the stiffness of a crystal computed with molecular dynamic simulations and K^{MD}_{1x1} is the stiffness of a 1x1 crystal computed in the same conditions. By dividing by the stiffness of a 1x1 crystal instead of the stiffness of a single chain it is possible to remove all non-bonded interactions effects except those produced by inter-chain hydrogen bonds present in center planes. This is possible because the 1x1 crystal has 2

origin planes (that do not contribute to the stiffness) and none center planes. A factor of 5

is used to compensate for the stiffness of the five cellulose chains inside the 1x1 crystal.

Only one force field parameterization (ReaxFF_CHO [141]) was analyzed following the

same minimization and stabilization procedure described in Chapter 8. Results are

summarized in Figure 9-6.
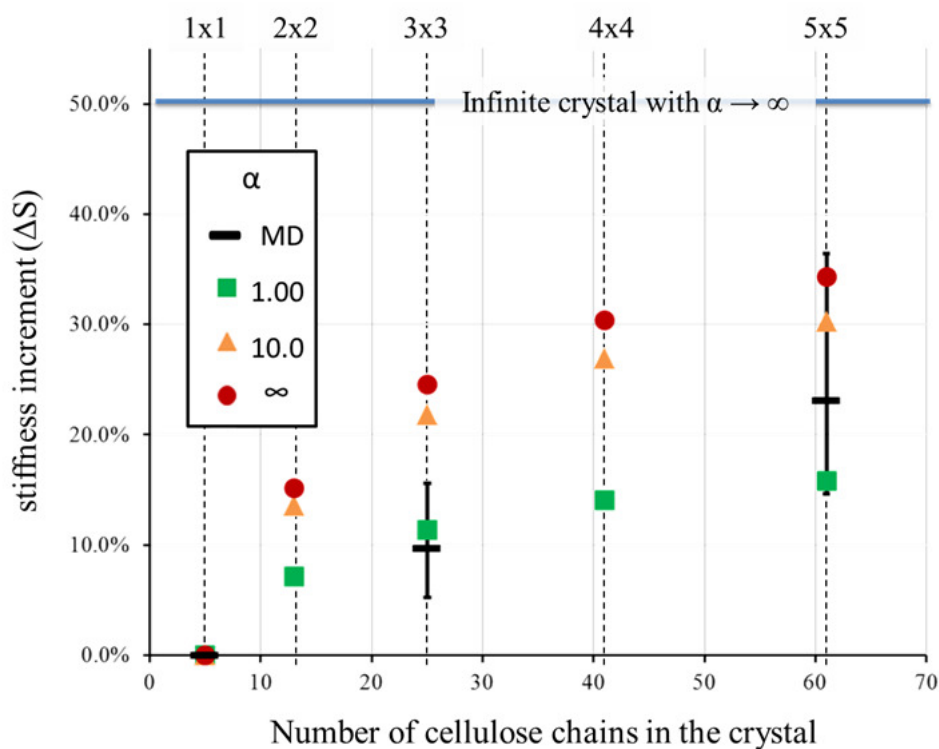
Figure 9-6 Normalized stiffness increment (ΔS) as a function of the crystalline size for different values of α. Molecular dynamics simulations computed using ReaxFF_CHO [141]. Error bars showing minimum and maximum values among all simulations.

The increase in the error bars with the size of the crystal suggests that deformation

mechanisms not present in the small cell are affecting the non-bonded interactions. The

general trend of the average stiffness increment appears to coincide with theoretical

predictions for $\alpha = \sim 1$. Unfortunately, the relatively large error bars make comparison

rather difficult. Moreover, for a 5x5 crystal, the upper limit of the error bar exceeds what was defined as the theoretical maximum for that size. It is important to remind the reader that molecular dynamics results are force field specific whereas the theoretical model is independent of any parameterization.

9.4.2 Crystalline shape and the effect of inter-chain hydrogen bond

The previous section studied the effect of inter-chain hydrogen bonds on square crystals as shown in Figure 9-4. Interesting results can be observed when the shape of the analyzed model changes. The simplifications introduced by the spring model suggest that each origin - hydrogen bonded plane added to the model will increase the stiffness only due to the added chains. On the other hand, each center – hydrogen bonded plane added will contribute with additional stiffness product of hydrogen bond interactions. It is natural to ask if a given crystalline size and shape is better to withstand axial deformations.

Two extreme cases are of particular interest. A column crystal is defined as a crystal constructed by repeating the unit cell only in the *a*-direction as defined by Nishiyama et al. [9]. By doing so, no center – hydrogen bonded planes are generated since only one center chain per unit cell is present in the crystal. As a result, this type of crystal will show no increase in the normalized stiffness increment (ΔS) based on the simplified model.

On the other hand, a row crystal is constructed by repeating a unit cell only in the *b*-direction as defined by Nishiyama et al. [9]. By doing so, each new unit cell added to the crystal will provide additional inter-chain hydrogen bond interactions that increase

the stiffness of the whole. Any crystalline shape can be constructed by applying this scheme as it is shown in Figure 9-7.

It is worth notice that repeating the unit cell in the *a* direction to form column crystals or in the *b* direction to form row crystal will produce models with intrinsically different conformational structures but with the same amount of cellulose chains in them. This generates the ideal conditions to compare stiffness values between them.
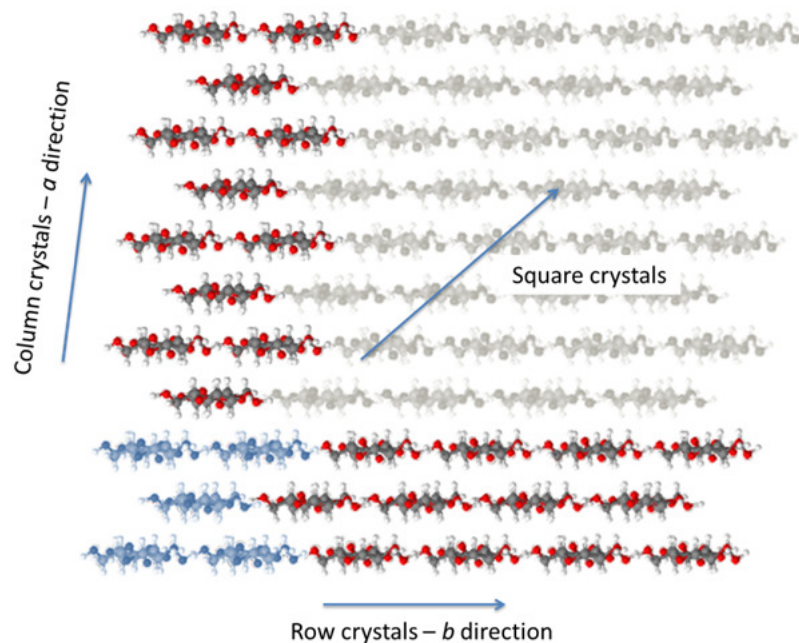
Figure 9-7 Atomistic representations of Row crystals, Square crystals and Column crystals based on the direction used in the repetition of the unit cell (depicted in blue). The unit cell represents a 1x1 crystal, the Row crystal is of the type 1x4, the Column crystal is of the type 4x1 and the square crystal (black and white background) is of the type 4x4.

Figure 9-8 presents a 3D chart with the normalized stiffness increment (ΔS) value as a function of the size and shape of the crystal. Crystalline values form 1x1 to 5x5 are analyzed for $\alpha = \infty$. Trends observed for $\alpha = \infty$ appear to be valid also for lower values of α since only a downscaling effect is detected in the normalized stiffness increment (ΔS)

(see Figure 9-5). Numerical values for normalized stiffness increment (ΔS) and total number of chains as a function of the size of the crystal are presented in Table 9-1 and Table 9-2 respectively.
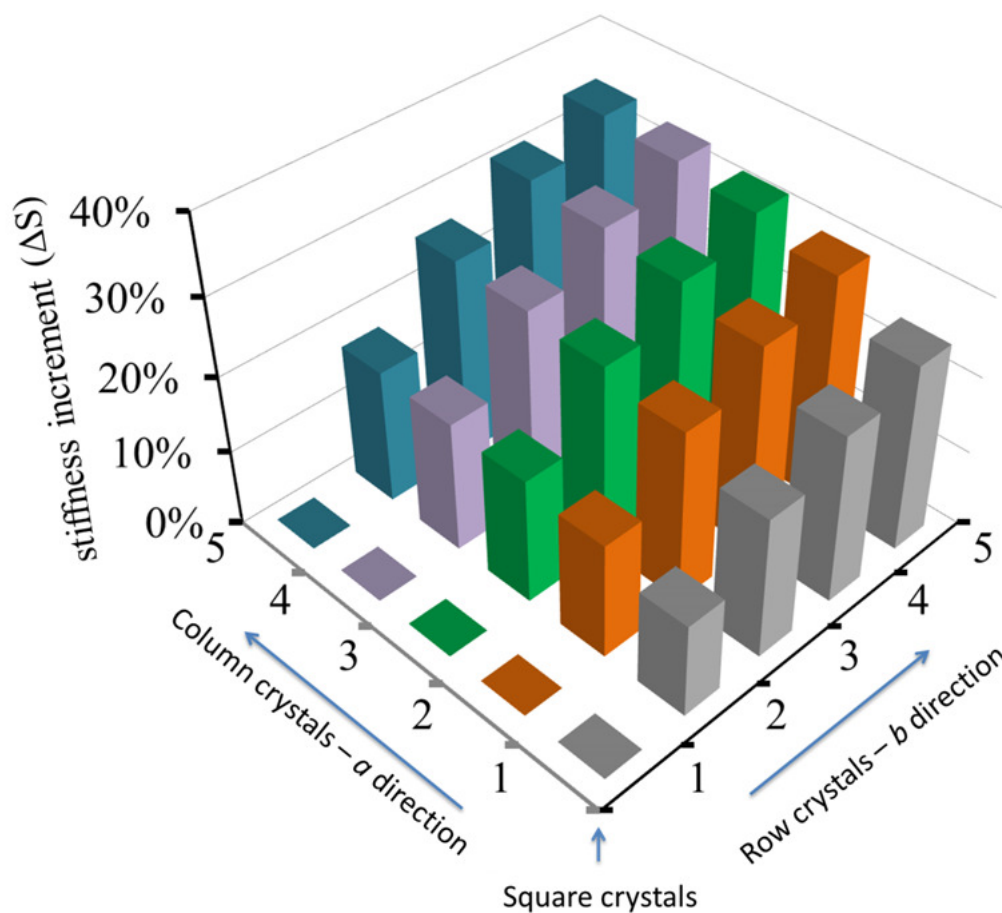
Figure 9-8 Normalized stiffness increment (ΔS) as a function of the crystalline size in the *a* and *b* directions as defined in Figure 9-7. Value of α = ∞. Notice the faster increase in normalized stiffness increment for the *b* direction compared to the *a* direction.

Assuming a given number of chains it is possible to determine which crystalline configuration will yield the best values for normalized stiffness increment (ΔS). For example, with ~24 chains it is possible to build a 3x3 crystal, a 2x4 and a 4x2 all of them containing a similar amount of cellulose chains (see Table 9-2) but different structural

configurations. Based on results presented in Table 9-1, the best possible configuration to withstand axial deformation is obtained with a 2x4 crystal (ΔS = 27.05%) followed by the 3x3 square configuration (ΔS = 24.53%) and ending with the 4x2 shape (ΔS = 17.10%). A similar analysis could be conducted for 32 or 40 chains yielding always more favorable results towards row shaped type of crystals.

Table 9-1 Normalized stiffness increment (ΔS) as a function of the crystalline size in the *a* and *b* directions as defined in Figure 9-7. Value of $\alpha = \infty$. Values for 3x3, 4x4 and similarly shaped crystals are highlighted in green and orange.

		b - direction				
		1	*2*	*3*	*4*	*5*
a-direction	*1*	0.00%	12.29%	18.58%	22.21%	24.61%
	2	0.00%	15.13%	22.71%	27.05%	29.88%
	3	0.00%	16.39%	24.53%	29.16%	32.18%
	4	0.00%	17.10%	25.55%	30.35%	33.46%
	5	0.00%	17.56%	26.20%	31.10%	34.29%

Table 9-2 Total number of chains as a function of the crystalline size in the *a* and *b* directions as defined in Figure 9-7. Values for 3x3, 4x4 and similarly shaped crystals are highlighted in green and orange.

		b - direction				
		1	*2*	*3*	*4*	*5*
a-direction	*1*	5	8	11	14	17
	2	8	13	18	23	28
	3	11	18	25	32	39
	4	14	23	32	41	50
	5	17	28	39	50	61

Based on the aforementioned results, it can be concluded that row shaped type of crystals have a theoretical advantage withstanding axial deformations compared to other shapes that contain the same amount of cellulose chains. This assumption is based purely on mechanical observations. It is worth notice that the stacking direction in crystalline

cellulose (*a*-direction) is governed by van der Waals interactions that were not taking in account in the simplified model.

9.5   Conclusion

A simplified continuum model was developed to analyze the role of inter-chain hydrogen bonding in the axial mechanical response of cellulose nanocrystals. This very simple approximation proved that inter-chain hydrogen bond interactions can increase the axial stiffness of a cellulose crystal and could potentially define the crystalline shape and size. The exact increase value could not be obtained without recurring to molecular dynamic simulations that depend on force field parameterizations. Nevertheless, an upper bound for the stiffness increment was obtained and reported. Considering $\alpha = \sim 1$ produce an increase up to 20% in the expected axial stiffness for a 5x5 crystal product of inter-chain hydrogen bonding with respect to a single chains. In other words, if the chain's Young modulus is 150 GPa, a 5x5 crystal can reach values up to 180 GPa. A value of $\alpha = \sim 30$ generates a 30% increment for a 5x5 crystal. In this case, if the chain's Young modulus is 150 GPa, a 5x5 crystal can reach values up to 195 GPa. Molecular dynamic simulations using ReaxFF_CHO parameterization were used to compare with the theoretical model producing good agreement in the range analyzed.

Size and shape effects were study using the theoretical model to predict the structural configuration that produced the biggest increase in the normalized stiffness increment (ΔS). Row shaped crystals proved to be better suitable for withstand axial loading when compared to other shapes that contain the same number of cellulose chains.

Changes in lateral stiffness product of inter-chain hydrogen bond interactions were not analyzed in this chapter. The structural arrangement shown in Figure 9-3a and b suggest an important role of this type of interactions making them worth of study.

CHAPTER 10. FINAL ELEMENT REPRESENTATION OF CELLULOSE NANOCRYSTALS

10.1 Introduction

Multiscale modeling have been particularly useful for polymers and biological materials where the characteristics of the system make it impossible to utilize full atomistic representations [169]. To access larger time and length scales, molecular models must be simplified or coarse-grained (CG) in such a way as to preserve only the degrees of freedom responsible for the macroscopic properties of interest [43]. Interactions between atoms are replaced by interaction between CG units dramatically decreasing the amount of degrees of freedom in the model. There is no unique way to formulate a CG model. In extreme cases, a whole molecule can be represented by a single particle and interactions between particles incorporate average properties of the whole molecule [170]. With this approach, the number of degrees of freedom is reduced practically to a minimum. This process results in a speed-up of simulation times by several orders of magnitude. Not surprisingly, the application of such methods to study entirely new problems of biological importance has been rapidly gaining increased attention in the biomolecular simulation community [169].

The first and most simple coarse-grained model is the 'dumbbell' model [171]. Molecules are treated as a pair of beads interacting via a harmonic potential. Using this model, it is possible to perform kinetic theory derivations and calculations for nonlinear rheological properties and flow problems. Modeling chain-like macromolecules, such as cellulose, require more advance models; the bead-rod and bead-spring model are available for this purpose. Beads in the bead-rod model do not represent the atoms of the polymer chain backbone, but some portion of the chain, normally 10 to 20 monomer units. These beads are connected by rigid and massless rods. While in the bead-spring model, a portion of the chain containing several hundreds of backbone atoms are replaced by a "spring" and the masses of the atoms are concentrated in the mass of beads [170]. Even though they can be consider as very simple models, different variations of coarse grained techniques have been used to simulate all kinds of bimolecular systems (i.e., RNA, DNA [172]). One of the existing limitations in the CG models previously described is that, in general, beads are considered as rigid-bodies. The deformation of the system can only occur at the links (springs). As a result, the model force localization of deformation based on the position and size of the representation being used. Successfully representing crystalline cellulose with a coarse grained model will require a different approach.

Virtually every phenomena in nature, whether biological, geological or mechanical can be described in terms of algebraic, differential or integral equations based on physical laws. A complete understanding of the physical processes involved in a given system is required to build its mathematical model. The formulation results often in differential or integral equations relating quantities of interest [61]. While the derivation of the governing equations for most problems is not a trivial task, their solution by exact

methods of analysis is generally not possible. The finite element method overcomes this problem by providing a systematic procedure for the derivation of an approximate solution over a given domain. Three basic features give the finite element method (FEM) a clear advantage over other methods. First, a geometrically complex domain of the problem is represented as a collection of geometrically simple subdomains, called finite elements. A collection of finite elements is called mesh. Second, each finite element is represented mathematically by approximation functions derived using the basic idea that any continuous field can be represented as a linear combination of algebraic polynomials. Third, the algebraic relations needed to solve the undetermined coefficients (i.e., nodal displacements, nodal temperatures) are obtained by satisfying the governing equations over each element.

The power of the FEM resides principally in its versatility, the method can be applied to various physical problems. The body analyzed can have arbitrary shape, loads and support conditions. The mesh can mix elements of different types, shapes and physical properties [173]. This great versatility is contained within a single computer program which gives an incredible advantage from the user's point of view. The finite element method also has disadvantages, for example, a specific numerical result is found for a specific problem. A finite element analysis provides no closed-form solution that permits analytical study of the effect of changing various parameters.

The finite element method and the coarse graining approach were combined to develop a continuum model for cellulose nanocrystals. The continuum based multiscale model is constructed based on the hypothesis that bonded and non-bonded interactions can be decoupled. Bonded interactions determine the cellulose chain behavior whereas non-

bonded interactions define inter-chain behavior (i.e., size of the crystal and lattice parameters). The response of the crystal as a whole arises from the mutual work of these two mechanisms. These hypotheses were consistently proven trough different simulations presented in Chapters 4 to 8 and theoretically based results obtained in Chapter 9.

The following subsections describe the derivations of the formulation being used in the continuum model. Relations between atomistic based simulations and the continuum formulation are also explained.

10.2   Beam element: modeling a single cellulose chain

The first step in modeling cellulose nanocrystals involves the mathematical description of a single chain. Extensive analyses have been done on single cellulose chains using atomistic simulations. The mechanical response under tension, bending and torsion has been studied providing the information needed to develop a continuum representation. A three dimensional Euler-Bernoulli beam element was specially modified to accommodate the needs of cellulose chains.

Beam elements are slender members capable of supporting axial and transverse loading [174]. In the FEM framework, beams are considered to be one of the most basic structural elements. However, several types of elements with increasingly complexity have been developed. Nowadays, beam elements can be found in FEM codes ranging from 2D symmetric linear elements to 3D finite deformation – co-rotational formulations [175].

The first challenge encountered when adapting the atomistic representations to the continuum formulation is the definition of geometrical and material properties: area (A),

cross sectional shape, moment of inertia (I, J), Young modulus (E) and Poisson's ratio (ν) are not uniquely determined for atomistic systems in general [162]. The use of a special developed beam element allows completely avoiding those definitions without losing simulation capabilities.

A 2-node – 6 degrees of freedoms (d.o.f.) – 3D beam element was developed on the basis that it is not possible to isolate section properties (A, I, J) from material properties (E, G). The element was formulated under small deformation hypothesis, allowing decoupling of axial, bending and twisting deformations. There is no coupling between deformation in different planes and shear is neglected accordingly to Euler-Bernoulli equations.
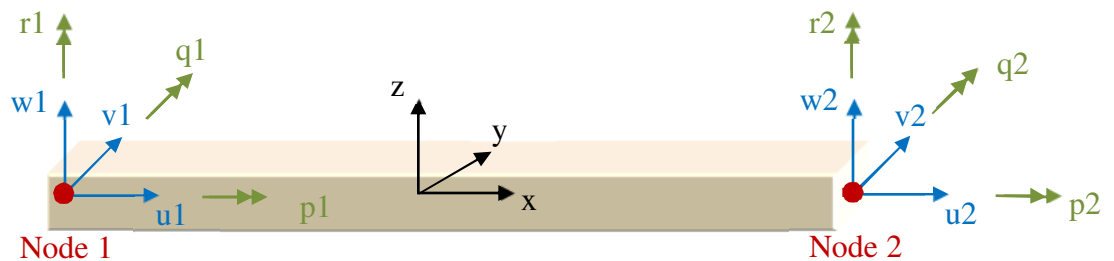
Figure 10-1 Schematic representation of a 2 node – 6 d.o.f. – 3D beam element. All the active degrees of freedom are explicitly shown in each node. The arrows indicate a positive value of deformation / rotation according to the local system of coordinates shown in the figure.

The 3D Euler Bernoulli beam element has been extensible studied [61, 173, 174, 176, 177]. Only the most important concepts are shown to avoid excessively large mathematical derivations. By using equilibrium equations it is possible to obtain four major differential equations that govern the response of the 3D linear beam element.

-Axial deformation (*u1, u2*):

$$EA\frac{d^2u}{dx^2} = 0 \qquad (17)$$

- Bending deformation in the X-Y plane (*v1, r1, v2, r2*):

$$\frac{d^2}{dx^2}\left[EI_{11}\frac{d^2v}{dx^2}\right] = 0 \qquad (18)$$

- Bending deformation in the X-Z plane (*w1, q1, w2, q2*):

$$\frac{d^2}{dx^2}\left[EI_{22}\frac{d^2w}{dx^2}\right] = 0 \qquad (19)$$

- Twisting deformation (*p1, p2*):

$$GJ\frac{d^2p}{dx^2} = 0 \qquad (20)$$

It is worth noticing that the four parameters that define the stiffness of the system always appear in pairs (EA, EI_{11}, EI_{22}, GJ) and in completely different equations. This apparently simple finding outlines the basis of the entire approach utilized to model CNC from a continuum point of view. Molecular dynamic simulations provide the values of those four stiffness constants (geometry + material) without any assumption over the geometry or material properties of a single chain. Reconstructing the beam equations taking care of never separating those four groups will generate a formulation that does not need individual information about the material or the section being analyzed.

The beam element formulation can be summarized as a stiffness matrix, Equation (21), and a force vector, Equation (22), that combined define the elastic behavior of the single cellulose chain.

$$[K_e] = \begin{bmatrix}
\frac{EA}{l_e} & 0 & 0 & 0 & 0 & 0 & \frac{-EA}{l_e} & 0 & 0 & 0 & 0 & 0 \\
0 & \frac{12EI_{11}}{l_e^3} & 0 & 0 & 0 & \frac{6EI_{11}}{l_e^2} & 0 & \frac{-12EI_{11}}{l_e^3} & 0 & 0 & 0 & \frac{6EI_{11}}{l_e^2} \\
0 & 0 & \frac{12EI_{22}}{l_e^3} & 0 & \frac{-6EI_{22}}{l_e^2} & 0 & 0 & 0 & \frac{-12EI_{22}}{l_e^3} & 0 & \frac{-6EI_{22}}{l_e^2} & 0 \\
0 & 0 & 0 & \frac{GJ}{l_e} & 0 & 0 & 0 & 0 & 0 & \frac{-GJ}{l_e} & 0 & 0 \\
0 & 0 & \frac{-6EI_{22}}{l_e^2} & 0 & \frac{4EI_{22}}{l_e} & 0 & 0 & 0 & \frac{6EI_{22}}{l_e^2} & 0 & \frac{2EI_{22}}{l_e} & 0 \\
0 & \frac{6EI_{11}}{l_e^2} & 0 & 0 & 0 & \frac{4EI_{11}}{l_e} & 0 & \frac{-6EI_{11}}{l_e^2} & 0 & 0 & 0 & \frac{2EI_{11}}{l_e} \\
\frac{-EA}{l_e} & 0 & 0 & 0 & 0 & 0 & \frac{EA}{l_e} & 0 & 0 & 0 & 0 & 0 \\
0 & \frac{-12EI_{11}}{l_e^3} & 0 & 0 & 0 & \frac{-6EI_{11}}{l_e^2} & 0 & \frac{12EI_{11}}{l_e^3} & 0 & 0 & 0 & \frac{-6EI_{11}}{l_e^2} \\
0 & 0 & \frac{-12EI_{22}}{l_e^3} & 0 & \frac{6EI_{22}}{l_e^2} & 0 & 0 & 0 & \frac{12EI_{22}}{l_e^3} & 0 & \frac{6EI_{22}}{l_e^2} & 0 \\
0 & 0 & 0 & \frac{-GJ}{l_e} & 0 & 0 & 0 & 0 & 0 & \frac{GJ}{l_e} & 0 & 0 \\
0 & 0 & \frac{-6EI_{22}}{l_e^2} & 0 & \frac{2EI_{22}}{l_e} & 0 & 0 & 0 & \frac{6EI_{22}}{l_e^2} & 0 & \frac{4EI_{22}}{l_e} & 0 \\
0 & \frac{6EI_{11}}{l_e^2} & 0 & 0 & 0 & \frac{2EI_{11}}{l_e} & 0 & \frac{-6EI_{11}}{l_e^2} & 0 & 0 & 0 & \frac{4EI_{11}}{l_e}
\end{bmatrix} \quad (21)$$

$$\{f_e\}^T = \{P_1 \quad Q_1^{xy} \quad Q_1^{xz} \quad T_1 \quad M_1^{xz} \quad M_1^{xy} \quad P_2 \quad Q_2^{xy} \quad Q_2^{xz} \quad T_2 \quad M_2^{xz} \quad M_2^{xy}\} \quad (22)$$

It is important to remark that the length of the cellulose chain and its relation to the length of the beam element (l_e) was never used in the development of Equations (21) and (22). As a result, the coarse graining parameter (cgp), number of glucose rings being represented by each finite element, is a free variable that can be defined by the user based on experimentation and observation.

Large rotations, especially under torsion and bending, have been observed in many atomistic simulations of free standing single chains. Although the current implementation of a 3D beam element is limited to small deformations, an extension to large rotations is possible and a topic for future development.

10.3 Hydrogen bond element: modeling inter-chain hydrogen bond interactions

A continuum representation of hydrogen bonds is needed to model cellulose nanocrystals using FEM. Hydrogen bond interaction occurring between atoms that belong to the same chain (intra-chain hydrogen bonds) are already considered in the beam element previously developed. Inter-chain hydrogen bond can occur between chains that belong to the same hydrogen-bonded plane or connecting chains that belong to different planes as it can be seen in Figure 10-2. A generic formulation, capable of representing both types of situations was developed.

(a)   (b)   (c)

(d)   (e)
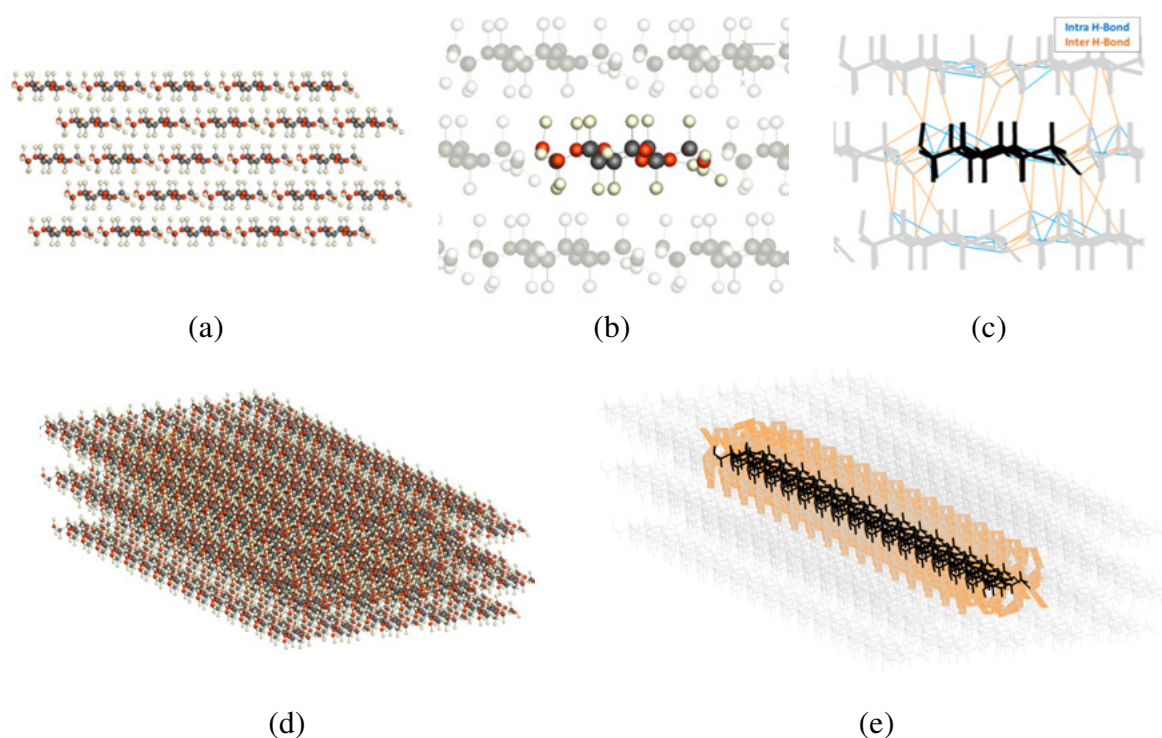
Figure 10-2 (a) 2D atomistic representation of a CNC. (b) Isolation of single cellulose chain inside the crystal. (c) Schematic representation of all possible hydrogen bond interactions for a given chain. (d) 3D atomistic representation of a CNC. (e) Schematic representation of inter-chain hydrogen bonds of an interior chain. The number of hydrogen bonds formed depends on the force field parameterization, figures only for illustration purposes.

Hydrogen bond elements will be used to connect several of the previously defined beam elements. A compatibility requirement must be satisfied between these two elements. Nodal displacements and rotations, at the shared nodes, must be equal for both elements. Schematics of the transition from atomistic to continuum representation for the hydrogen bond element are shown in Figure 10-4.

(a)

(b)

(c)

(d)
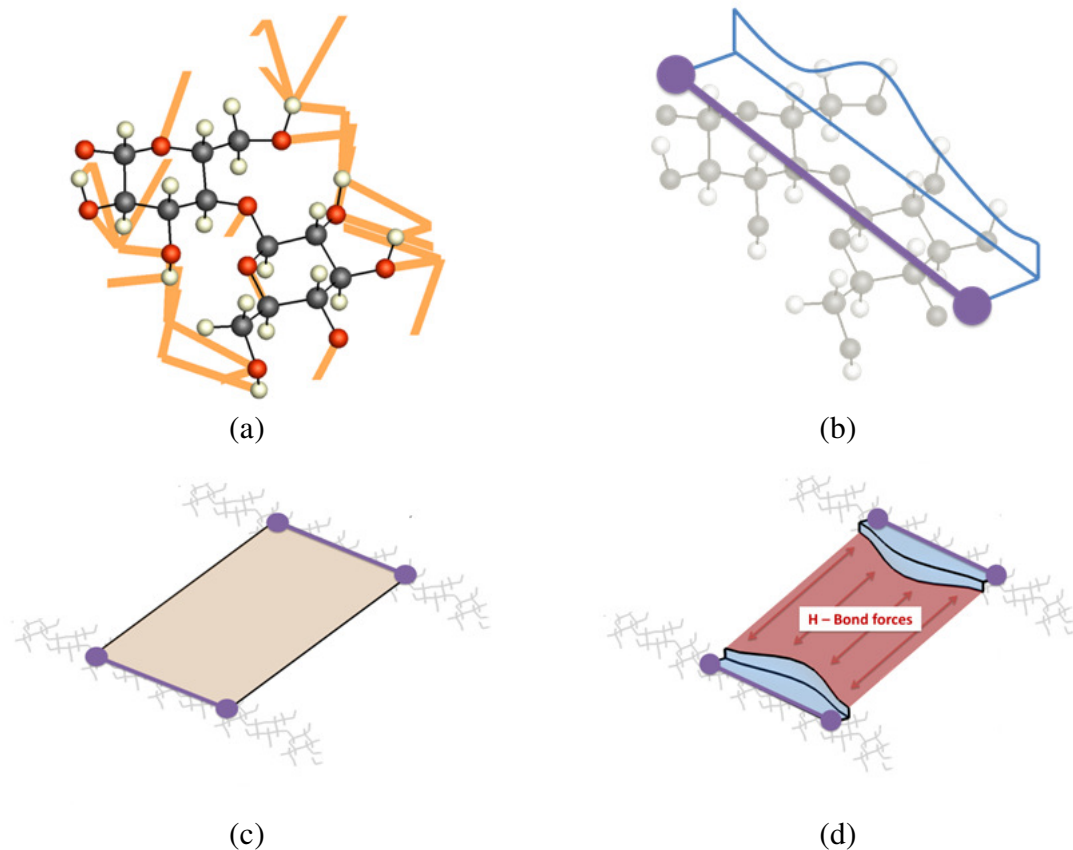
Figure 10-3 Schematics of the transition from atomistic to continuum representation for the hydrogen bond element. Internal description of the hydrogen bond element. Each panel reveals different levels of detail. (a) Representation of inter-chain hydrogen bonds for two glucose rings. (b) Conversion into a beam element (purple) and estimation of the hydrogen bond virtual surfaces (blue). (c) Numerical representation of the hydrogen bond element (membrane connecting 4 nodes). (d) Insides of the hydrogen bond element showing the continuum representation of hydrogen bond forces (red surface).
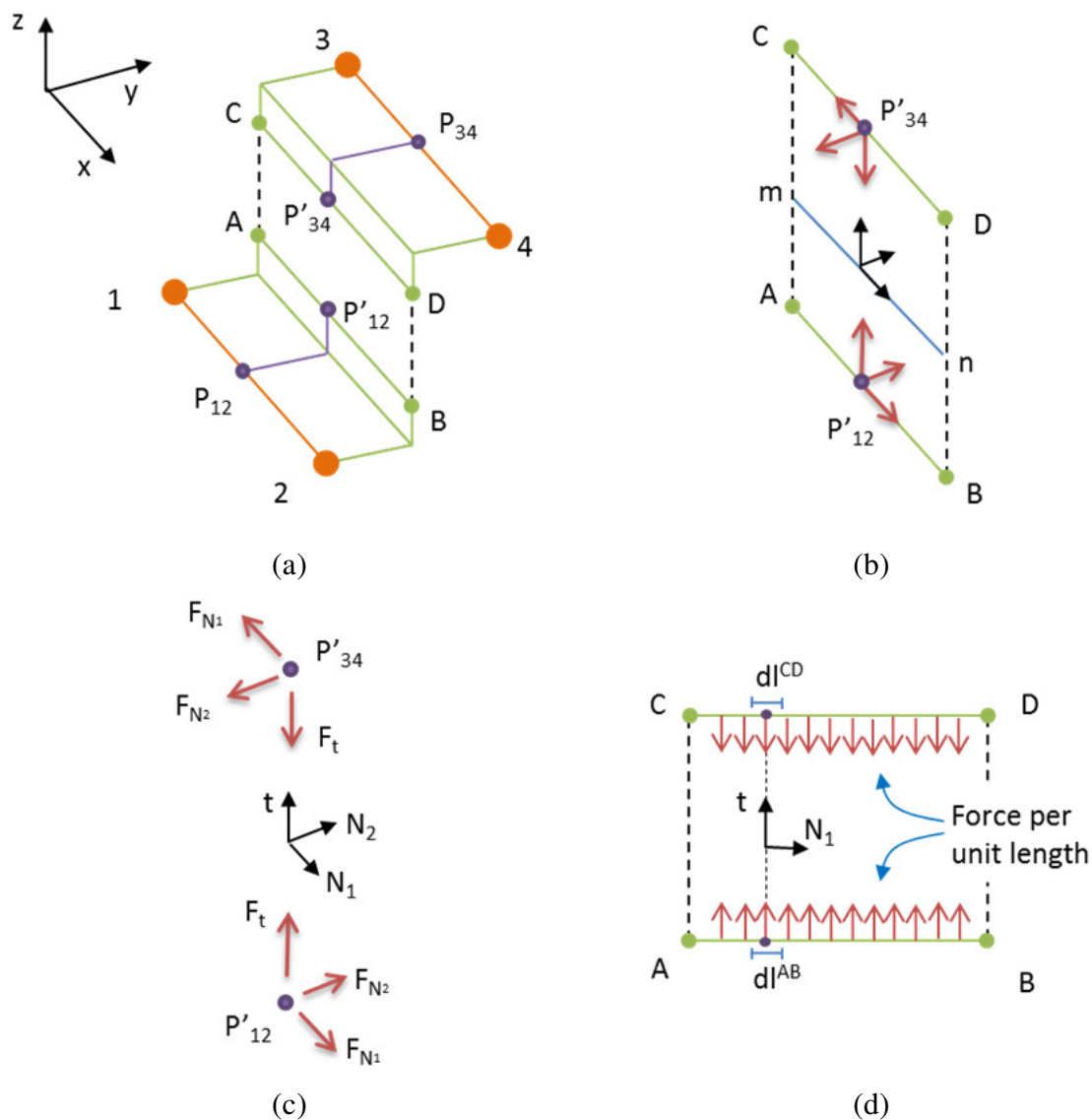
Figure 10-4 Internal description of the hydrogen bond element. Each panel reveals different levels of detail. (a) Hydrogen bond element connecting two beam elements (orange lines), virtual surfaces replacing atomic coordinates in green, generic points inside the surface in purple. (b) Integration line mn (in blue) and schematic representation of forces for a generic point P'. (c) Local coordinate system and detailed representation of forces acting over a generic point P'. (d) 2D representation of distributed forces acting over the virtual surfaces AB and CD.

The principle of virtual work was used to derive the governing differential equations.

Equation (23) defines the internal virtual work as:

$$\delta W_I = -f_I \times \delta u \tag{23}$$

Where f_I represents internal forces and δu displacements. The infinitesimal virtual work can be expanded as:

$$d\delta W_I = -\Big[\ \Big(F_t \times dl^{AB} \times \delta u^t_{P'_{12}} - F_t \times dl^{CD} \times \delta u^t_{P'_{34}}\Big)$$
$$+ \Big(F_{N_1} \times dl^{AB} \times \delta u^{N_1}_{P'_{12}} - F_{N_1} \times dl^{CD} \times \delta u^{N_1}_{P'_{34}}\Big) \qquad (24)$$
$$+ \Big(F_{N_2} \times dl^{AB} \times \delta u^{N_2}_{P'_{12}} - F_{N_2} \times dl^{CD} \times \delta u^{N_2}_{P'_{34}}\Big) \Big]$$

Where forces and directions correspond to Figure 10-4. The internal virtual work can be computed by integrating Equation (24) over the virtual surfaces AB and CD (see Figure 10-4d)

$$\delta W_I = \int_C^D \Big(F_t \times \delta u^t_{P'_{34}} + F_{N_1} \times \delta u^{N_1}_{P'_{34}} + F_{N_2} \times \delta u^{N_2}_{P'_{34}}\Big) \times dl^{CD}$$
$$- \int_A^B \Big(F_t \times \delta u^t_{P'_{12}} + F_{N_1} \times \delta u^{N_1}_{P'_{12}} + F_{N_2} \times \delta u^{N_2}_{P'_{12}}\Big) \times dl^{AB} \qquad (25)$$

Whereas the forces F_t, F_{N1} and F_{N2} can be computed as:

$$F_t = K_t \times \Big(u^t_{34} - u^t_{12}\Big)$$
$$F_{N_1} = K_{N_1} \times \Big(u^{N_1}_{34} - u^{N_1}_{12}\Big) \qquad (26)$$
$$F_{N_2} = K_{N_2} \times \Big(u^{N_2}_{34} - u^{N_2}_{12}\Big)$$

With K_x : stiffness factor in the x direction (not necessarily constant) and u^x_{yz} : displacement of the point P'_{yz} in the direction x. Moving the integration line from AB and CD to mn (Figure 10-4b) simplifies Equation (25) as:

$$\delta W_I = \int_m^n \Big(\delta \Delta u^t \times K_t \times \Delta u^t + \delta \Delta u^{N_1} \times K_{N_1} \times \Delta u^{N_1} + \delta \Delta u^{N_2} \times K_{N_2} \times \Delta u^{N_2}\Big) \times S \times dl^{mn} \qquad (27)$$

With S being a correction factor for the change in the integration interval and Δu^x computed as: $\Delta u^x = u^x_{34} - u^x_{12}$.

Finally, the integration domain in changed from [m,n] to [-1,1] to facilitate the use of numerical integration:

$$\delta W_I = \frac{l_{mn} \times S}{2} \int_{-1}^{1} \left(\delta \Delta u^t \times K_t \times \Delta u^t + \delta \Delta u^{N_1} \times K_{N_1} \times \Delta u^{N_1} + \delta \Delta u^{N_2} \times K_{N_2} \times \Delta u^{N_2} \right) \times d\zeta \quad (28)$$

The final form presented in Equation (28) is remarkable simple but the calculation of the relative displacements: Δu^t, Δu^{N1} and Δu^{N2} proved to be extremely challenging. These values depend upon the exact configuration of the virtual surfaces used to represent hydrogen bonded atoms and need to be computed based only on nodal displacements. Only the most fundamental relations will be presented in this document in an attempt to avoid overwhelming the reader with unnecessary details. The relative displacements can be computed as:

$$\Delta u^{N_1} = \Delta N_1 = \left[B_{N_1} \right]_{1x24} \{U\}_{24x1} = \left[\left. \frac{\partial \Delta N_1}{\partial u_1} \right|_0 \quad \left. \frac{\partial \Delta N_1}{\partial v_1} \right|_0 \quad \left. \frac{\partial N_1}{\partial w_1} \right|_0 \quad \cdots \quad \left. \frac{\partial N_1}{\partial p_4} \right|_0 \quad \left. \frac{\partial N_1}{\partial q_4} \right|_0 \quad \left. \frac{\partial N_1}{\partial r_4} \right|_0 \right] \begin{Bmatrix} u_1 \\ v_1 \\ w_1 \\ \vdots \\ p_4 \\ q_4 \\ r_4 \end{Bmatrix} \quad (29)$$

$$\Delta u^t = \Delta t = \left[B_t \right]_{1x24} \{U\}_{24x1} = \left[\left. \frac{\partial \Delta t}{\partial u_1} \right|_0 \quad \left. \frac{\partial \Delta t}{\partial v_1} \right|_0 \quad \left. \frac{\partial \Delta t}{\partial w_1} \right|_0 \quad \cdots \quad \left. \frac{\partial \Delta t}{\partial p_4} \right|_0 \quad \left. \frac{\partial \Delta t}{\partial q_4} \right|_0 \quad \left. \frac{\partial \Delta t}{\partial r_4} \right|_0 \right] \begin{Bmatrix} u_1 \\ v_1 \\ w_1 \\ \vdots \\ p_4 \\ q_4 \\ r_4 \end{Bmatrix} \quad (30)$$

$$\Delta u^{N_2} = \Delta N_2 = \left[B_{N_2} \right]_{1x24} \{U\}_{24x1} = \left[\left. \frac{\partial \Delta N_2}{\partial u_1} \right|_0 \quad \left. \frac{\partial \Delta N_2}{\partial v_1} \right|_0 \quad \left. \frac{\partial N_2}{\partial w_1} \right|_0 \quad \cdots \quad \left. \frac{\partial N_2}{\partial p_4} \right|_0 \quad \left. \frac{\partial N_2}{\partial q_4} \right|_0 \quad \left. \frac{\partial N_2}{\partial r_4} \right|_0 \right] \begin{Bmatrix} u_1 \\ v_1 \\ w_1 \\ \vdots \\ p_4 \\ q_4 \\ r_4 \end{Bmatrix} \quad (31)$$

Where [B] are derivative matrices and {U} is the displacement vector containing displacement and rotations for the 24 d.o.f. related to the hydrogen bond element. As a result, Equation (28) could be rewriting as:

$$\delta W_I = \{\delta U\}^T \left[\frac{l_{mn} \times S}{2} \int_{-1}^{1} \left(\left[B_t \right]^T K_t \left[B_t \right] + \left[B_{N_1} \right]^T K_{N_1} \left[B_{N_1} \right] + \left[B_{N_2} \right]^T K_{N_2} \left[B_{N_2} \right] \right) d\zeta \right] \{U\} \quad (32)$$

By doing so, it is possible to shift the problem from computing Δu to obtaining the derivative matrices [B]. A matrix form was developed to compute the value of B_t, B_{N1} and B_{N2} for each d.o.f.. The process needs to be repeated 24 times at each integration point to complete the B matrices. Equation (33) shows the matrix form previously mentioned for a generic degree of freedom xx:

$$\begin{Bmatrix} \left. \frac{\partial \Delta N_1}{\partial xx} \right|_0 \\ \left. \frac{\partial \Delta t}{\partial xx} \right|_0 \\ \left. \frac{\partial \Delta N_2}{\partial xx} \right|_0 \end{Bmatrix} = \left[\lambda_1 \right] \left[\lambda_{34} \right]^T \left(\begin{bmatrix} 1 & 0 & 0 & 0 & 0 & 0 \\ 0 & 1 & 0 & 0 & 0 & 0 \\ 0 & 0 & 1 & 0 & 0 & 0 \end{bmatrix} \left[L_{34} \right] \left[T_{34} \right] \frac{\partial}{\partial xx} \begin{Bmatrix} u_3^g \\ v_3^g \\ w_3^g \\ \vdots \\ p_4^g \\ q_4^g \\ r_4^g \end{Bmatrix} + \frac{\partial}{\partial xx} \left[R_{34} \right] \begin{Bmatrix} 0 \\ L_{34}(\zeta) \\ h_{34}(\zeta) \end{Bmatrix} \right) +$$

$$- \left[\lambda_1 \right] \left[\lambda_{12} \right]^T \left(\begin{bmatrix} 1 & 0 & 0 & 0 & 0 & 0 \\ 0 & 1 & 0 & 0 & 0 & 0 \\ 0 & 0 & 1 & 0 & 0 & 0 \end{bmatrix} \left[L_{12} \right] \left[T_{12} \right] \frac{\partial}{\partial xx} \begin{Bmatrix} u_1^g \\ v_1^g \\ w_1^g \\ \vdots \\ p_2^g \\ q_2^g \\ r_2^g \end{Bmatrix} + \frac{\partial}{\partial xx} \left[R_{12} \right] \begin{Bmatrix} 0 \\ L_{12}(\zeta) \\ h_{12}(\zeta) \end{Bmatrix} \right) \quad (33)$$

Where $[L_{12}]$ and $[L_{34}]$ are shape function matrices for the beam element connecting node 12 and 34 respectively; $[\lambda_{12}]$ and $[\lambda_{34}]$ are direction cosine matrices to interchange between global and local coordinates; $[T_{12}]$ and $[T_{34}]$ are expanded versions of $[\lambda_{12}]$ and $[\lambda_{34}]$; $[R_{12}]$ and $[R_{34}]$ are rotation matrices; $[\lambda_1]$ is the direction cosine matrix for the local system of coordinates; and finally, $L_{12}(\zeta)$, $L_{34}(\zeta)$, $h_{12}(\zeta)$ and $h_{34}(\zeta)$ are geometrical parameters that define the virtual hydrogen bond surfaces (depicted in green on Figure 10-4a). Using the above mention relations and numeric integration, the internal virtual work could be rewritten as:

$$\delta W_I = \{\delta U\}^T \frac{l_{mn} \times S}{2} [M]\{U\} \tag{34}$$

The correction parameter, S, can be computed as:

$$S = \frac{l_{CD} + l_{AB}}{2l_{mn}} \tag{35}$$

Special attentions needs to be applied in the calculation of l_{AB}, l_{CD} and l_{mn} since the integration paths connecting points AB, CD and mn are not necessarily straight lines. Finally, the internal force is reduced to:

$$\{f_I\} = \frac{l_{mn} \times S}{2} [M]\{U\} \tag{36}$$

This final form provides a great deal of flexibility in defining all the parameters that describe the internal behavior of the hydrogen bond element.

10.4 Modeling long-range interactions

Non-bonded interactions can be divided into two classes; short and long range interactions. Being a strong dipole-dipole attraction, hydrogen bonds are classified as

short range interactions allowing a relatively easy conversion into a continuum form. On the other hand, Coulomb and van der Waals interaction are long range interactions [178]. These types of interactions are difficult to represent due to its non-local nature (interaction of pairs that are not necessary neighbors), which represents a challenge for regular finite element codes.

Two solutions were implemented to account for these types of interactions. The first approach reduced the non-local behavior to an approximated local scheme. As a result, interactions between atoms that are not neighbors (from the chain point of view) are discarded. This approximation allows treating van der Walls and Coulomb interaction the same way hydrogen bonds are being considered. An additional element, directly related to the hydrogen bond element was used to such purposes.

The second approach allows a better representation of non-local interactions by modifying the basic implementation of a finite element code. A homemade umbrella code was developed to run on top of a finite element simulation software. Nodal coordinates of each node in the model were registered before each integration step. Long range interactions based on current nodal coordinates were computed between all nodes in the model. The resultant force over each node was added to the force vector inside the finite element code. This approach was successfully tested in a in house version of FEAP [175] finite element simulation code available at the *Computational Multi-Scale Materials Modeling Laboratory*. A clear disadvantage of this approach is the need to stop the simulation each time the non-bonded interactions needed to be computed.

10.5 Proof of concept: combining elements

Each individual element was extensively tested in their ability to fulfill the requirements imposed during development. Analytical solutions as well as simple computer simulations were used to verify the correct implementation in to the finite element code: FEAP [175]. This section provides a quantitative *proof of concept* simulation in an attempt to verify the potential usability of the finite element framework developed in this work.

The analysis consists in three cellulose chains arranged side by side to form a hydrogen bonded plane. Molecular dynamic simulations as well as continuum modeling techniques were used to simulate a small pullout perturbation in the middle chain (0.5 Å displacement in the end node). The initial atomistic structure was probed to define the basic needed parameters for the continuum model (dimensions, hydrogen bond virtual surfaces). One beam element per glucose ring was used; the number of degrees of freedoms in the system decrease from 3798 for the atomistic simulation to 378 for the continuum model. The simulation time was reduced from 2 hours to less than 1 minute. Both systems share the same boundary conditions but whereas molecular dynamics involved explicit type computations, the continuum model was solved using an implicit scheme (stiffness matrix inversion).

Figure 10-5 and Figure 10-6 show the simulation evolution in terms of the atomistic and continuum models. It is worth notice that the continuum elements were implemented to consider the initial configuration as the equilibrium position (minimum of potential energy). This implies that the continuum model will not modify its original configuration unless a perturbation is introduced in the simulation.
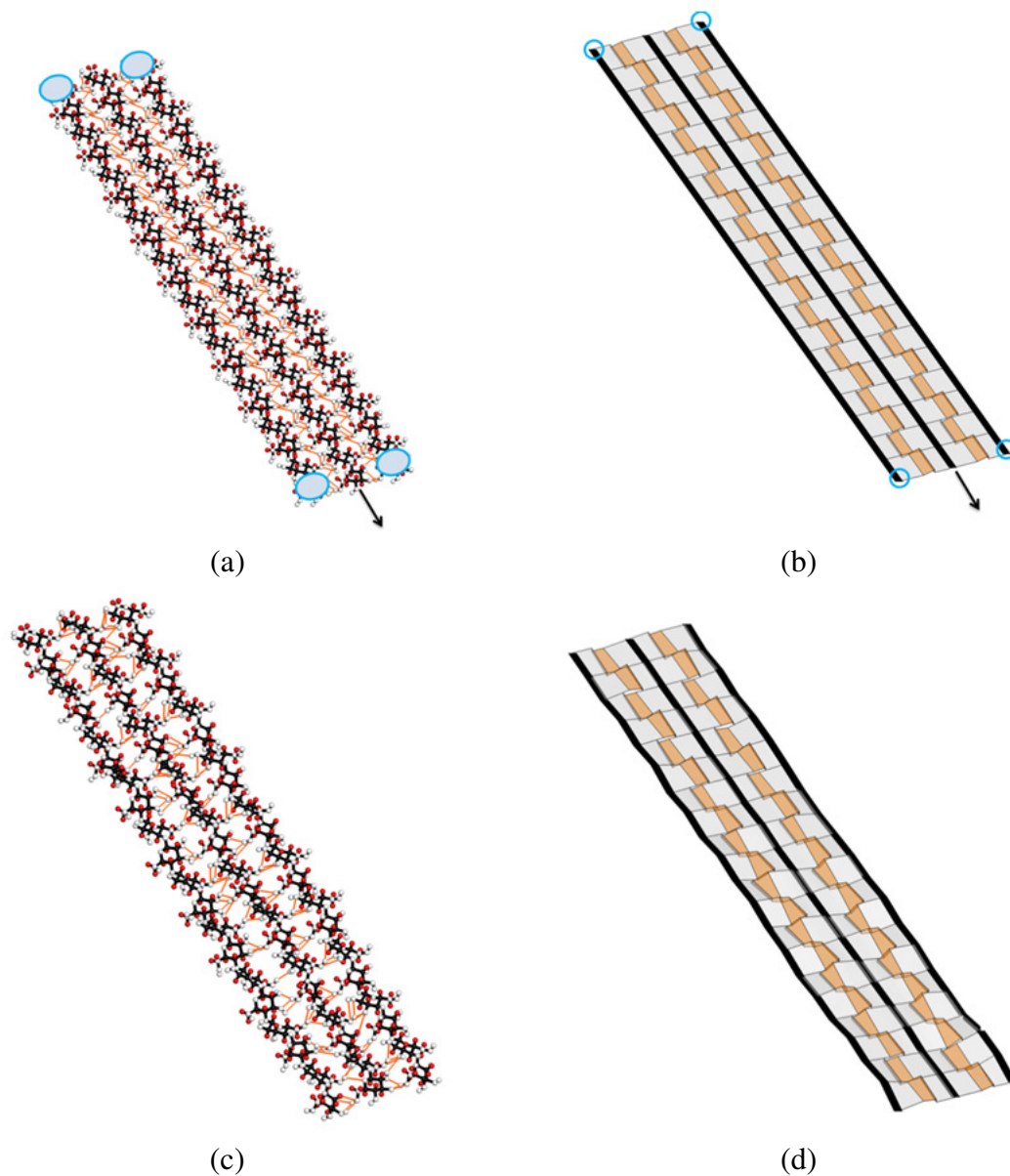
Figure 10-5 Pullout test using atomistic and continuum representation methods. Three dimensional view of: (a) Initial atomistic structure; (b) Initial continuum structure. Blue circles represent clamped boundary conditions, the black arrow indicates the direction of the pullout displacement; (c) Final atomistic structure; (d) Final continuum structure. Inter-chain hydrogen bonds represented in orange for both models. A displacement value of 0.5 Å was applied at the end of the center chain.

(a)   (b)

(c)   (d)
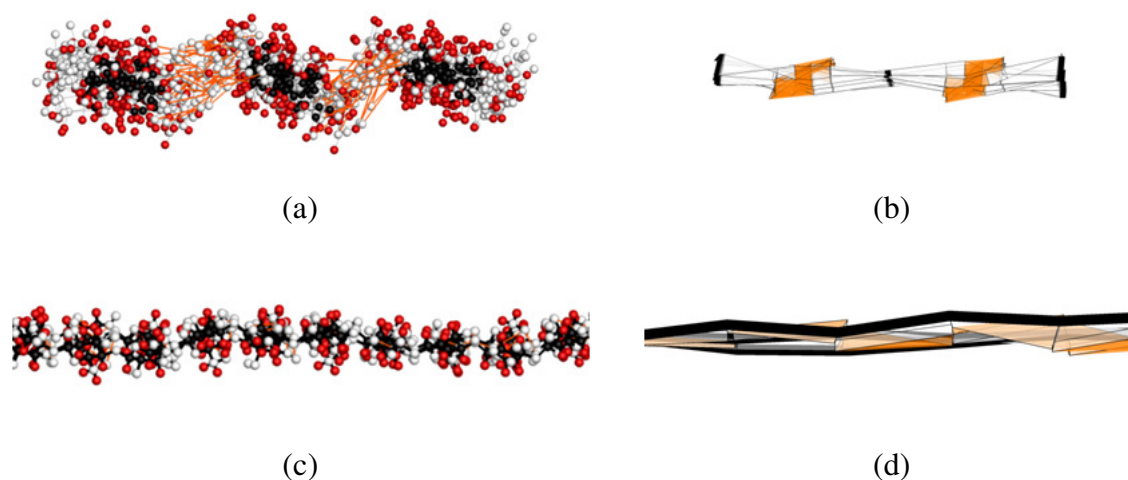
Figure 10-6 Pullout test using atomistic and continuum representation methods. Front view: Final atomistic (a) and continuum (b) structures. Detailed lateral view: Final atomistic (c) and continuum (d) structures. Inter-chain hydrogen bonds represented in orange for both models. A displacement value of 0.5 Å was applied at the end of the center chain.

Figure 10-7 Pullout force as a function of the applied displacement for the continuum based model. Notice the apparent initially linear response followed by an unstable behavior. Linear fitting for the unstable region shown in black.

Figure 10-7 shows the force applied at the end of the middle chain as a function of the applied displacement for the continuum model. An initially linear response is observed followed by an unstable behavior. Additional analyses need to be perform to confirm the representation provided by the model.

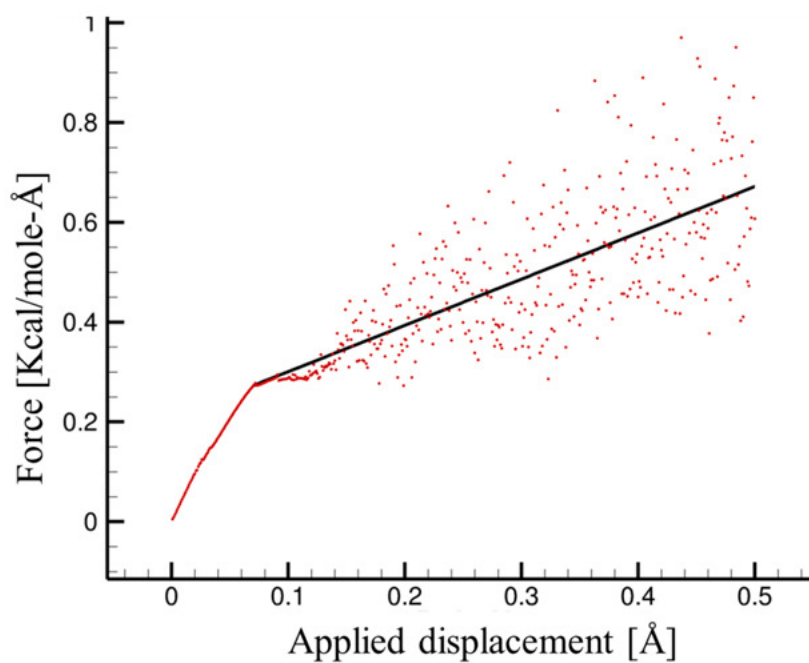## 10.6 Conclusion

A comprehensive solution to model cellulose nanocrystals from a continuum point of view was presented and discussed. It was shown that continuous theories can be applied to molecular systems under certain conditions but not without specific modifications.

A 3D Euler Bernoulli beam element was specially developed and implemented to simulate the mechanical response of cellulose chains. Four parameters: EA, EI_{11}, EI_{22} and GJ of a single chain were identified as key to feed the continuum model. No geometric or material approximations were needed to compute these parameters from atomistic simulations.

Inter-chain hydrogen bonds were reduced to a continuum form using a specifically developed element. Variable virtual surfaces were used to map atomistic positions to the continuum element allowing a better representation of hydrogen bond interaction. Two possible solutions were presented to model van der Waals and Coulomb interactions. A local approach was preferred due to implementation advantages.

Proof of concept simulations were conducted resulting in good conformational agreement between atomistic simulation and continuum modeling. The total simulation time was reduced by two orders of magnitude!

CHAPTER 11. SUMMARY AND CONCLUSIONS

11.1 Summary

A multiscale framework has been developed to predict and describe the thermo-mechanical behavior of cellulose nanocrystals using state-of-the-art computational tools capable of connecting atomistic based simulations to experiments through continuum based modeling techniques.

First-principle density functional theory and molecular dynamic simulations were utilized at the atomistic level. Longstanding issues regarding the elastic and thermal expansion anisotropies for crystalline cellulose have been probed in terms of the single-crystal elasticity tensor and the thermal expansion tensor components. First-principles phonon calculations via Van der Waals density functionals as well as reverse non-equilibrium molecular dynamics simulations were used to gain a fundamental understanding of defect-free, crystalline cellulose thermo-mechanical properties. Entropy, enthalpy, constant pressure heat capacity, thermal expansion tensor, thermal conductivity coefficients, Young's modulus, and Poisson's ratio, were computed over a wide range of temperatures. A comprehensive study of the hydrogen bond structure that characterize crystalline cellulose has been conducted in an attempt to ascertain the roles of inter- and intra- molecular hydrogen bonds in the mechanical properties of CNCs.

Five different force fields/parameter sets were compared with experimental results and first-principles simulations in terms of their ability to predict the following properties: lattice parameters and angles, linear elasticity tensor and linear thermal expansion tensor. Continuum based modeling techniques were used to answer fundamental questions regarding the role of hydrogen bonding in the mechanical response of CNCs. A variety of finite element-based continuum models were specifically developed for cellulose chains and non-bonding interactions (van der Waals, Coulomb and hydrogen bonds). As a result, a complete multiscale framework capable of reproducing the behavior of cellulose nanocrystals and that can be extended to any material with similar characteristics such as other polysaccharides (e.g. α-chitin, amylose) has been successfully developed.

11.2 Conclusion

The key mechanisms that govern the thermo-mechanical response of CNCs were identified and investigated. First-principle density functional theory simulations provided groundbreaking information regarding the extreme anisotropies of crystalline cellulose. A clear correlation between the stiffness of the crystal and the different deformation mechanisms was noted. The largest Young's modulus (206 GPa) was found to be aligned with the *c*-axis were covalent bonds govern the mechanical response of the crystal. Perpendicular to the cellulose chain axis, the *b*-direction shows the next greatest value for the Young modulus (98 GPa); this can be explained by the presence of the hydrogen bond network linking the cellulose chains. Finally a value for the Young modulus of only 19 GPa was computed along the direction perpendicular to the previous two, where only weak van der Waals forces play a role in the mechanical response of the material.

Additionally, 3D contour surfaces and 2D polar plots of the Young's Modulus and Poisson's ratio variations with crystallographic orientations were used for the first time to explain the substantial variability in the literature experimental data on the Young's modulus for cellulose, and to understand the Poisson's effect in selected planes.

The extreme anisotropies of the thermal expansion properties were also probed In terms of the van der Waals density functionals. It was found that ξ_1 is extremely large (10.7×10^{-5} K^{-1} at 300K), whereas ξ_2 (1.12×10^{-5} K^{-1} at 300K) and especially ξ_3 (0.42×10^{-5} K^{-1} at 300K) are quite small. The predicted results, such as the large ξ_1 and C_{33}, and the quick decrease of C_{11} with respect to temperature, are traceable from the weak van der Waals force between layers perpendicular to a-axis direction and the strong hydrogen bond along c-axis direction. These features of cellulose I$_\beta$ were observed quantitatively by the stretching force constants between atomic pairs. Thermal conductivity coefficients were calculated for the first time for crystalline cellulose showing results that were consistent with the thermal expansion coefficients and the bonding patterns in the structure. The thermal conductivity had its maximum along the chain direction (0.90 ± 0.06 W/mK), where the strongest bonds are present. As a result of this first analysis, a deep understanding of the role of covalent bonds, hydrogen bonds and van der Waals interactions in the thermo-mechanical response of CNCs was obtained. The ground was set to study the natural interaction between these mechanisms.

An exhaustive analysis of crystalline cellulose thermo-mechanical response was conducted using molecular dynamics simulations focusing on defining the right set of parameters needed to advance the model towards a continuum representation. Comparison with QM-DFT results were used to asses many of the issues encountered

during the analysis. It is well known that molecular dynamics simulations depend heavily on the force field and the parameterization that is used to describe energetic interactions. Researchers have been performing molecular dynamics simulations of cellulose for years but still there is no force field specially developed for cellulose. Five different force fields/parameter sets were compared with experimental results and quantum mechanics simulations in terms of their ability to predict three different properties: lattice parameters, elastic constants and thermal expansion coefficients. Not surprisingly, none of the tested force fields yield results in perfect agreement with experimental data for all predicted properties. It is possible to select a particular force field that will give moderately good results for a given case but the same force field may fail miserably when used for some other case. This situation makes analyzing combined cases (i.e., mechanical response and thermal expansion) rather difficult. However, a specific property can be predicted quite accurately if an appropriate force field is chosen. For example, ReaxFF_CHO provides the most promising results regarding hydrogen bond configuration patterns showing the capability of interchanging hydrogen bond patterns on-the-fly and producing consistent results through the entire analysis. Nevertheless, the apparently good results show for hydrogen bonds patterns needs to be leveraged with relatively poor performance in predicting mechanical properties. On the other hand, ReaxFF_Glycine performed remarkably well in predicting longitudinal mechanical properties (compared with QM-DFT) but failed in maintaining a stable hydrogen bond configuration.

Hydrogen bond patterns were extensible study for both crystals and isolated chains in an initial and relaxed (minimum potential energy) atomic configuration. By keeping track of each hydrogen bond interaction inside the simulation cell it was possible to explain the

increase in mechanical properties produced by this interaction. Values of energy, force and stiffness for each hydrogen bond in the system were extracted an analyzed providing the fundamental information required to model this particular interaction in a continuum framework.

A new approach was proposed to analyze the mechanical properties of single cellulose chains based on the linear relation between the changes in energy density and the half of the square of the compressive or tensile strains. This particular approach had the advantage that does not require a definition of stress or cross-sectional area solving what is known to materials scientists working with carbon nanotubes as the "Yakobson's Paradox".

Finally, it was possible to directly correlate hydrogen bonds interactions with the longitudinal mechanical response of a single cellulose chain. A decrease in the axial stiffness of a single chain was observed when hydrogen bonds were deactivated showing the reinforcement capabilities of this particular interaction. Nevertheless, the effect measured was different for each parameterization. A limited amount of simulations were conducted to address the bending and torsional stiffness of single chains. The extreme deformations observed during minimization procedures suggest that the bending and torsional stiffness of the chain are extremely low compared to the axial stiffness and could be regarded as zero.

As a result of the extensive analysis conducted with QM-DFT and MD simulation it was possible to develop a simplified continuum model to study the longitudinal mechanical response of isolated CNCs. Initially developed to analyze the role of inter-chain hydrogen bonding in the axial mechanical response of cellulose nanocrystals, the simplified model

proved to be more valuable. Size and shape effects were study using the theoretical model to predict the structural configuration that produced the biggest increase in the normalized stiffness increment (ΔS). Row shaped crystals proved to be better suitable for withstand axial loading when compared to other shapes that contain the same number of cellulose chains.

Finally, a comprehensive solution to model cellulose nanocrystals from a continuum point of view using FEM was presented and discussed. It was shown that continuous theories can be applied to molecular systems under certain conditions but not without specific modifications. A 3D Euler Bernoulli beam element was specially developed and implemented to simulate the mechanical response of cellulose chains with parameters (EA, EI_{11}, EI_{22} and GJ) directly extracted from atomistic simulations. Inter-chain hydrogen bonds were reduced to a continuum form using a specifically developed element. Variable virtual surfaces were used to map atomistic positions to the continuum element allowing a better representation of hydrogen bond interaction. Two possible solutions were presented to model van der Waals and Coulomb interactions. A local model was preferred due to implementation advantages. A proof of concept simulations was introduced resulting in good conformational agreement between atomistic simulation and continuum modeling. The total simulation time was reduced by two orders of magnitude!

Extensive analyses need to be conducted to demonstrate the validity of the FEM continuum model by comparison with molecular dynamics and quantum mechanics simulations. For the first time, length and time scales on the order of laboratory experiments could be reached allowing direct comparison between experimental setups

and computer simulations. Extension to include CNC – CNC interactions, water influence and CNC-matrix interaction are expected in the near future.

LIST OF REFERENCES

LIST OF REFERENCES

1.   Moon, R.J., et al., *Cellulose nanomaterials review: structure, properties and nanocomposites.* Chemical Society Reviews, 2011. **40**(7): p. 3941-3994.

2.   Habibi, Y., L.A. Lucia, and O.J. Rojas, *Cellulose Nanocrystals: Chemistry, Self-Assembly, and Applications.* Chemical Reviews, 2010. **110**(6): p. 3479-3500.

3.   Peng, B., et al., *Chemistry and applications of nanocrystalline cellulose and its derivatives: a nanotechnology perspective.* The Canadian Journal of Chemical Engineering, 2011. **89**(5): p. 1191-1206.

4.   Klemm, D., et al., *Cellulose: Fascinating Biopolymer and Sustainable Raw Material.* Angewandte Chemie International Edition, 2005. **44**(22): p. 3358-3393.

5.   Azizi Samir, M.A.S., F. Alloin, and A. Dufresne, *Review of recent research into cellulosic whiskers, their properties and their application in nanocomposite field.* Biomacromolecules, 2005. **6**(2): p. 612-626.

6.   O'Sullivan, A., *Cellulose: the structure slowly unravels.* Cellulose, 1997. **4**(3): p. 173-207.

7.   Samir, M.A.S.A., F. Alloin, and A. Dufresne, *Review of recent research into cellulosic whiskers, their properties and their application in nanocomposite field.* Biomacromolecules, 2005. **6**(2): p. 612-626.

8.   Klemm, D., et al., *Nanocelluloses: A New Family of Nature-Based Materials.* Angewandte Chemie-International Edition, 2011. **50**(24): p. 5438-5466.

9.   Nishiyama, Y., P. Langan, and H. Chanzy, *Crystal Structure and Hydrogen-Bonding System in Cellulose Iβ from Synchrotron X-ray and Neutron Fiber Diffraction.* Journal of the American Chemical Society, 2002. **124**(31): p. 9074-9082.

10.   Nishiyama, Y., et al., *Crystal Structure and Hydrogen Bonding System in Cellulose Iα from Synchrotron X-ray and Neutron Fiber Diffraction.* Journal of the American Chemical Society, 2003. **125**(47): p. 14300-14306.

11.   Parthasarathi, R., et al., *Insights into Hydrogen Bonding and Stacking Interactions in Cellulose.* The Journal of Physical Chemistry A, 2011. **115**(49): p. 14191-14202.

12.   Nishiyama, Y., et al., *Neutron Crystallography, Molecular Dynamics, and Quantum Mechanics Studies of the Nature of Hydrogen Bonding in Cellulose Iβ.* Biomacromolecules, 2008. **9**(11): p. 3133-3140.

13.   Bucko, T., et al., *Ab Initio Study of Structure and Interconversion of Native Cellulose Phases.* Journal of Physical Chemistry A, 2011. **115**(35): p. 10097-10105.

14.   Parthasarathi, R., et al., *Insights into Hydrogen Bonding and Stacking Interactions in Cellulose.* Journal of Physical Chemistry A, 2011. **115**(49): p. 14191-14202.

15.   Wagner, R., et al., *Uncertainty quantification in nanomechanical measurements using the atomic force microscope.* Nanotechnology, 2011. **22**(45).

16.   Wu, X., R.J. Moon, and A. Martini, *Crystalline cellulose elastic modulus predicted by atomistic models of uniform deformations and nanoscale indentation.* Cellulose, In press.

17.   Elazzouzi-Hafraoui, S., et al., *The shape and size distribution of crystalline nanoparticles prepared by acid hydrolysis of native cellulose.* Biomacromolecules, 2007. **9**(1): p. 57-65.

18.   Rahimi, M. and R. Behrooz, *Effect of cellulose characteristic and hydrolyze conditions on morphology and size of nanocrystal cellulose extracted from wheat straw.* International Journal of Polymeric Materials, 2011. **60**(8): p. 529-541.

19.   Revol, J.-F., *On the cross-sectional shape of cellulose crystallites in< i> Valonia ventricosa</i>.* Carbohydrate Polymers, 1982. **2**(2): p. 123-134.

20.   Beck-Candanedo, S., M. Roman, and D.G. Gray, *Effect of reaction conditions on the properties and behavior of wood cellulose nanocrystal suspensions.* Biomacromolecules, 2005. **6**(2): p. 1048-1054.

21.   Langan, P., et al., *Synchrotron X-ray structures of cellulose Iβ and regenerated cellulose II at ambient temperature and 100 K.* Cellulose, 2005. **12**(6): p. 551-562.

22.   Nishiyama, Y., et al., *Looking at hydrogen bonds in cellulose.* Acta Crystallographica Section D, 2010. **66**(11): p. 1172-1177.

23.   Sakurada, I., T. Ito, and K. Nakamae, *Elastic moduli of polymer crystals for the chain axial direction.* Die Makromolekulare Chemie, 1964. **75**(1): p. 1-10.

24.   Sakurada, I., Y. Nukushina, and T. Ito, *Experimental determination of the elastic modulus of crystalline regions in oriented polymers.* Journal of Polymer Science, 1962. **57**(165): p. 651-660.

25.   Matsuo, M., et al., *Effect of orientation distribution and crystallinity on the measurement by x-ray diffraction of the crystal lattice moduli of cellulose I and II.* Macromolecules, 1990. **23**(13): p. 3266-3275.

26.   Sugiyama, J., R. Vuong, and H. Chanzy, *Electron diffraction study on the two crystalline phases occurring in native cellulose from an algal cell wall.* Macromolecules, 1991. **24**(14): p. 4168-4175.

27.   Finkenstadt, V.L. and R.P. Millane, *Crystal Structure of Valonia Cellulose Iβ.* Macromolecules, 1998. **31**(22): p. 7776-7783.

28.   Wada, M., et al., *The structure of celluloses.* Powder Diffraction, 2008. **23**(2): p. 92-95.

29.   Wada, M., *Lateral thermal expansion of cellulose Iβ and IIII polymorphs.* Journal of Polymer Science Part B: Polymer Physics, 2002. **40**(11): p. 1095-1102.

30.   Nishino, T., K. Takano, and K. Nakamae, *Elastic modulus of the crystalline regions of cellulose polymorphs.* Journal of Polymer Science Part B: Polymer Physics, 1995. **33**(11): p. 1647-1651.

31.   Ishikawa, A., T. Okano, and J. Sugiyama, *Fine structure and tensile properties of ramie fibres in the crystalline form of cellulose I, II, IIII and IVI.* Polymer, 1997. **38**(2): p. 463-468.

32.   Diddens, I., et al., *Anisotropic Elastic Properties of Cellulose Measured Using Inelastic X-ray Scattering.* Macromolecules, 2008. **41**(24): p. 9755-9759.

33.   Wagner, R., et al., *Uncertainty quantification in nanomechanical measurements using the atomic force microscope.* Nanotechnology, 2011. **22**(45): p. 455703.

34.   Pakzad, A., et al., *Size effects on the nanomechanical properties of cellulose I nanocrystals.* Journal of Materials Research, 2012. **27**(3): p. 528-536.

35.   Lahiji Rr Fau - Xu, X., et al., *Atomic force microscopy characterization of cellulose nanocrystals.* 2010(1520-5827 (Electronic)).

36.   Nakamura, K.I., et al., *Poisson's ratio of cellulose Iβ and cellulose II.* Journal of Polymer Science Part B: Polymer Physics, 2004. **42**(7): p. 1206-1211.

37.   Hidaka, H., U.-J. Kim, and M. Wada, *Synchrotron X-ray fiber diffraction study on the thermal expansion behavior of cellulose crystals in tension wood of Japanese poplar in the low-temperature region.* Holzforschung, 2010. **64**(2): p. 167-171.

38.   Hori, R. and M. Wada, *The thermal expansion of wood cellulose crystals.* Cellulose, 2005. **12**(5): p. 479-484.

39.   Wada, M., *Lateral thermal expansion of cellulose I-beta and IIII polymorphs.* Journal of Polymer Science Part B-Polymer Physics, 2002. **40**(11): p. 1095-1102.

40.   Wada, M., et al., *X-ray diffraction study on the thermal expansion behavior of cellulose I beta and its high-temperature phase.* Polymer Degradation and Stability, 2010. **95**(8): p. 1330-1334.

41.   Shimazaki, Y., et al., *Excellent thermal conductivity of transparent cellulose nanofiber/epoxy resin nanocomposites.* Biomacromolecules, 2007. **8**(9): p. 2976.

42.   Weinan, E., *Principles of multiscale modeling*2011: Cambridge University Press.

43.   Derosa, P. and T. Cagin, *Multiscale modeling: from atoms to devices*2010: Taylor & Francis US.

44.   Ferreira, M.A. and H.K. Lee, *Multiscale modeling: a Bayesian perspective*2007: Springer.

45.   Bertaud, J., Z. Qin, and M.J. Buehler, *Atomistically informed mesoscale model of alpha-helical protein domains.* International Journal for Multiscale Computational Engineering, 2009. **7**(3).

46.   Buehler, M.J., *Atomistic Modeling of Materials Failure*: Springer. 560 pages.

47.   Buehler, M.J., *Multiscale aspects of mechanical properties of biological materials.* Journal of the Mechanical Behavior of Biomedical Materials, 2011. **4**(2): p. 125-127.

48.   Buehler, M.J., *Multiscale mechanics of biological and biologically inspired materials and structures.* Acta Mechanica Solida Sinica, 2010. **23**(6): p. 471-483.

49.   Cranford, S. and M.J. Buehler, *Coarse-Graining Parameterization and Multiscale Simulation of Hierarchical Systems. Part I: Theory and Model Formulation*, 2010, DTIC Document.

50.   Keten, S., et al., *Nanoconfinement controls stiffness, strength and mechanical toughness of [beta]-sheet crystals in silk.* Nat Mater, 2010. **9**(4): p. 359-367.

51.   Li, S. and X.-l. Gao, *Handbook of Micromechanics and Nanomechanics*2013: Pan Stanford Pub.

52.   Mano, J.F., *Biomimetic approaches for biomaterials development*2013: Wiley. com.

53. Steinhauser, M.O., *Computational multiscale modeling of fluids and solids: theory and applications*2007: Springer.

54. Simons, J., *An introduction to theoretical chemistry*2003: Cambridge University Press.

55. Dove, M.T., *An introduction to atomistic simulation methods.*

56. Yang, L., et al. *Atomistic Simulation: Molecular Statics and Molecular Dynamics.* October 13, 2010; Available from: https://www-pls.llnl.gov/?url=about_pls-condensed_matter_and_materials_division-eos_materials_theory-methods-md.

57. Meller, J., *Molecular dynamics.* eLS.

58. Li, X.-Z., B. Walker, and A. Michaelides, *Quantum nature of the hydrogen bond.* Proceedings of the National Academy of Sciences, 2011. **108**(16): p. 6369-6373.

59. Ippoliti, E., *What is Molecular Dynamics?* 2011.

60. Bower, A.F., *Applied mechanics of solids*2011: CRC press.

61. Reddy, J.N., *Introduction to the Finite Element Method*, McGraw-Hill Science/Engineering/Math. p. 896 pages.

62. Kohn, W. and L.J. Sham, *Self-consistent equations including exchange and correlation effects.* Physical Review, 1965. **140**(4A): p. A1133.

63. Bučko, T.s., et al., *Improved Description of the Structure of Molecular and Layered Crystals: Ab Initio DFT Calculations with van der Waals Corrections.* The Journal of Physical Chemistry A, 2010. **114**(43): p. 11814-11824.

64. Le Page, Y. and P. Saxe, *Symmetry-general least-squares extraction of elastic data for strained materials from ab initio calculations of stress.* Physical Review B, 2002. **65**(10): p. 104104.

65. Kresse, G. and J. Hafner, *Ab initio molecular-dynamics simulation of the liquid-metal–amorphous-semiconductor transition in germanium.* Physical Review B, 1994. **49**(20): p. 14251-14269.

66. Kresse, G. and J. Furthmuller, *Efficiency of ab-initio total energy calculations for metals and semiconductors using a plane-wave basis set.* Computational Materials Science, 1996. **6**(1): p. 15-50.

67. Kresse, G. and J. Furthmuller, *Efficient iterative schemes for ab initio total-energy calculations using a plane-wave basis set.* Physical Review B, 1996. **54**(16): p. 11169-11186.

68.   Hafner, J., *Ab‑initio simulations of materials using VASP: Density‑functional theory and beyond.* Journal of Computational Chemistry, 2008. **29**(13): p. 2044-2078.

69.   Zuluaga, M.G., et al. *Crystalline cellulose – atomistic toolkit* 2013; Available from: https://nanohub.org/members/46523/contributions.

70.   Šturcová, A., et al., *Structural details of crystalline cellulose from higher plants.* Biomacromolecules, 2004. **5**(4): p. 1333-1339.

71.   Matthews, J.F., et al., *Comparison of Cellulose Iβ Simulations with Three Carbohydrate Force Fields.* Journal of Chemical Theory and Computation, 2012. **8**(2): p. 735-748.

72.   Perdew, J.P., K. Burke, and M. Ernzerhof, *Generalized gradient approximation made simple.* Physical Review Letters, 1996. **77**(18): p. 3865-3868.

73.   Bučko, T.s., et al., *Ab Initio Study of Structure and Interconversion of Native Cellulose Phases.* The Journal of Physical Chemistry A, 2011. **115**(35): p. 10097-10105.

74.   Li, Y., M. Lin, and J.W. Davenport, *Ab Initio Studies of Cellulose I: Crystal Structure, Intermolecular Forces, and Interactions with Water.* The Journal of Physical Chemistry C, 2011. **115**(23): p. 11533-11539.

75.   Jones, R.M., *Mechanics of composite materials.* Vol. 2. 1975: Taylor & Francis London.

76.   Blöchl, P.E., *Projector augmented-wave method.* Physical Review B, 1994. **50**(24): p. 17953-17979.

77.   Grimme, S., *Semiempirical GGA-type density functional constructed with a long-range dispersion correction.* Journal of Computational Chemistry, 2006. **27**(15): p. 1787-1799.

78.   Antony, J. and S. Grimme, *Density functional theory including dispersion corrections for intermolecular interactions in a large benchmark set of biologically relevant molecules.* Physical Chemistry Chemical Physics, 2006. **8**(45): p. 5287-5293.

79.   Hector Jr, L.G., J.F. Herbst, and T.W. Capehart, *Electronic structure calculations for LaNi5 and LaNi5H7: energetics and elastic properties.* Journal of Alloys and Compounds, 2003. **353**(1–2): p. 74-85.

80.   Hector Jr, L.G. and J.F. Herbst, *Electronic and elastic properties of RCo5 and RCo5Hn (R = La, Ce, Pr).* Journal of Alloys and Compounds, 2004. **379**(1–2): p. 41-53.

81. Hector Jr, L., et al., *Ab Initio thermodynamic and elastic properties of alkaline-earth metals and their hydrides.* Physical Review B, 2007. **76**(1): p. 014121.

82. Qi, Y., et al., *Threefold increase in the Young's modulus of graphite negative electrode during lithium intercalation.* Journal of The Electrochemical Society, 2010. **157**(5): p. A558-A566.

83. Shang, S.-L., et al., *Lattice dynamics, thermodynamics and elastic properties of monoclinic Li2CO3 from density functional theory.* Acta Materialia, 2012. **60**(13–14): p. 5204-5216.

84. Qi, Y. and L.G. Hector Jr, *Adhesion and adhesive transfer at aluminum/diamond interfaces: A first-principles study.* Physical Review B, 2004. **69**(23): p. 235401.

85. Qi, Y. and L.G. Hector, *Planar stacking effect on elastic stability of hexagonal boron nitride.* Applied physics letters, 2007. **90**(8): p. 081922-081922-3.

86. Shang, S., et al., *First-principles study of elastic and phonon properties of the heavy fermion compound CeMg.* Journal of Physics: Condensed Matter, 2009. **21**(24): p. 246001.

87. Wróbel, J., et al., *Thermodynamic and mechanical properties of lanthanum–magnesium phases from density functional theory.* Journal of Alloys and Compounds, 2012. **512**(1): p. 296-310.

88. Woodward, C., et al., *Prediction of dislocation cores in aluminum from density functional theory.* Physical Review Letters, 2008. **100**(4): p. 045507.

89. Zuluaga, M.G., et al. *Anisotropy Calculator - 3D Visualization Toolkit.* 2013; Available from: https://nanohub.org/members/46523/contributions.

90. Roberts, R., R. Rowe, and P. York, *The Poisson's ratio of microcrystalline cellulose.* International journal of pharmaceutics, 1994. **105**(2): p. 177-180.

91. Eichhorn, S.J. and G.R. Davies, *Modelling the crystalline deformation of native and regenerated cellulose.* Cellulose, 2006. **13**(3): p. 291-307.

92. Wu, X., R. Moon, and A. Martini, *Crystalline cellulose elastic modulus predicted by atomistic models of uniform deformation and nanoscale indentation.* Cellulose, 2013. **20**(1): p. 43-55.

93. Bergenstrahle, M., L.A. Berglund, and K. Mazeau, *Thermal response in crystalline I beta cellulose: A molecular dynamics study.* Journal of Physical Chemistry B, 2007. **111**(30): p. 9138-9145.

94.   Shang, S.L., et al., *First-principles thermodynamics from phonon and Debye model: Application to Ni and Ni3Al.* Computational Materials Science, 2010. **47**(4): p. 1040-1048.

95.   Shang, S.L., Y. Wang, and Z.K. Liu, *First-principles calculations of phonon and thermodynamic properties in the boron-alkaline earth metal binary systems: B-Ca, B-Sr, and B-Ba.* Physical Review B, 2007. **75**(2): p. 024302.

96.   Shang, S.L., et al., *Lattice dynamics, thermodynamics and elastic properties of monoclinic Li2CO3 from density functional theory.* Acta Materialia, 2012. **60**: p. 5204-5216.

97.   Wang, Y., Z.K. Liu, and L.Q. Chen, *Thermodynamic properties of Al, Ni, NiAl, and Ni3Al from first-principles calculations.* Acta Materialia, 2004. **52**(9): p. 2665-2671.

98.   Shang, S.L., et al., *Temperature-dependent elastic stiffness constants of alpha- and theta-Al2O3 from first-principles calculations.* Journal of Physics-Condensed Matter, 2010. **22**(37): p. 375403.

99.   Wang, Y., et al., *A first-principles approach to finite temperature elastic constants.* Journal of Physics-Condensed Matter, 2010. **22**(22): p. 225404.

100.   Nishiyama, Y., P. Langan, and H. Chanzy, *Crystal structure and hydrogen-bonding system in cellulose 1 beta from synchrotron X-ray and neutron fiber diffraction.* Journal of the American Chemical Society, 2002. **124**(31): p. 9074-9082.

101.   Kresse, G. and D. Joubert, *From ultrasoft pseudopotentials to the projector augmented-wave method.* Physical Review B, 1999. **59**(3): p. 1758-1775.

102.   Bucko, T., et al., *Improved Description of the Structure of Molecular and Layered Crystals: Ab Initio DFT Calculations with van der Waals Corrections.* Journal of Physical Chemistry A, 2010. **114**(43): p. 11814-11824.

103.   Parlinski, K., Z.Q. Li, and Y. Kawazoe, *First-principles determination of the soft mode in cubic ZrO2.* Physical Review Letters, 1997. **78**(21): p. 4063-4066.

104.   Parlinski, K., *Software PHONON as implemented in MedeA 2.8*2008, Angel Fire, New Mexico: Materials Design.

105.   Wrobel, J., et al., *Thermodynamic and mechanical properties of lanthanum-magnesium phases from density functional theory.* Journal of Alloys and Compounds, 2012. **512**(1): p. 296-310.

106. Shang, S.L., et al., *First-principles study of elastic and phonon properties of the heavy fermion compound CeMg.* Journal of Physics-Condensed Matter, 2009. **21**(24): p. 246001.

107. Le Page, Y. and P. Saxe, *Symmetry-general least-squares extraction of elastic coefficients from ab initio total energy calculations.* Physical Review B, 2001. **63**(17): p. 174103.

108. Hector Jr., L.G., et al., *Ab Initio thermodynamic and elastic properties of alkaline-earth metals and their hydrides.* Physical Review B, 2007. **76**(1): p. 014121.

109. Hector Jr., L.G., J.F. Herbst, and T.W. Capehart, *Electronic structure calculations for LaNi(5) and LaNi(5)H(7): energetics and elastic properties.* Journal of Alloys and Compounds, 2003. **353**(1-2): p. 74-85.

110. Qi, Y. and L.G. Hector Jr., *Planar stacking effect on elastic stability of hexagonal boron nitride.* Applied Physics Letters, 2007. **90**(8): p. 081922.

111. Blöchl, P.E., O. Jepsen, and O.K. Andersen, *Improved tetrahedron method for Brillouin-zone integrations.* Phys. Rev. B, 1994. **49**: p. 16223-16233.

112. Shang, S.L., et al., *Lattice dynamics, thermodynamics, and bonding strength of lithium-ion battery materials LiMPO(4) (M = Mn, Fe, Co, and Ni): a comparative first-principles study.* Journal of Materials Chemistry, 2012. **22**(3): p. 1142-1149.

113. Dri, F., et al., *Anisotropy of the Elastic Properties of Crystalline Cellulose Iβ from First Principles Density Functional Theory with Van der Waals Interactions.* in preparation, 2013.

114. Davies, G.F., *EFFECTIVE ELASTIC-MODULI UNDER HYDROSTATIC STRESS .1. QUASI-HARMONIC THEORY.* Journal of Physics and Chemistry of Solids, 1974. **35**(11): p. 1513-1520.

115. Muller-Plathe, F. and D. Reith, *Cause and effect reversed in non-equilibrium molecular dynamics: an easy route to transport coefficients.* COMPUTATIONAL AND THEORETICAL POLYMER SCIENCE, 1999. **9**(3-4): p. 203-209.

116. Nishiyama, Y., et al., *Neutron Crystallography, Molecular Dynamics, and Quantum Mechanics Studies of the Nature of Hydrogen Bonding in Cellulose I-beta.* Biomacromolecules, 2008. **9**(11): p. 3133-3140.

117. Cabrera, R.Q., et al., *Nanomechanical and Structural Properties of Native Cellulose Under Compressive Stress.* Biomacromolecules, 2011. **12**(6): p. 2178-2183.

118. Li, Y., M. Lin, and J.W. Davenport, *Ab Initio Studies of Cellulose I: Crystal Structure, Intermolecular Forces, and Interactions with Water.* Journal of Physical Chemistry C, 2011. **115**(23): p. 11533-11539.

119. Shang, S.L., et al., *Phonon and thermodynamic properties of Al-Mn compounds: A first-principles study.* Computational Materials Science, 2011. **50**(7): p. 2096-2103.

120. Blokhin, A.V., et al., *Thermodynamic Properties of Plant Biomass Components. Heat Capacity, Combustion Energy, and Gasification Equilibria of Cellulose.* Journal of Chemical and Engineering Data, 2011. **56**(9): p. 3523-3531.

121. Iwamoto, S., et al., *Elastic Modulus of Single Cellulose Microfibrils from Tunicate Measured by Atomic Force Microscopy.* Biomacromolecules, 2009. **10**(9): p. 2571-2576.

122. Matsuo, M., et al., *EFFECT OF ORIENTATION DISTRIBUTION AND CRYSTALLINITY ON THE MEASUREMENT BY X-RAY-DIFFRACTION OF THE CRYSTAL-LATTICE MODULI OF CELLULOSE-I AND CELLULOSE-II.* Macromolecules, 1990. **23**(13): p. 3266-3275.

123. Sakurada, I., Y. Nukushina, and T. Ito, *EXPERIMENTAL DETERMINATION OF ELASTIC MODULUS OF CRYSTALLINE REGIONS IN ORIENTED POLYMERS.* Journal of Polymer Science, 1962. **57**(165): p. 651-&.

124. Sturcova, A., G.R. Davies, and S.J. Eichhorn, *Elastic modulus and stress-transfer properties of tunicate cellulose whiskers.* Biomacromolecules, 2005. **6**(2): p. 1055-1061.

125. Diddens, I., et al., *Anisotropic Elastic Properties of Cellulose Measured Using Inelastic X-ray Scattering.* Macromolecules, 2008. **41**(24): p. 9755-9759.

126. Eichhorn, S.J., et al., *Review: current international research into cellulose nanofibres and nanocomposites.* Journal of Materials Science, 2010. **45**(1): p. 1-33.

127. Nakamura, K., et al., *Poisson's ratio of cellulose I-beta and cellulose II.* Journal of Polymer Science Part B-Polymer Physics, 2004. **42**(7): p. 1206-1211.

128. Shang, S.L., et al., *First-principles calculations of pure elements: Equations of state and elastic stiffness constants.* Computational Materials Science, 2010. **48**(4): p. 813-826.

129. Simmons, G. and H. Wang, *Single Crystal Elastic Constants and Calculated Aggregate Properties*1971, Cambridge (Mass.): MIT press.

130. Materials Design, I., *pcff+ forcefield*, 15 July 2012.

131. Plimpton, S., *Fast Parallel Algorithms for Short-Range Molecular Dynamics.* Journal of Computational Physics, 1995. **117**(1): p. 1-19.

132. *MedeA v2.11*, 2012, Materials Design, Inc.: Santa Fe, NM, USA.

133. Leach, A.R., *Molecular modelling: principles and applications*2001: Pearson Education.

134. Hehre, W.J., *A guide to molecular mechanics and quantum chemical calculations*2003: Wavefunction Irvine, CA.

135. Sun, H., *COMPASS: An ab Initio Force-Field Optimized for Condensed-Phase ApplicationsOverview with Details on Alkane and Benzene Compounds.* The Journal of Physical Chemistry B, 1998. **102**(38): p. 7338-7364.

136. Tanaka, F. and T. Iwata, *Estimation of the Elastic Modulus of Cellulose Crystal by Molecular Mechanics Simulation.* Cellulose, 2006. **13**(5): p. 509-517.

137. Kirschner, K.N., et al., *GLYCAM06: A generalizable biomolecular force field. Carbohydrates.* Journal of Computational Chemistry, 2008. **29**(4): p. 622-655.

138. Qiong, Z., et al., *A molecular dynamics study of the thermal response of crystalline cellulose Iβ.* Cellulose, 2011.

139. Maurer, R.J. and A.F. Sax, *Molecular dynamics of cellulose crystal surfaces with ChemShell.* Procedia Computer Science, 2010. **1**(1): p. 1149-1154.

140. Yui, T., et al., *Swelling behavior of the cellulose Ibeta crystal models by molecular dynamics.* Carbohydrate Research, 2006. **341**(15): p. 2521-2530.

141. van Duin, A.C.T., et al., *ReaxFF: A Reactive Force Field for Hydrocarbons.* The Journal of Physical Chemistry A, 2001. **105**(41): p. 9396-9409.

142. Bergenståhle, M., L.A. Berglund, and K. Mazeau, *Thermal Response in Crystalline Iβ Cellulose: A Molecular Dynamics Study.* The Journal of Physical Chemistry B, 2007. **111**(30): p. 9138-9145.

143. Matthews, J., M. Himmel, and J. Brady, *Simulations of the Structure of Cellulose*, 2010, National Renewable Energy Laboratory (NREL), Golden, CO.

144. Plimpton, S., A. Thompson, and P. Crozier. Available from: http://lammps.sandia.gov/.

145. Mattsson, T.R., et al., *First-principles and classical molecular dynamics simulation of shocked polymers.* Physical Review B, 2010. **81**(5): p. 054103.

146.   Rahaman, O., et al., *Development of a ReaxFF Reactive Force Field for Glycine and Application to Solvent Effect and Tautomerization.* The Journal of Physical Chemistry B, 2010. **115**(2): p. 249-261.

147.   Dri, F., et al., *Comparison of Force Fields for Prediction of the Mechanical and Thermal Stress-Dependent Structure of Cellulose Nanocrystals.* in preparation, 2013.

148.   Luzar, A. and D. Chandler, *Hydrogen-bond kinetics in liquid water.* Nature, 1996. **379**(6560): p. 55-57.

149.   Dri, F., et al., *Study of Thermodynamic and Mechanical Properties of Crystalline Cellulose.* in preparation, 2013.

150.   Jensen, J.H., et al. *Effective fragment method for modeling intermolecular hydrogen-bonding effects on quantum mechanical calculations.* in *ACS Symposium Series.* 1994. ACS Publications.

151.   Breneman, C.M., et al. *Modeling the Hydrogen Bond with Transferable Atom Equivalents.* in *ACS Symposium Series.* 1994. ACS Publications.

152.   Valeri, I.K., *Crystalline cellulose: structure and hydrogen bonds.* Russian Chemical Reviews, 2010. **79**(3): p. 231.

153.   Wada, M., et al., *X-ray diffraction study on the thermal expansion behavior of cellulose Iβ and its high-temperature phase.* Polymer Degradation and Stability, 2010. **95**(8): p. 1330-1334.

154.   Duin, A.v. *ReaxFF User Manual.* December 2002; Available from: http://www.wag.caltech.edu/home/duin/reax_um.pdf.

155.   Mazeau, K., *Structural micro-heterogeneities of crystalline Iβ-cellulose.* Cellulose, 2005. **12**(4): p. 339-349.

156.   Matthews, J.F., et al., *Computer simulation studies of microcrystalline cellulose Iβ.* Carbohydrate Research, 2006. **341**(1): p. 138-152.

157.   Sarko, A. *Crystalline polymorphs of cellulose: prediction of structure and properties.* in *Applied polymer symposia.* 1976.

158.   Northolt, M. and H. De Vries, *Tensile deformation of regenerated and native cellulose fibres.* Die Angewandte Makromolekulare Chemie, 1985. **133**(1): p. 183-203.

159.   Santiago Cintrón, M., A.D. French, and G.P. Johnson, *PRELIMINARY MODULUS CALCULATIONS FOR CELLULOSE.* cal, 2010. **2**: p. 1.5.

160. Wu, X.M., Robert J.; Martini, Ashlie, *Calculation of single chain cellulose elasticity using fully atomistic modeling.* TAPPI Journal, 2011. **10**(4): p. 37-42.

161. Zimmerman, J., et al., *Calculation of stress in atomistic simulation.* Modelling and Simulation in Materials Science and Engineering, 2004. **12**(4): p. S319.

162. Huang, Y., J. Wu, and K.C. Hwang, *Thickness of graphene and single-wall carbon nanotubes.* Physical Review B, 2006. **74**(24): p. 245413.

163. Eichhorn, S.J., R.J. Young, and G.R. Davies, *Modeling crystal and molecular deformation in regenerated cellulose fibers.* Biomacromolecules, 2005. **6**(1): p. 507-513.

164. Tashiro, K. and M. Kobayashi, *Theoretical evaluation of three-dimensional elastic constants of native and regenerated celluloses: role of hydrogen bonds.* Polymer, 1991. **32**(8): p. 1516-1526.

165. Santiago Cintrón, M., G. Johnson, and A. French, *Young's modulus calculations for cellulose Iβ by MM3 and quantum mechanics.* Cellulose, 2011. **18**(3): p. 505-516.

166. Tanaka, F., Y. Doi, and T. Iwata, *The deformation of the chain molecules and crystallites in poly ([R]-3-hydroxybutyrate) and poly (4-hydroxybutyrate) under tensile stress.* Polymer Degradation and Stability, 2004. **85**(2): p. 893-901.

167. Maple, *Waterloo maple software.* University of Waterloo, Version 13, 2009.

168. Freindorf, M., E. Kraka, and D. Cremer, *A comprehensive analysis of hydrogen bond interactions based on local vibrational modes.* International Journal of Quantum Chemistry, 2012. **112**(19): p. 3174-3187.

169. Vries, A.d. and S.-J. Marrink. *Coarse-Grained Biomolecular Modeling*. October 17, 2011; Available from: http://www.cecam.org/workshop-0-501.html.

170. Centre for Molecular Simulation, S.U.o.T. *Molecular dynamics simulation* Available from: http://www.swinburne.edu.au/ict/research/cms/documents/disertations/Tu%20Cam%20Le/Chapter%204%20Molecular%20dynamics%20simulation.pdf.

171. Musacchio, S., *Effects of friction and polymers on 2d turbulence*, in *Dipartimento di fisica generale ``A. Avogadro''* 2004, Università degli studi di Torino.

172. Morriss-Andrews A Fau - Rottler, J., S.S. Rottler J Fau - Plotkin, and S.S. Plotkin, *A systematically coarse-grained model for DNA and its predictions for persistence length, stacking, twist, and chirality.* (1089-7690 (Electronic)).

173. Cook, R.D., et al., *Concepts and Applications of Finite Element Analysis*. 4th Edition ed: Wiley. 784 pages.

174. Chandrupatla, T.R. and A.D. Belegundu, *Introduction to Finite Elements in Engineering*: Prentice Hall College Div. 461 pages.

175. Taylor, R.L. *FEAP - - A Finite Element Analysis Program*. Available from: http://www.ce.berkeley.edu/projects/feap/.

176. Zienkiewicz, O.C., R.L. Taylor, and J.Z. Zhu, *The Finite Element Method: Its Basis and Fundamentals*. 6 edition ed: Butterworth-Heinemann.

177. Stærdahl, J.W. *Beam elements in 3D*. Available from: http://www.wind.civil.aau.dk/lecture/7sem_finite_element/lecture_notes/Lecture_6_7.pdf.

178. Rappé, A.K. and C. Casewit, *Molecular mechanics across chemistry*1997: University Science Books.

179. Klimeck, G., et al., *nanohub. org: Advancing education and research in nanotechnology*. Computing in Science & Engineering, 2008. **10**(5): p. 17-23.

180. Jmol, J., *an open-source Java viewer for chemical structures in 3D*. HYPERLINK http://jmol. sourceforge. net, 2012.

APPENDICES

Appendix A   Crystalline cellulose – Atomistic toolkit

Crystalline Cellulose -Atomistic toolkit [69] is a NanoHUB [179] simulation tool capable of generating and running molecular dynamic simulations of cellulose nanocrystals (CNCs).

LAMMPS [144] simulation code coupled with ReaxFF force field [141] provide the necessary simulations platform. C code capable of generating CNCs structures is used to populate the initial atomic positions based on Nishiyama et al. [9] reported coordinates. Different sizes and shapes, ranging from single chains to fully sized crystals, can be created with a simple but very powerful graphical user interface within the NanoHUB framework.
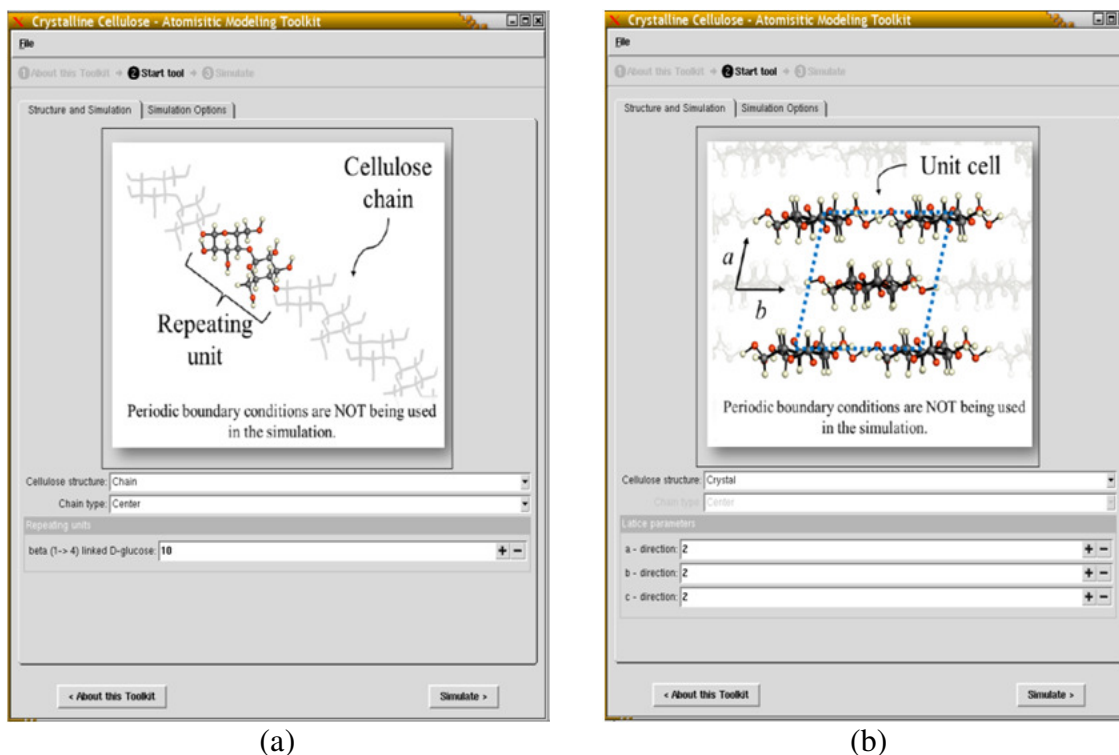

(a)   (b)

Figure A 1 Crystalline Cellulose - Atomistic toolkit [69] graphical user interface. (a) Panel used to define a single chain structure and length. (b) Panel used to define the size (in number of unit cells) of crystalline models.

Figure A 1 shows the "Structure" panel that defines the model characteristics. Two basic structures are available for selection, a single chain (Figure A 1a) and an entire crystal (Figure A 1b). Single chains are divided in *center* or *origin* according to the conformational types defined by Nishiyama et al. [9]. The number of glucose ring present in the chain, that is, the length of the chain, is also defined by the user.

Crystalline structures are constructed by repetition of the unit cell reported by Nishiyama et al. [9]. The repetition number for each lattice direction (*a*, *b* and *c*) is controlled by the user.

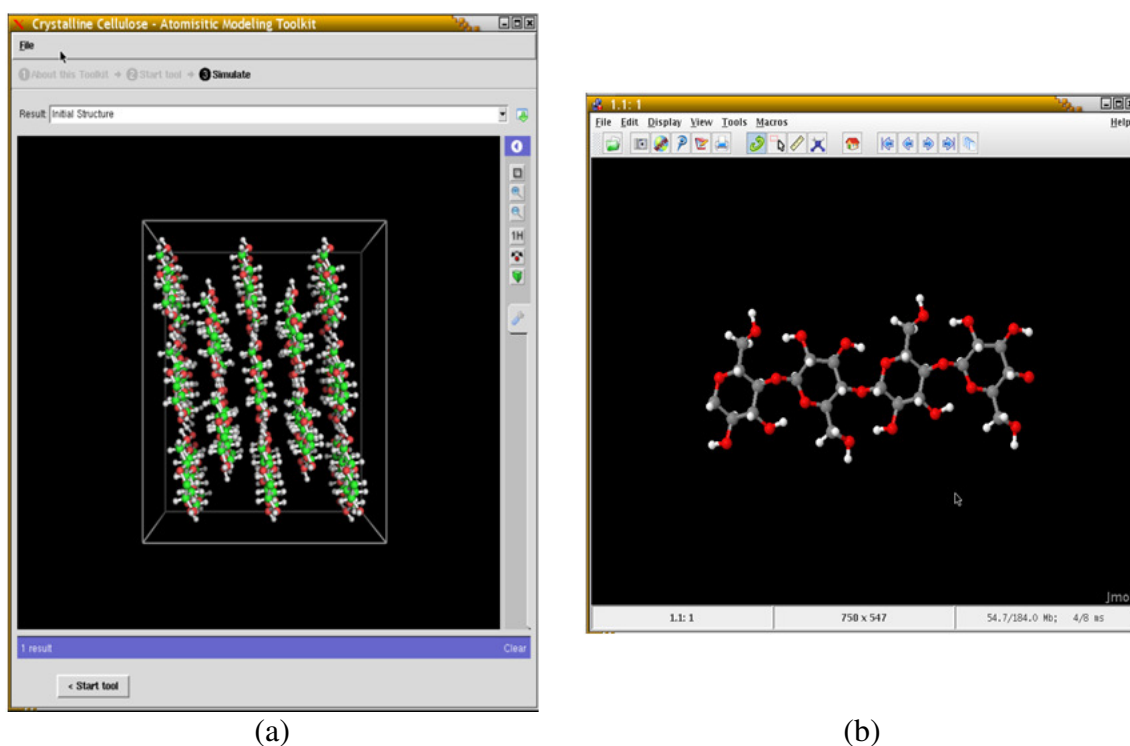(a)   (b)

Figure A 2 Crystalline Cellulose - Atomistic toolkit [69] graphical user interface. Results for: (a) 2x2x1 crystalline structure, (b) Single chain made of four glucose rings.

Molecular dynamic simulations are performed in LAMMPS [144] The system is equilibrated in a NVT ensemble (constant number of atoms, volume and temperature).

Several simulation parameters can be defined by the user, such as: temperature, timestep, total simulation time, hydrogen bond cutoff distance and force field parameterization.

JMOL viewer [180] provides state-of-the-art post-processing capabilities of atom trajectories as it can be observed in Figure A 2. XY-plots of temperature, potential energy, kinetic energy, total energy and hydrogen bonds energy are being automatically generated to help understanding the thermodynamic evolution of the simulated system (Figure A 3).
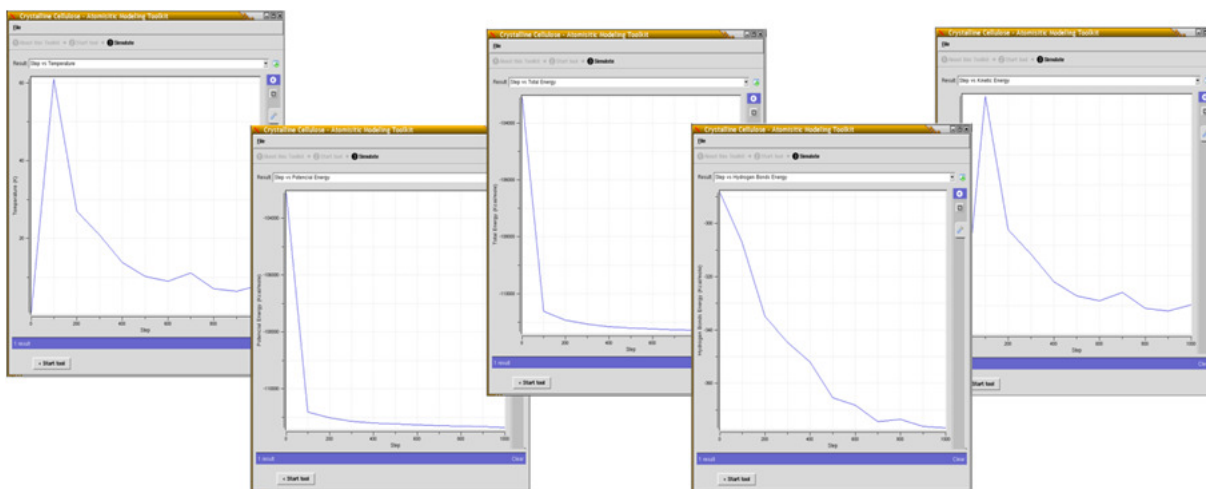

Figure A 3 Superposition of XY-plots for temperature, potential energy, kinetic energy, total energy and hydrogen bonds energy to demonstrate the output capabilities of Crystalline Cellulose - Atomistic toolkit [69].

Appendix B   <u>Anisotropy calculator - 3D visualization toolkit</u>

Anisotropy Calculator - 3D Visualization Toolkit [89] is a NanoHUB [179] visualization tool specifically developed to generate surface contour plots of Young's modulus based on a material compliance matrix (S_{ij}).
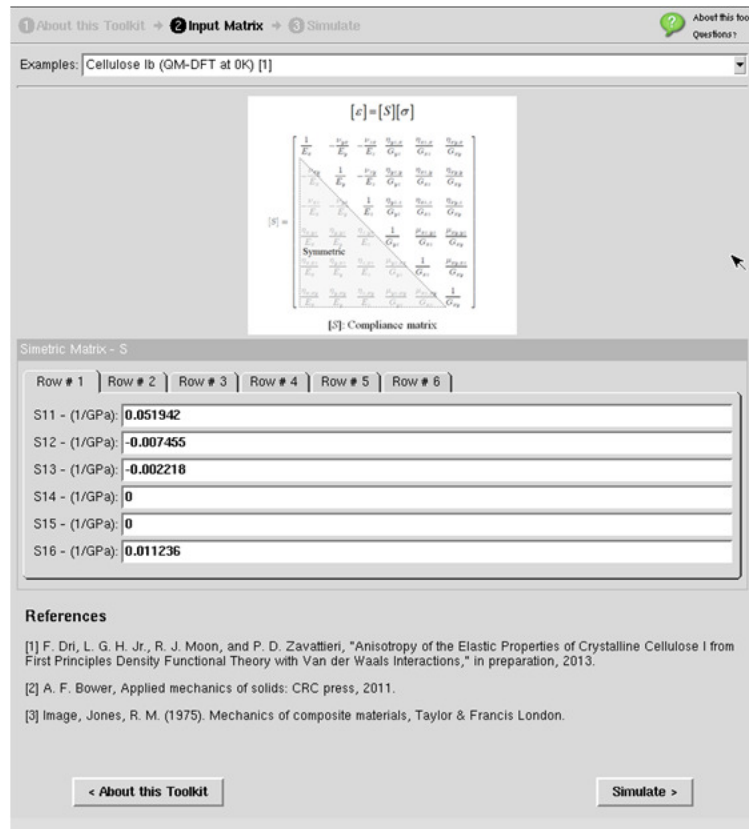

Figure B 1 Anisotropy Calculator - 3D Visualization Toolkit [89] input panel. Components of the compliance matrix are introduced by the user ordered by row. The simulate bottom triggers the visualization module.

Each point on the surface represents the magnitude of Young's modulus in the direction of a vector from the origin of the surface (i.e., at the intersection of the *1*, *2*, and *3* axes in the interior of the surface) to a given point on the surface. The shape of this surface is indicative of the anisotropy of the analyzed material. Additionally, color contours of

Young modulus values help identifying variations within a particular direction. For instance, the computed Young modulus surface for a linearly elastic isotropic material would be a perfect sphere with the same value (surface color) in any direction.

Figure B 1 shows the input panel where the user introduces the components of the compliance matrix for the material under analysis. Once the simulate bottom is pressed, the tool generates 3d contour plot to be manipulated in real time, as shown in Figure B 2a. A Tecplot data file (.dat) is also available for downloading (Figure B 2b).
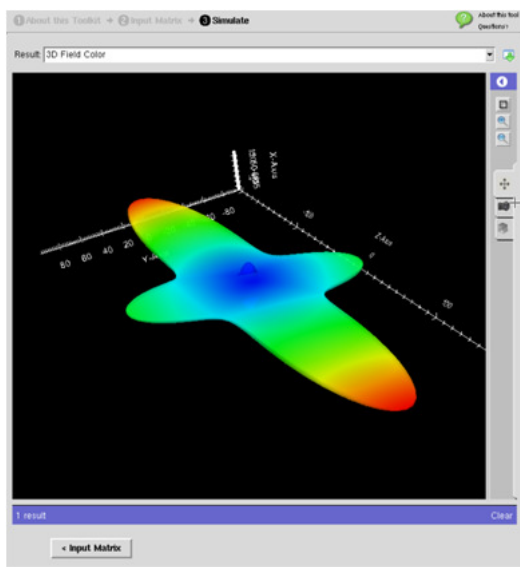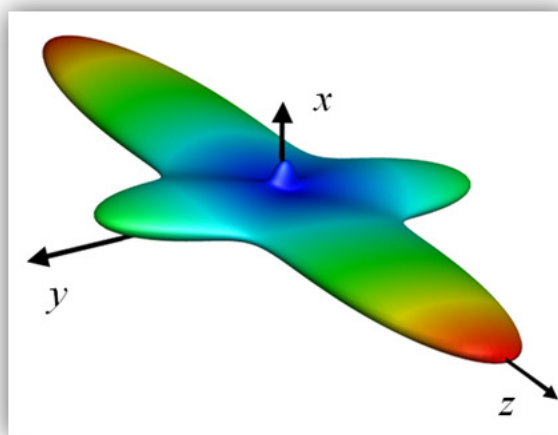
(a)   (b)

Figure B 2 Visualization options: (a) real time 3D manipulation capability provided by the tool. (b) Post-processing capabilities provided by the Tecplot data file.

Appendix C   Modified version of LAMMPS

LAMMPS (Large-scale Atomic/Molecular Massively Parallel Simulator) [131] is a classical molecular dynamics simulation code capable of modeling a wide range of materials from biomolecules and polymers to solid state metals and coarse-grained or mesoscopic systems. It can be used to model atoms or, more generally, as a parallel particle simulator at the atomic, meso, or continuum scale [144]. LAMMPS can run on single processors desktop machines or in high performance parallel computers. It was designed in C/C++ to be easy to modify or extend with new functionalities and it is distributed as an open source code under the terms of the GPL.

Several modifications were introduced in the original LAMMPS code. A new user interface was developed along with several futures for visualization and post-processing, increasing the productivity of the software. All the implementations were done using Message Passing Interface (MPI) retaining the ability of the original code to run in large parallel machines.

The first modification allows to change atomic coordinates between simulation steps directly from memory direction (RAM addresses). The user is now capable of introducing a deformation map directly into the simulation model, using LAMMPS powerful minimization capabilities to run molecular mechanics studies. The implementation is based on an umbrella code that manages boundary conditions and calls LAMMPS to perform energy minimizations [144]. This capability can be used with any of the force fields available in LAMMPS.

The second modification was applied to the ReaxFF force field implementation inside LAMMPS. All the computed parameters for the Hydrogen bonds including: donor and acceptor atoms, distance between donor and acceptor, hydrogen bond angle, interaction energy and bond order, are extracted directly from the force field source files during each time step in the simulation. This guarantees that the data being analyzed is exactly the one that is being computed inside the simulation code.

Finally, the modified version of LAMMPS is capable of generating Tecplot data files and layouts for: atom trajectories, hydrogen bond maps and energy curves, facilitating the post-processing of the results.

VITA

VITA

Fernando Luis Dri was born on August 11, 1985 in Buenos Aires, Argentina. After receiving his elementary and secondary education, he enrolled in the National University of La Plata where he earned his degree in Aeronautical Engineering. After working for one year as teaching assistant at the same university, he enrolled as a Ph.D. student at Purdue University on fall 2010.